Characterization of co-axial mixing systems to blend highly viscous and non-Newtonian fluids

vorgelegt von
Diplom-Ingenieurin Luciana Rudolph
aus Salvador

von der Fakultät III – Prozesswissenschaften
der Technischen Universität Berlin
zur Erlangung des akademischen Grades

Doktor der Ingenieurwissenschaften
Dr.-Ing.

genehmigte Dissertation

Promotionsausschuss:

Vorsitzende: Prof. Dr. rer. nat. Sabine Enders
Berichter: Prof. Dr.-Ing. Matthias Kraume
Berichter: Prof. Dr.-Ing. Reinhard Sperling

Tag der wissenschaftlichen Aussprache: 12. Dezember 2008

Berlin 2009
D 83

DANKSAGUNG

Die vorliegende Arbeit entstand während meiner Tätigkeit als Ingenieurin im Bereich Forschung und Entwicklung des Chemiekonzerns The Dow Chemical Company am Standort Schkopau (Sachsen-Anhalt). An dieser Stelle möchte ich meine Dankbarkeit und Anerkennung gegenüber meinem Arbeitgeber - The Dow Chemical Company - für die Möglichkeit, dieses Thema zu erforschen und zu veröffentlichen sowie für die Bereitstellung von sämtlichen für das Gelingen dieser Arbeit unverzichtbaren Mitteln und die Freiheit bei der Bearbeitung und fachlichen Ausrichtung der Arbeit ausdrücken. Diese Arbeit wäre in dieser Form ohne die Ermutigung und Unterstützung von Dr. Victor Atiemo-Obeng als Coach und Mentor dieses Forschungsthemas bei The Dow Chemical Company nicht möglich gewesen.

Mein besonderer Dank gilt meinem Doktorvater, Herrn Prof. Dr.-Ing. Matthias Kraume für seine kompetente und motivierende Betreuung meiner externen Arbeit, sein Interesse an der Thematik, seine stete freundliche Bereitschaft zu Diskussionen und die hervorragende Gelegenheit, mit ihm und seiner Gruppe in Berlin zusammen zu arbeiten. Herrn Prof. Dr.-Ing. Reinhard Sperling danke ich herzlich für die Übernahme des Zweitgutachtens und die vielen konstruktiven Anregungen. Weiterhin danke ich der Vorsitzenden des Promotionsausschusses, Frau Prof. Dr. rer. nat. Sabine Enders für die Übernahme der mit der Durchführung des Promotionsverfahrens verbundenen Tätigkeiten.

Meinem Kollegen, Herrn Dr. Matthias Schäfer danke ich sehr für die zahlreichen anregenden Fachgespräche und sein stetes Interesse am Fortgang der Arbeit. Dank gilt weiterhin Frau Kristin Weidner für ihr Engagement und ihre sorgfältige Unterstützung bei der Durchführung der Experimente.

Nicht zuletzt gilt mein ganz herzlicher Dank meinen Eltern für ihre bedingungslose und stets gewährte Unterstützung aller Art. Meinen Schwiegereltern – Lutz und Siegrun Rudolph - bin ich herzlichst dankbar für die unermüdliche Hilfsbereitschaft und den Beistand, speziell bei den unzähligen Kinderbetreuungstagen für meinen kleinen Sohn Bruno.

Aus tiefstem Herzen danke ich meinen Ehemann Dr. Jürgen Rudolph und meinen Sohn Bruno Lutz für den anhaltenden Beistand, die stetige Motivation und Geduld und vor allem für das Vertrauen in das Gelingen des Promotionsvorhabens. Euch widme ich diese Arbeit.

ACKNOWLEDGEMENTS

The present work was conducted during my job as Engineer in the Research and Development group of The Dow Chemical Company - site Schkopau (Saxony-Anhalt). At this point I want to thank and acknowledge the support of The Dow Chemical Company for allowing this research to be pursued and published, providing with the necessary resources for the realization of this thesis. This work would not have been possible without the encouragement and assistance of Dr. Victor Atiemo-Obeng, who coached and mentored this research topic at Dow.

I would like to express my gratitude and appreciation to my PhD supervisor Prof. Dr.-Ing. Matthias Kraume for his competent and motivating guidance of my external doctoral thesis, his interest in the topic and his always friendly willingness to discuss and interact. I am deeply grateful for the tremendous opportunity he presented me with to work with him and his group in Berlin. I also would like to thank Prof. Dr.-Ing. Reinhard Sperling for being the second examiner of this thesis as well as for his constructive suggestions. Many thanks to the president of my examination board Prof. Dr. rer. nat. Sabine Enders.

I would like to thank my colleague Dr. Matthias Schäfer for our several and always fruitful discussions and his interest in the progress of this thesis. Especial thanks to Kristin Weidner for her engagement and thorough support in conducting the experiments.

I cannot end without thanking my parents for their unconditional help that was always granted to me. I am also very grateful for the tireless assistance of my parents in law, Siegrun and Lutz Rudolph, especially in baby-sitting my little son many times.

From the bottom of my heart I thank my husband Dr. Jürgen Rudolph and my son Bruno Lutz for their persistent support, continued motivation and pacience and in particular for their trust. It is to them that I dedicate this work.

ABSTRACT

This doctoral thesis addresses the blending of highly viscous and non-Newtonian fluids in co-axial agitation systems, in particular in the laminar regime. An experimental and numerical study using a pilot-scale co-axial agitation system was carried out to explore and characterize the mixing performance. The characterization was based on blend time and power consumption measurements at different operating conditions. Two co-axial mixer configurations were employed in this investigation: a dual set of pitched-blade turbine (PBT) combined with a proximity impeller: the anchor or the Paravisc® (EKATO Rühr- und Mischtechnik GmbH).

The effects of the mutual interactions between the open and proximity impellers in the laminar regime for Newtonian and non-Newtonian fluids on the power consumption of each impeller were analyzed and described. It was shown that the power consumption of the proximity impeller is affected by the tip speed ratio and rotating mode, but no influence of the proximity impeller speed and rotational direction on the power drawn by the pitched blade turbines was observed. The results obtained in the numerical simulations (Computational Fluid Dynamics) demonstrated the ability to calculate the flow field with reasonable accuracy to describe these interactive effects on the power consumption of the impellers. The power curves were processed into single power master curves by introducing a parameter to account for the effect of the tip speed ratio.

Mixing time characteristic curves were developed to describe the efficiency of different mixer configurations in the laminar regime. Within the range of investigated operation, the results indicated that the co-axial mixer composed of Paravisc® and pitched blade turbines was found to be the most efficient configuration among the investigated co-axial mixer designs. The performance of all investigated co-axial mixer configurations was in general higher than the single impeller systems in the laminar regime. The data in the transitional regime suggested that the performance of the open impellers as single system becomes equivalent to the performance of the co-axial mixer configuration with the anchor and pitched-blade turbines. It was also shown that the anchor combined with PBT in co-rotating mode was more efficient than in counter-rotating mode in the laminar regime, but the performance of the both configurations apparently became similar as the transitional regime begins.

ZUSAMMENFASSUNG

Im Rahmen der vorliegenden Dissertation wurde die Homogenisierung hochviskoser und nicht-Newtonischer Flüssigkeiten in koaxialen Rührsystemen, insbesondere im laminaren Bereich, untersucht. Experimente und numerische Simulationen wurden mit dem Ziel durchgeführt, die Durchmischungsleistung von koaxialen Rührsystemen zu charakterisieren. Experimentelle Daten der Mischzeit und Rührerleistung, die als Basis zur Charakterisierung von Rührsystemen dienen, wurden in einem Behälter mit einem Koaxialrührwerk im Pilotmaßstab für verschiedene Betriebsbedingungen gewonnen. Zwei verschiedene Konfigurationen koaxialer Rührsysteme wurden untersucht. Ein zweistufiger Schrägblattrührer (SBR) wurde mit einem wandnahen Ankerrührer bzw. einem PARAVISC® (EKATO Rühr- und Mischtechnik GmbH) kombiniert.

Die Wechselwirkungseffekte der Rührer in den koaxialen Rührsystemen auf die Leistungsaufnahme für newtonsche und nicht-Newtonsche Flüssigkeiten im laminaren Bereich wurden beschrieben. Es wurde gezeigt, dass der Leistungsbedarf der wandnahen Rührer vom Drehfrequenzverhältnis und der Rührerdrehrichtung beeinflusst wurde, aber keinerlei Einfluss von der durch den wandnahen Rührer hervorgerufenen Strömung auf den Leistungsverbrauch der inneren Rührer beobachtet werden konnte. Die Ergebnisse der numerischen Simulationen zeigten, dass mit Hilfe der numerischen Strömungssimulation (Computational Fluid Dynamics) die komplexe Strömung mit hinreichender Genauigkeit beschrieben werden konnte, um die interaktiven Auswirkungen auf den Stromverbrauch der Rührer zu kennzeichnen. Die Leistungskurven wurden hierbei in Form von Einzelmasterkurven durch Einführung eines Parameters zur Berücksichtigung von Effekten des Drehfrequenzverhältnisses verarbeitet.

Es wurden Mischzeitcharakteristika zur Unterstützung der Effizienzbeschreibung im laminaren Bereich bei verschiedenen Rühreranordnungen entwickelt. Im untersuchten Bereich zeichnete sich das koaxiale Rührsystem aus Paravisc® und Schrägblattrührer als das effizienteste Design unter den untersuchten Rührsystemen aus. Insgesamt war die Effizienz aller untersuchten Koaxialrührer höher als diejenige der Einzelrührsysteme. Im Übergangsbereich gaben die Daten zu erkennen, dass sich die Performance der Innenrührer als Einzelsystem der Performance der koaxialen Rührerkonfiguration Anker mit SBR nahezu ebenbürtig zeigten. Es wurde gezeigt, dass der Ankerrührer in Kombination mit dem zweistufigen Schrägblattrührer in gleichsinniger Drehrichtung höhere Effizienz als in gegensinniger Drehrichtung aufweist. Die Durchmischungsleistung beider Konfigurationen gleicht sich hingegen im Übergangsbereich an.

CONTENTS

Nomenclature

C	constant	-
c	impeller clearance	m
D	impeller diameter	m
e_{ij}	rate of deformation	s^{-1}
F	force	N
F_D	drag force	N
G’	storage modulus	Pa
G”	loss modulus	Pa
g	gravitational acceleration	m/s^2
H	liquid level of a stirred tank	m
k	consistency index	Pa s^n
K_P	power constant	-
K_S	shear rate or Metzner Otto constant	-
L	length	m
M	torque	Nm
N	rotational impeller speed	rpm or s^{-1}
N_R	relative rotational impeller speed	rpm or s^{-1}
N_1	first shear stress difference	Pa
n	shear thinning index	-
P	power consumption	W
p	pressure	Pa
p_r	impeller pitch	m
R	impeller radius or radial length	m
S	Impellers distance	m
T	tank diameter	m
t	temperature	°C
tr	tip speed ratio, $\frac{v_i}{v_o}$	-
u	velocity of the continuum phase	m/s

u_P	velocity of the particle	m/s
v	tip speed, $2\pi DN$	m/s
W	impeller blade width	m
w_i	velocity vector in direction i	m/s

Dimensionless numbers:

Re	Reynolds number, $Re = \frac{\rho v D}{\eta}$	-
Ne	Newton number, $Ne = \frac{P}{\rho N^3 D^5}$	-
Fo	Fourier number, $Fo = \frac{1}{Re_V} = \frac{\eta\theta}{\rho T^2}$	-
Fr	Froude number, $Fr = \frac{N^2 D}{g}$	-
Fl	Flow number, $Fl = \frac{Q}{ND^3}$	-
Pe	Péclet number, $Pe = \frac{\rho v L}{\Gamma}$	-
Re_V	vessel Reynolds number, $Re_V = \frac{\rho T^2}{\eta\theta}$	-

Greek letters:

Γ	diffusion coefficient	m^2/s
ε_M	power input per unit mass	W/kg
ϕ	arbitrary scalar or variable	-
$\dot{\gamma}$	shear rate	s^{-1}
η or μ	dynamic viscosity	Pa s
θ or Θ	mixing time	s
ρ	density of fluid	kg/m^3
τ	shear stress	Pa
τ_o	yield stress	Pa

Indexes:

co-axial	co-axial impellers
i	inner (open) impeller
i, j, k	vector directions
o	outer (proximity) impeller
P	particle
r	radial component
tip	tip speed
z	axial component
θ	tangential component

1 Introduction and Motivation

The importance of mixing unit operations including gas-liquid, miscible liquid-liquid, immiscible liquid-liquid, solid-liquid, and gas-solid-liquid, in the petrochemical industries is beyond all question. The most common mixing unit is certainly a mechanically agitated vessel, which usually consists of a jacketed vessel, impeller, baffles, nozzles, instrumentation, variable speed drives and other components. Figure 1-1 shows a standard configuration of a mechanically agitated vessel. The primary task of the mixing equipment is to reduce the gradients of scalar variables of the fluid (temperature, concentration, density, viscosity, etc.) throughout the vessel, which are caused by differences in temperature, physical or chemical properties between feeds and vessel content. The process objective determines the desired degree of homogeneity to be delivered by the mixing unit.

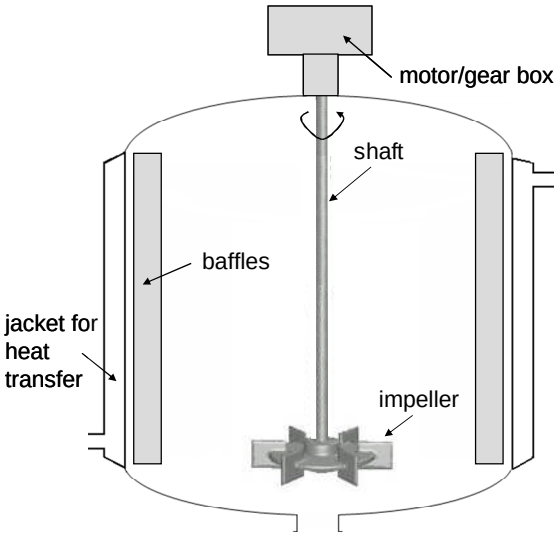

Figure 1-1: Common features of a mechanically agitated tank

The relevance of the mixing step in the industrial processes is better understood by measuring the consequences of an ineffective design of the mixing system. Scale-up errors and poor mixing result in significant increase in cost of manufacturing, long cycle time causing delays in marketing of the product and, in worst case, increase of safety risks. The cost of poor mixing was estimated to be of the order of US$ 1 to 10 billion in the U.S. chemical industry alone. In one large multinational chemical company, a lost value of US$100 million per annum was estimated in 1993 due to an inadequate understanding of the mixing (Paul *et al.* 2004).

The design of mixing equipment must go beyond the selection of mixer types for a given application that satisfies industrial duties. The poor understanding of mixing processes can be hidden by the overdesign; and this may then go undetected if assessed by product quality. However, the penalty of ignorance in terms of capital and operating costs can be severe (Harnby *et al.* 1992). Mixing solutions must consider primarily the most effective design to achieve the key process objectives.

Many of the industrial mixing processes involve highly viscous fluids with complex rheology. Such processes can be found in polymer based industries involved in the manufacturing and processing of rubbers, plastics, fibers, resins, coatings, sealants and adhesives as well as in the food processing industries, biotechnological operations and in the manufacturing of fertilizers, detergents, propellant, explosives, etc. Although the mixing of highly viscous fluids is a widely used operation in the industry, it is a very difficult operation, and often considered as the limiting step in chemical processes. The power input necessary to create enough turbulence in the vessel with highly viscous fluid is economically and/or technically prohibitive and the mixing has to occur in the laminar regime, where viscous forces overwhelm inertial forces. The understanding of laminar mixing is still not perfect and the understanding of turbulent mixing is still limited (Paul *et al.*, 2004). However the common working definitions available today allow us to describe turbulent mixing as the complex interaction and layering of a myriad of small and large fluid structures, such as eddies, vortices and sweeps, reflecting in intense velocity fluctuations in time and in all three dimensions in space. In turbulent mixing, there is a continuous reorientation of the fluid particles. The energy input per mass unit in turbulent mixing is relatively low to reach the target mixing time – and much lower than the one necessary in laminar flow at the same rotational speed. In laminar mixing, the fluid structures and any infinitesimal disturbances are damped out, so that fluid particles can follow concentric and closed streamlines (by applying time-independent forces) for a very long period of time. Thus, it is crucial to disrupt the continuous trajectory of the fluid and create a certain degree of chaos to achieve the desired degree of uniformity in the system. The reorientation of the fluid elements, the repetition of cycles of deformation mechanisms, like shearing, upsetting, stretching, folding, kneading and exploiting back and secondary flows, are highly necessary to increase the contact area of both materials and, hence, increasing the molecular diffusive transport.

In the industry, most of the highly viscous fluids exhibit non-Newtonian flow behavior. The shear dependent viscosity and viscoelasticity are common rheological complexities, which pose additional challenges in the design of the mixing equipment, so also are features such as thixotropy and yield stress. All of these properties increase the complexity in selecting, designing and operating the mixer. In shear-thinning fluids, the energy input transferred to the fluid through the impellers remains localized in the vicinity of the impellers. As the distance from the impeller blades increases, the shear rates decrease and the viscosity increases, resulting in an inhomogeneous viscosity distribution in the tank. The formation of compartmentalized flow, caverns and dead zones appear quite often in mixing tanks with highly viscous and non-Newtonian fluids. For manufacturing poor macro-mixing problems result in reduction of end-product quality, increase of by-products, broad chain of polymer, long cycle time, cleaning problems, fouling, etc.

The challenge in the design of the agitated vessel system is the selection of the most efficient impeller, which is optimized for a certain mixing operation (blending, dispersion, suspension of solids and heat transfer) and a viscosity range.

In the low viscosity range, open impellers operating at high speeds in baffled tanks are preferred, e.g. turbine impellers. The mixing action of open impellers at high rotational speeds in low viscous liquids relies on the turbulence that carries the energy from the impeller into far sections of the vessel.

In high viscosity mixing, open impellers are inefficient due the viscous damping of the momentum transport resulting often in stagnant zones far from the impeller. Large or close-clearance impellers (also called proximity impellers) are more commonly employed to fulfill this task. Because of their size they are able to move a large portion of fluid, primarily by tangential induction. Examples include gate impellers, anchor, helical ribbon, helical screw and combined screw-ribbon. The high efficiency of the ribbon impellers in the high viscosity mixing is mainly due to their good pumping capacity and efficiency to promote top-to-bottom mixing, which enables the re-arrangement, recirculation and secondary flows inside the entire vessel. Added to this capability, the small clearance between impeller blade and vessel wall makes this type of impellers very appropriate for processes, in which homogenization and heat transfer are required simultaneously.

The choice of a suitable mixer is particularly challenging when the mixing process occurs over a wide range of viscosity. A common process, in which the fluid viscosity increases during the manufacturing, occurs, for instance, in polymerization reactors. The

initial viscosity is that of monomer and/or solvents and the final viscosity is that of the polymer or polymer solution, which can easily vary by a factor greater than 10,000.

Co-axial impeller systems offer a very promising and versatile alternative for such processes because they consist of a combination of high speed open impellers and a close-clearance impeller; and both impellers rotate independently on the same reactor axis (Figure 1-2). The co-axial mixing system combines the effectiveness of open impellers in the low viscosity range and proximity impellers in the high viscosity range. At low viscosities, the proximity impeller can serve as a baffle for the open impeller that would have the primary mixing task. At high viscosities, the inner impeller would gradually loose its efficiency and the outer impeller would do the major mixing work. Moreover, co-axial mixers are efficient in high viscosity mixing because of the synergistic fluid dynamic effects of two independent rotating impellers. The flexibility of co-axial mixers is also appreciated; and it seems also very favorable, in particular, in the modern production plants, since it makes possible the manufacturing of a broad spectrum of products with a broad range of viscosities. In the manufacturing of specialty chemicals, for instance, where “time-to-market” plays an important role, the co-axial mixers have the best performance features to fulfill the mixing challenges in this type of business: the processing of diverse products over a wide range of viscosities in the same vessel, the achievement of high yields and high end-product quality at low cycle batch times.

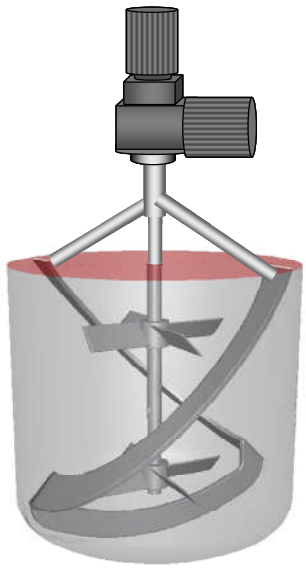

Figure 1-2: Co-axial mixer

The design of co-axial mixers today is essentially based on the vendor's experience and/or trial-and-error approach. Consequently, the utilization of such non-conventional mixing technology in industrial processes today is not common.

An important consideration in the design of an agitated system is the power required to drive the impeller and the mixing time to achieve process objectives. A reliable design and scale-up of important mixing tasks such as blending and heat transfer is generally achieved by invoking geometric and fluid dynamic similarity based on selected dimensionless parameters. For single impellers in standard baffled tanks the utilization of dimensionless numbers, such as Reynolds, Newton, Prandtl, Nusselt is very well established. For complex mixing systems such as co-axial mixers it is not trivial, because of the presence of two impellers that have different geometries and rotate with different speeds in the same vessel. This poses a challenge to determine the appropriate scaling parameters that govern the flow and mixing phenomena. Therefore, the understanding of the fluid mechanics characteristics is absolutely required to establish the design and scale-up guidelines.

The present work addresses the blending of highly viscous and non-Newtonian fluids with co-axial agitation systems, in particular in the laminar regime. The objective is the establishment of new fundamental knowledge about the fluid dynamics and performance of co-axial mixers in non-Newtonian viscous blending. Experimental data of mixing time and power consumption, which are the general basis for the characterization of the performance of agitation systems, were obtained in a pilot-scale-tank equipped with fully instrumented co-axial mixers. The extensive experimental program included the investigation of different operating conditions such as viscosity, rotational speed ratio, rotating mode (co- and counter-rotation) and total energy input per mass unit.

Experiments play a central role to characterize the power and mixing time of co-axial mixers in this work, since the few available experimental data in the open literature today are very specific for the tested geometry and operation conditions. Co-axial mixers with the configurations used in the present work, which are very suitable for chemical processes, had not been previously investigated or published yet.

The experiments were supported by numerical simulations carried out in the commercial Computational Fluid Dynamics (CFD) code FLUENT® version 6.3. Simulations enable the visualization of the flow patterns created by the impellers in the tank, serving as a primary tool to support the experimentally observed phenomena and also to understand them. In addition, CFD yields the complete three-dimensional flow field that allows its interpretation

in a much easier form than in the experiments. Last, but not least, numerical simulations with CFD open the possibility to reduce the costs linked to the experimental studies that are normally necessary in the design of large scale of co-axial mixing systems, or when any other design modification in the system takes place.

2 Blending of Highly Viscous Fluids - Literature Review

In this chapter, the status of today's knowledge about the laminar blending of highly viscous fluids in standard mechanically agitated vessel as well as in co-axial mixers is reviewed. The nomenclature used to describe the geometry of agitated tanks in the following sections is illustrated in Figure 2-1.

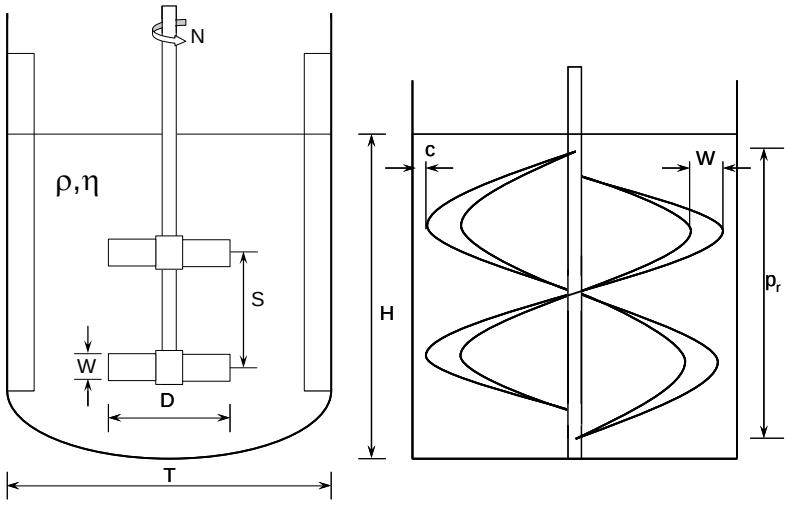

Figure 2-1: Nomenclature of a stirred tank equipped with open impellers and baffles (left) and close clearance impeller (right)

2.1 Impeller power characteristics

2.1.1 Newtonian fluids

The power input is the rate of energy that the impellers dissipate within the fluid. The power consumption (P) of an agitated system is a function of diverse parameters:

$$P = f(\rho, \eta, N, g, D, T, W, H, ...) \tag{2-1}$$

Depending on the configuration of the agitated system, other geometrical dimensions, such as the distance between impeller and vessel bottom, number of impeller blades, number of baffles, baffle width (W), pitch of the impeller blade (p_r) and in case of a dual set of impellers, the distance between the upper and lower impellers (S) can be added to the list of influencing parameters.

The application of the dimensionless analysis can describe the power consumption of an agitated system. According to the Theorem of Π-Buckingham, the number of independent dimensionless groups that can be used to describe the power consumption, which is a function of n variables, is equal to (n-r), where r is usually the number of the basic dimensions necessary to express the variables (mass, length, time). Considering the present example, there are nine influencing variables, which become six dimensionless numbers:

$$\frac{P}{\rho N^3 D^5} = C\left(\frac{\eta}{\rho N D^2}\right)\left(\frac{N^2 D}{g}\right)\left(\frac{T}{D}\right)\left(\frac{W}{D}\right)\left(\frac{H}{D}\right),... \qquad (2\text{-}2)$$

where, the following dimensionless numbers are well known:

$$Ne = \frac{P}{\rho \cdot N^3 \cdot D^5} \qquad \text{Newton number or Power number} \qquad (2\text{-}3)$$

$$Re = \frac{\rho \cdot N \cdot D^2}{\eta} \qquad \text{Reynolds number} \qquad (2\text{-}4)$$

$$Fr = \frac{N^2 D}{g} \qquad \text{Froude number} \qquad (2\text{-}5)$$

The effects of the gravity forces are described by Froude number. This is usually important only in tanks, where vortexing exists. It can be negligible for tanks with baffles and in laminar flows (Nagata, 1975). Neglecting the Froude number, the Newton number becomes a function of Reynolds number and geometrical ratios. Considering geometrically similar systems, the Newton number becomes a function only of the Reynolds number. A log-log plot of Newton number versus Reynolds number is referred as a power curve. The general features of power curves are shown in Figure 2-2. Three regimes are differentiated in the plot depending on the Reynolds number. In the laminar regime of the power curve the Newton number decreases linearly in logarithmic scale with the Reynolds number (Re < 100). The slope of the curve is -1, indicating that:

$$Ne\ Re = K_P \quad \text{or} \quad log(Ne) = -log(Re) + log(K_P) \qquad (2\text{-}6)$$

K_P is a constant depending upon the system geometry. Each particular impeller has a value of K_P.

Table 2-1 summarizes published data for the constant K_P of different impellers, which were experimentally measured. The deviation between the published values for the same impeller type is due to slight differences in the geometry of the mixing systems.

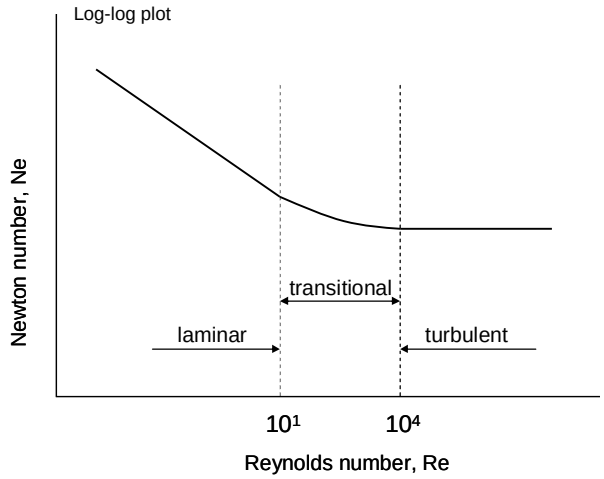

Figure 2-2: Impeller power curve

In the turbulent regime of the power curve the Newton number is independent of the Reynolds number ($Re > 10^4$). Each particular impeller has a characteristic value for the Newton number in the turbulent regime. In the transitional regime, there is no simple mathematical relationship between Newton number and Reynolds number.

The power curve is an individual feature of each agitation system. Thus, the power requirement of the impeller can be read from the power curve if the impeller speed is known. Power curves for many impeller types are available in the open literature, which can be used to design the power consumption of the impeller in a larger agitated system, for instance. However, this can only be used, if the system is geometrically similar, i.e. it depends on the impeller geometry in relation to the vessel geometry.

The prediction of the power consumption of a given impeller for a Newtonian fluid of viscosity η and density ρ is quite simple in laminar regime. Knowing the K_P, the diameter and rotational speed of the impeller, it is possible to calculate the Newton number. However, this procedure doesn't apply for non-Newtonian fluids, because the viscosity is not constant.

2.1.2 Non-Newtonian fluids

During the process of mixing, the fluid is subjected to shear deformation. This shearing flow is caused by significant flow velocity variation within the vessel, on one side the fluid rotates with the impeller and on the other side it adheres to the tank wall. The mixing of

highly viscous liquids is complex because the viscosity can have a complex correlation with the shear deformation applied by the impeller. In order to accurately design agitation systems for highly viscous fluids, it is important to understand appropriately the effect of the fluid behavior on the mixing process.

Table 2-1: Some published K_P values for several impeller types

Impeller	K_P	Reference	Detail
Anchor	420	Zlokarnik (1967)	
	260	Oldshue (1983)	
	253	Thibault and Tanguy (2002)	
	185	Kuriyama et *al.* (1982)	c/T=0.05
	203	Takahashi *et al.* (1980)	c/T=0.025; W/T=0.102
	194	Novàk and Rieger (1975)	D/T=0.9; c/D=0.05
Double Helical Ribbon	1000	Zlokarnik (1999)	p_r/D; D/T;
	276.6	Rieger *et al.* (1985)	p_r/D=1.5; c/D=0.03; W/T=0.1
	351	Takahashi *et al.* (1980)	c/T=0.031; p_r/T=0.98
	326	Kuriyama *et al.* (1982)	Numerical analysis
	330	Nagata *et al.* (1972)	p_r/D=1; D/T=0.95
	296	Novàk and Rieger (1975)	p_r/D=1 D/T=0.95; c/D=0.025
PARAVISC®	315	Delaplace *et al.* (2000a)	
	329	Barar Pour *et al.* (2007)	
	290	Stein (1993)	
Pitched blade turbine (45°, 4 blades)	44.5	Oldshue (1983)	
	54	Kuncewicz and Pietrzykowski (2001)	
	34.4	Ascanio *et al.* (2003)	
Rushton Turbine (6 blades)	70	Nagata *et al.* (1971)	D/T=0.5
	72	Espinosa-Solares *et al.* (1997)	

Newton introduced the dynamic viscosity η as quotient of the shear stress, τ , and shear rate, $\dot{\gamma}$, as the measure for the internal resistance to flow in fluids under shear. Figure 2-3 shows the most common flow curves and viscosity curves for different materials. For Newtonian fluids the shear rate is directly proportional to the shear stress (curve "a"). Any deviation from a straight line in the diagrams therefore indicates non-Newtonian behavior.

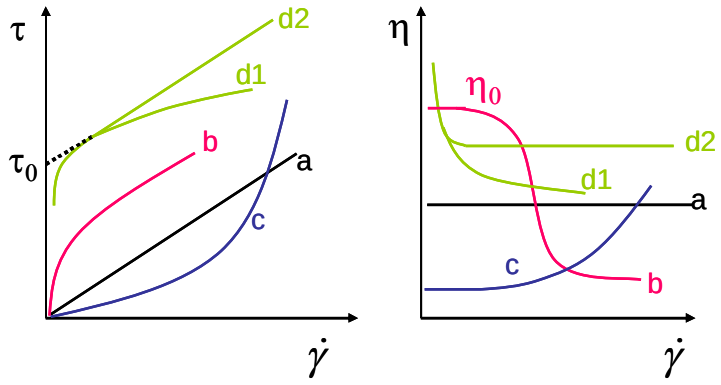

Figure 2-3: Typical flow and viscosity curves; (a) Newtonian, (b) shear thinning, (c) dilatant or shear thickening, (d1) plastic with yield stress, (d2) Bingham

The different flow behavior can be described by different mathematical models. The most widely used models are discussed here, but other models are described, for instance in (Ulbrecht and Patterson, 1985). The simplest model describes the linear correlation between shear stress and shear rate:

Newton: $$\tau = \eta \cdot \dot{\gamma} \quad , \eta = const. \tag{2-7}$$

Shear thinning and shear thickening behavior, represented by curve "b" and curve "c", respectively, in Figure 2-3, can be described by the Ostwald-de Waele model, also known as power law model:

Ostwald-de Waele: $$\tau = k \cdot \dot{\gamma}^{n} \qquad \eta = k \cdot \dot{\gamma}^{n-1} \tag{2-8}$$

The power law model can describe the flow or viscosity curve for many fluids with an acceptable accuracy over a range of shear rates. The parameter k is the consistency index and n is the shear thinning index or flow behavior index.

For the materials with plastic behavior, represented by curves "d_1" and "d_2"in Figure 2-3, the viscosity rises steeply with decreasing shear rates. These materials behave like a solid until a finite shear stress is exceeded. The threshold stress, τ_0, is called the yield stress.

Fluid begins to flow only when the shear stress exceeds the yield stress. Bingham fluids (curve "d_2") follow such behavior and can be described by the following model:

Bingham: $$\tau = \tau_o + \eta \cdot \dot{\gamma} \tag{2-9}$$

The Herschel-Bulkley model takes nonlinear shearing effects into account and has been successful in describing the flow behavior of materials with complex rheology. This model is a combination of a simplified Bingham model and power law:

$$\tau = \tau_o + k \cdot \dot{\gamma}^n$$

Herschel-Bulkley: $$\eta = \frac{\tau_o}{\dot{\gamma}} + k \cdot \dot{\gamma}^{n-1} \tag{2-10}$$

For $\tau_o = 0$, the Herschel-Bulkley model becomes the power law model and for n=1, it becomes the Bingham flow model.

It is very common that viscosity depends on temperature. Furthermore, fluids can also exhibit a time dependent viscosity. If the viscosity increases with time at constant shear rate, this effect is called rheopexy. More frequently however, is the effect of thixotropy, which describes the decrease of the viscosity with time at constant shear rate. Thixotropic materials are liquified by shaking, solidified again after a period of time.

Besides the described viscous fluid characteristics, a non-Newtonian fluid can also exhibit viscoelastic behavior. The viscoelastic behavior of a fluid can be observed when it is stirred. A peculiar phenomenon occurs, i.e. part of the liquid rises along the shaft of the impeller. It is also described as Weissenberg effect and this phenomenon is basically attributed to a force generated in the liquid by the rotational flow which competes with the centrifugal forces of inertia. The effect of the fluid's viscoelasticity on the power draw of the impellers is not yet completely understood, but it appears that its influence is slight in the viscous regime (Ulbrecht and Patterson, 1985).

In the mixing of shear thinning fluids, impeller viscosity and process viscosity are differentiated. The impeller viscosity is the fluid viscosity in the immediate vicinity of the impeller blades. The process viscosity will vary throughout the fluid in proportion to the shear rate variation throughout the fluid. The impeller viscosity is the controlling factor in the design, with respect to power consumption calculations. It is also called apparent viscosity or effective viscosity. The effective viscosity in the mixing tank is determined by

the relationship of the viscosity and the shear rate as well as the relationship between shear rate and impeller speed, which can be estimated by using the Metzner-Otto concept.

Metzner and Otto concept stipulates that the effective rate of deformation by an impeller, $\dot{\gamma}$, is proportional to the impeller rotational speed (*N*) in the laminar flow regime (Metzner and Otto, 1957):

$$\dot{\gamma} = K_s \cdot N \tag{2-11}$$

The constant of proportionality, K_S in Eq.(2-11) is the mixer shear rate constant, also called as Metzner and Otto constant. The Metzner-Otto relationship applies for non-Newtonian fluids with shear-thinning behavior only. In shear-thickening fluids and Bingham plastics, for instance, the shear rates are highly localized around the impeller and the fluid is almost stagnant in the rest of the vessel. The Metzner-Otto approach is not applicable in turbulent flow either (Paul *et al.*, 2004).

For illustration of the concept, one may consider two identical sets of mixing equipment, one of which contains a Newtonian fluid and the other a non-Newtonian fluid. These fluids are agitated in the laminar region, with the same impeller speed used in each setup. One then varies the viscosity of the Newtonian fluid by thickening it or diluting it as needed, so that the power draw is the same for the Newtonian fluid and non-Newtonian fluid. Then, because all variables are identical, one may say that the viscosities affecting the impellers are the same in both pieces of equipment. Upon measuring the viscosity of the Newtonian fluid, one knows the apparent viscosity of the non-Newtonian fluid existing under the given experimental condition (Metzner and Otto, 1957).

To determine the Metzner-Otto constant one measures the power consumption in the non-Newtonian fluid at various impeller speeds. The measured power consumption at each impeller speed is converted into Newton number versus impeller speed (N) by using Eq.(2-3). The Newton numbers are used to read the corresponding Reynolds numbers out of a power curve measured in a Newtonian fluid. The apparent viscosity is then calculated from the Reynolds numbers by using Eq.(2-4). By doing so, the measured curve for the power consumption as function of the impeller rotational speed (N) is converted into a curve for the apparent viscosity as function of the impeller rotational speed. In the next step, the function of apparent viscosity over impeller rotational speed is compared with the function of viscosity over shear rate. This function is measured in a rheometer or viscometer. Thus, a

linear function of shear rate over rotational speed is obtained in the laminar regime, in which the slope is the Metzner-Otto constant.

The use of the Metzner-Otto-concept in impeller design is such that one starts with the required impeller diameter and impeller speed for engineering reasons. With the impeller speed and the Metzner-Otto constant, the effective shear rate is calculated. The effective shear rate is used to determine the apparent viscosity from the measured function of viscosity over shear rate. With the apparent viscosity, the impeller Reynolds number is calculated, so that the corresponding Newton number can be determined from an available power curve achieved for Newtonian liquids. With the obtained Newton number, the required shaft power can be calculated by using Eq.(2-3).

The Novák-Rieger approach (Rieger and Novák, 1973) can be applied in cases when viscosity as function of the shear rate is not known. For highly complex fluids it can be very appropriate. This approach requires the measurement of the power curve for Newtonian fluids and the power as function of the rotational speed of the impeller system for the non-Newtonian fluid. The Newton number is calculated from the measured power at the corresponding impeller speed, so that a curve of Newton number versus impeller speed is plotted. Here, the Newton numbers are used to read the corresponding Reynolds numbers out of a power curve measured in a Newtonian fluid as well. A representative viscosity can be calculated from each corresponding Reynolds number:

$$\eta_{rep} = \frac{\rho N D^2}{Re} \tag{2-12}$$

The representative viscosities can be plotted as function of the rotational impeller speed. The advantages of the Novák-Rieger method are: it is valid in the turbulent regime, it does not require viscosity versus shear rate measurements, and it can be applied for complex rheological fluids. The disadvantage is that the impeller system and fluids are highly coupled.

Novák-Rieger approach can be applied in a different manner to determine the constant K_S in laminar regime. The representative viscosity of non-Newtonian fluids must be described by power law, Eq.(2-8), and the shear rate is determined by employing the Metzner-Otto approach, Eq.(2-11), so that:

$$k\left(K_S N\right)^{n-1} = \frac{\rho N D^2}{Re} \tag{2-13}$$

After some algebraic transformations, K_S is expressed as:

$$K_S^{\,n-1} = \frac{\rho N^{2-n} D^2}{k\, Re} \tag{2-14}$$

If a power law Reynolds number Re_{pl} is defined as:

$$\mathrm{Re}_{pl} = \frac{\rho N^{2-n} D^2}{k} \tag{2-15}$$

and replacing the power-law Reynolds number Re_{pl} in Eq.(2-14), the following expression can be found for the constant K_S:

$$K_S = \left(\frac{\mathrm{Re}_{pl}\, Ne}{K_P} \right)^{\frac{1}{n-1}} = \left(\frac{K_P(n)}{K_P(n=1)} \right)^{\frac{1}{n-1}} \tag{2-16}$$

In Table 2-2, some published values of the shear rate constant K_S for different impellers are summarized.

Table 2-2: Some published values for the shear rate constant K_S of several impellers

Impeller	K_S	Reference
Anchor	25	Nagata *et al.* (1972)
	22	Foucault *et al.* (2005)
Double helical ribbon	28.2	Takahashi (1984)
	30.6	Chowdhury and Tiwari (1979)
	30	Nagata *et al.* (1972)
Paravisc	33.7	Delaplace *et al.* (2000a)
Rushton	12	Paul *et al.* (2004)
	11.5	Harnby *et al.* (1992)
	11.8	Nagata *et al.* (1972)
	10	Foucault *et al.* (2005)
A200	8.58	Kelly and Gigas (2003)

2.2 Simple systems of impellers

The power drawn by the impeller gives a measure of the energy dissipation within the stirred tank. The impeller rotational movement creates in the liquid a three dimensional

flow and each type of impeller dissipates the energy differently, because they create distinct flow patterns in the tank. Thus, the mixing process result is highly influenced by the impeller flow patterns. The impeller flow patterns in a stirred vessel are the result of several parameters, such as:

- rotational speed of the impellers
- geometry of the impellers
- number of impellers
- spacing between impellers
- position of the impeller in the vessel
- presence of baffles or internals
- viscosity of the fluid

2.2.1 Turbulent flow patterns for turbine impellers

The bulk flow pattern in an agitated tank is typically characterized by the prevailing flows generated by the impellers as radial or axial flow patterns. The axial flow impellers, including propellers, pitched-blade turbines and hydrofoils, produce dominantly a flow pattern throughout the entire tank volume as a single loop. Radial flow impellers, such as flat-bladed and disk turbines (Rushton) produce a strong radial jet outwards from the impeller that deflects near the wall, creating two circulating loops, one below and one above the impeller. A recirculation flow enters the center of the turbine from above and below. The flow patterns illustrated in Figure 2-4 are created by two widely used open impellers in baffled tanks with flat bottom, disk turbine and pitched blade turbine (PBT with 45° angle of inclination) in turbulent regime. The flow patterns were calculating by using the CFD code FLUENT®. The numerical simulations used the standard k-ε turbulence model and it was assumed a flat liquid free surface (no vortex effect).

In the turbulent regime, agitated tanks are commonly equipped with four baffles to prevent gross vortexing. The function of the baffles is to convert rotational (tangential) flow, induced by the impeller rotational speed, into axial and radial flow. Hence, internal circulation and mixing in the tank is promoted, but at cost of higher power consumption. In laminar regime, the viscous forces at the wall are sufficient to avoid the formation of a vortex, and baffles are not needed.

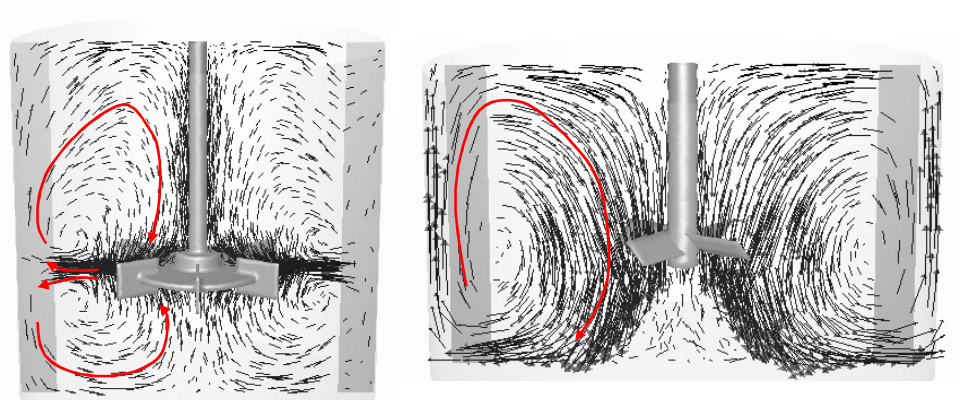

Figure 2-4: Flow patterns created by the radial flow impeller disk turbine (left) and the axial flow impeller pitched-blade turbine (right) at Re~104, Viscosity 0.001 Pas. Flow field calculated with FLUENT® software.

2.2.2 Laminar flow patterns for turbine impellers

The flow pattern of any axial pumping impeller will shift to that of a radial pumping impeller with increasing viscosity. In general, as the Reynolds number decreases the fluid's resistance to flow increases and thus the axial flow discharge of these impellers becomes more radial. In the laminar region, i.e. high viscosity applications, it can result in 0° discharge angle and pure radial flow (Weetman and Coyle, 1989). Later, Weetman (1991) studied the performance of the impeller A410 from Lightnin, which is a highly axial-flow impeller and his experiments in transitional regime indicated that the discharge from the A410 impeller exhibited some radial character in this flow regime. Fangary *et al.* (2000) also showed that A410 and A320 axial flow impellers behaved predominantly as radial flow impellers as the fluid viscosity was increased.

Figure 2-5 shows the flow patterns for the same disk turbine and pitched blade turbine, rotating at the same rotational speeds in a liquid with higher viscosity (20 Pas). The numerical simulations were also calculated by using the CFD code FLUENT®. The structure of the flow patterns produced by the disk turbine remains basically the same. The familiar radial jet flowing toward the vessel wall and splitting into two loops is still present, one above and the other below the turbine. The magnitude of the flow field is certainly different, as the size of the velocity vectors indicates, and this has a significant effect on the size of the recirculation loops and the slow moving zones. The structure of the bulk flow patterns changes more significantly for the pitched blade turbine than for Rushton turbine. The jet flowing from the impeller loses its predominantly axial character as the viscosity increases. The predominant flow pattern of the pitched blade turbine becomes very similar

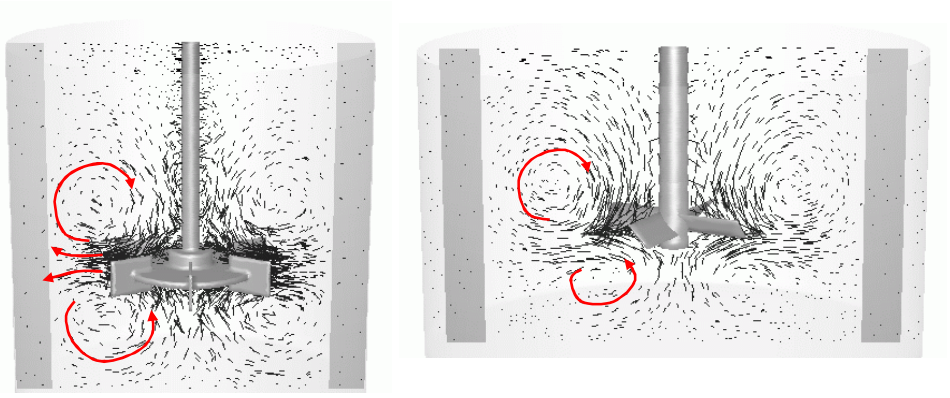

Figure 2-5: Flow patterns created by the radial flow impeller disk turbine (left) and the axial flow impeller pitched-blade turbine (right) at Re~5, Viscosity 20 Pas. Flow field calculated by using FLUENT® software.

to the flow pattern created by the disk turbine in fluids, i.e., at high viscosity, the pitched blade turbine creates two recirculation loops, one above and one below the impeller.

The objective of the numerical simulations of the agitated tank models shown in Figure 2-4 and Figure 2-5 was exclusively to qualitatively support the discussion of the flow patterns.

As the flow patterns change with the viscosity, the mixing performance of these impellers changes as well. It is desirable to have a flow pattern that moves the fluid readily into all parts of the mixing tank. Slow moving zones are not easily mixed. These zones of slow movement are often found in viscous liquids because viscous drag quickly consumes the kinetic energy of a moving fluid. The mixing performance of open impellers becomes more difficult for shear-thinning fluids because the viscosity is quite low in the impeller region, but quite high in zones distant from the impeller. Caverns and stagnant regions are usually present in the mixing tank depending on how strong the non-Newtonian behavior of the fluid is. Nienow and Elson (1988) investigated the disk turbine and observed caverns for power law fluids with low shear thinning indices (n). Hoogendoorn and den Hartog (1967) observed very stable toroidal vortices formed under and over the stirrer tip of the disk turbine in laminar regime. Long mixing times due to the presence of toroidal vortices were also measured by the authors in a vessel equipped with three pitched blade paddles. When turbines or propellers are used, unmixed zones appear as tori above and below the impellers and as dead zones behind baffles.

2.2.3 Flow patterns of proximity impellers

Open impellers, such as turbines and propellers require extremely high power requirements to induce turbulent mixing in highly viscous material. Therefore, it is a non-economical and non-practical way to mix high viscosity materials. Also under the point of view of the machinery, it can be a very difficult practice, when possible at all. The mixing has to occur by using a mechanism other than inducing turbulence. It is common in many industrial mixing operations, in particular, in the mixing of non-Newtonian highly viscous fluids, to encounter large and close-clearance impellers often called proximity impellers. Large impellers are able to move a large portion of fluid in the vessel, because of their size, primarily by tangential induction. They normally operate at lower rotational speeds but require high motor power. The most typical large impellers are gate, anchor and helical ribbon impellers. Large impellers with small clearance between vessel wall and impeller blade are efficient to minimize unmixed zones at the wall and provide a high shear region to enhance heat transfer and to aid the dispersion of aggregates and lumps. The flow patterns in laminar regime of these impellers were investigated by Murakami *et al.* (1972) and described as follows: “In anchor-agitated tanks, the tangential flow is dominant and becomes smaller with distance away from the impeller. Axial flow does not exist except in the bottom region at a low Reynolds number. Radial flow is recognizable near the impeller, but it should be noted that the essential exchanges in a radial direction hardly exist because of creeping flow”. Kuriyama *et al.* (1982) reported results of the numerical investigation of the flow characteristics of the anchor impeller and validated their results with experimental data from Peters and Smith (1969). Kuriyama *et al.* (1982) calculated shear rate distributions and observed that the shear rate distributions change with increasing Reynolds number. Pedrosa and Nunhez (2000) also investigated the flow patterns of the anchor impeller and concluded that the fluid is poorly mixed at the center of the recirculation zones, independent of the level of agitation or height of the impeller blade.

Murakami *et al.* (1972) described the flow created by a helical ribbon as: “It produces almost the same tangential flow as for the anchor impellers. Axial flow is strong and forms an assumed complex flow tube which has an elliptical section along the blade. The fluid elements are circulated in this flow tube, where the shear action is poor inside the tube and strong on the outside. They are given a high shear action and there exists a strong exchange of fluid elements. Radial flow is not large”. For sake of clarification, a numerical flow simulation of a standard helical ribbon in a vessel was carried out using the CFD software

FLUENT® and the results are plotted in Figure 2-6. The standard double helical ribbon has a diameter of 0.9 meters and rotates at 15 rpm in counter-clockwise direction in a vessel (diameter of 1 meter) with a flat bottom. The fluid is Newtonian (ρ=1200 kg m^{-3} and η= 10 Pa s) and the regime is laminar. The plot showing the normalized axial velocity at three horizontal sections in three dimensional shows the pumping action top-to-bottom of the double helical ribbon. It can be seen that there is one large vortex of secondary circulation from the bottom of the tank to the top. In the vicinity of the wall, a strong downward flow is promoted by the blades' movement. The blades induce a high shear field around them and at the wall, but the shear rates are lower elsewhere inside the vessel.

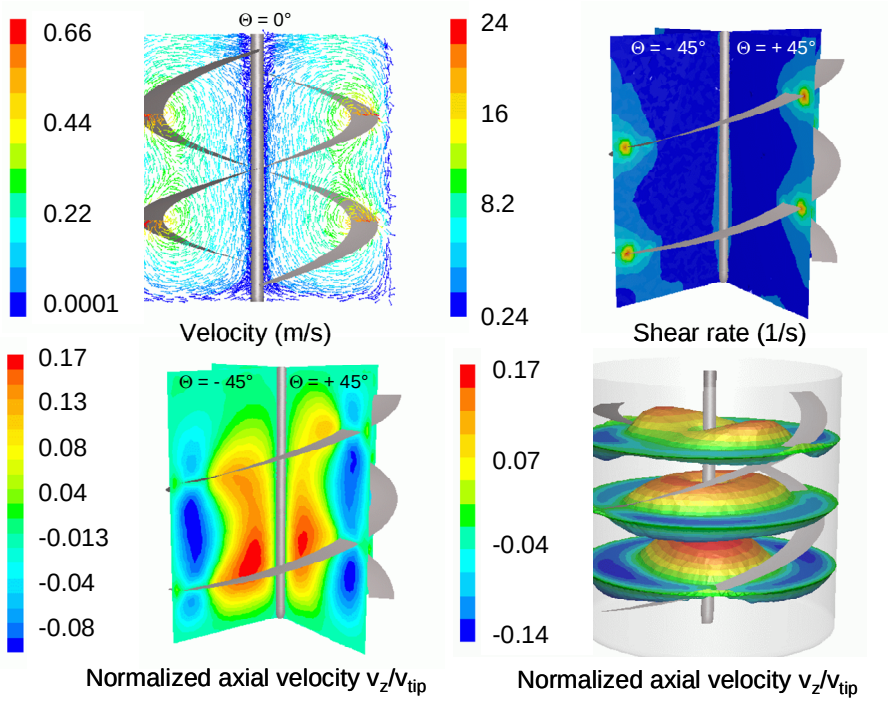

Figure 2-6: Calculated flow field created by a double helical ribbon (Re=24.3) using the CFD FLUENT® software

The usefulness of the close-clearance ribbon impellers in the high viscosity blending has been acknowledged, proved and emphasized by many authors, e.g. Hoogendoorn and Den Hartog (1967), Chavan (1983) and Delaplace *et al.* (2006). The efficiency of the ribbon impellers is mainly due to their good pumping capacity and efficiency to promote top-to-bottom movement. The combination with a central screw support the mixing near the shaft increases the overall mixing performance.

The Ekato Paravisc® is a non-standard helical ribbon impeller manufactured by Ekato GmbH (Figure 2-7). It is a combination of anchor and helical ribbon (Ekato Handbook, 2000). The two vertical blades are like the anchor blades, but pitched with a certain angle. The blades form a half ellipse. The anchor blade at the bottom of the vessel remains in the Paravisc to avoid stagnant zone in the bottom region. One of the most important particularities of this mixer is the larger pitch ratio compared to typical helical ribbons ($0.5 < p_r/D < 1.2$), where p_r is the blade pitch (Delaplace *et al.* 2000a). Because of the twisted blades, the flow patterns produced by the Paravisc impeller are similar to the ones created by typical double helical ribbons. The impeller creates a flow with tangential and axial components.

Delaplace *et al.* (2000a) reviewed the existing literature on the mixing performance (power consumption and mixing time) of helical ribbon impellers. Qualitative analyses were provided on the influence of the main geometrical parameters of the helical ribbons on the mixing effectiveness. The authors also investigated the homogenization effectiveness of the Paravisc and compared it to the classical helical ribbon impellers. They concluded that the mixing performance of Paravisc was quite similar to that of the classical helical ribbon impellers. Delaplace *et al.* (2000b) investigated the flow patterns of the Ekato Paravisc impeller numerically and with experimental observations of tracer particles. It was observed that the tracer particles sank around the stirring shaft and subsequently rose in the vicinity of the vessel wall when the impeller is up-pumping. The calculated flow field with the finite volume code FLUENT® was discussed in detail. Iranshahi *et al.* (2006) compared the mixing performance of the Paravisc with a double helical ribbon and anchor. The authors used a finite element computational fluid dynamics (CFD) software for the study. The authors concluded that the complex flow field created by the Paravisc impeller can achieve homogeneous mixing for highly viscous materials. The studies showed that the mixing efficiency of Paravisc was lower than for the double helical ribbon.

Figure 2-7 shows examples of large impellers. The impeller MAXBLEND® by Sumitomo Heavy Industries Ltd., Japan represents the gate impeller, since it is a large blade impeller. Maxblend was developed for challenging processes involving highly viscous fluids and multiphase flow (Takahashi *et al.*, 2006).

The complexity of the mixing processes in highly viscous fluids varies widely, such as processes that involve fluids with complex rheology, complex chemistry, and/or fluids that change viscosity during the mixing process. These are commonly accompanied with

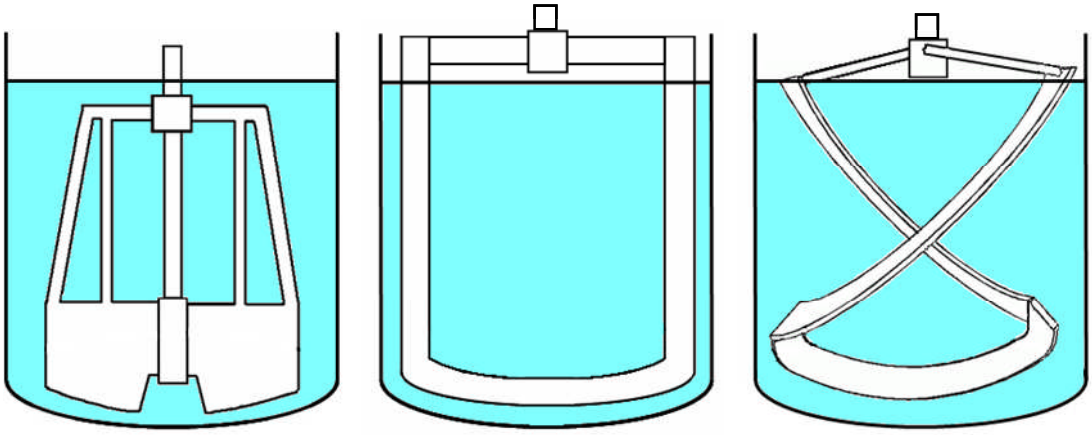

Figure 2-7: Maxblend® (left), anchor (middle) and Paravisc® (right) impeller

difficult operational problems, such as formation of gels and lumps, fouling and build up on surfaces, too low heat transfer, too low mixing times, poor dispersion of solids, presence of stagnant zones, etc. The result is that such complex and challenging mixing tasks in highly viscous fluids might not be effectively accomplished in standard agitated tanks; and it possibly requires the evaluation of more sophisticated mixing systems, such as planetary mixers, non-standard multi-shaft mixers, kneaders, as described by Pahl in (Kraume, 2003). Some examples of these sophisticated hybrid equipment are illustrated in Figure 2-8. The variety of equipment and component geometries available in the market today is very large, and also bewildering. The selection guidelines are often too general and not always useful. The mixing systems are too complex to understand and operate, which typically require a significant amount of trial-and-error tests to achieve the desired results. There is a lack of fundamental understanding of power, flow and shear characteristics.

Co-axial mixers, as shown in Figure 1-2, belong to this class of hybrid mixing systems that are certainly able to handle effectively several of the mentioned complexities and operational challenges in the high viscosity mixing tasks. Co-axial mixers are attractive though, because they are potentially the most likely and easy to implement in industrial processes. Not only because of their similarities to standard agitated tanks in respect to the familiar maintenance and operation, but also because they are certainly the easiest to understand and to characterize.

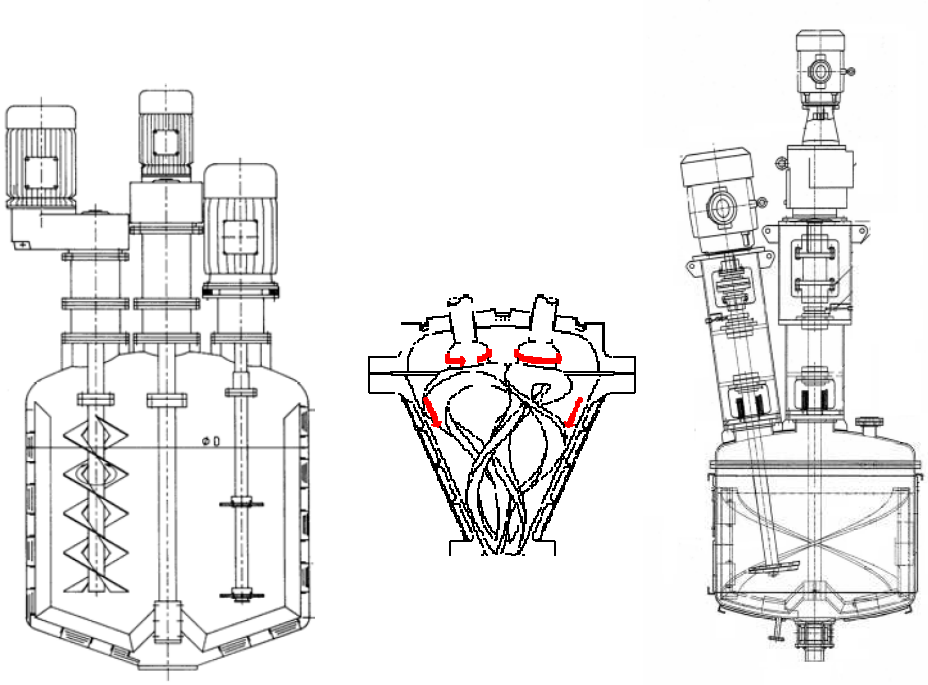

Figure 2-8: Examples of hybrid mixing systems. PRG multi-shaft mixer with anchor, dispersers and screw from Präzisions-Rühr GmbH (left); Helicone mixer from DIT, Inc. (middle); Dual-shaft mixer with helical and angled disperser (right).

2.3 Complex systems of impellers (co-axial mixers)

Co-axial mixers are used in industry but detailed analysis of their performance characteristics have only recently appeared in the open literature. In 1990, Todtenhaupt and Schneider discussed the performance of a co-axial mixer consisting of an anchor and a dual set of VISCOPROP® (Ekato Rühr- und Mischtechnik GmbH) with respect to blend time and heat transfer. The authors concluded in this work that the anchor assumed the function of baffles in the mixing system when water was used. In high viscous fluids, however, the rotation of the close-clearance impeller had a positive influence on the mixing time of the co-axial mixer. The heat transfer also improved significantly for the stirred tank with an anchor equipped with scrapers, and even more when the inner impellers were rotating. The authors gave no information about the rotation mode or power consumption.

In 1992, Tschuor and Widmer investigated a co-axial mixer in the turbulent regime. The consisted of two high speed impellers counter-rotating in the same axis. The authors used a hollow shaft to accomplish this configuration, in which the top impeller pumps downwards and the lower impeller pumps upwards. With this mixing system, vortex could be avoided in a non-baffled vessel and mixing times were reduced.

Relevant contributions on the subject have been conducted by Tanguy and co-workers. Tanguy and Espinosa-Solares (1997) evaluated numerically and experimentally the power consumption of a dual co-axial impeller composed of a Rushton turbine and a helical ribbon impeller in co-rotating mode. In the range of the investigated conditions, it was shown that the co-axial mixer achieved better mixing than the standard helical ribbon when fluid rheology changes during the process of mixing, however, consuming higher power. In a later publication, Espinosa-Solares *et al.* (1997) reported that the power consumption for the investigated co-axial system was not the sum of the individual impeller contributions. The possible explanation must be found based on the flow pattern created by the impellers.

The work of Thibault and Tanguy (2002) determined the power consumption of a co-axial mixer composed of wall-scraping arm (anchor) as proximity impeller combined with a series of rods positioned 90 degrees from each other and a pitched blade turbine of 2 blades located at the bottom of the vessel. The inner and anchor operated in counter-rotating mode. It was shown that the Metzner-Otto concept could be extended to account for the speed ratio between impellers. This allows the representation of the total power consumption for the co-axial mixer in form of a single power master curve, as shown in Eq.(2-17) and Eq.(2-18). The curve, however, does not allow for the independent evaluation of the influence of each agitator on the total power consumption.

$$Ne_{co\text{-}axial} = \frac{P_{total}}{\rho N_o^3 D_o^5} \tag{2-17}$$

$$Re_{g\,anchor} = \frac{\rho N_o^{2-n} D_o^2}{k \cdot K_{RN} \cdot K_{S,anchor}^{n-1}} \tag{2-18}$$

where

$K_{RN} = 0.1017R_N^2 + 0.345R_N + 1$ and $K_{S,anchor} = 8.04R_N + 22.97$

Foucault *et al.* (2004) investigated the co-axial combinations of the wall proximity anchor impeller and three commercial sawtooth dispersion impellers (Deflo, Sevin and Hybrid) in Newtonian and non-Newtonian fluids. The authors concluded that the power draw of the inner impeller was not affected by the speed of the anchor in both rotating modes, but the power drawn by the anchor was influenced by the inner impeller. The lowest

mixing times were obtained for the co-rotating co-axial mixer consisting of anchor and the open impeller with the highest pumping-down capacity, i.e. a so-called hybrid impeller.

In contrast to these findings, Köhler *et al.* (2003) observed that the power consumption of the inner impeller (four-blade paddle) was affected by the speed of the anchor in the transitional and turbulent regime (Re>100) for counter-rotating mode. In this work, the authors also showed that the speed ratio has a stronger influence on power consumption than the diameter ratio. Reducing the inner impeller diameter results in a weaker countercurrent flow against the anchor blades and therefore smaller Newton numbers for the anchor for all speed ratios. Another finding was that the higher the speed ratio, the higher is the critical Reynolds number of the anchor, i.e. the turbulent regime starts later. The authors developed correlations for the Newton numbers ($Ne_{i,\ co\text{-}axial}$ and $Ne_{o,\ coaxial}$) of their co-axial mixing system in terms of Reynolds number and impeller speed, as described in Eq.(2-19) for the cross beam agitator and in Eq.(2-20) for the anchor impeller. The fitting parameters of Köhler's correlations are geometry specific, i.e. if the mixer configuration changes, new correlations and/or new adjustable parameters have to be established.

$$Ne_{i,coaxial} = \sqrt{\left(\frac{160}{Re_i}\right)^2 + \left(2.97 - \frac{1}{Re_i^{0.3}}\right)^2} + 3\left[1 - \frac{1}{1 + \frac{10^6}{Re_i^{2.5}}}\right]\left(\frac{N_i}{N_o}\right)^{-1.2} + 4.45\left[1 - \frac{1}{1 + \frac{Re_i^{2.5}}{10^6}}\right]\left(\frac{N_i}{N_o}\right)^{-0.84} \tag{2-19}$$

$$Ne_{o,coaxial} = \frac{426}{Re_o} + 0.73\left(\frac{10^3 + 1.2Re_o^{0.66}}{10^3 + 3.2Re_o^{0.66}}\right)^{0.82} + 1.11\left[1 - \frac{1}{1 + \frac{10^5}{Re_o^{1.9}}}\right]\left(\frac{N_i}{N_o}\right)^{1.64} + 1.38\left[1 - \frac{1}{1 + \frac{Re_o^{1.9}}{10^5}}\right]\left(\frac{N_i}{N_o}\right)^{1.7} \tag{2-20}$$

Foucault *et al.* (2005) characterized the power consumption of co-axial mixers consisting of an anchor and different radial dispersion impellers (Deflo, Sevin, Hybrid, Rushton, Cowles). The authors proposed to use as a characteristic parameter for a co-axial mixing system the difference in rotational speed between open impeller and proximity

impeller for co-current mode of rotation and the sum of rotational speeds for counter-current mode as following:

$$N_{co\text{-}rotating} = N_i - N_o \tag{2-21}$$

$$N_{counter\text{-}rotating} = N_i + N_o \tag{2-22}$$

The Metzner-Otto constant of the inner impeller was introduced in the calculation of the apparent viscosity to obtain a modified Reynolds number in the laminar regime for tip speed ratios between 10 and 20. The proposed expressions by Foucault *et al.* (2005) however were only applicable for speed ratios above 10 and inner impellers with equal diameters.

Foucault *et al.* (2006) applied the characteristic speeds defined in Eq.(2-21) and Eq.(2-22) to their co-axial mixing systems to obtain exponential dependencies between dimensionless mixing time and modified Reynolds number for three combinations of co-axial mixers, different speed ratios, laminar and turbulent regime, co-rotating and counter-rotating modes. The outer impeller was the anchor combined with three inner dispersing impellers: Rushton, Rayneri-Sevin and Hybrid. The results showed that the co-rotating mode gives the lowest mixing times, followed by the Rushton turbine with stopped anchor and the counter-rotating mode. For high Reynolds numbers, the dimensionless mixing times are constant regardless of the operating mode. Again, the proposed correlations are valid for speed ratios between 10 and 20 and inner impellers with the same diameters.

Bonnot *et al.* (2007) investigated the mixing effectiveness of a co-axial mixing system consisting of an anchor and a Rushton turbine in both Newtonian and non-Newtonian fluids using flow visualization. This work concluded that co-rotating mode was more effective in comparison with counter-rotating mode to promote axial circulation in the tank, while counter-rotating mode is better to generate shear. The authors added a second turbine and it increased the mixing effectiveness in the co-rotating mode.

Heiser *et al.* (2007) investigated the performance of a co-axial mixer consisting of a helical ribbon and a central screw impeller. The authors concluded that the power consumption of each impeller was affected by the other regardless of the chosen rotating mode. The proposed correlations by Tanguy and co-workers as described in Eq.(2-21) and Eq.(2-22) were applied in Heiser's co-axial mixer configuration and a strong deviation from a single power curve was found. The reason given by the authors for the deviation was the

relative significant difference between the outer and inner impeller area. In Heiser's configuration the ratio between the impeller areas is smaller compared to Foucault's (2005) configurations.

Farhat *et al.* (2007) compared the performance of a radial and an axial impeller in terms of power consumption and mixing time. The studies concluded that the axial impeller Mixel TT was more efficient compared to a Rushton turbine. The co-rotating mode was also found to be superior to the counter-rotating mode.

Farhat *et al.* (2008) investigated the performance of a co-axial mixer that combines anchor and Rushton for different diameter ratios, rotating modes in laminar and transitional regimes. The authors proposed a new characteristic speed for the co-axial mixers, which is defined for all mixing modes as expressed in Eq.(2-23):

$$N' = \frac{N_i D_i + N_o D_o}{D_i} \tag{2-23}$$

With Eq.(2.23), a modified Newton and Reynolds numbers, as given in Eq.(2-24) and Eq.(2-25), were used to obtain the power curves. The power curves for all rotating modes could collapse in a single power curve, also using axial and radial impellers. The correlations proposed by Farhat (2008) proved to be applicable to a broader range of case scenarios than the ones previously proposed by Foucault *et al.* (2005).

$$Ne_{co\text{-}axial} = \frac{P_{total}}{\rho\left(N_i D_i + N_o D_o\right)^3 D_i^2} \tag{2-24}$$

$$Re_{co-axial} = \frac{\rho\left(N_i D_i + N_o D_o\right) D_i}{\eta} \tag{2-25}$$

The mentioned works, summarized in Table 2-3, are good examples to demonstrate a clear trend to develop practical design hints and rules to be applied in the co-axial mixing technology. The driver of such search is always the end user, i.e. the industries. However, universal rules quite often require intense and long studies combined with deep understanding of the physics involved.

Table 2-3: Overview of the most relevant studies of co-axial mixing systems

Author	Year	Impellers configuration	Vessel size	Rotation mode	Measured Variable	Varied variables
Todtenhaupt	1990	Dual Viscoprop® + anchor	T=400mm	no information	Blend time, heat transfer coefficient	impeller speed ratio, viscosity
Espinosa-Solares*	1997	Rushton + helical ribbon	T=210mm	co-rotating	power draw	viscosity, shear-thinning fluids
Thibault*	2002	series of rods, PBT + anchor	V=60 l	counter-rotating	power draw	speed ratio, viscosity, shear-thinning fluids
Köhler	2003	cross beam stirrer with 4 blades + anchor	T=397mm V=50 l	counter-rotating	power draw	diameter and speed ratio, viscosity
Foucault*	2004	sawtooth dispersion impellers + anchor	T=380mm	counter- and co-rotating	power draw, just-suspended speed, blend time	inner impeller type, speed ratio, viscosity, shear thinning fluids
Foucault*	2005	sawtooth dispersion impellers + anchor	T=380mm	counter- and co-rotating	power draw	inner impeller type, speed ratio, viscosity, shear thinning fluids
Foucault*	2006	sawtooth dispersion impellers + anchor	T=380mm	counter- and co-rotating	blend time	inner impeller type, speed ratio, viscosity, shear thinning fluids
Bonnot*	2007	Rushton turbine + anchor	T=380mm	counter- and co-rotating	blend time	speed ratio, viscosity, shear thinning fluids
Farhat*	2007	Mixel TT, Rushton turbine + anchor	T=380mm	counter- and co-rotating	power draw, blend time	speed ratio, viscosity
Heiser	2007	central screw + helical ribbon	DN200	counter- and co-rotating	mixing time, power draw, velocity field (LDA)	speed ratio, viscosity, shear thinning fluids, diameter ratio

Barar Pour*	2007	Deflo (eccentric) + Paravisc	T=390mm V=50 l	co-rotating	power draw, blend time	off-bottom clearance, viscosity, speed ratio
Farhat*	2008	Rushton + anchor	T=380mm	counter- and co-rotating	power draw, blend time	diameter ratio, viscosity, speed ratio

* Research work led by Professor Philippe Tanguy, Ecole Polytechnique, Montreal, Canada

2.4 Mixing time characteristics

The required time to achieve a determined mixing quality or degree of uniformity in a batch trial is defined as mixing time. The mixing quality is typically defined as the temporal change of the tracer concentration from c_0 to c_∞:

$$M(t) = \frac{c_0 - c(t)}{c_0 - c_\infty} \tag{2-26}$$

where c_0 is the initial concentration and c_∞ is the concentration after an infinite time. Usually mixing times for a mixing quality of 95% are reported, i.e. M(t)=0.95. Comparison of mixing times from different sources is only meaningful if they are related to the same mixing quality.

There are several methods to measure mixing time (Kraume and Zehner, 2001). The techniques to measure the homogenization degree in a stirred vessel generally utilizes a small amount of tracer that is added to the liquid in the vessel. Each method requires a different type of tracer. The most common methods are:

- utilization of probes of pH or conductivity;
- utilization of probes of temperature;
- colored dye addition method;
- dye discoloration method.

The major disadvantage of the method utilizing probes is that they are intrusive due to the bulk flow perturbation caused by the probes and probe supports. Besides, they only provide a point-wise data as a function of time. To measure the correct mixing, it is important to place at least one probe in the most poorly mixed regions. These regions are the last ones to be mixed and will control and limit the mixing rate for the entire mixing vessel (Paul *et al.*, 2004). The greatest advantage of these methods is the high

reproducibility and the possibility of acquiring quantitative information on the progress of the homogenization at each location in the vessel.

The optical methods, such as colored dye addition, dye discoloration and Schlieren are advantageous because there is no effect on the mixing process and the observer gets an insight of the dynamics of the mixing evolution. However, they require a transparent vessel and a clear fluid. In the method of adding a colored dye to a liquid (preferably clear fluid), the mixing in the early stages can be followed very clearly, but the last mixed zones in the vessel finally will not be detected because of the mask effect caused by the colored dye when it is behind or in front of theses zones. This effect might result in measured lower mixing times than the mixing times obtained with other methods. The dye discoloration method is more effective in following the homogenization in the final stages. In this technique, an instantaneous chemical reaction is used. Generally, a chemical specie is added to the liquid giving it a specific color. A second chemical specie is added to react with the first chemical specie and to gradually change the color of the vessel content, preferably making the liquid clear. Thus, stagnant or unmixed zones remain as colored patches while the bulk mixed liquid is clear. The most typical reactions used to measure mixing time in stirred tanks are:

I. acid-base reaction in the presence of one or more pH indicators,

II. iodine-iodide reaction in the presence of starch solution.

In method (I), the experiment usually starts by adding a pH indicator, such as bromophenol, methyl red, thymol blue or phenolphthalein, to the vessel content. The properties of an acid–base indicator that are most important are the colors or the acid and base forms, the pH at which the color changes, and the sensitivity to environmental (temperature and ionic strength) effects. Of course, the indicator should also be commercially available, inexpensive, and of low toxicity. For example, a small amount of acid or base is added and uniformly mixed to the vessel content, which causes a pH change and consequently, the bulk liquid appears colored. The mixing time measurement starts when the same amount (or slightly in excess) of base or acid is added, so that an instantaneous neutralization reaction takes place. Because this type of reactions is mixed-limited, the mixing time is obtained by the time when the last colored region disappears, i.e. the entire liquid in the vessel is clear.

The experiments using iodine-iodide reaction (II) start by adding the iodine to the liquid, which becomes colored (deep blue) in the presence of starch. The discoloration stage (i.e. the mixing time measurement) starts when the sodium thiosulfate solution is added to the vessel contents. The reaction is also instantaneous.

The measurement of the mixing time in laminar regime using pH, conductivity and temperature probes must be conducted with great care, because in some situations, these methods may generate false results. For instance, the utilization of temperature probes in laminar regime when the mixing times are long, is not suitable. In this case, the temperature changes due to heat conduction before it changes due to the homogenization process. In mixing time experiments of highly viscous fluids, it is very common to use close clearance impellers, such as anchor or helical ribbons. Such large impellers have normally cross bars to support the blades to the shaft, which makes the installation of probes inside the vessel very cumbersome, if possible at all. Complex impeller systems, such as planetary, multi-shaft and co-axial mixers are generally equipped with close-clearance impellers. The mixing time measurement using probes is not only difficult due to space constraints, but also because of the challenges imposed by the highly viscous liquids themselves. It was observed, for instance by Baltussen (2005), in measurements in shear thinning viscous liquids using probes that tracer is trapped in the corner of the probes and supports, and also in the spiral around the measurement tip (Figure 2-9). This may lead to erroneous results.

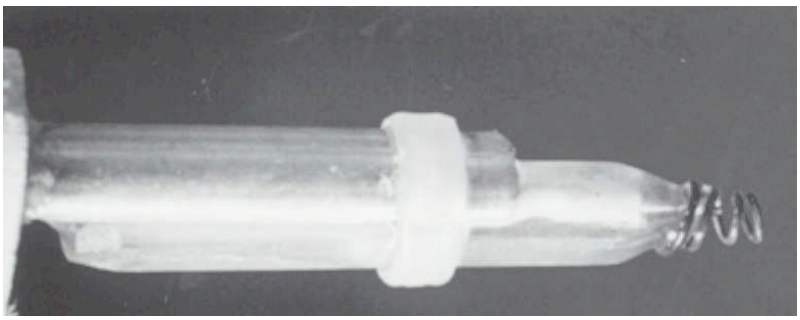

Figure 2-9: Commonly used probe for mixing time measurements

The mixing times obtained by different measuring techniques may differ considerably due to the differences both in the technique used and in the definition of mixing time. Hoogendoorn and Den Hartog (1967) investigated this effect in highly viscous fluids by applying different techniques and using the same mixing time definition. They observed that discoloration and thermal method yield similar mixing times except in cases where large stagnant zones occur. In this work, it was observed that the discoloration method is very suitable to give a good idea of the flow pattern, in particular in small scales (in that

case, a vessel with 0.24 m diameter vessel was considered the small scale and 1.8m the large scale).

It is usually desirable to compare the process of homogenization of different mixer designs. The dimensionless mixing time $N\theta_{95}$ is often used to characterize mixing time. The blending or mixing time θ_{95}, which is the time to achieve the mixing degree M(t)=0.95, depends mainly on the viscous properties of the fluids, the geometry of the vessel and internals (baffles, coils, etc.) and the impeller geometry. With a given vessel geometry the function depends on the following measured variables:

$$f(\Theta_{95}, N, \rho, \eta, D) = 0 \tag{2-27}$$

By applying the rules of the dimensionless analysis, two dimensionless numbers are found to be related and the relationship between them is known as the mixing time characteristic curves of the impeller:

$$N\Theta_{95} = f(Re) \tag{2-28}$$

The expression $N\theta_{95}$ or simply $N\theta$ is called the dimensionless mixing time number and gives the number of impeller rotations to achieve the desired homogenization level. The dimensionless mixing time is constant under turbulent conditions in a standard baffled tank, and in the laminar regime for forced convection impeller, such as the helical ribbon impeller. A number of correlations to estimate mixing times from operational parameters can be found in the open literature (Kraume, 2003; Paul *et al.*, 2004). These correlations are usually very sensitive to the flow conditions and geometrical parameters.

3 Experimental Set-up

In the present work, the characterization of the agitation performance is based on blending time and power consumption measurements for various mixer design configurations using open impellers alone or in co-axial combination with proximity impellers over a broad range of operating conditions. The number of operating parameters that influence the power consumption and the mixing time for a co-axial mixing system are significantly higher than for a single impeller system, i.e. a conventional standard baffled tank because of the presence of two different impellers rotating at different rotational speeds. The intent of the experimental design is to cover a large field that the governing parameters span. Table 3-1 shows the parameters that have been varied in the present experimental program and their discrete values or range.

Table 3-1: Varied parameters in mixing time experiments

Parameter	Value
Mixer configuration	Single impeller (baffled) and co-axial
Type of outer (proximity) impeller	Anchor, Paravisc
Type of inner (open) impeller	Pitched-blade turbine
Tip Speed ratio [-]	Single impeller, 2, 4, 6
Rotational mode	Co-rotating, counter-rotating
Total power input per unit mass [W/kg]	1 – 4
Inner impeller rotational speed (rpm)	39 – 350
Outer impeller rotational speed (rpm)	9 – 60
Newtonian viscosity [Pas]	4 – 175
Consistency index, k [Pas^{-n}]	20 – 155
Flow index, n	0.3 – 0.7
Reynolds number (inner) [-]	2 to 100
Reynolds number (outer) [-]	1 to 40

Single impellers in a tank as well as different co-axial configurations were investigated in this work. The impellers and co-axial configurations were selected because of their suitability for chemical processes. Two close clearance impellers were chosen for this

work, anchor and a modified helical ribbon from EKATO Rühr- und Mischtechnik GmbH, known as PARAVISC®. Anchor is a standard impeller used in high viscosity applications for renewal of the fluid near the wall in order to reduce wall fouling and improve heat transfer where it is needed. Paravisc is a compromise between anchor and helical ribbon. It is a non-standard impeller with good axial pumping capacity; an attractive design for high viscosity mixing applications that has been little investigated so far. A pitched-blade turbine is also a very common axial impeller in many applications in industrial processes. The impellers are described in detail in a later section.

In a co-axial impeller system, the impellers rotate with different rotational speeds. Impeller tip speed is calculated by multiplying impeller rotational speed, N, with πD, where D is the impeller diameter. The tip speed ratio (tr) is calculated by dividing the tip speed of the open impeller by the tip speed of the proximity impeller. The outer and inner impellers can rotate not only with different speeds, but also in different directions. The co-rotating mode means that the outer and inner impellers rotate in the same direction, whereas counter-rotating mode means they are rotating in opposite directions.

The majority of the blend time experiments were carried out for three different energy inputs, 1, 2 and 3 W/kg. The energy input is defined as the total power imparted by the impellers (inner and outer) in Watt per kg of fluid mass.

The rotational speeds set in the measurements of power curves and blend time were in the range of 39 – 350 rpm and 9 – 60 rpm for the inner impellers and outer impeller, respectively.

Different Newtonian and non-Newtonian fluids were employed in the experimental design to cover a large range of viscosities and Reynolds number.

3.1 Test fluids and rheology

In this investigation, fluids were prepared to determine the power consumption and mixing time, namely, Newtonian fluids based on glucose syrup (sugar solution) and non-Newtonian fluids consisting of aqueous solutions of cellulosics products.

Two instruments were applied to measure the viscosity curves of the test fluids:

- A cylinder rotation viscometer (Searle-Type), Viscosimeter V88 from Malvern Instruments GmbH Company.

- Rotation rheometer, Bohlin CVO120 (Malvern Instruments GmbH Company) using a cone-plate configuration.

The cylinder viscometer apparatus measures viscosity in the range of 6 mPas to 350 Pas, which depends on the rotational speed and type of cylinder. The selection of the cylinder system must be in accordance with the load of the measuring range of the viscometer and a relative error of 5% is expected in the measurements. Measured curves start at a minimum shear rate of 14.2 s^{-1}, and increases continuously during the measurement. The maximum shear rate depends on the maximum load of the measuring range of the viscometer, i.e. the higher the viscosity, the higher is the load and the lower is the maximum shear rate. A thermostatic bath was used during the measurement to keep the working temperature constant.

The measurements conducted in the rotation rheometer, a cone-plate geometry having a radius of 40 mm and a cone of 4° was used. During the rotation experiment the rotor rotates with a given shear stress, τ. The experimental quantity is the shear rate, γ. The rotation experiment was performed using step-by-step increasing shear stress. The temperature is measured via a PT100 sensor directly installed on the plate. All measurements were carried out at least two times.

3.1.1 Newtonian fluids

Table 3-2 summarizes the properties of the used Newtonian fluids. The sugar solutions were very sensitive to temperature changes. In the early stage of the experimental program, measurements were carried out in a non-jacketed vessel. In that case, a relationship between the temperature and the viscosity was established by means of measurements and used to correct the viscosity. During the power curves measurement, the bulk temperature was measured before and after a set of torque measurements. The later experiments were executed in a jacketed vessel, so that the fluid temperature was kept constant during power and mixing time measurements.

The viscosities of the C*Sweet Syrup were measured with the cylindrical rotational viscometer (Searle-Type), whereas the viscosities of the glucose syrup Glucomalt 571 were measured with the rheometer Bohlin CVO120 using a cone-plate configuration.

Table 3-2: Properties of the Newtonian fluids

Fluid name	weight concentration	Density (kg/m^3)	Viscosity (Pas)	Manufacturer
C* Sweet M01623 (SWE)	Pure	1415	4 - 50	Cerestar Deutschland GmbH, Germany
Glucomalt 571 (GLU)	96.2%	1400	92 - 175	Tate&Lyle Europe N.V., Belgium

3.1.2 Non-Newtonian fluids

Two polymer solutions were employed as non-Newtonian fluids in the experimental program:

- Hydroxyethyl cellulose (HEC), or CELLOSIZE™ HEC QP300, a product of Dow Wolff Cellulosics.
- Sodium carboxymethyl cellulose (CMC), or WALOCEL® CRT 20000, a product of Dow Wolff Celullosics.

The non-Newtonian test liquids were prepared by thickening water with the cellulosics product at different weight concentrations to obtain solutions of different rheological behaviors. Aqueous solutions of HEC and CMC have a density of 1000 kg/m^3.

3.1.2.1 Shear-dependent viscosity

Hydroxyethyl cellulose (HEC)

Rheological measurements for hydroxyethyl cellulose (HEC) solutions were conducted in a cylinder rotation viscometer (Searle-Type). The measured rheological data for different HEC solutions at a temperature of 25°C are plotted in Figure 3-1. It can be seen that the rheological behavior of HEC solutions depends very strongly on the HEC weight concentration. The viscosity varies over several orders of magnitudes depending on the HEC concentration. The shear thinning effects become stronger with increased HEC concentration as well. The much diluted solution, for instance the HEC with 1% concentration, exhibits a very weak non-Newtonian behavior since the viscosity remains almost constant in the entire range of the shear rate. The rheological behavior of the HEC solutions can be described by the power law model, Eq.(2-8).

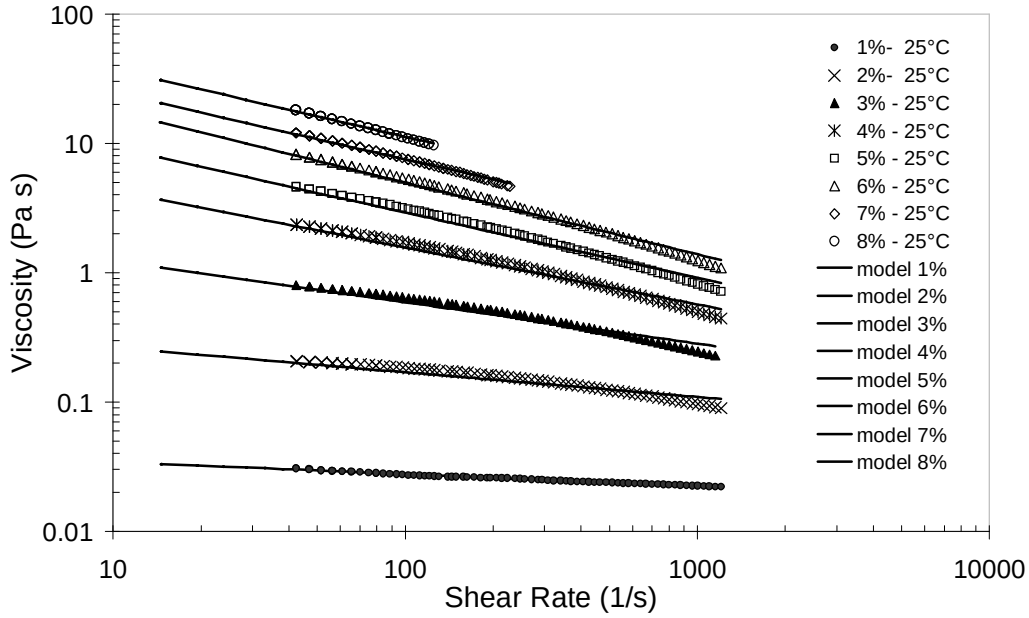

Figure 3-1: Viscosity of HEC solutions as function of shear rate and weight concentration measured in a cylindrical rotational viscometer and correlated with power law model

Table 3-3 summarizes the rheological parameters of power law for HEC solutions. The mathematical correlations for the power law model parameters' dependence on the weight concentration of HEC in water can be found in the appendix section.

Table 3-3: Rheological parameters of power law model for HEC solutions at 25°C

HEC Concentration weight %	Consistency index k [Pa s ^{n}]	Shear-thinning index n [-]
1	0.046	0.89
2	0.3639	0.83
3	2.6398	0.71
4	10.71	0.59
5	29.2	0.51
6	61.45	0.47
7	101.18	0.44
8	154.75	0.42

As mentioned previously, the early stage experiments were conducted in a vessel without a jacket. Therefore, the temperature of the fluid had to be measured for each experiment, which varied from 25°C to 30°C. The influence of temperature on the viscosity

of HEC solutions was investigated and the results are plotted in Figure 3-2. The measured data were obtained in the rheometer Bohlin CVO120 using a cone-plate configuration. The viscosity curves were measured for 7% weight concentration HEC solution at 20°C, 22°C and 25°C. The deviation between the maximum and the minimum values of the curves was found to be 25% for low shear rates (around 1.5 s^{-1}) and ca. 5% for higher shear rates (around 20 s^{-1}).

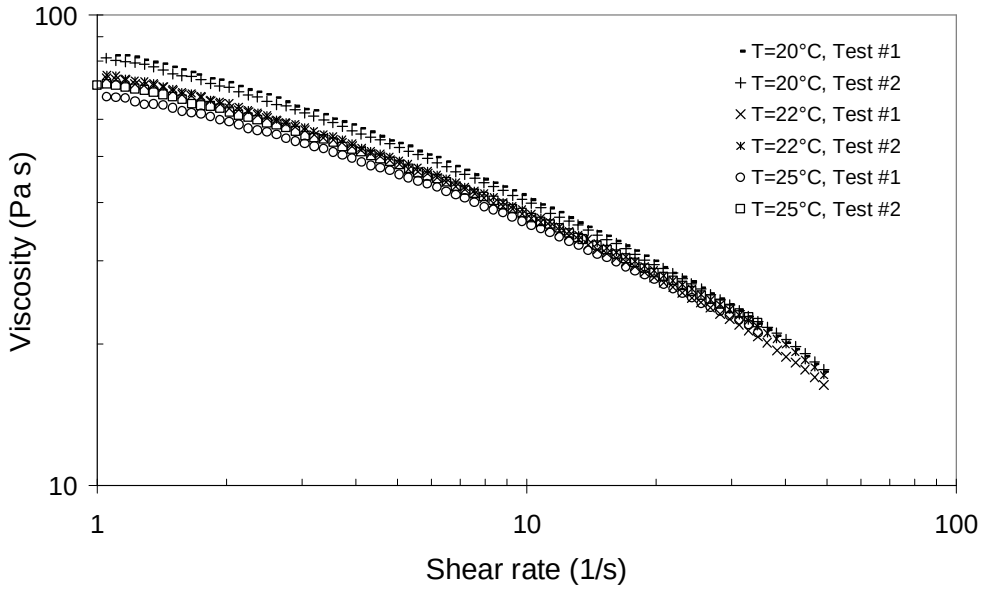

Figure 3-2: Viscosity dependence on temperature of HEC solution of 7% weight

The experimental program initiated in a later stage was conducted in a jacketed vessel equipped with a thermostat (WK2400, Lauda Dr. R. Wobser GmbH CO. KG) that used the recirculation of tap water to temper the test fluid. The fluid temperature was kept at 20°C. Only HEC solutions of 5%wt. and 7%wt. were used in the experiments with jacketed vessel. The rheological behavior of the HEC solutions at this temperature was measured in the previously described rheometer using a cone-plate configuration. As plotted in Figure 3-3, the viscosity curves were obtained for shear rates from 1 to 50 s^{-1} for HEC solutions of 5% and from 1 to 20 s^{-1} for HEC solutions of 7%. Additionally, viscosity data of solutions of HEC 7% were obtained in the cylinder rotation viscometer for a higher shear rate range. The data set of HEC solution with 7% wt. concentration shows that the measured data of both employed instruments agree well. Each HEC solution was measured twice and power law model was employed to fit the data. The power law parameters for the HEC solutions at 20°C in the range of shear rate of 1 to 100 s^{-1} are listed in Table 3-4.

The use of aqueous solution of acid (HCl) and base (NaOH) to measure the mixing time caused a continuous dilution of the test fluid in the tank. In order to minimize the dilution effect and, consequently, the alteration in the viscosity, the HEC concentration in the tank was tracked, so that a corrected viscosity curve could be obtained for each experiment. Additionally, a sample of HEC test fluids in the tank was taken for viscosity measurement every day. After a number of experiments, the test fluid was thickened with a certain amount of HEC to return to the desired set concentration.

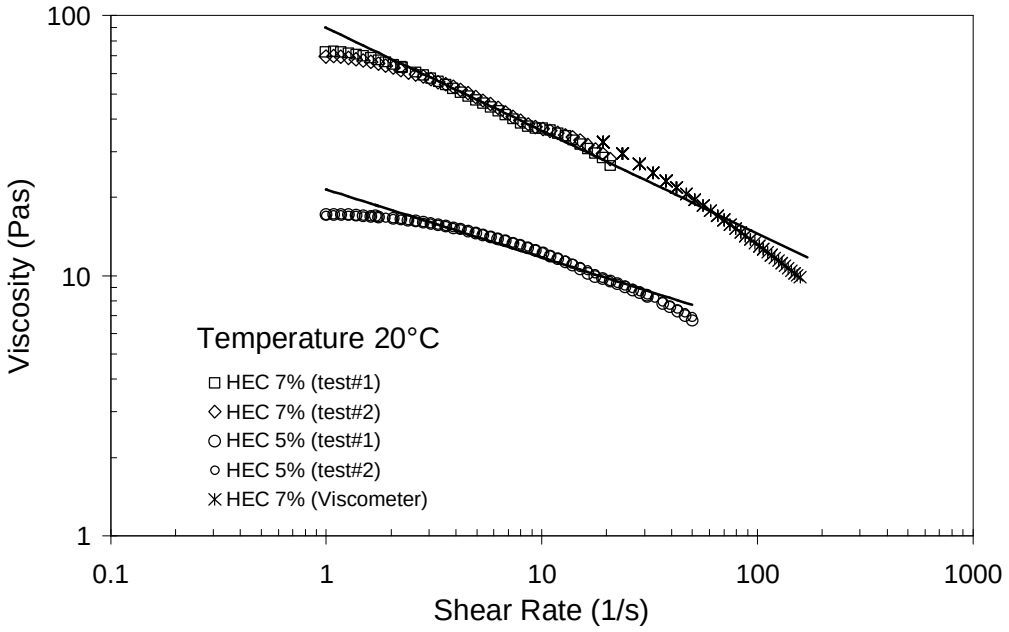

Figure 3-3: Viscosity of HEC solutions as function of shear rate and weight concentration measured in a rheometer at 20°C and fitted with the power law model

Table 3-4: Power law parameters for HEC solutions at 20°C

HEC concentration weight %	Consistency index k [Pa s ^{n}]	Shear-thinning index n [-]
5	21.43	0.739
7	89.75	0.605

Sodium carboxymethyl cellulose (CMC)

Solutions of sodium carboxymethyl cellulose (CMC) with 2% and 2.5% weight concentration were also employed in the experimental program as non-Newtonian fluids. CMC is a biodegradable fluid, so that a small concentration of biocide was added to preserve the fluid for several days. The selected biocide product was Preventol® D7 from

Lanxess Deutschland GmbH, which is an aqueous formulation containing 1.5% of isothiazolinones. No alteration in the viscosity or pH of the CMC solution could be observed by adding this product to the CMC test charges.

The viscosity curves of the solutions of CMC with 2% and 2.5% weight concentration were measured in the rotation rheometer Bohlin CVO120 using a cone-plate configuration and are pltotted in Figure 3-4 and Figure 3-5, respectively. The measured viscosity data were averaged and the power law model, Eq.(2-8), was used to describe the rheological behavior of the test fluids. The fitting parameters of the power law was found to be k=41.34 (in Pa s ^{n}) and n=0.39 for CMC with 2% weight concentration and k=66.1 (in Pa s ^{n}) and n=0.32 for CMC with 2.5% weight concentration. The density of CMC solutions are 1000 kg/m^{3}.

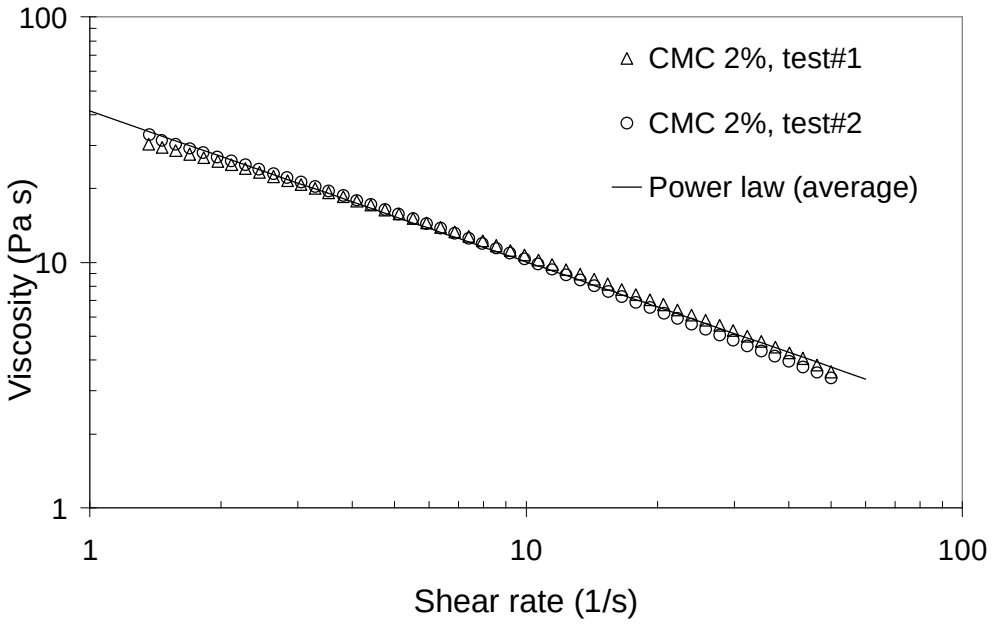

Figure 3-4: Viscosity curve of CMC solution with 2% weight concentration measured in a rotation rheometer at 20°C and fitted with the power law model

The temperature effect on the rheological behavior of the solution CMC 2% was not investigated because all the experiments using CMC solutions were carried out in a jacketed tank. Therefore, the temperature of the test fluid in the tank remained at 20°C constant.

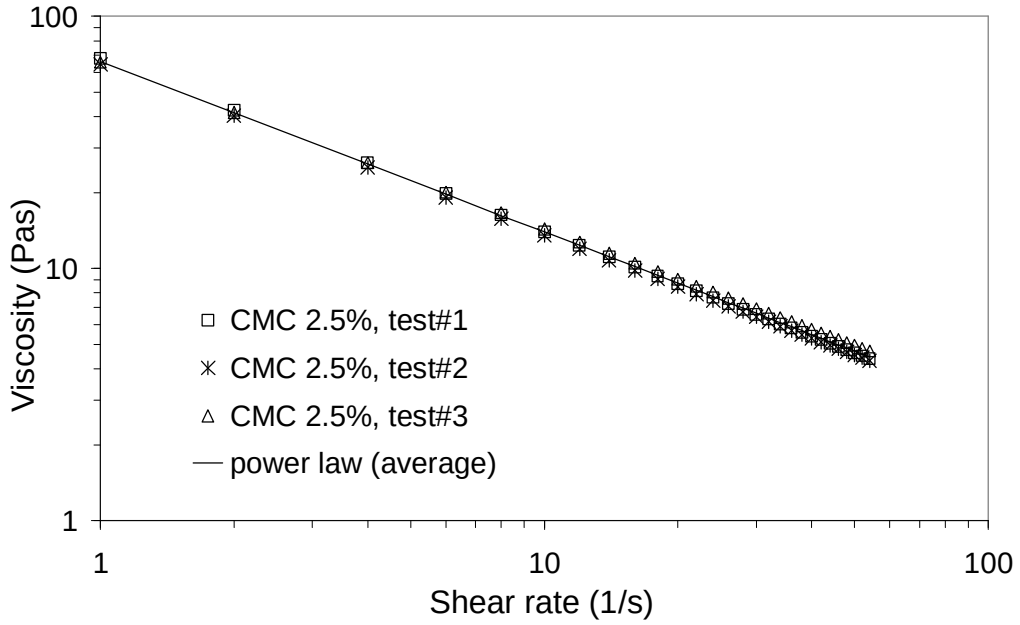

Figure 3-5: Viscosity curve of CMC solution with 2.5% weight concentration measured in a rotation rheometer at 20°C and fitted with the power law model

The same dilution effect, as previously mentioned for HEC solutions, occurred in CMC solutions as well. The CMC concentration in the tank changed continuously during the mixing time measurements. Similar measures for HEC solutions were taken here to track the viscosity and to minimize the dilution effect.

3.1.2.2 Shear-dependent viscoelasticity

The viscoelasticity is a rheological property of the fluid that can influence the mixing power consumption and the mixing time. Although the influence of the viscoelasticity on the mixing performance of the impeller systems goes beyond the scope of this research work, the question whether the elastic properties of the test fluids, in particular HEC, plays a role on the power consumption and mixing time must be considered.

The effect of the liquid climbing up the rotating shaft, known as Weissenberg effect, is always an indication of the viscoelasticity effect on the mixing. Although the Weissenberg effect was not observed during the present measurements, Shervin *et al.*, (1991) reported shear dependent viscoelastic properties for the aqueous solution of hydroxyethylcellulose (HEC) called Natrosol 250 HHR in low weight concentrations. Rheological properties of solutions of HEC QP300 were not published yet. Therefore, measurements were conducted to evaluate the viscoelastic properties of employed HEC solutions.

Measurements of the viscoelastic properties of HEC solutions with different concentrations were carried out in a rotation rheometer, RS600 Instrument (Thermo-Haake Germany) equipped with a cone-plate geometry having a radius of 20mm and a cone of 1°. The non-Newtonian fluids were examined also under non-destructive conditions of oscillatory shear to determine the viscoelastic properties. In an oscillation experiment the viscoelastic polymer solution is exposed to a slight shear deformation, γ^*, which changes sinusoidally with time between the deformation values, γ_0:

$$\gamma^* = \gamma_0 \sin(\omega t) \tag{3-1}$$

The response function of the system in the form of a stress, τ^*, also oscillates sinusoidally with the same frequency, ω, but with a lower amplitude, τ_0, than would be expected for a purely elastic solid and with phase shift, α, which is caused by the viscous component of the solution.

$$\tau^* = \tau_0 \sin(\omega t + \alpha) \tag{3-2}$$

A phase shift of $\alpha=0$ describes purely elastic behavior and one of $\alpha=\pi/2$ describes purely viscous behavior. The viscoelastic properties of the solution can be calculated from the amplitude and phase shift of the response signal. This method is a non-destructive measurement but also remain independent of the amplitude of the energizing signal, the deformation must not leave the linear viscoelastic range. In this range the deflection of a polymer segment responds in a linear manner to the exerting force, and the material functions that determine the proportionality are independent of the deformation. The proportionality factor, G*, between the deformation, γ^*, and the shear stress, τ^*, is called the complex shear modulus.

$$\tau^* = G^* \gamma^* \tag{3-3}$$

$$G^* = G' + iG'' \tag{3-4}$$

The real part of the complex shear modulus is termed the storage modulus, G', and is a measure of the deformation energy, which can be stored reversibly by the polymer solution. G' describes the elastic component of the solution.

$$G' = \frac{\tau_0}{\gamma_0} \cos \alpha \tag{3-5}$$

On the other hand, the imaginary part of the complex shear modulus describes the viscous properties of the solution and is called loss modulus. It represents a measure of the energy irreversibly dissipated by viscous flow.

$$G'' = \frac{\tau_0}{\gamma_0} \sin \alpha \tag{3-6}$$

The storage and loss modulus are usually determined as functions of the frequency at constant amplitude in the linear viscoelastic range.

Results of the oscillation experiments are plotted in Figure 3-6, which show as in the shear dependent viscosity measurements the influence of concentration on the rheological properties. These curves can serve as measure of how strong the elastic part is over the viscous part. For all HEC solutions, the viscous contribution, characterized by the loss modulus G", prevailed over the elastic contribution, characterized by the storage modulus G', in the entire frequency range, with exception of HEC solution of 7%. At frequencies higher than 10 s^{-1}, the elastic behavior of the HEC 7% begins to be slightly predominant. The storage modulus for the sample containing 1% HEC is zero over broad frequency range. The elastic part of the HEC solutions increases with increasing frequency and increased weight concentration. The qualitative behavior change with the concentration as well. Therefore, as the impeller speed increases in a mixing tank with HEC solution, the elastic contribution increases as well. Depending on the concentration of HEC in the solution, the elastic properties will prevail over the viscous ones.

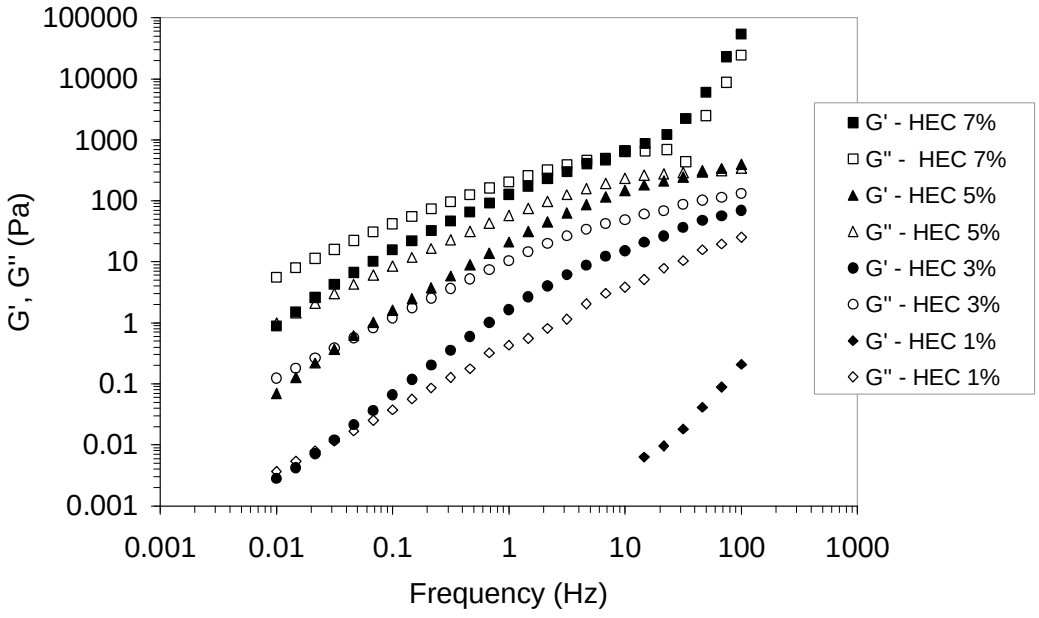

Figure 3-6: Storage and loss modulus as function of frequency for different HEC solutions

The loss tangent tan δ is commonly employed to characterize the relationship between the two parameters G' and G'' and is described as the ratio of the energy lost (G") to energy stored (G') in an oscillatory cycle (Jones *et al.*, 1997):

$$tan\,\delta = \frac{G''}{G'} \tag{3-7}$$

Values of tan δ smaller than 1 indicate that the elastic properties are predominant over the viscous properties, and therefore, the fluid exhibits strong viscoelastic behavior (Shervin *et al.*, 1991). Figure 3-7 shows the curves of the loss tangent versus frequency for different HEC solutions. Solutions of HEC displayed decreased tan δ values associated with increasing frequency. The tan δ values for HEC 1% were greater than 100, thus not plotted in the graph. Solution of HEC 3% has tan δ values greater than 1 over the measured frequency range. Solution of HEC 5% has tan δ values less than 1 for frequencies greater than 68 Hz. This corresponds to impeller rotational speeds greater than 370 rpm, considering a pitched blade turbine (PBT) as impeller and a Metzner Otto constant $K_S = 11$. Such high impeller speeds for PBT were not employed in the present experiments. For HEC 7%, however, the tan δ values are less than 1 for frequencies greater than 10 s^{-1}, which correspond to open impeller rotational speeds greater than 55rpm using $K_S = 11$ for PBT and to proximity impeller rotational speeds greater than 25rpm using $K_S = 25$.

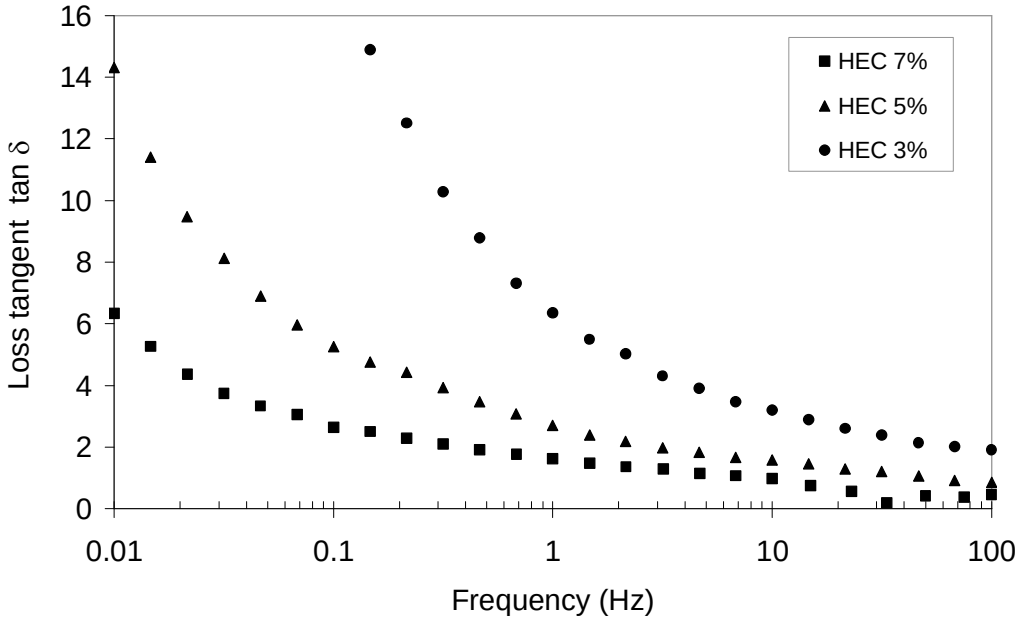

Figure 3-7: Loss tangent (tan δ) as function of the frequency (Hz) for different HEC solutions

In this work, it was assumed that the simple shear non-Newtonian viscosity is adequate to describe the viscous behavior of the HEC solutions around the blade. This assumption is reasonable for low elasticity fluids and low values of impeller rotational speeds (as normally used in proximity impellers, but not for open impellers). In the results section of the present work, the power consumption and mixing time in fluid tests using HEC, CMC and Newtonian fluids are compared to each other to evaluate whether this assumption was valid.

3.2 Co-axial mixing tank

The experimental mixing tank is illustrated in Figure 3-8. The geometrical dimensions are in mm. The cylindrical tank of 490 mm inner diameter (T=490mm) is made of Plexiglas with a dished bottom in torispherical shape ("Kloepper"). The vessel volume is 130-liter with a fluid volume of 86 liter. The tank is equipped with two electric drive-motors of 3 kW and 1.5 kW; one drives the inner impellers and the other the outer impeller, respectively. The co-axial combination of impellers could be realized by using a combination of a hollow and a solid shaft. Another possibility is to simply use a top mounted drive in combination with a bottom mounted drive. The coaxial design was selected as a lower cost option.

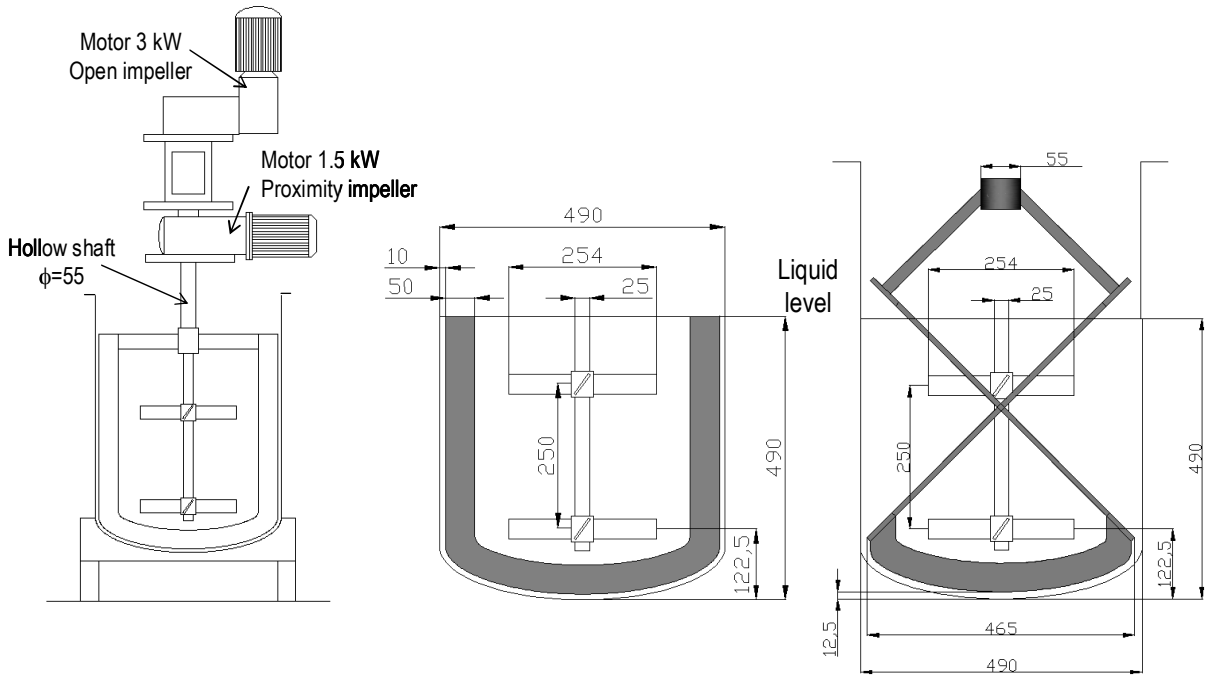

Figure 3-8: Experimental setup (dimensions in mm)

3.2.1 Open impeller

A dual set of 4-bladed, pitched turbine with 45° blade angle (PBT) was employed in the present experiments (Figure 3-9). The diameter is 254 mm (D = 0.52 T). The blade width (W) is a function of impeller diameter (D), e.g. W/D=1/5. The PBT produces a mix of axial and radial flow. Its main application is found in the low to mid viscosity range.

In general, with this open impeller, as the Reynolds number decreases the fluid's resistance to flow increases and thus the axial flow discharge of these impellers becomes more radial. In the laminar region, i.e. high viscosity applications, it can result in 0° discharge angle and pure radial flow (Weetman and Coyle, 1989). The maximum energy dissipation in the open impellers is close to their blades. In this region, the mixing effectiveness is expected to be the highest.

Figure 3-9: Pitched blade turbine

3.2.2 Proximity impellers

Figure 3-8 illustrates the configuration for the proximity impellers anchor and Paravisc® in the tank. Anchor is very simple in its construction form. It is a two-bladed impeller that induces a principally tangential flow in the direction of the anchor rotation. The main purpose of an anchor impeller is the renewal of wall layers. The traditional application is promotion of heat transfer, but it can also be used to provide wall shear for suppression of wall fouling, as long as the mixing task is handled by another device. Since it produces mainly tangential flow, the anchor impeller itself provides very poor top-to-bottom mixing.

Anchor impellers are used for high viscosity fluid systems, where stagnant fluid may be found next to the vessel wall. At low viscosities there is not enough viscous drag to promote pumping, resulting in swirling conditions. At too high viscosities the anchor performance declines, because the impeller "slips" in the fluid.

On the right side of Figure 3-8, Ekato Paravisc® is shown. Like the anchor impeller, it sweeps close to the wall, eliminating the stagnant fluid in this region and intensifying the heat transfer. It is a forced convection impeller for high viscosities and it is able, due to its angled flights, to induce axial flow. The rotation direction of the shaft can be changed to achieve upwards- or downwards-pumping effect.

For both proximity impellers, the maximum energy dissipation and shear rate occur in the region between the blades and the wall. It is expected that decreasing the radial clearance of the blades from the vessel wall significantly increases the power draw. This effect is not investigated in the present work, but it is addressed in Delaplace *et al.*(2000a).

3.3 Measurement techniques

3.3.1 Torque and power

The instrumentation enables the continuously measurement of the torque (M) and rotational speed of the inner impellers (N_i) as well as the power (P) and rotational speed of the installed outer impeller, (N_o) in the present experimental set-up.

Since the measured total power consumption for the outer impeller includes motor friction losses, it is necessary to correct the power measured to give the power consumption by the impeller, i.e. the shaft power. An issue is that the frictional losses depend not only on the rotational speed, but also on the temperature of the drive, especially the temperature of lubricants. Since the motor of the outer impeller is cooled by a ventilator rotating with the same speed as the drive, different motor temperatures are obtained at different rotational speeds. Several measures were taken to minimize this effect: i) the motor was warmed up at least one hour before the measurements to make sure the lubricant oil in the motor was warm, ii) a power value was read only after the power display remained constant.

The approach to correct the power consists of determining a correction function or a calibration curve that can be subtracted from the measured power (shown at the display of the instrumentation) to give the correct shaft power. To determine the calibration curve, which should include all the motor friction losses, firstly, the power consumption was measured at different rotational speeds by just driving the shaft in the air. Secondly, the power of the outer impellers was measured as a function of rotational speed in different fluids with different viscosities. Glycerin at different concentrations was employed in the present measurements. Figure 3-10 shows the results of the measurement for the impeller anchor. The total power was then replotted versus viscosity and a curve for each impeller

speed was obtained, as shown in Figure 3-11. The extrapolation to zero viscosity gives the power consumption from mechanical losses as function of impeller speed, from which the total power consumption can be converted into shaft power, as shown in Figure 3-12. The power curves measured in the air and in different fluids with different viscosities do not differ significantly. For this work though, the calibration curve used to correct the displayed power was determined by averaging all the functions measured in the air and in different fluids (different viscosities).

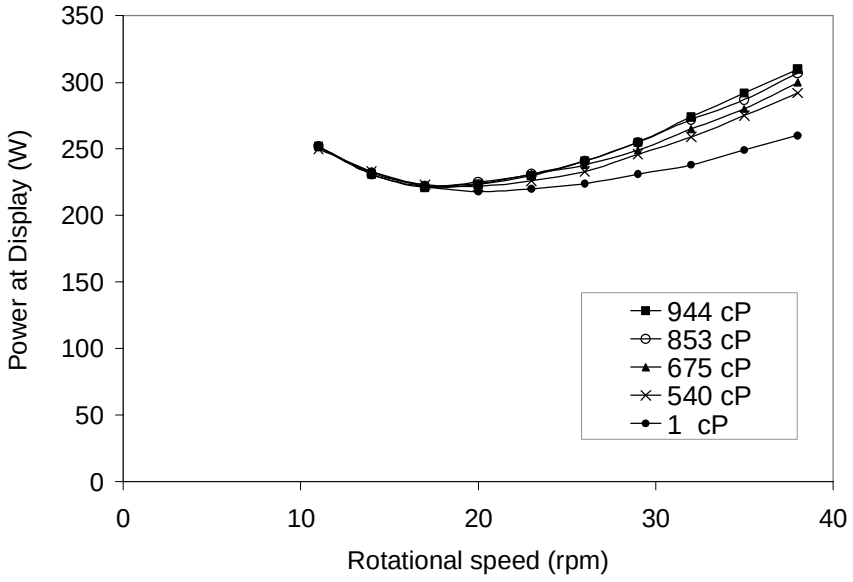

Figure 3-10: Displayed power of anchor impeller as function of shaft rotational speed for different fluid viscosities

Hence, the calibration curve is a power versus shaft speed function, Eq.(3-8), which gives the power at a given speed that must be subtracted from the power shown at the display of the instrumentation , Eq.(3-9):

$$P_{friction}(Watt) = 0.0000783x^4 - 0.013x^3 + 0.847x^2 - 21.49x + 403.52 \qquad (3\text{-}8)$$

$$P_{corrected} = P_{display} - P_{friction} \quad \text{(in Watt)} \qquad (3\text{-}9)$$

The maximal error of the power measurement system of the outer impeller was estimated from all measured data acquired for the calibration curves using different fluids to be 5W. This confirmed the accuracy of the power measurement system given by the manufacturer (former FLUID Misch- und Dispergiertechnik GmbH – Today EKATO Rühr- und Mischtechnik GmbH). Therefore, the accuracy of the system increases with increased

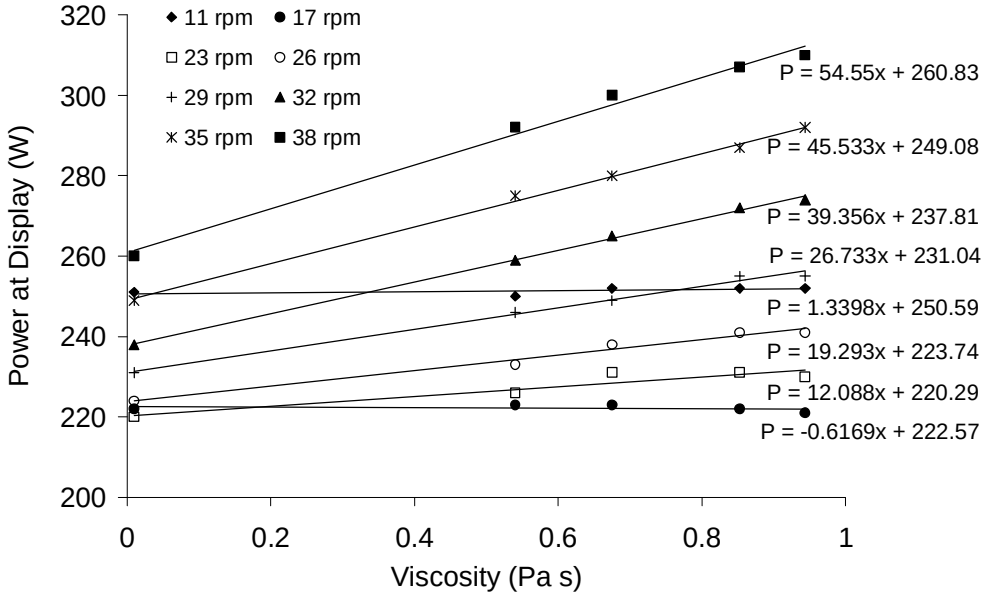

Figure 3-11: Displayed power of anchor impeller as function of fluid viscosities for different shaft speeds

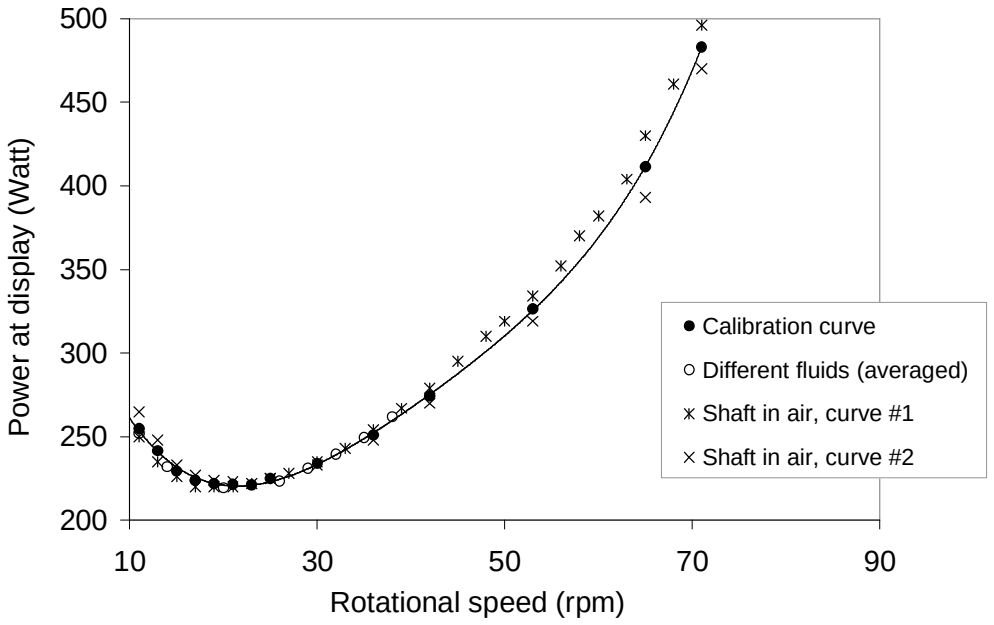

Figure 3-12: Measured power of the anchor impeller as function of rotational speed in air and in different fluids

load – it was to be expected, since the motor drive was designed for high viscosity mixing tasks. Measured data of power with error greater than 5% were excluded.

The torque of the inner impellers was measured directly, i.e. no mechanical friction losses were necessary to be subtracted. The measurement error of the torque measurement

system of the inner impeller was ±0.1Nm. Measured data of torque with error greater than 5% were excluded as well. The power dissipated by the impeller in the tank is calculated by the following equation:

$$P = 2\pi NM \quad \text{(in Watt)} \qquad (3\text{-}10)$$

At the higher rotational speeds considerable care must be taken to avoid entrainment of bubbles from the headspace into the liquid. The viscosity of the test fluid with small bubbles is expected to be smaller than for the test fluid without bubbles.

3.3.2 Mixing time

A non-intrusive technique based on direct visualization of a color change, DISMT method "Determination of Mixing Time through Color Changes" (Lipp *et al.*, 2002), was applied for measurements of the mixing time. DISMT is a visualization method that makes use of two pH sensitive indicators, methyl red (red to yellow, pK ~ 5) and thymol blue (yellow to blue, pK ~ 9). The range of color change of both indicators overlaps so that three colors can be distinguished depending on the pH.

A red (acidic) solution is mixed with a blue (basic) solution, and in those regions where the mixing fraction is within 5% of the mixing fraction at infinite time, the solution is yellow. With a clear mixing vessel, an observer may see distinct red and green/blue regions, as well as the later emergence of yellow regions. With DISMT, the 95% mixing time for the entire vessel may be defined as the time for the entire liquid volume to become yellow. DISMT is a reaction-based diagnostic, and thus color changes occur only when reactants have been mixed at the molecular level. The advantage of DISMT method over "one indicator" methods is that the latter cannot give information about a range, say +/- 5% of ideal, for the mixing fractions.

The experiment begins with the acidification of the neutral vessel content. The system is operating with a constant impeller rotational speed, which was previously determined based on the desired power input per unit of mass, for instance. A molar amount of base, equal to the amount of acid used to acidify the mixture, is added between the shaft and vessel wall to start the neutralization reaction. Mixing time refers to the time measured from the instant of the addition until the vessel contents meet the specified criterion, which is the 95% homogenization. Measurements were repeated two or three times until the deviation of the measured blend times became less than 15%.

The DISMT method was originally applied to very transparent fluids such as water. The present experiments using the investigated test fluids, CMC and HEC, demonstrated that the DISMT was also suitable for these aqueous polymer solutions. CMC solutions demonstrated, however, the best suitability for this method in comparison to HEC solutions, due to the clearness of CMC solutions in neutral pH. HEC solutions in high concentrations (7%, for example) have a slightly yellow color in the neutral pH. The color change was from red to green (instead of blue) and from green to orange. The visualization of the color change was more difficult for HEC than for CMC solutions. It was also observed that from time-to-time it was necessary to add amounts of sodium hydroxide to correct the pH of the test solution of HEC to neutral.

4 Computational Fluid Dynamics (CFD)

In the last twenty years the rapid increase in computational performance and development of efficient numerical methods has created the pre-requisites for a detailed simulation of fluid flows. The full integration of grid generation, modeling and solver as well as the post processing of the results in single commercial packages under the name Computational Fluid Dynamics (CFD) leads to a continuous increase in its utilization, also in the industry.

The primary interest of the chemical industry in applying CFD is the optimization of existing processes and design of new ones in a short period of development time based on the gained understanding of the chemical and fluid dynamics in the processes. In the past, deeper understanding could only be gained by experimental experience, supported by similarity considerations. Today, however, efficient simulation tools predict with some considerable accuracy the spatial and temporal behavior of coupled processes within the apparatus (Birtigh *et al.*, 2000) at least for single phase.

In industry, it is often common to find apparatuses operating at high temperatures and pressures involving highly hazardous materials. Such kind of processes are always challenging to reproduce in experiments – and they are often found in stirred tanks, which normally offer very limited access, if any at all, to process variables during the operation. The performance is often measured in terms of the outputs of this unit or even of other unit further downstream. Detailed measurements during the operation are normally not practical.

The CFD commercial codes available on the market have been widely applied to calculate a variety of three-dimensional, numerical flows in stirred tanks (i.e. single phase laminar and turbulent flow, multi-phase flows, reactive flow, etc). In this work, the Computational Fluid Dynamics code FLUENT®, version 6.3 (Fluent User's Manual, 2006) was employed to simulate the fluid flow in tank mixing systems.

4.1 Numerical fundamentals

The fluid motion is mathematically described by conservation equations and auxiliary models. The CFD code FLUENT® solves the coupled system of partial differential

equations and the final solution of the coupled partial differential equations is obtained by basically performing three steps, as shown in Figure 4-1.

In the pre-processing step a computational model is created by specifying the dimensions of the equipment or process. The geometry defines the computational domain, i.e. the region in which the fluid equations are being solved. The mesh generation is the discretization of the computational domain into several control elements (cells). For each model boundary, a boundary condition is attributed, e.g. walls, inlet, outlet, etc.

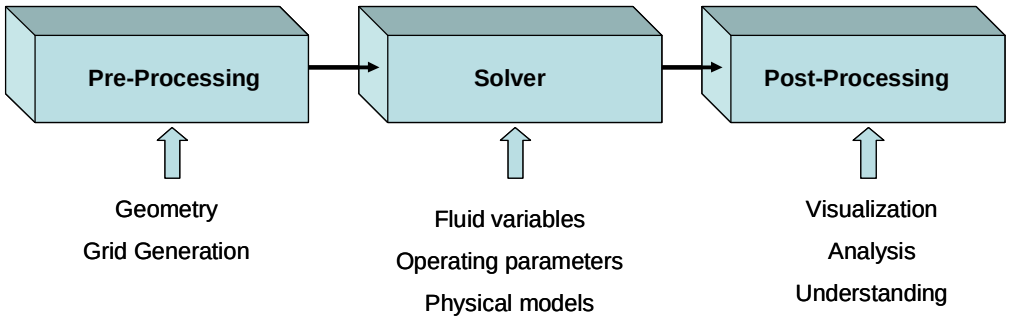

Figure 4-1: General methodology of Computational Fluid Dynamics

In the solver, a series of parameters are defined: fluid properties (viscosity, density, etc.), operating parameters (gravity, operating pressure, etc.), physics in the process (turbulent flow, multi-phased flow, reacting flow, non-Newtonian fluids, etc) applied by activating the specific equations, initial conditions and solver settings (type of solver, numerical schemes, number of iterations, convergence criteria, relaxation parameters, etc.). The solver itself is a set of numerical algorithms intended to solve the governing equations and specific models for each cell or control element. FLUENT® uses the most widely used CFD technique, the finite volume method (FVM) to discretize the equations.

The post-processing step is the fluid flow visualization itself. The results for pressure field, flow velocity, etc. can be displayed and reported in different ways. Full details of the available visualization techniques are given in FLUENT® user's manual (Fluent User's Manual, 2006). The visualization and the analysis of the process relevant variables provide a better understanding of the problem.

The specific models and solution techniques that are commonly employed in the analysis of tank mixing processes are briefly presented and discussed in the next sections of this chapter. A comprehensive description of the equations, specific models, solver and solution techniques are included, for instance, in Paschedag (2004) and Patankar (1980).

4.1.1 Transport equations

In the present work, the simulation of the fluid flow in stirred tank systems is carried out by solving the three-dimensional time-dependent conservation equations for an isothermal system. The appropriate equations for incompressible fluids in Cartesian coordinates can be described as follows.

Continuity equation of the mass conservation:

$$\frac{\partial}{\partial x_i}\left(\rho \cdot w_i\right) = 0 \tag{4-1}$$

Momentum equation of the momentum conservation:

$$\rho\left(\frac{\partial w_i}{\partial t} + w_k \frac{\partial w_i}{\partial x_k}\right) = \frac{\partial \tau_{ij}}{\partial x_j} + \rho F_i \tag{4-2}$$

The Cartesian coordinates are described by x and w describes the Cartesian components of the velocity vector. The direction is given by i, j and k, i.e. i=x, j=y, k=z. F_i represents the external forces (centrifugal, gravitational, Coriolis, electromagnetic, etc.). Eq.(4-2) is known as Cauchy's equations and they are valid for any continuum. They provide the equations of motion for the fluid knowing the state of stress (characterized by the stress tensor τ_{ij}) the fluid is in. The constitutive equations provide the missing link between the rate of deformation and the resulting stresses in the fluid. Newtonian fluids exhibit a linear relation between the shear rate of strain and the shear stresses; and their constitutive equation can be expressed as:

$$\tau_{ij} = -p\delta_{ij} + 2\eta e_{ij} \tag{4-3}$$

where τ_{ij} is the viscous stress tensor, η is the viscosity, p is the fluid pressure and e_{ij} is the rate of deformation or rate of strain tensor:

$$\mathrm{e_{ij}} = \frac{1}{2}\left(\frac{\partial w_i}{\partial x_j} + \frac{\partial w_j}{\partial x_i}\right) \tag{4-4}$$

Inserting the constitutive equations for an incompressible Newtonian fluid into Cauchy's equations, the famous Navier-Stokes equations are obtained:

$$\rho\left(\frac{\partial w_i}{\partial \mathrm{t}} + w_k \frac{\partial w_i}{\partial x_k}\right) = \rho \mathrm{F_i} - \frac{\partial p}{\partial x_i} + \eta \frac{\partial^2 w_i}{\partial x_j^2} \tag{4-5}$$

In Newtonian fluids, the viscosity η depends on temperature and pressure only. For non-Newtonian fluids, the viscosity η is a function of the rate of strain tensor e_{ij}, Eq.(4-4), and/or τ_{ij}, as well as temperature and pressure. For power law fluids, the viscosity is expressed as:

$$\eta = \left(\frac{1}{2} D_{II}\right)^{\frac{n-1}{2}} \tag{4-6}$$

where n is the power law index and D_{II} is the second invariant of the strain rate, given by:

$$\frac{1}{2} D_{II} = 2\left[\left(\frac{\partial w_i}{\partial x_j}\right)^2 + \left(\frac{\partial w_j}{\partial x_i}\right)^2\right] + \left(\frac{\partial w_i}{\partial x_i} + \frac{\partial w_j}{\partial x_j}\right) \tag{4-7}$$

In contrast to laminar flows, turbulent flows require a turbulence model, i.e. LES (Large Eddy Simulation) and RANS (Reynolds Averaged Navier Stokes), which enables a simplified calculation of the turbulent fluctuations. The available models require different grid resolution (quality and size) to resolve the turbulent structures. Full description of the turbulence models and their applicability can be found in (Paschedag, 2004). The calculation of laminar flows, in turn, requires a high grid quality in order to minimize the numerical diffusion. This topic is discussed in more detail in a later section.

4.1.2 Numerical solution: finite volume method

The governing equations are solved over a solution domain, subject to certain boundary conditions. The numerical formulation involves discretization of terms in the governing equations, such as transient term, advection term, diffusion term and source term. Conventional methods for such discretization include the finite difference method, finite volume method and the finite element method. The finite volume technique is briefly described in this section. Special literature should be consulted for further detailed information, for instance (Paschedag, 2004).

The numerical solution processed by the finite volume method starts with the division of the fluid domain into a number of non-overlapping finite volumes such that there is one control volume surrounding each grid point. The partial differential equations are discretized by integrating the differential form of the governing equations over each control volume element. The result is a number of integral equations, which is equal to the number of control volumes. The volume integrals are converted to surface integrals, and these are

fragmented into parts that are evaluated as fluxes at each surface of the corresponding control volume. Interpolation or piecewise profiles describe the variation of the variable between the grid points and are auxiliary relations for evaluating the required integrals. It is not necessary to use the same profile for all terms in the equation. The discretization of the convective terms is of special interest, because it requires numerical schemes with implications in the solution accuracy of the problem, such as numerical or false diffusion. The present calculations were done using the numerical upwind scheme.

The behavior of the numerical schemes is characterized by the Péclet number, which is defined as the ratio between the advection rate to rate of diffusion:

$$Pe = \left(\frac{\rho \quad v \quad L}{\Gamma} \right) \tag{4-8}$$

Diffusion dominated transport is characterized by small Péclet number and a convection dominated transport by a large Péclet number. The upwind scheme assumes a linear profile between the dependent variable ϕ and the spatial variable χ, which is nearly true for small Péclet numbers, i.e. small grid size. When the Péclet number is large, the value of the variable ϕ at the interface is nearly equal to the value of it at the upwind boundary. The upwind scheme always calculates the diffusion term from a linear ϕ - χ profile and thus overestimates diffusion (Patankar, 1980).

The numerical error derived from this numerical scheme has a diffusive character and its name “numerical diffusion” is given because it presents itself as equivalent to an increase in the diffusion coefficient. Thus in the solution of the momentum equation, the fluid will appear more viscous; in the solution of the energy equation, the solution will appear to have a higher conductivity; in the solution of the species equation, it will appear that the species diffusion coefficient is larger than in actual fact. These errors are most noticeable when diffusion is small in the actual problem definition (Marshall and Bakker, 2002).

The numerical diffusion can be minimized by (1) building the grid such that the grid lines align with the flow direction. Quadrilateral or hexahedral grid can provide better alignment with the flow. (2) Reduce the grid size (and so the Péclet number), especially in regions where most accuracy is sought. (3) Use higher order schemes, which increase the computational efforts and may decrease the stability of the solution. A comprehensive explanation of this numerical effect can be found in Patankar (1980) as well.

The fact is that the flow is rarely aligned with the grid throughout the entire flow field; extremely fine grid is often not practical, so that numerical diffusion remains always present at a certain degree in the solution.

4.2 Approaches to solve rotating grids in stirred tanks

The simulation of fluids in stirred tanks requires the incorporation of the motion of the impeller. In this work, two techniques were employed to model the impellers and both require real impeller geometry and a grid that consists of static and rotating regions. The solution is achieved by using either a steady-state (multiple reference frames) or a time-dependent (moving mesh or sliding mesh) technique. Both the MRF and the sliding mesh techniques have produced reasonable predictions of flow of Newtonian fluids in mixing tanks (Kelly and Gigas, 2003).

4.2.1 Multiple reference frames

The multiple reference frames (MRF) method (Luo *et al.*, 1994) is a steady-state approach that enables the modeling of stirred tanks equipped with baffles and/or (rotating or stationary) internals. The grid region encapsulating the impeller must be a perfect surface of revolution, and is defined as rotating frame, while the remaining region between impeller and wall, including stationary baffles and internals is defined as stationary frame. This method can be used for multiple impeller shafts in a tank, because each impeller can be modeled with separate rotating frames (with separate rotational speeds) while the remaining space can be modeled as a stationary frame. The stationary and rotating grid regions used for the MRF approach are coupled with a common surface (interface). The transfer of information occurs constantly at the MRF interface as the solution progresses. The approach uses a rotating coordinate system for the rotating frame, so that the unsteady interactions between rotating and stationary frames are considered. A solution with sufficiently small residuals is relatively fast to achieve, because the geometric arrangement of the impeller blades relative to the baffles remains unchanged during the solution. However, the transient effects resulting from a change in position of the impeller may not be resolved.

4.2.2 Moving mesh

The moving mesh model (Murthy *at al.*, 1994) is a time-dependent solution approach in which two computational grids are employed like in MRF method: one grid region is

moving with the impeller and the other is fixed to the tank. However, the moving grid is allowed to slide relative to the stationary grid in the moving mesh approach. The motion of the impeller(s) is physically modeled because the grid region encapsulating it rotates. Thus, a time-accurate simulation of the impeller-baffle interactions can be accomplished. The motion of the grid occurs in discrete steps. The impeller moves for each step a certain rotation angle, which is determined by its frequency and the given time step. For each discrete motion, the set of conservation equations is solved until convergence is achieved. Convergence requires very small time steps, and so, the impeller moves only a small rotation angle every step. The calculation time is in comparison to MRF method significantly higher. During the solution, information is exchanged between the sliding interfaces, which are two superimposed surfaces of revolution. During the solution, the cells will not necessarily line up exactly, or conform to each other. When information is passed between the surfaces, interpolation is required to match each cell with its many neighbors across the interface.

4.3 Mixing time calculation

The prediction of the mixing quality is one of the most important process criteria in the reactor design. It depends strongly on the flow patterns predicted by the code that, in turn, depends on a series of numerical factors that were presented and discussed previously. The most used method to determine the mixing time in a stirred tank is to track a species blending along with a transient calculation. This method, however, must be used with care for laminar flow (Birgith *et al.*, 2000). The molecular diffusion is a very slow process. Therefore, sharp concentration gradients remain present in the laminar flow and simulations overestimate the mixing efficiency due to the numerical diffusion, as previously described. To predict accurately species concentration distributions in laminar flow and the mixing time is therefore not feasible today (Hirschberg *et al.*, 2006).

The common approach to determine the mixing time in laminar flow is the Lagrangian particle tracking, because this depends only on the streamlines of the flow within the tank, and the numerical diffusion effect is eliminated. In fact, this eliminates the real molecular diffusion as well. The distribution of the tracer particles within the vessel is determined by convection only. The difficulties encountered in this method are related to the computational time, since a large number of particles must be tracked to obtain meaningful results, and to the formulation of a criterion to quantitatively measure the distribution of the

discrete phase (tracer) within the tank, and so predict the mixing goodness at a certain time. Harvey *et al.* (2000) pointed out another difficulty related to the particle trajectory calculations: the inherent sensitivity of chaotic trajectories to errors and the rate of propagation of errors in numerical integration schemes. The integration error can grow proportionally to the square of the integration time and, in the face of the very long mixing time inherent in laminar flows, imposes serious limitations on the accuracy of the particle tracking method.

There are a few published works evaluating the homogenization in laminar flows using the particle tracking method. Zalc *et al.* (2002) studied computationally the laminar mixing performance in a stirred tank equipped with three Rushton turbines. The authors used the particle tracking method to evaluate the distribution of the dye concentration in the stirred tank. A very large number of tracer particles were recorded after a certain number of impeller rotations. The approach used by the authors was to compute the amount of tracer in each region of the tank by dividing the volume into several cells in radial and vertical direction only. The mixing in azimuthal direction was neglected in the data analysis. The concentration of particles in each cell volume is simply equal to the number of particles that fall within a cell divided by the volume of the cell. The percentage of the flow domain, which contains tracer particles, was used as a measure of the homogeneity at a given time during the mixing process. This simple method to evaluate homogeneity of laminar flows in stirred tanks can also give an insight of the stagnant zones by plotting the concentration of particles in each defined square cell in the radial-axial plane.

A similar approach was used by Liu *et al.* (2006) to determine the goodness of mixing of shear thinning fluids in a SMX static mixer. The authors used particle tracking instead of species transport because the numerical diffusion in a pseudo concentration method to track changes in mixing quality causes a much faster mixing process than the real physical diffusion in laminar flow. Statistical sampling methods were used to quantify the mixing degree in a cross-sectional flow area. This was divided in several squares and the concentration of particles in each square was computed. The COV (coefficient of variation) was calculated by determining the deviation of the concentration of particles from the "perfect" concentration divided by the "perfect" concentration. The smaller the value of COV is, the better the homogeneity of the mixture.

Aubin and Xuereb (2006) investigated the effect of multiple Intermig impeller configuration on mixing performance in a stirred tank in laminar regime. Interactions

between impeller stages and compartmentalization were assessed using Lagrangian particle tracking. Probability of the presence of a particle is computed to analyze the mixing quality, which is determined by computing the time spent by a particle in a zone divided by the total time of trajectory. The particles are released in different compartments and the time spent by the particles in each compartment is calculated in terms of percentage of the total time. The study using particle tracking enabled a description of the interaction between the impeller stages.

4.3.1 Species transport

The dynamic distribution of the tracer inside the stirred volume is calculated by solving a time-dependent scalar transport equation, based on the assumption that the tracer is distributed in the vessel by convection and diffusion.

$$\frac{\partial \rho \phi}{\partial t} + \frac{\partial}{\partial x_i}\left(\rho w_i \phi - \Gamma \frac{\partial \phi}{\partial x_i}\right) = S\phi \qquad (4\text{-}9)$$

where ϕ is an arbitrary scalar that here represents the species mass fraction. Γ is the molecular diffusion coefficient and $S\phi$ is a source term. The species equation is a statement of conservation of a single species. Multiple species equations can be used to represent fluids in a mixture with different physical properties.

The strategy to use this method is to first solve the flow field. The equations of flow are then deactivated. A tracer concentration in the whole vessel volume is patched to zero, except for the injection region that can be either a large portion of a surface or a small number of cells, where a volume fraction of tracer equal to one is considered. Now only the scalar ϕ is calculated in a transient calculation.

The use of species transport with the sliding mesh model requires extremely high computational time, because the flow field data are required for each time step, so it is not possible to disable the flow field calculation to perform the species transport calculation (Marshall and Bakker, 2002). Mixing times in laminar flows are often very long, which makes the combination of both methods very disadvantageous.

4.3.2 Lagrangian discrete phase model

The Lagrangian discrete phase model in FLUENT® follows the Euler-Lagrange approach and describes a dispersed phase consisting of a large number of particles, droplets or bubbles in the calculated flow field. The movement of an individual particle results from

the forces and moments acting on this particle. These forces are fluid dynamic forces exerted on the particle and can be also body forces due to gravitation and electrical or magnetic forces. Collision of the particle with walls or with another particle results in a change in the direction movement of the particle as well.

The trajectory of a discrete phase particle is calculated by integrating the force balance on the particle. This force balance equates the particle inertia with the forces acting on the particle, and can be written (for the x direction in Cartesian coordinates) as follows:

$$\frac{\partial u_P}{\partial t} = F_D(u - u_P) + g_x \frac{(\rho_P - \rho)}{\rho_P} + F_x \tag{4-10}$$

where u is the fluid velocity (in x direction) and u_P is the particle velocity. F_x represents an additional acceleration (force per unit particle mass) term. The first term on the right side of the equation is the drag force per unit particle mass:

$$F_D = \frac{18\eta}{\rho_P d_P^2} \frac{C_D Re}{24} \tag{4-11}$$

C_D is the drag coefficient that can be calculated using laws for spherical and non-spherical particles as described in the documentation of the CFD code FLUENT®. Re is the relative Reynolds number, which is defined as:

$$Re = \frac{\rho\, d_P (u - u_P)}{\eta} \tag{4-12}$$

The position of each particle is known for each time step of the calculation. In that manner, statistical sampling methods can be applied to analyze and evaluate the distribution of the particle within the stirred vessel. Different approaches to evaluate in a semi-quantitative manner the mixing performance of the impeller system have been proposed in the open literature, as previously mentioned (Zalc *et al.*, 2002; Liu *et al.* 2006; Aubin and Xuereb, 2006).

4.4 Modeling of co-axial impellers in stirred tanks

The CFD modeling and simulation of the co-axial mixers consisting of a dual set of 45° pitched blade turbines combined with a proximity impeller (anchor or Paravisc) is addressed in this section. The specifications and statements made here are referred to the CFD code FLUENT® version 6.3.

4.4.1 Geometry and grid

The tank and impeller geometries were built with the software GAMBIT® (Gambit®, 2006) and then exported to ICEM CFD™ version 5.0 (ANSYS®, 2005) for meshing. The geometries of the investigated co-axial mixers are illustrated in Figure 4-2. The tanks were three dimensionally meshed with unstructured hexahedral elements. Because the flow in a co-axial mixer is expected to be highly complex, no flow symmetry or periodicity was applied. Figure 4-3 illustrates the grid construction of the inner impeller zone in the stirred tank. The inner impeller zone was duplicated and patched together with a separately meshed model of the stirred tank containing an outer impeller (anchor or Paravisc). The

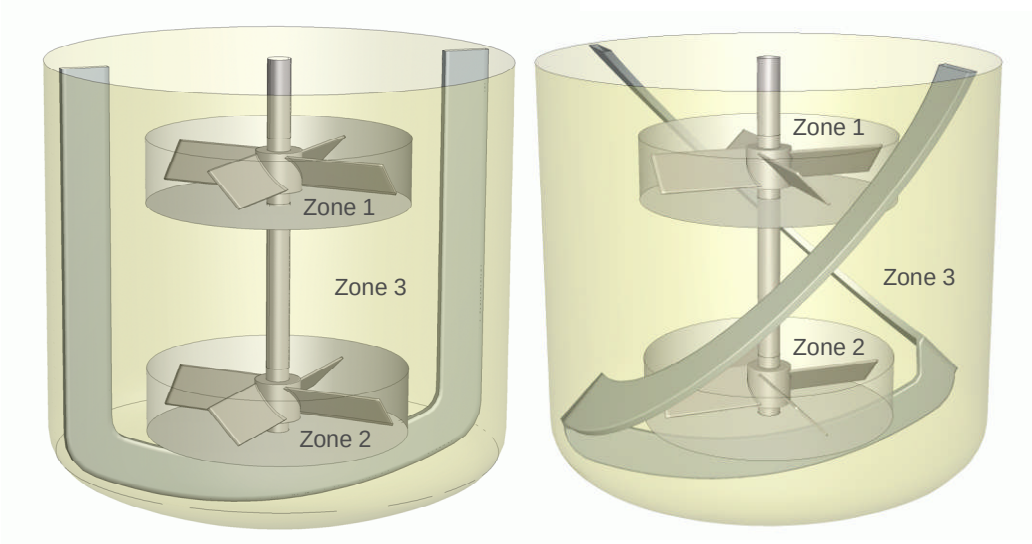

Figure 4-2: Rotating grid zones for the co-axial mixers (left: anchor/PBT, right: Paravisc/PBT)

spaces inside the pitched blade turbine were transformed into several symmetrical regions, which could be fully mapped with a hexahedral grid. In Figure 4-4 the surface grid for the impellers is illustrated. The rectangular cells are roughly uniformly spaced through the blades of the outer impellers with exception of the bottom region of the outer impellers due to the necessary projection of the cells attached to the shaft region. The O-grid boundary meshes were used around the impellers as well as in the bottom of the tank, which are illustrated in Figure 4-5. The high number of cells encountered in regions near the outer impeller and shaft is smoothly distributed throughout the vessel boundaries. This is a

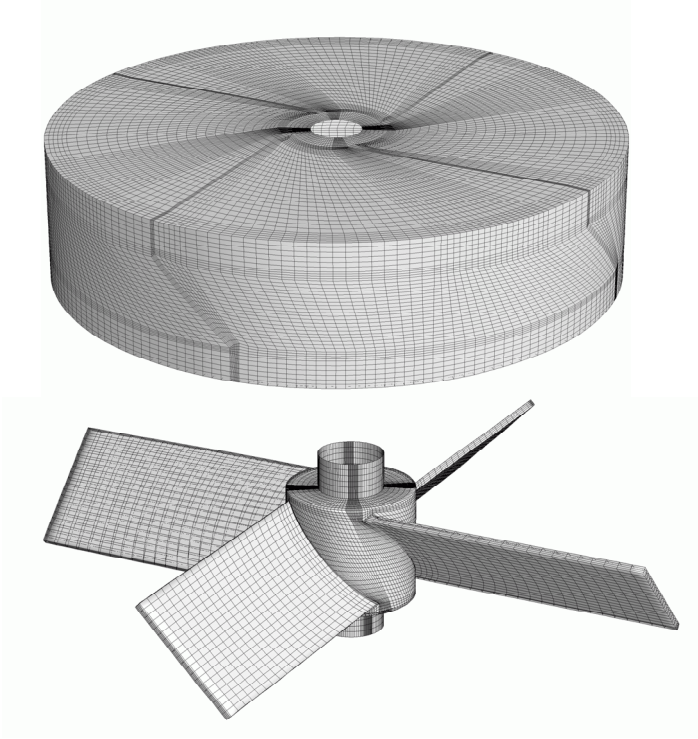

Figure 4-3: Grid structure for the pitched blade impeller zone

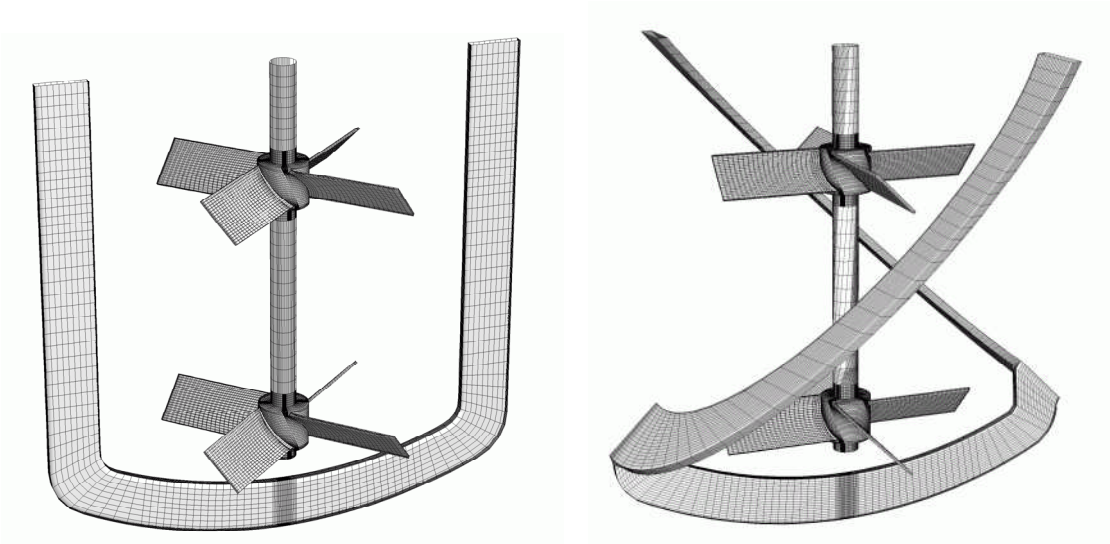

Figure 4-4: Surface grid for the impellers

powerful grid generation feature encountered today in ANSYS® ICEM CFD™ software that enables a dense number of rectangular cells in solution relevant boundaries and/or regions without having to couple the same high number of cells to other boundaries, like it normally occurs in a block-structured grid technique. The O-grid feature can produce hexahedral grids of high quality in complex geometries without being penalized by an

extremely large computational grid. The quality of a hexahedral grid is a function of the aspect ratio (length and width of a cell), angle and size interval from one cell to another. The total number of grid cells used in the co-axial mixer model with anchor was 1,005,560 and in the model using Paravisc was 1,094,856. Although both models have roughly the same number of cells, the grid "quality" of the models is different. In contrast to the model for anchor/PBT, cell angles of nearly 90° could not be achieved in a large portion of the domain for the Paravisc model because of the angled blades of the Paravisc impeller. The Paravisc model used in this work ensured, however, reasonable aspect ratios (ideal ratio is one) in regions near the impeller blades. In other regions, the gradients are not expected to be high, so that the cells with higher aspect ratios and angles diverging from 90° should not interfere significantly in the quality of the results.

The size of the cells in the co-axial mixer models is in the range of $7.7x10^{-5}$ and $8.5x10^{-1}$ cm^3 for the anchor and in the range of $7.7x10^{-5}$ and 1.91 cm^3 for the Paravisc.

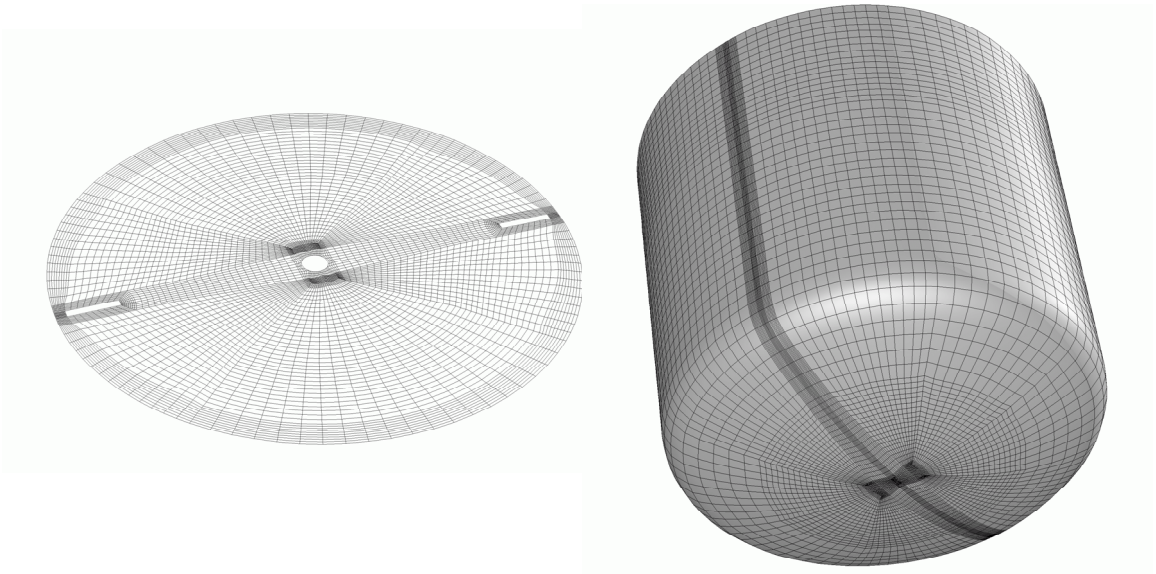

Figure 4-5: Surface grid for the liquid surface (left) and stirred tank wall (right)

For the calculation of the impellers' rotation in a co-axial mixer, the transient Moving Mesh approach was used. A combination of rotating grid zones was used: the grid zone of the proximity impeller (zone 3) encapsulates two grid zones; one with the upper (zone 1) and the other with the lower inner impeller (zone 2), as shown in Figure 4-2. The size of the inner impeller rotating zones was kept constant for all cases studied. The grid zone of the proximity and the inner impellers rotate with different rotational speeds. The two regions are implicitly coupled at the interface separating the two domains via a sliding-grid

algorithm, which takes into account the relative motion between the two sub-domains and performs the required interpolations (Brucato *et al.*, 1998).

The top surface of the tank was assumed to be flat and a zero shear-stress boundary condition was set. The cases were simulated in the laminar regime. The upwind second scheme was employed for the equations discretization. The SIMPLE algorithm was chosen to couple velocity and pressure.

The fact that multiple reference frames (MRF) can provide only a stationary solution of the flow field for a given position of the inner impellers with respect to the proximity impeller, and the interactions between inner and outer impellers were expected to be strong, this method was right from the start discarded. However, the models using MRF were used as initial condition for the moving mesh models. In that manner, the computational time to achieve a quasi-steady state and periodic solution could be reduced. The convergence criterion was to have the residuals reduced by at least three orders of magnitude in each calculated time step.

The time step size is an important parameter in the moving mesh method. The time step was chosen to be the time necessary to rotate the inner impellers one degree (one revolution required 360 time steps). This criterion was used to determine the time step size for all cases studied in this work. Further reductions of the time step did not demonstrate any significant influence on the calculated torque or the monitored velocity at selected points in the tank.

The cell density around the blades was set to be high enough to capture all flow scales. However, the effect of the grid size was then investigated by applying additional mesh refinements near the walls of the impellers and on cells with a certain level of velocity gradient. The torque values again did not change significantly with further scale reduction, indicating that the selected grid sizes were providing grid independent solutions.

A number of revolutions of the impellers were necessary to yield a quasi-steady state solution. In most cases, after 8 complete revolutions of the inner impellers, a periodic solution was achieved, which required approximately 100 hours of computational time, when ran in parallel on a Linux cluster (2.0 GHz Opteron, 4GB Memory, Gigabit Ethernet) using 4 CPU’s.

4.4.2 Fluid dynamics

The characterization of the three dimensional flow fields of the individual impellers in stirred tanks is quite well established, especially in the turbulent regime. The description of three-dimensional laminar flow fields, however, has only begun to emerge recently, when local measurements with classical techniques, such as laser Doppler velocimetry and PIV, have been applied (Zalc *et al.* 2001, Szalai *et al.* 2004).

In high viscosity mixing applications, the use of complex agitation systems composed of at least two different impeller types are quite common. The understanding of the complex three-dimensional laminar flow fields of those complex agitators is even more limited. To the best of the author's knowledge, no measured data of velocity for co-axial mixing configurations, object of research in this work, could be found in the open literature. Even if measured velocity data were available, a direct comparison would be very difficult, since each complex mixing system pursues a very singular configuration. Like in co-axial mixers, the configuration of such complex mixing systems is often a combination of two or more impellers in the same vessel.

The complex velocity field of a co-axial mixing system is made out of the interaction of at least two impellers in the vessel, a proximity impeller and at least one open impeller. In this work, single impeller systems are an agitated vessel equipped with two types of impellers (proximity and open impellers), in which one of the impeller types is rotating while the other remains stationary. Measurements of the three dimensional flow fields of the investigated single mixing systems are also not available for a quantitative validation of the calculated flow field either. Nevertheless, a qualitative validation analysis of the calculated flow field of the individual impellers was conducted using data from published works for single impellers in stirred tanks with geometry and flow conditions as similar as possible to the ones investigated in this work.

4.4.2.1 Flow field validation of the pitched blade turbine (PBT)

The calculated flow field of a two stage pitched blade turbine in a stirred tank with a stationary anchor is presented in Figure 4-6. The Reynolds number was 21 and therefore the flow is laminar. The rotating impellers cause the fluid to flow radially outward, like a jet directed at the tank wall. At low Reynolds numbers, the pitched blade turbine is purely a radial pumping device. This flow behavior was also observed by Harvey *et al.* (1995), in which the flow field in a baffled tank with a single 45° pitched blade turbine was

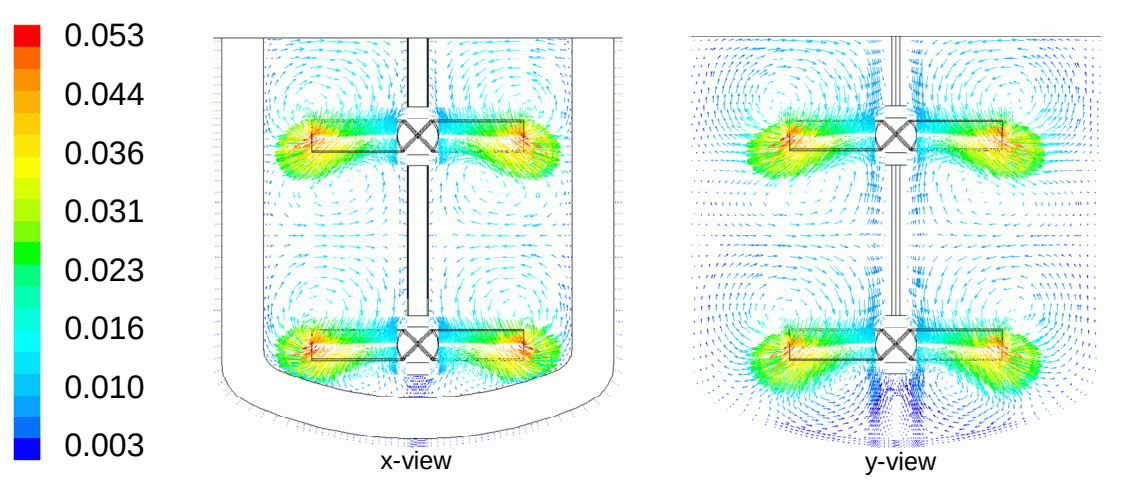

Figure 4-6: Plots of the calculated velocity fields for a dual set of PBT rotating with stopped anchor, laminar regime (Re=21).

experimentally measured and numerically calculated. The authors compared the numerical results with velocity data obtained experimentally using laser doppler velocimetry (LDV). A rigorous comparison with Harvey's data was not possible because of some critical geometrical differences in both mixing systems. The pitched blade turbine in Harvey's tank rotates alone in a four baffled vessel of 0.145m diameter (D/T=0.35) and is located at half the distance from the bottom to the liquid level height. A comparative analysis was carried out qualitatively by considering only the velocity components data from sections underneath the upper turbine.

The calculated data were taken at 6 axial locations, which are labeled as z1 – z6 in Figure 4-7. The data plotted in Figure 4-8 show the velocity profiles at the selected 6 axial stations. The grid was non-dimensionalized by the impeller radius (R=0.127m) and the velocity was normalized by the impeller tip speed (v_{tip} = 0.053 m/s). The computed data of the velocity components (axial, radial and tangential) for each axial location were extracted and then averaged from 18 rakes that were distributed in angular planes (from 0° to 180°, plus 45° and 135°); only half of the vessel was accounted for flow symmetry reasons. Each rake initiated at the shaft and ended up at the vessel wall.

The velocity profiles obtained in sections underneath the upper pitched blade turbine with anchor stopped showed similar trends as the measured velocity profiles in a four-baffled tank equipped with one single pitched blade turbine. The analysis shows that even the velocity magnitudes of the profiles were reasonably comparable to the experimental

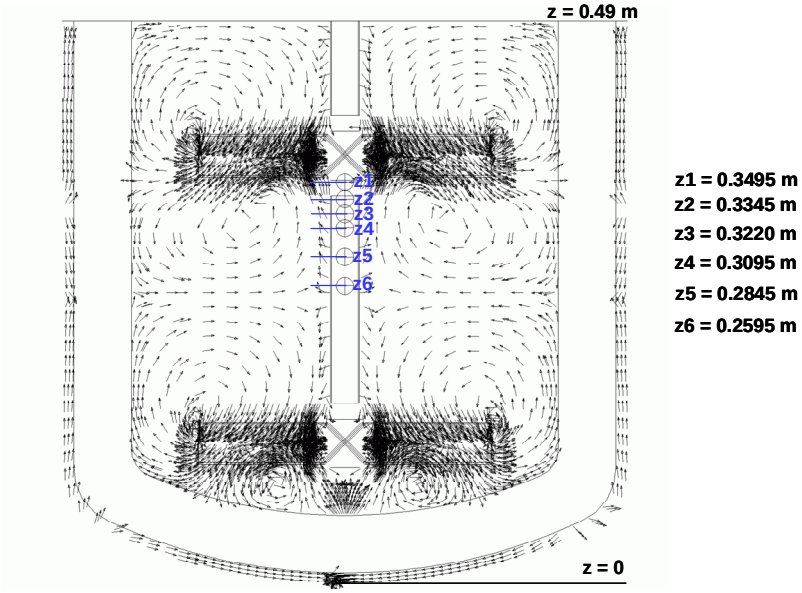

Figure 4-7: Locations of the axial sections, labeled z1 – z6

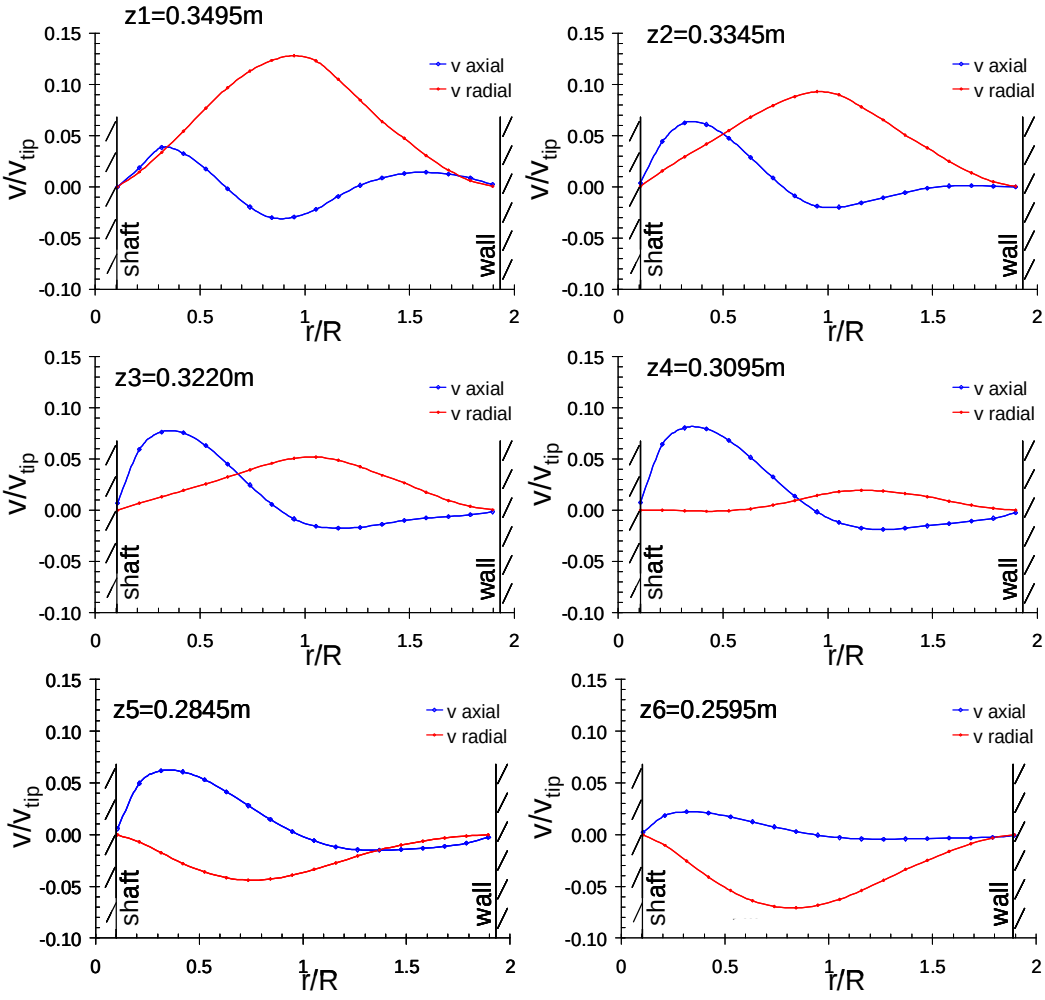

Figure 4-8: Calculated axial and radial velocity profiles, locations z1 – z6

data published by Harvey *et al.* (1995). The shape of the axial velocity profiles becomes shallower as the distance from the impeller increases. The axial velocity profiles achieve their maximum at the same position, ca. r/R=0.35. Harvey's data show a maximum at ca. r/R=0.5. This is due to the difference in the ratio of impeller to tank diameter in both systems. The minimum of the axial velocity profiles, however, is shifted toward the vessel wall as the distance from the impeller grows. The data indicate that the axial components increase in magnitude as the distance from the impeller increases (z1 to z4), and then they decrease (z5 to z6). This was also observed in Harvey's data for locations underneath the turbine. In section z6, which denotes approximately the middle of both turbines, the axial components of the velocity are very weak.

The trends of the radial velocity profiles are also in good agreement with Harvey's data. The radial velocity components are the highest in the position immediately under the impeller (z1) and damps out quickly as the distance from the impeller increases (z2 – z4). At location z5, the radial components show a direction change, denoting the presence of a recirculation loop. At axial location z6, the flow becomes strongly radial again and its direction is opposite to the one encountered at station z1.

The calculated tangential velocity profiles at locations z1 - z6 are plotted in Figure 4-9. Here, again, the profiles exhibited similar trends to the ones found by Harvey *et al.* (1995). The tangential velocity components become weaker for axial stations away from the impeller. The profiles are flatter with maximum at the same r/R position (~r/R=0.84). Harvey's experimental data indicate a maximum at ~r/R=0.9.

4.4.2.2 Flow field validation of the anchor impeller

The calculated flow field of the investigated mixing vessel equipped with an anchor impeller is illustrated in Figure 4-10. The two pitched blade turbines are stopped whereas the anchor impeller rotates at 12 rpm in a fluid of viscosity of 60 Pas. The flow regime is laminar, Reynolds number Re=1. The velocity vectors are plotted at $\theta=0°$, which corresponds to the anchor impeller plane. The pitched blade turbines are positioned ±45° relative to the anchor impeller. It can be seen that the flow is primarily circumferential. Although vectors in axial direction can be seen, their velocity magnitudes are small. In the bottom region of the tank, the bottom blade of the anchor together with the lateral blades of the anchor impeller is inducing the flow around the stopped blades of the lower PBT, which

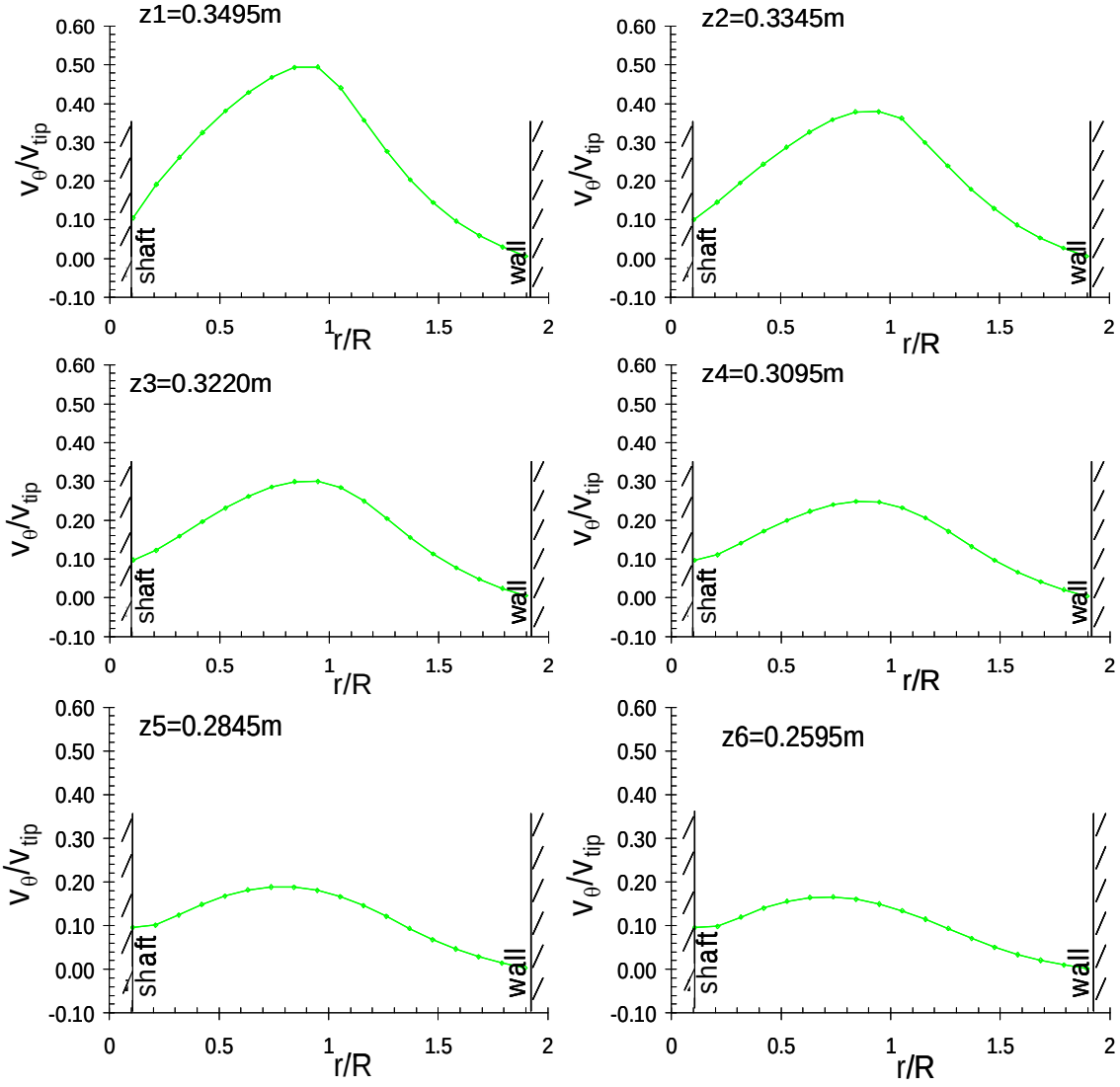

Figure 4-9: Calculated tangential velocity profiles, stations z1 – z6

are acting as baffles. The flow is deflected, promoting the recirculation of the flow and axial flow components in the bottom region of the vessel (Figure 4-10).

The obtained velocity profiles in the calculations at Reynolds number of 1 were qualitatively compared to the data given in Kuriyama *et al.* (1982). The radial velocity profiles for different radial locations (r/R= 0.96; r/R=0.7; r/R=0.6; r/R=0.4) at two axial positions (z/T=0.5 and z/T=0.76) are plotted in Figure 4-11. The z/T=0.76 position corresponds to the upper PBT impeller plane. The velocity was non-dimensionalized by the tip speed (v_{tip}), which is the tangential velocity of the outer tip of the anchor impeller. The calculated data show similar trends as the measured data. The shape of the radial velocity profiles and the order of magnitude of the velocity components are in good agreement to the published data in Kuriyama *et al.* (1982). The radial velocity profiles

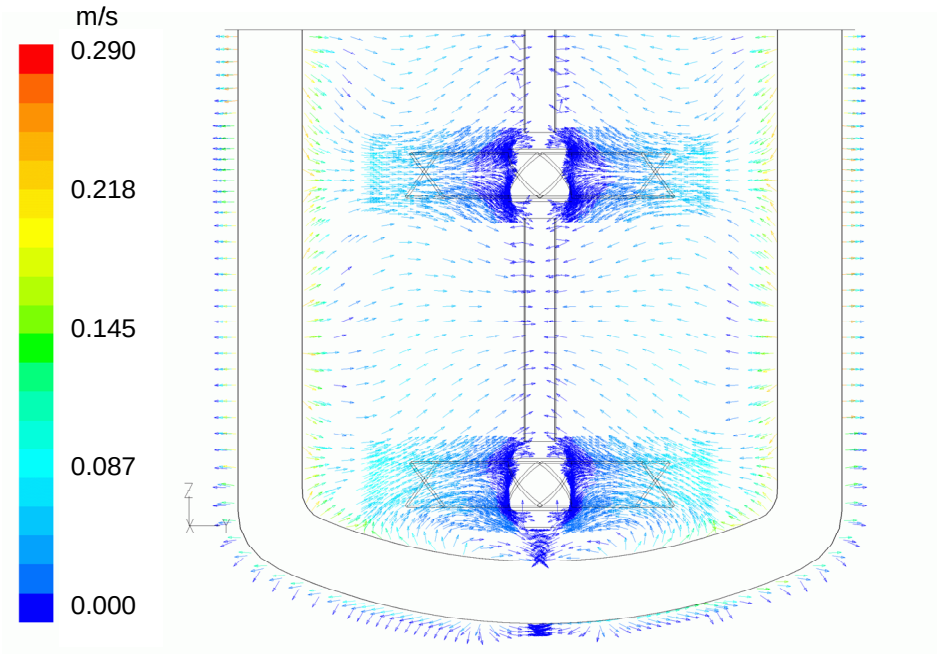

Figure 4-10: Calculated velocity field at Re=1 (view projected onto the impeller plane) with stopped pitched blade turbines

taken at both axial locations (z/T) are quite different, with the exception of the profile at r/R=0.96. At this radial position, the PBT blades (baffles) are quite far away. Thus, the effect of the PBT blades is no longer significant on the radial velocity profiles. As the distance from the stopped impeller blades decreases, the deviation considerably increases between the profiles at both axial positions (z/T), which indicates an effect of the stationary PBT blades on the radial velocity profiles.

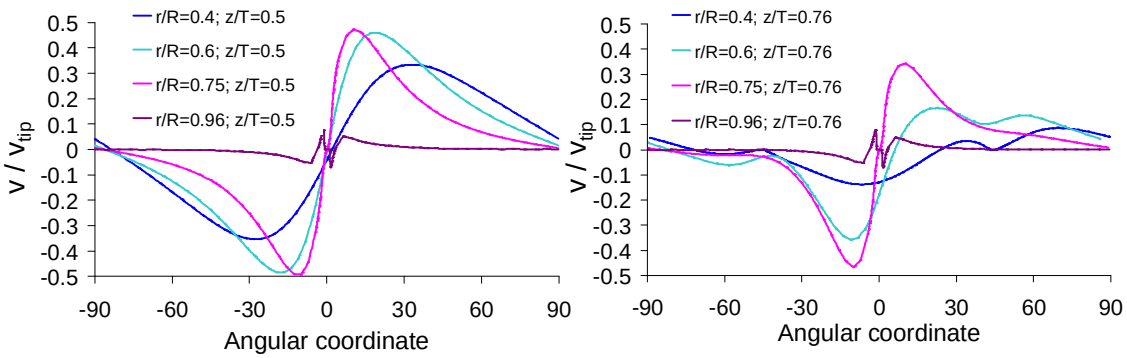

Figure 4-11: Radial velocity profiles (Re=1) at two different axial positions (z/T)

Also the tangential velocity profiles at two axial positions (z/T=0.5 and z/T=0.76) were calculated and plotted in Figure 4-12 and Figure 4-13. The anchor impeller is located at θ=0°, whereas the blades of the PBT are found at θ=45° and θ= -45°. The tangential velocity data were taken at several lines positioned in angles from -90° to 90° relative to the anchor blade, as shown in Figure 4-12. The rotational direction of the anchor impeller is shown in the bottom of Figure 4-12. The lines positioned ahead the anchor blade have positive angles and lines positioned behind the anchor blade have negative angles. The tangential flow is stronger behind the anchor blades than ahead of the blades, as also reported by Kuriyama *et al.* (1982). The maximum of the curve shifts to the inner of the vessel and its magnitude decreases as the distance from the anchor impeller increases. The distribution of the curves is in good agreement with the reported data by Kuriyama *et al.* (1982). Comparing the profiles for both axial positions, it is clear that the tangential profiles are also slightly affected by the stationary inner impellers. The difference is more pronounced in the low range of r/R, which corresponds to the radial positions smaller than the inner impeller radius (r/R~0.5). The tangential velocities are damped out in the region inside the inner blades.

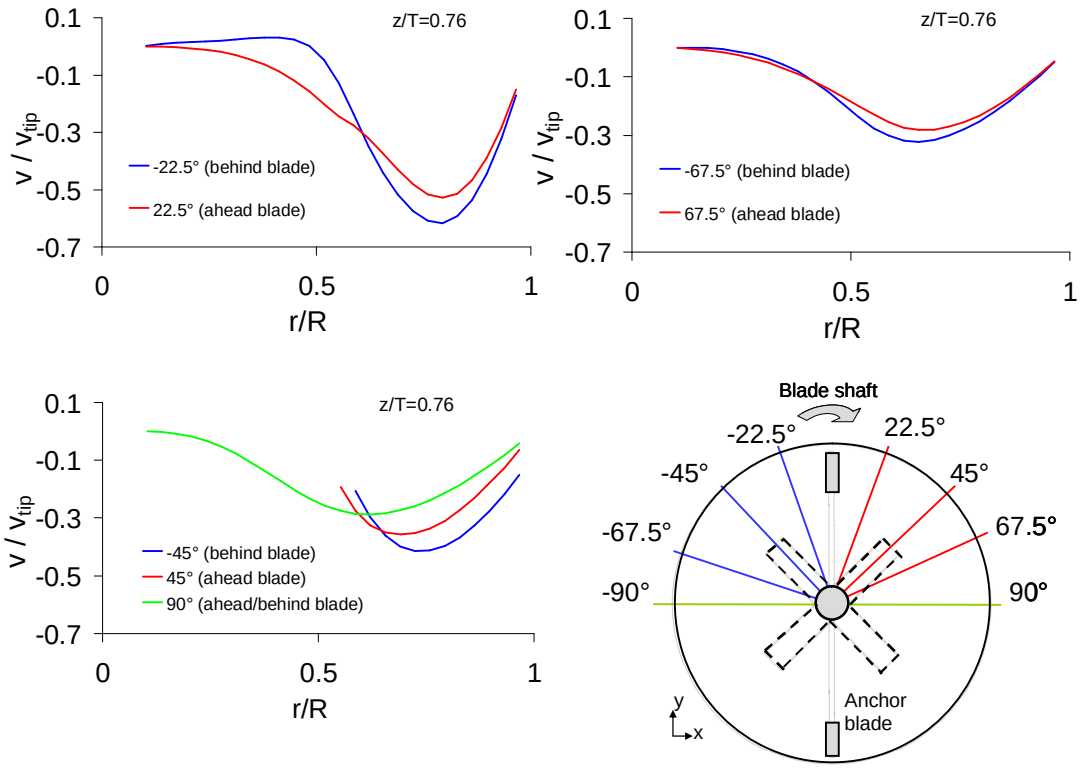

Figure 4-12: Tangential velocity profiles generated by the anchor impeller (Re=1) at z/T=0.76 and angular positions of the lines

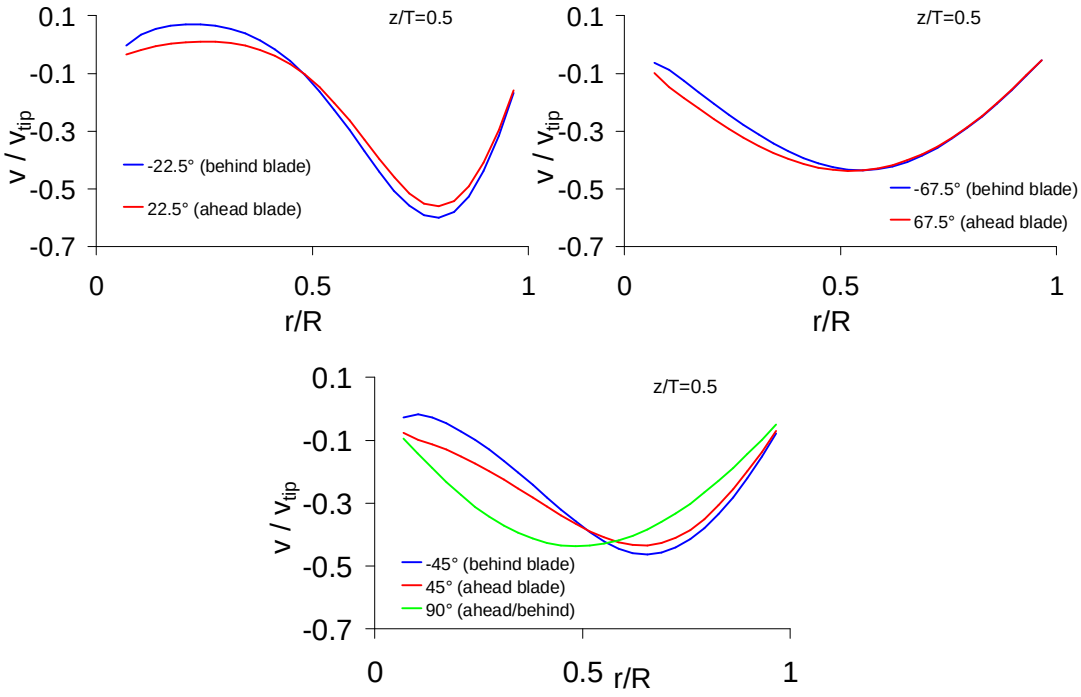

Figure 4-13: Tangential velocity profiles generated by the anchor impeller (Re=1) at z/T=0.50

4.4.2.3 Flow field verification of the PARAVISC® impeller

To the best of the author's knowledge, measured velocity data of the flow field created by the Ekato Paravisc® impeller has not been published yet. Thus, the validation of the calculated flow field of the Paravisc impeller with experimental data is not feasible today. The works of Delaplace *et al.* (2000b) and later Iranshahi *et al.*, (2006), however, are worthwhile to discuss here, since they reported numerical results of the flow characteristics of the Ekato Paravisc impeller with very similar configuration and flow conditions. Delaplace (2000b) and Iranshahi (2006) investigated the same impeller and vessel geometry, which consists of a vessel of 346mm diameter and a Paravisc impeller with 320mm diameter. The Paravisc has two vertical bars to support the blades. Delaplace (2000b) used the commercial CFD finite volume software FLUENT® and Iranshahi (2006) employed a finite element-based code to calculate the flow field induced by the Paravisc impeller. A verification of the calculated flow field of the single mixing system, e.g. Paravisc impeller combined with a dual set of stopped PBT was conducted by using the results of both published works and is discussed here.

Figure 4-14 shows the numerical results obtained for dimensionless axial velocity (axial velocity divided by impeller tip speed) for a Newtonian fluid (ρ=1415 kg m^{-3}, η=12 Pa s).

The impeller rotates at 17 rpm in the clockwise direction, which gives a Reynolds number of Re=7.2. The inner impellers are not shown in the plots for the sake of clearer illustration. The pumping action of this non-standard helical ribbon impeller can be visualized in the plots in Figure 4-14. The Paravisc generates an upward flow at the wall and a downward flow in the center of the vessel. The results show that the downward flow structures, denoted by blue colors, change position in counter clockwise direction as the horizontal planes moves to the top. The flow field created by the Paravisc impeller is three dimensional and complex. The convergence history of the velocity of three monitoring points, plotted in Figure 4-15, indicates the time dependency of the tank flow field per revolution. Besides, it suggests a complex shape of the velocity profiles as a function of the calculation time. It also shows the typical flow periodicity encountered in the mixing tank calculations using transient methods (i.e. sliding mesh), indicating that the sliding mesh has reached a revolution independent solution.

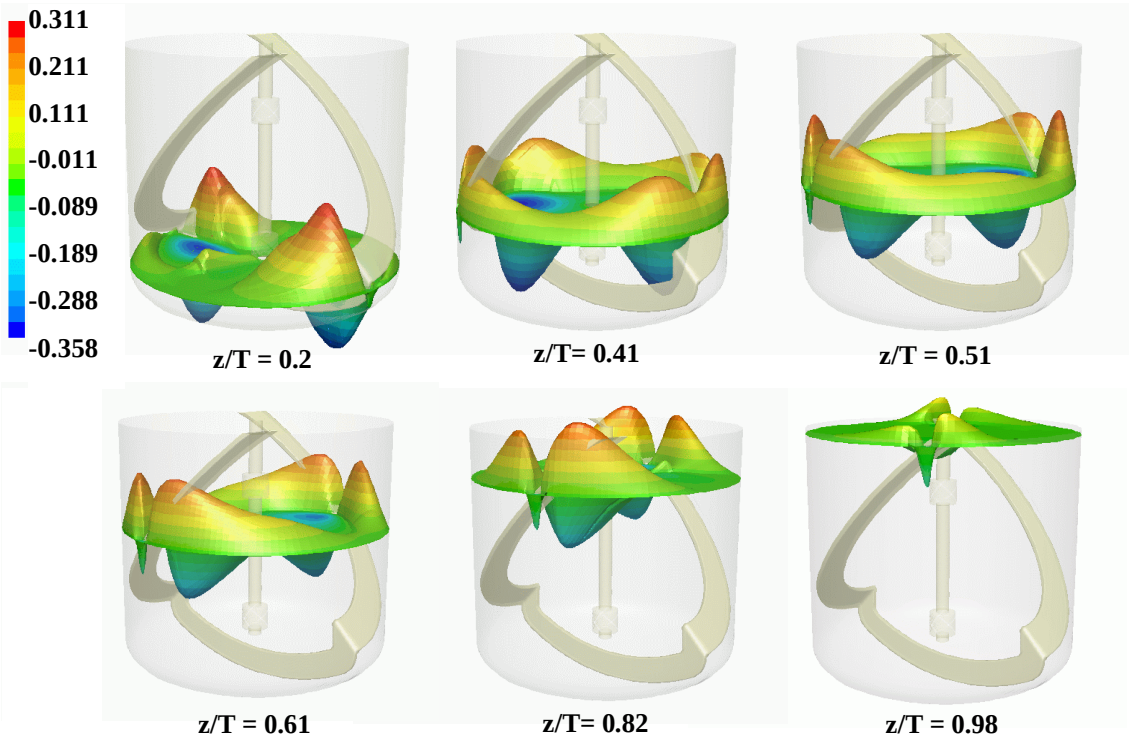

Figure 4-14: Contours of normalized axial velocity (v_z / v_{tip}) in various horizontal sections

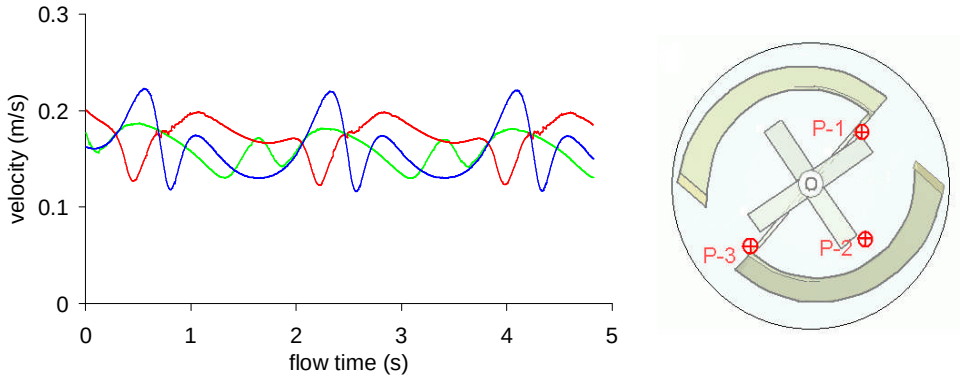

Figure 4-15: Velocity history of three monitoring points: P-1(0.1m; 0.1m; 0.22m), P-2(0.1m; -0.1m; 0.18m) and P-3(-0.1m; -0.1m; 0.45m)

The tangential, radial and axial velocity profiles for several angular locations in the vessel at the axial section z/T=0.562 are plotted in Figure 4-16. The position of the Paravisc blades and the angular locations of the velocity data points can be found in the bottom of Figure 4-16 as well. The radial locations covered by the Paravisc blade and shaft have also been plotted. The results show that the Paravisc blade (approximately at angular location 75°) generated significant local tangential velocity components. In locations close to the impeller blades, i.e. only 15° behind and ahead the blade (curves at 90° and 60° respectively), the tangential velocity components were still significant, but reduced in locations far away from the impeller blade. Significant axial flow was generated by the Paravisc impeller: strong upwards flow at the wall region and downwards flow in the middle of the vessel, approximately for 0.25< r/R<0.75. The axial flow was significantly attenuated at angular locations away from the blades of the agitator. The radial velocity components are very strong in the region close to the agitator blade, with maximum between 0.6 <r/R<0.75. The radial flow are more significant in regions behind the impeller blade than ahead the blade, considering the same relative angular position to the blade. The calculated profiles have similar trends as the reported results by Delaplace *et al.* (2000b) for a system at Re=28.7. The magnitudes of the normalized velocities presented in this work were however higher. The deviation is due to the fact that Delaplace normalized the velocities using the maximum tangential velocity encountered at the outside edge of the vertical bars and not the maximum tangential velocity of the Paravisc, as it is done in this work. The authors pointed out that the two vertical cylinders that support the blades promote significant local tangential and radial velocity components, actually higher than the ones generated by the Paravisc blades.

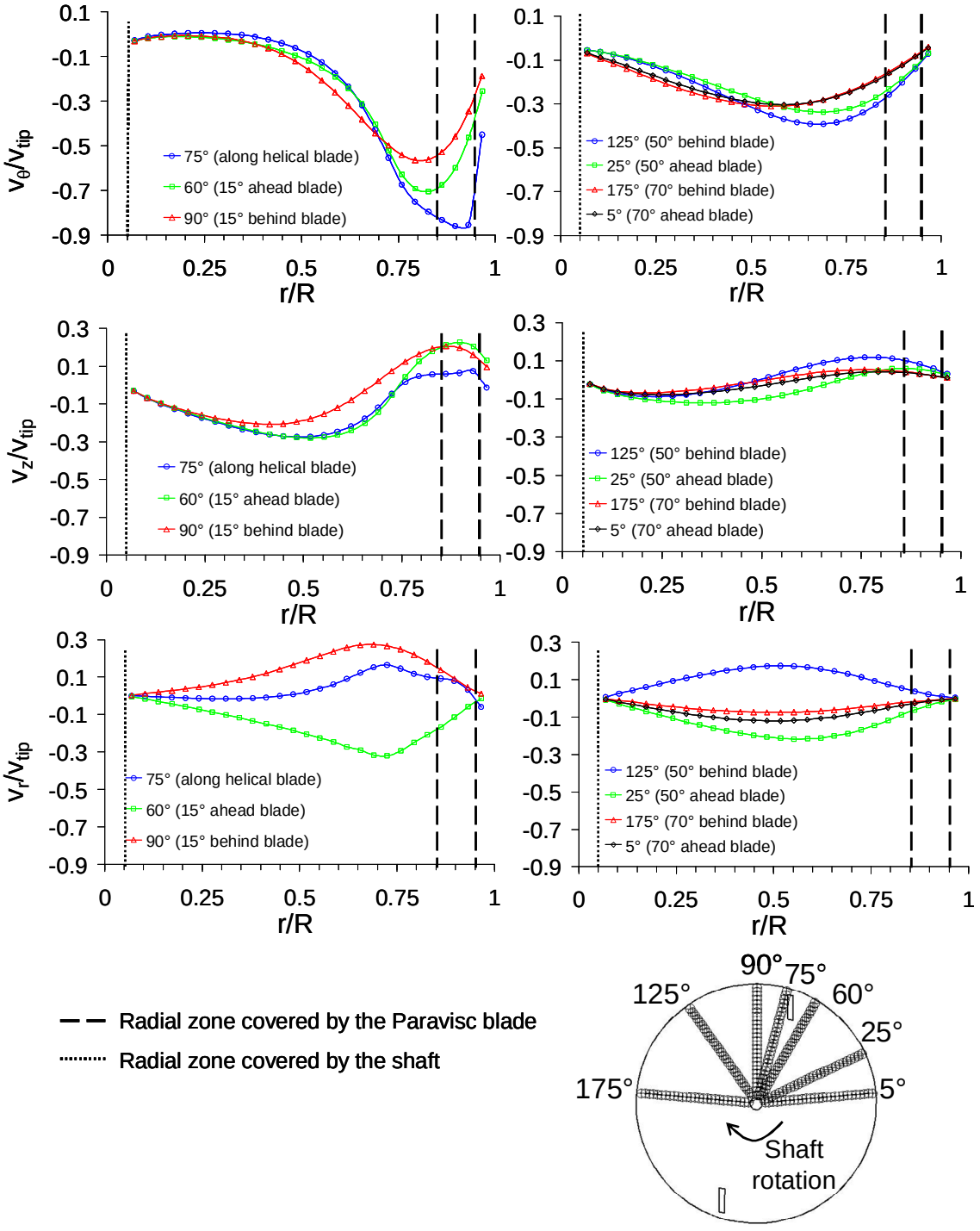

Figure 4-16: Velocity profiles created by the Paravisc (Re=7.2) at axial section z/T=0.562 for various angular locations

The stationary PBT blades in the middle of the vessel have an effect on the flow field created by the Paravisc, as it is shown in Figure 4-17. The plot of velocity vectors was taken from the axial section z=0.3725 (z/T=0.76), which corresponds to the upper impeller middle plane. The colors of the vectors denote the magnitude of the velocities. The flow

swept by the two Paravisc blades is deflected by the PBT blades and two vortices are created in the vicinity of the impeller tips. The vortices are created when the Paravisc impeller passes the stationary PBT blades and accompanies them. The vortices are weaker in the horizontal sections far away from the stationary impeller blades, but remain from bottom to top of the vessel.

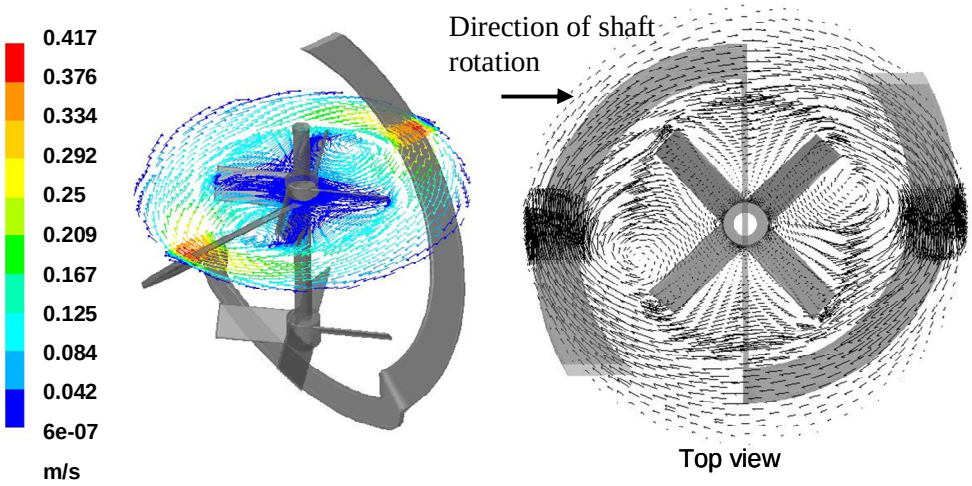

Figure 4-17: Recirculation created by the Paravisc with stationary open impeller blades (plot of velocity vectors at horizontal plane at z/T=0.76)

4.4.2.4 Flow field in co-axial mixing systems (preliminary discussion)

Simulations enable the visualization of the flow in the tank, and serve as critical tool for understanding the experimentally observed phenomena. In this section, a preliminary discussion about the flow characterization of the co-axial mixing systems is carried out. Few designs of co-axial mixers are analyzed with the aim of gaining firstly an insight of the primary flow patterns and velocity fields created in co-axial agitated systems in the laminar regime. A more detailed discussion about the influence of some key design parameters in co-axial mixers, such as tip speed ratio, outer impeller design, rotation mode and fluid properties on the mixer performance is carried out in Chapter 5.

Co-axial mixer: pitched blade turbines with Paravisc

Figure 4-18 shows snap shots of the flow field of a co-axial mixer equipped with the Paravisc proximity impeller in a co-rotating direction. The Paravisc impeller was designed to pump upwards or downwards near the wall depending on the direction of rotation (Ekato Handbook, 2000). The highest efficiency can only be achieved if the Paravisc pumps

upwards and the pitched blade turbines pump downwards. Hence, the counter clockwise rotation mode of Paravisc was not investigated in the scope of the present work. The outer impeller rotates (N_o) at 17 rpm and the inner impellers (N_i) rotate at 124 rpm, and so the tip speed ratio (tr) is 4. The fluid is Newtonian and has a viscosity of 12 Pas. The results of CFD calculations are presented as two-dimensional velocity vector fields. The colors of the vectors denote the magnitude of the velocities. The maximum velocity achieved is the tip speed of the pitched blade turbines. The view planes of the plots are fixed to the PBT, but relative to the Paravisc impeller. The plots show that the velocity fields change with the relative position of inner and outer impellers. It is important to point out that such highly complex, three-dimensional and unsteady flows should be analyzed with care, because two-dimensional and stationary plots can give misleading impressions about the flow.

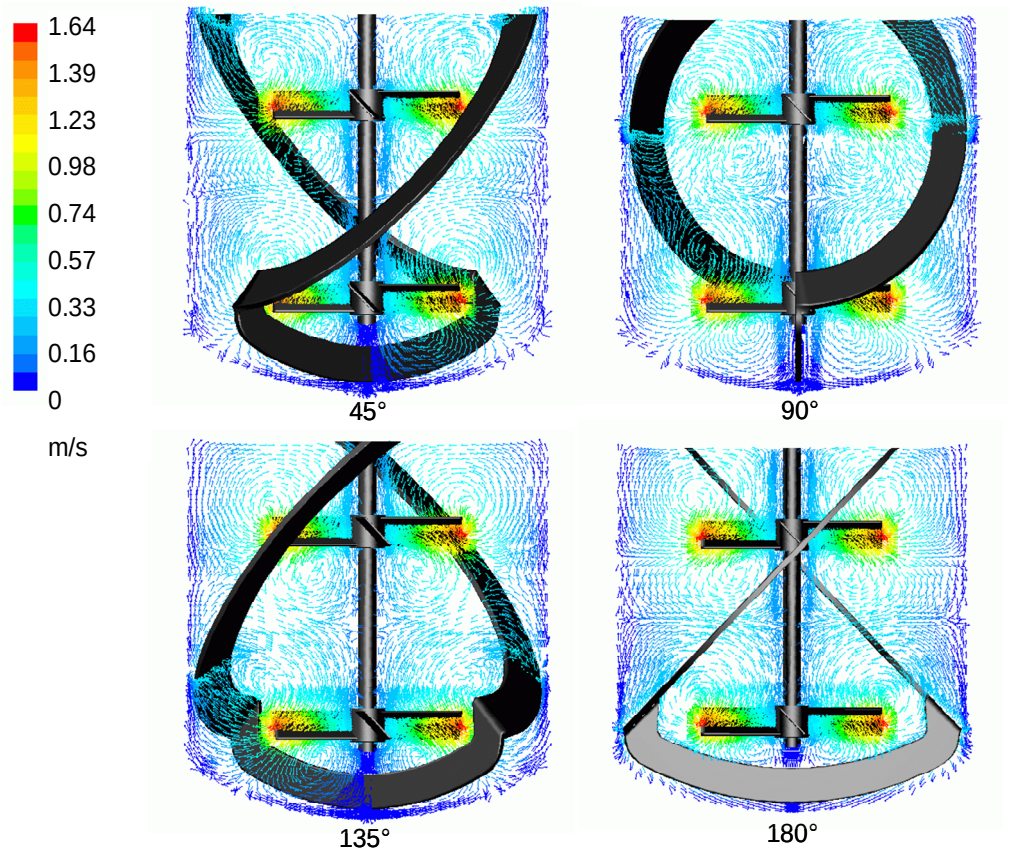

Figure 4-18: Snap shots of the flow field of a co-axial mixer (tr=4) with Paravisc. Colors denote velocity magnitude in m/s.

The primary features of the flow patterns remain essentially unchanged in all plotted views, and similar to the flow patterns created by the single impeller system, i.e. a dual set of PBT rotating with a stopped proximity impeller (Figure 4-6). In a co-axial mixing system, the typical vortices above and below the PBT blades are also present because at

low Reynolds number, PBT is a radial pumping device. However, the vortices slightly change positions as the Paravisc rotates. The radially induced jet is dampened at the moment the Paravisc blade aligns with the PBT blade (as shown in the plot with view θ=90°). At θ=135°, when the Paravisc blade moved 45° away from the considered PBT blade, the jet seems to be still regenerating, but at θ=180°, when the Paravisc blade has moved already 90° away from the blade, the full radial jet is again present. Because of the axial pumping capacity of the Paravisc, the radial velocity components created by the PBT impellers at low Reynolds numbers are dampened, whereas the velocity components become more axial. This effect occurs periodically, i.e. at times when the Paravisc blades are very near or aligned with the PBT blades.

In Figure 4-19 plots of the normalized axial components of the velocity for three agitated systems are shown. On the upper left, the pitched blade turbines are rotating at 124rpm alone in the vessel, i.e. Paravisc serves as a baffle. On the upper right, the Paravisc is rotating alone in the vessel and the turbines are stopped. In the bottom, the outer and the inner impellers are operating in co-axial mode with N_i=124 rpm and N_o=17 rpm. The fluid was Newtonian with viscosity of 12 Pas.

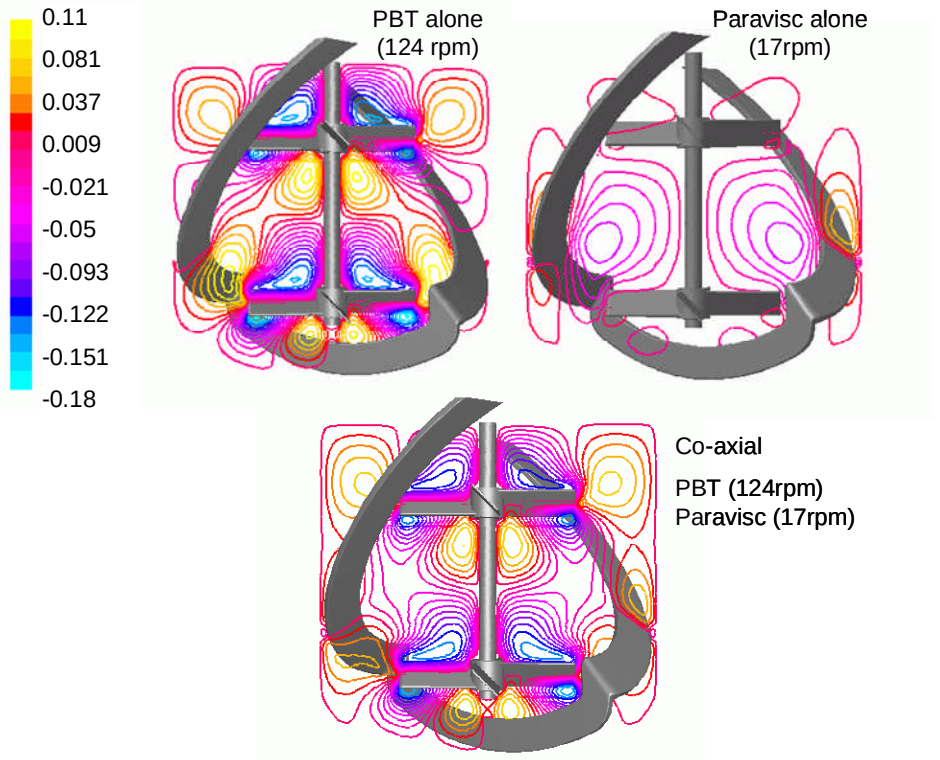

Figure 4-19: Normalized axial velocity fields of single impeller systems and co-axial mixing system with Paravisc in Newtonian fluid

The plots show the contours of the normalized axial velocities at the angular plane aligned with the PBT blades. The relative position of the outer and inner impellers is 45°. The normalization of the velocities was undertaken by dividing them by the maximum velocity, which is the PBT tip speed ($v_{tip,i} = \pi N_i D_i$). It can be observed that the axial flow field of the co-axial mixer combines elements of the axial flow fields of both single impeller mixing systems (i.e. PBT alone and Paravisc alone). The Paravisc promotes an upward flow motion at the wall in the co-axial mixer as well as in the corresponding single impeller system. The axial flow patterns generated by the inner impellers remain essentially the same in both mixing systems. However, the axial velocity field changes in the co-axial mixer. The axial flow is enhanced by the rotation of the pitched blade turbines.

In Figure 4-20, the three dimensional surface contours of the normalized axial velocity are plotted at three horizontal sections (z/T=0.7; z/T=0.51; z/T=0.19). The plots show that the axial pumping action in both single impeller systems is very distinct. The Paravisc impeller contributes in general to the upward pumping in the vessel at the tank wall. The inner turbines pump essentially radial jets that impinge at the wall and form recirculation loops. The axial pumping action is strongest in the vicinity of the inner impellers. In the middle plane, the pumping action of the inner turbines is significantly weak. In the co-axial mixer, however, the axial pumping action can be found at the wall region due to the action of the outer impeller Paravisc. Along the center, the pumping action is almost non-existent.

In Figure 4-21, the contours of normalized radial velocity for the three agitation systems are plotted. Again, the view plane is aligned with the inner impellers and the outer impeller is 45° relative positioned from the PBT blades. The radial velocities were normalized using the PBT tip speed as well. It can be seen that, in contrast with the axial velocity field, the radial velocity field of the co-axial mixing system is distinct from the calculated fields of the corresponding single impeller systems. The highest radial velocities in the vicinity of the inner impeller blade tips are attenuated in the co-axial configuration. These preliminary results indicate some displacement of the flow patterns in the co-axial mixing configuration using the Paravisc impeller. Therefore, consequences on the power consumption of each impeller, and the overall mixing time are expected, and are discussed in the next chapter.

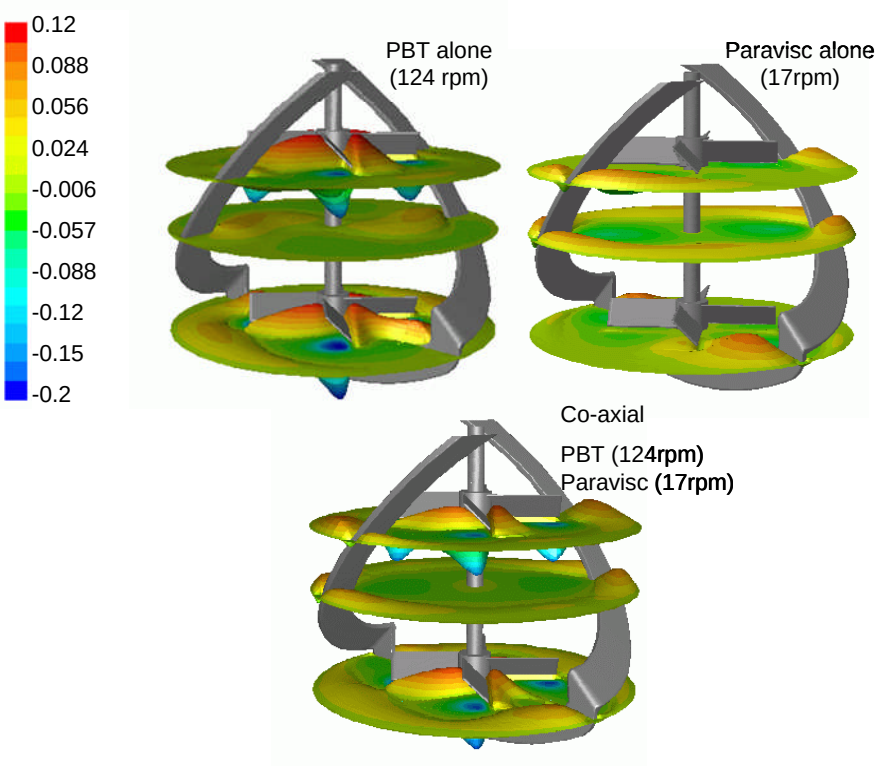

Figure 4-20: Three dimensional surface contours of normalized axial velocity in various horizontal sections for three agitation systems with Paravisc

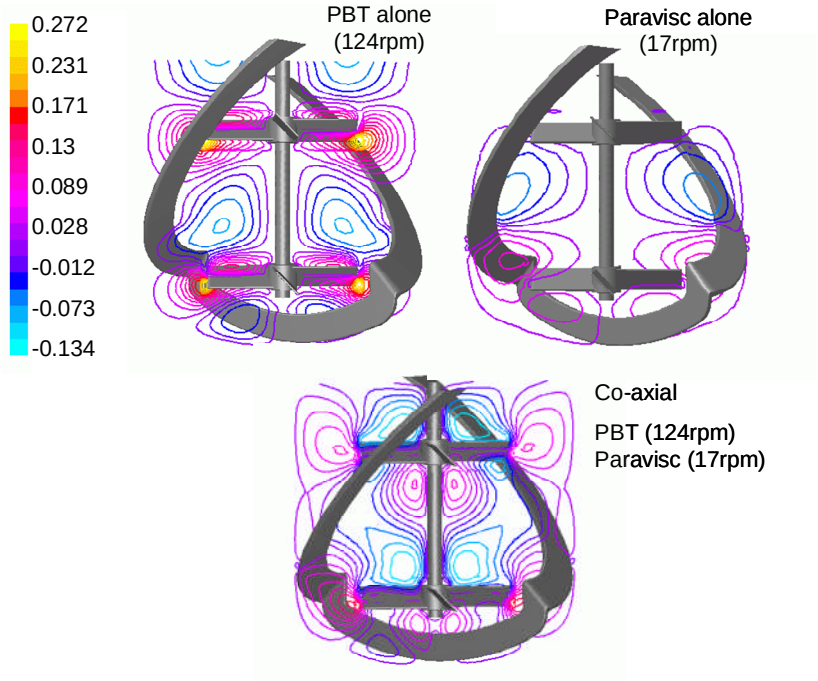

Figure 4-21: Normalized radial velocity fields of single impeller systems and co-axial mixing system with Paravisc in Newtonian fluid

Co-axial mixer: pitched blade turbines with Anchor (co-rotating mode)

In this section, analogous analyses of the velocity flow fields are performed for the single mixing systems and the co-axial mixer with the anchor as proximity impeller. Both co-axial configurations with anchor rotating in clockwise and counter clockwise direction are respectively presented and discussed.

Figure 4-22 shows snap shots of the flow field of a co-axial mixer equipped with the anchor proximity impeller in co-rotating mode (clockwise direction). The outer impeller rotates (N_o) at 17 rpm and the inner impellers (N_i) rotate at 124 rpm, and so the tip speed ratio (tr) is 4. The fluid is Newtonian and has a viscosity of 12 Pas. As done for the agitation configurations with Paravisc, the results of the CFD calculations are presented as two-dimensional velocity vector fields, in which the colors of the vectors denote the magnitude of the velocities. The maximum velocity achieved is the tip speed of the pitched blade turbines. The view planes of the plots are fixed to the inner impellers, but relative to the outer impeller. In the laminar regime, the flow patterns of the co-axial mixer with anchor as proximity impeller are very comparable with the flow patterns induced by the single inner impeller system with anchor as baffles (as shown in Figure 4-6 for $Re_i = 21$). The typical eddies below and above the inner impeller tips dominate the macro pattern in the vessel. Another characteristic feature is the compartmentalized flow pattern generated by the pitched blade turbines in the laminar regime. Whether the interface between the compartments is disturbed by the rotation of the anchor impeller and thus reduce the overall mixing time is a key question explored.

The contours of the normalized axial velocities for the agitator systems (PBT alone and co-axial mixer with anchor) are plotted in Figure 4-23. The axial and radial velocities were normalized by diving them with the tip speed of the inner impellers (1.65 m/s). As expected, the axial velocity component is almost nonexistent in the single anchor impeller system (between -0.036 and 0.016) and is not plotted in Figure 4-23.

The axial flow fields of both systems are very similar. The anchor impeller generates essentially no axial flow and the flow patterns of the axial flow in the co-axial mixing tank are thus only influenced by the flow induced by the inner impellers.

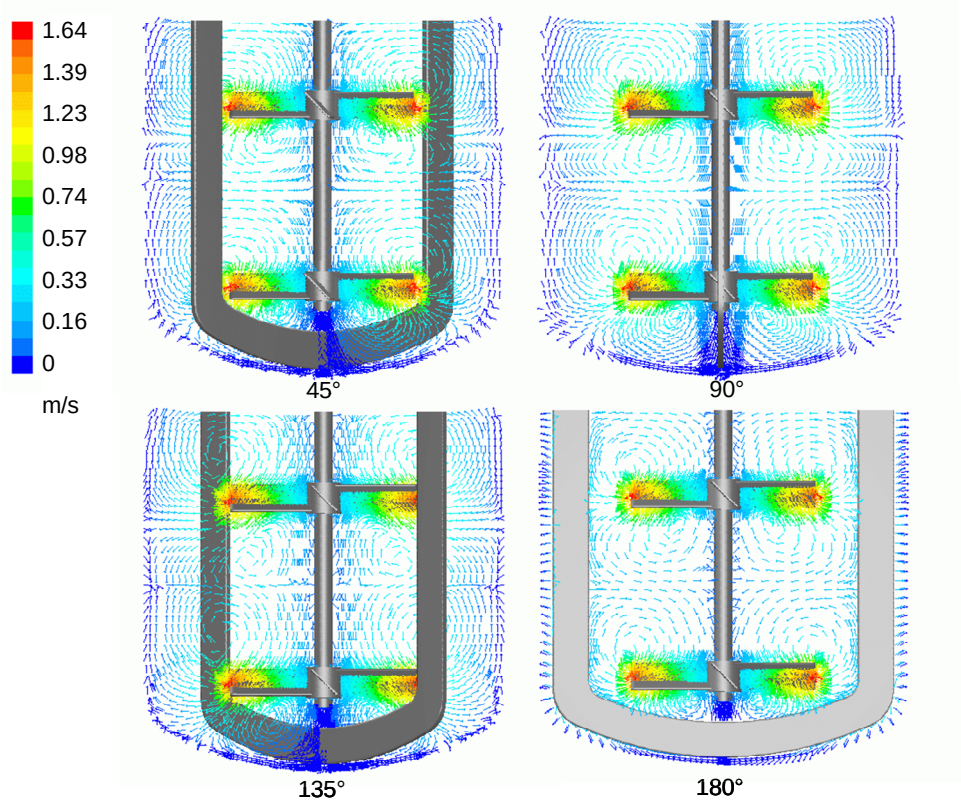

Figure 4-22: Snap shots of the flow field of a co-axial mixer (tr=4) with anchor (both PBT and outer impeller in clockwise direction). Colors denote velocity magnitude in m/s.

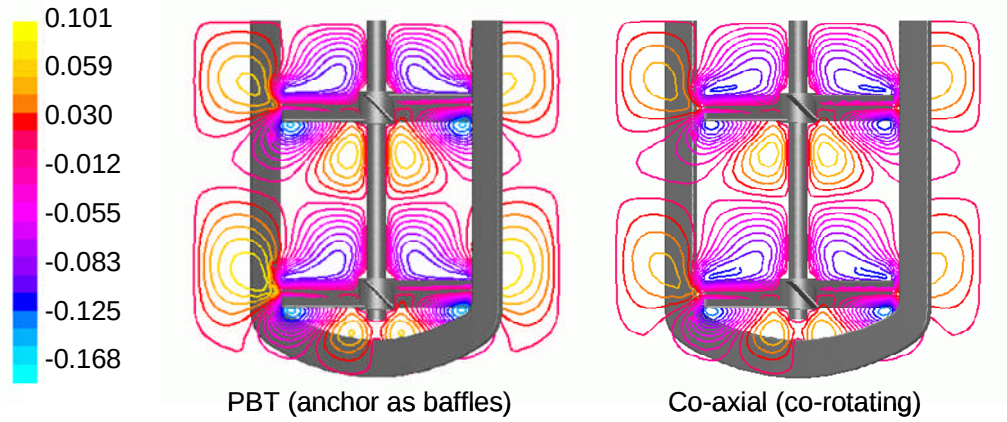

Figure 4-23: Normalized axial velocity fields of the single impeller system PBT and the co-axial mixing system (both PBT and anchor in clockwise direction) in Newtonian fluid

The axial pumping action of the agitation systems is visualized in Figure 4-24, in which three dimensional surface contours of the normalized axial velocities at three cross sections (z/T=0.7; 0.51 and 0.19) are plotted. The plots show that the axial pumping is essentially identical in the single impeller system with PBT alone and in co-axial configuration with anchor. However, the pumping action of the single inner impeller system is slightly

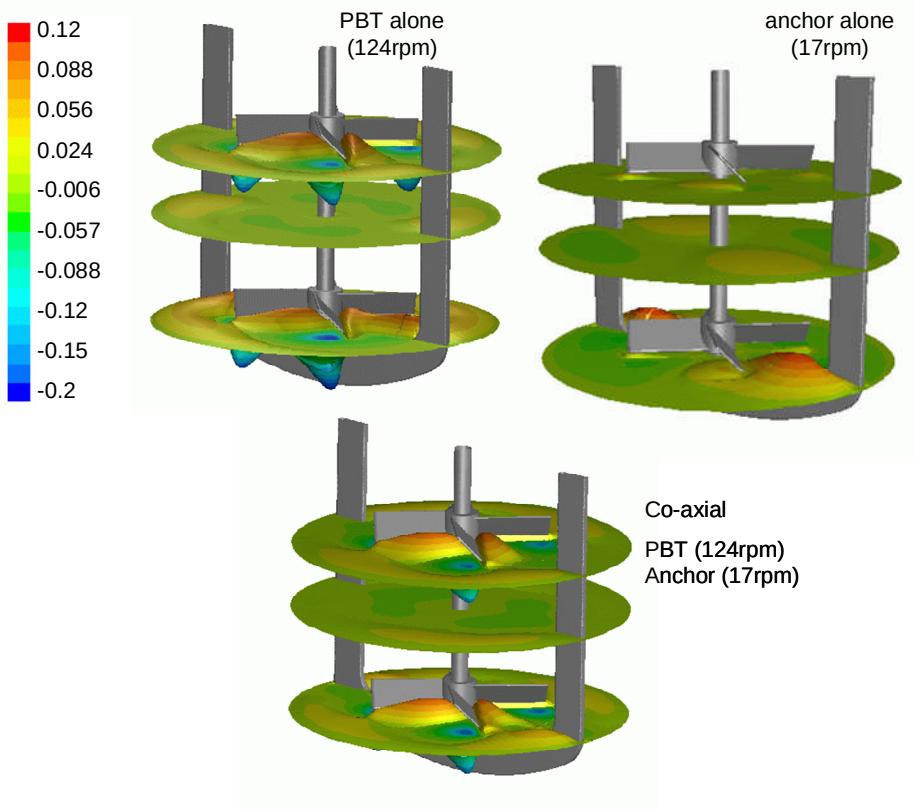

Figure 4-24: Three dimensional surface contours of normalized axial velocity in various horizontal sections for three agitation systems with anchor (clockwise direction)

different from the outer impellers serving as baffles. Furthermore, the axial velocities are in magnitude roughly higher in the system with Paravisc as baffles. The anchor impeller alone, in turn, is able to generate axial flow in the bottom region of the vessel only, because of the bottom blade.

The radial velocity fields of these impeller systems are illustrated in Figure 4-25. The plot of the anchor impeller is not shown because the calculated radial velocities are very low for comparison (between -0.003 and -0.076). The plots in Figure 4-25 show that the radial velocity fields created in the single impeller system and the corresponding co-axial configuration are slightly different in the middle part of the vessel. The velocities at the vicinity of the inner impeller remain fairly the same in both configurations. As expected, the anchor impeller is a weak generator of axial and radial flow in the vessel - it is able to create predominantly tangential flow. However, when combined with other mixers, like in co-axial mixers, the anchor impeller can contribute more than only renew fluid layers at the vessel wall due to the synergistic effects of both rotating impellers. In Chapter 5, the

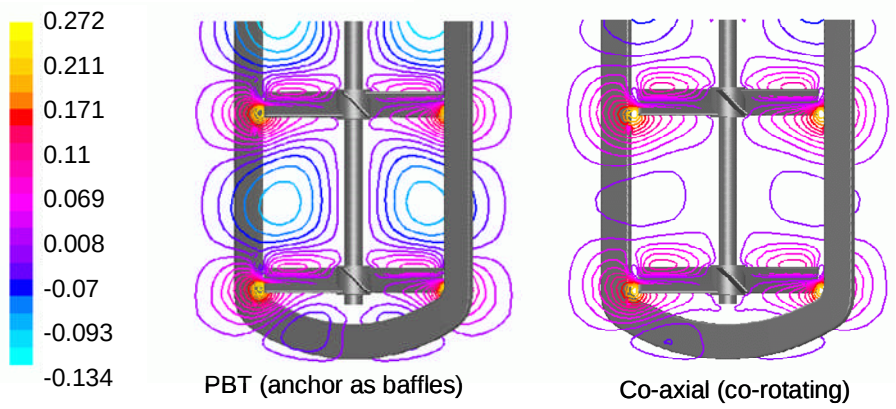

Figure 4-25: Normalized radial velocity fields of the single impeller systems PBT and the co-axial mixing system (both PBT and anchor in clockwise direction) in Newtonian fluid

analysis of the measured data of power consumption and mixing times enables a quantification of the strength of the synergetic effects.

Co-axial mixer: pitched blade turbines with Anchor (counter-rotating mode)

The counter-rotating configuration of the co-axial mixer with anchor impeller was investigated in a similar way as previously done for the co-rotating mode. The normalized axial velocity fields of the co-rotating co-axial configuration and counter-rotating mode are plotted in Figure 4-26 for comparison. The calculated axial velocities fields are almost identical as expected, since the anchor impeller creates almost no axial flow in the vessel, expect only in the bottom area, as shown in Figure 4-27. The axial flow patterns in the mixing vessel are predominantly generated by the pitched blade turbines regardless of the rotation mode.

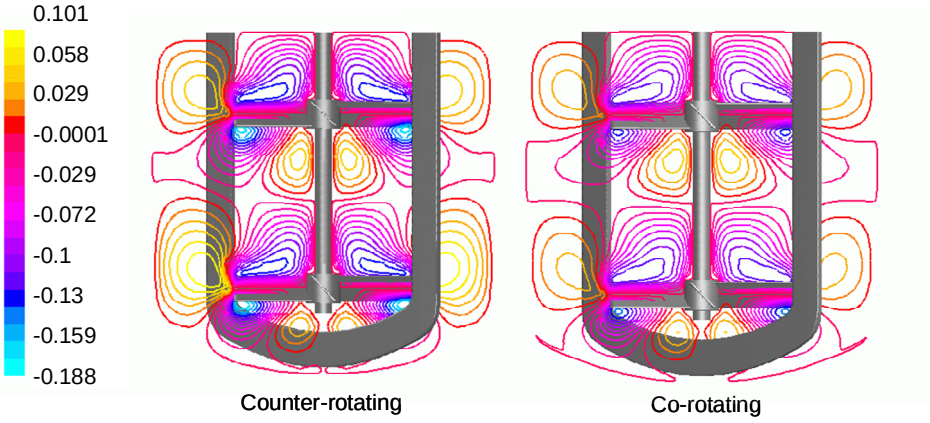

Figure 4-26: Normalized axial velocity fields of co-axial mixing system with anchor impeller rotating in counter clockwise (left) and clockwise (right) direction

In Figure 4-27, the axial pumping ability of both co-axial agitation systems can be visualized and compared. Three dimensional surface contours of the normalized axial velocities are plotted at three cross sections (z/T=0.7; 0.51 and 0.19). The axial velocity components in the bottom area of the co-axial configuration in counter-rotating mode are higher than in the co-rotating mode. The rotation of the anchor bottom blade in the opposite direction enhances the axial velocities in this region, whereas the anchor bottom blade rotating in the same direction of the pitched blade turbines dampens the axial velocity components.

The normalized radial velocities are plotted in Figure 4-28 for co-axial mixers both in co- and counter-rotating modes. The radial velocity fields present similar primary patterns in both configurations, but differ in magnitude, in particular in the region between the inner impellers.

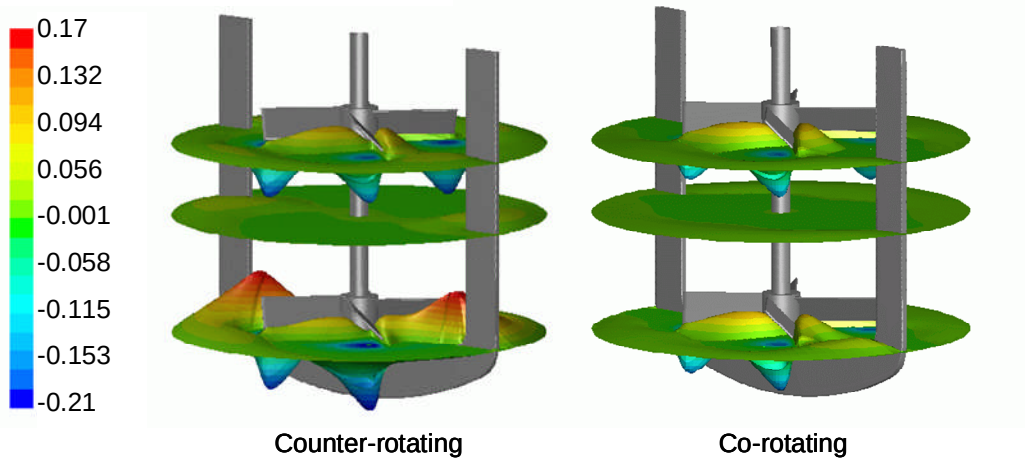

Figure 4-27: Three dimensional surface contours of normalized axial velocity for co-axial mixing systems with anchor impeller rotating in counter clockwise (left) and clockwise (right) direction

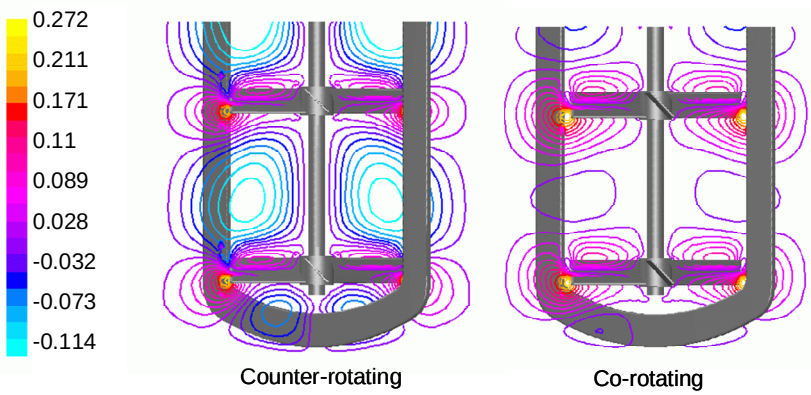

Figure 4-28: Normalized radial velocity fields of co-axial mixing system with anchor impeller rotating in counter clockwise (left) and clockwise (right) direction

The shear rates created in both co-axial configurations are plotted in Figure 4-29. As the outer and inner impellers rotate in opposite directions, the shear rates are higher in regions between outer and inner impellers in the co-axial mixer configuration in the counter-rotating mode. In the lower inner impeller zone, the shear rates are remarkable higher than in the co-rotating mode. Such high shear rate distribution in the lower region of the vessel is not found in the co-axial mixer with the Paravisc as the outer impeller.

The analyses of the primary flow fields in co-axial mixers show so far that the created flow patterns by the individual impellers are responsible for the flow displacement and interactions found in the co-axial mixing systems. The primary flow pattern produced by axial and radial pumping impellers are sketched in Figure 4-30. It can also be understood as the primary flow patterns produced by the pitched blade turbines in turbulent and laminar regimes. A multi-staged axial pumping impeller provides ideally a single flow circulation loop through the vessel as indicated on the left side of Figure 4-30. If the outer impeller provides primarily tangential flow as occurs with the anchor, then a weak flow displacement and interactions with respect to the axial and radial flow field occurs. On the other hand, an outer impeller, like the Paravisc, designed to pump upwards, will enhance the flow pattern created by the inner impellers. This situation occurs in turbulent regime, which is not investigated in this work.

The situation is different for a radial pumping open impeller, or pitched blade turbine in the laminar regime. The discharge flow is directed radially outward towards the cylindrical wall of the vessel where it splits into two circulation loops, one above the impeller plane and one below. If the outer impeller produces predominantly tangential flow like the anchor, again, weak flow displacement and interactions are expected regardless of the rotation mode. As a result, the axial pumping ability remains the same as it is in the single inner impeller system. On the other hand, if the outer impeller (e.g. Paravisc) induces an axial flow component, the flow produced by the inner impeller near the wall of one of the circulation loops is in the opposite direction to the flow the outer impeller induces (indicated by the red arrows in Figure 4-30). As a result, a stronger flow displacement in the co-axial mixer with Paravisc could be observed, both in axial and radial flow fields.

It is relevant to point out that the strength of the interactions of the flow patterns induced by the open impellers is expected to depend strongly on the tip speed and on the fluid viscosity as well.

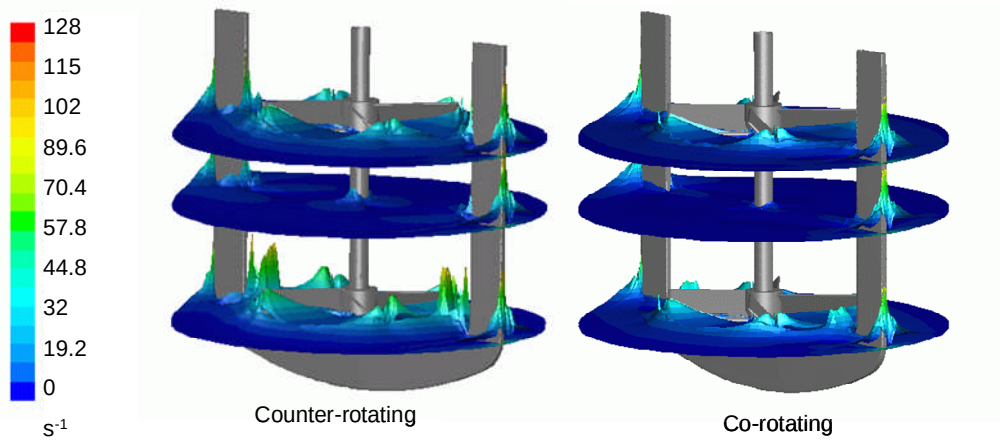

Figure 4-29: Three dimensional surface contours of shear rates for co-axial mixing systems with anchor impeller rotating in counter clockwise (left) and clockwise (right) direction

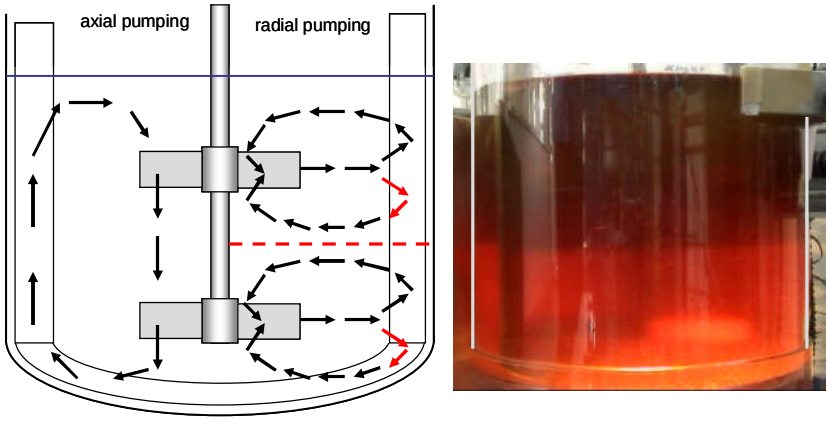

Figure 4-30: Sketch of flow pattern produced by axial and radial pumping impellers (left) and example for segregated flow (right)

Figure 4-30 indicates that in cases, where the open impellers induce a pure radial flow pattern, two distinct zones can exist in the vessel with little exchange between them. In the sketch, the border between those two zones is indicated by the red dotted line. As one can see, velocity vectors are parallel in this plane, resulting in a limited axial exchange of a transport property and segregated flow. The photo on the right side shows an example for a segregated flow from the experimental trials using anchor and a dual set of pitched blade turbines combined co-axially. The neutralizing agent was added from the top and mixed relatively fast in the upper zone of the vessel. It takes significantly longer to transport the agent into the lower half of the vessel. The border line between the two zones can clearly be seen.

Based on the primary characteristics of the calculated axial and radial velocity fields as well as on the flow patterns generated in the investigated mixing systems presented in this chapter, the following parameters could be identified as relevant in the efficiency characterization of the investigated co-axial mixing configurations in lamina regime:

- Outer impeller design
- Tip speed between inner and outer impeller (tip speed ratio)
- Rotation mode (co and counter rotating)

Obviously, fluid properties, such as viscosity and non-Newtonian rheology influence the flow patterns of single impeller systems and it is certainly expected to influence the flow patterns in co-axial mixing systems as well. Other design parameters, such as impeller diameters and inner impeller design, have a significant influence on the flow patterns in single impeller systems, and it is expected to have also a significant effect on co-axial mixing tank design. However, they were kept constant in the present work.

In the next Chapter, the effect of the identified key parameters on the velocity field and consequently on the power consumption of the impellers and mixing time are presented and discussed in the light of the experimental measurements.

5 Results

5.1 Power consumption analysis

An important consideration in the design of an agitated system is the power required to drive the impeller. The power consumption of the impellers in stirred tanks is often analyzed using the impeller power curves, which are log-log plots of Newton number versus Reynolds number. These dimensionless numbers are determined by measuring the torque or power as function of the rotational speed of the impeller. Because the Reynolds number is dependent on the viscosity, which is a function of the shear rate for non-Newtonian fluids, the determination of an effective viscosity is an important task in the power consumption characterization. The effective viscosity was determined by applying the Metzner-Otto concept, as previously discussed in Chapter 2. The shear rate constant K_S necessary to correlate the impeller rotational speed and the average shear rate around the impeller was determined experimentally for each of the investigated impellers.

The characterization of the power consumption of a co-axial mixing system is not trivial. The definition of the characteristic length and velocity is ambiguous because there are two different impellers, with different geometries rotating at different rotational speeds in the same tank. In this chapter, approaches to correlate and design the power consumption of co-axial mixers are presented, validated and discussed.

5.1.1 Single impellers

The characteristic power curves for each of the investigated impellers were measured in Newtonian and non-Newtonian fluids. Power curves of a single pitched blade turbine in a standard baffled tanks can be found in most common references in the field of mixing, for example (Oldshue, 1983). The single impeller tank configurations in this work are not standard, therefore, not available in the open literature. The non-standard characteristics of the single impeller systems are described as follows:

- dual set of pitched blade turbines in a tank with a stationary anchor or Paravisc serving as baffles.
- proximity impeller anchor or Paravisc rotating alone with a stationary dual set of PBT in the center of the tank.

5.1.1.1 Pitched blade turbines

Power curves of a dual set of pitched blade turbines were measured in three different Newtonian fluids and plotted in Figure 5-1. The curves were measured with a stationary proximity impeller, anchor or Paravisc. The set of the measured data in all Newtonian fluids was fitted to obtain a single relation between Newton and Reynolds numbers, $NeRe=K_P$, in the laminar regime. A power constant K_P = 89 was determined for the dual pitched blade turbines. This value is in good agreement with previously published data for a single pitched blade turbine in a standard baffled tank (Table 2-1 in Chapter 2).

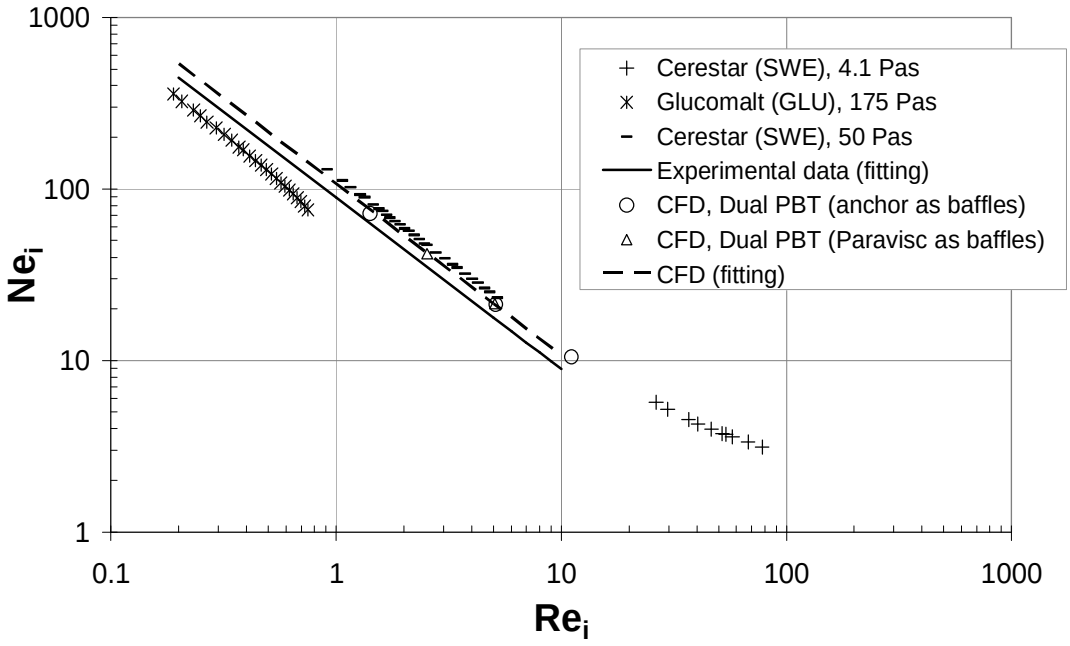

Figure 5-1: Measured and calculated power curve of a dual set of pitched blade turbines in Newtonian fluids

The power consumption of the dual set of pitched blade turbines was calculated using both co-axial mixing tank models, one had anchor as baffles and the other had the Paravisc as baffles. The calculated K_P for the two stage pitched blade turbines with anchor as baffles was 107.2 and K_P for the pitched blade turbines with Paravisc as baffles was 107.5, which show a very good consistency. Fitting the numerical data for both models, a power constant K_P=107.3 was determined. The calculated K_P is higher than the measured value with a relative deviation of 20.5%. The possible reasons for the discrepancy found in the power curve of the pitched blade turbines are discussed at the end of this section.

Power consumption of the PBT as function of speed was measured in non-Newtonian fluids using HEC and CMC solutions of different concentrations. To obtain the power

curve, it was necessary to determine the effective viscosity to calculate the Reynolds number. This was done using the impeller shear constant K_S=10.9, which was experimentally determined according to the Metzner-Otto approach described in Chapter 2. The impeller shear constant is dependent on the geometry of the impeller. The K_S measured for PBT is also in good agreement with previously published data. Kelly and Gigas (2003) reported K_S=8.58 for the pitched blade turbine. The power curves of a dual set of PBT in Newtonian and non-Newtonian fluids in the laminar and transitional regime are plotted in Figure 5-2.

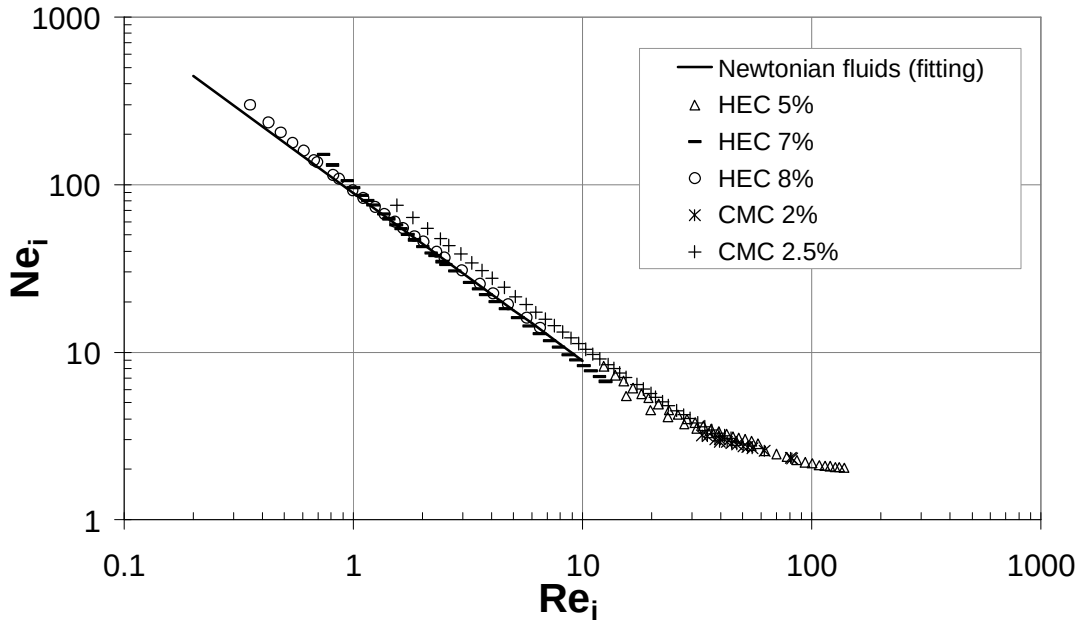

Figure 5-2: Power curves of a dual set of pitched blade turbines for non-Newtonian fluids

HEC solutions exhibit both shear thinning as well as viscoelastic properties, as previously presented and discussed in Chapter 3. The measured data indicate no effect of the viscoelastic properties of the HEC solutions on the power consumption of the PBT impellers in the laminar regime. The measured data of the HEC solutions collapse with the data of the inelastic CMC solutions and the Newtonian curve. In the early transitional flow regime, the power consumption data in HEC solutions is slightly higher than in CMC solutions. However, it is not clear and very difficult to determine whether the observed deviation is due to shear thinning, to viscoelastic behavior or due to both. Experimental errors in the viscosity and torque measurements can not be completely excluded either. The effect of the viscoelastic properties of fluids in power consumption is discussed in depth, for instance in Höcker (1979) and Carreau *et al.* (1993).

Effect of baffle replacement by proximity impeller

Figure 5-3 shows power curves of a dual set of pitched blade turbines by using either a standard baffled tank (SBT) or a stopped proximity impeller as baffles. In the laminar regime, the data indicate that baffling has no effect on power consumption under the conditions evaluated. This was also observed by Metzner and Otto (1957) where power curves were measured in baffled and unbaffled systems. In the transition and turbulent regime (measured using HEC concentration of 1%, 3% and 5%) the effect of baffles is more pronounced, where Paravisc as baffles gives the lowest power draw, followed by the anchor and standard baffles. This behavior can be explained by the shape and number of

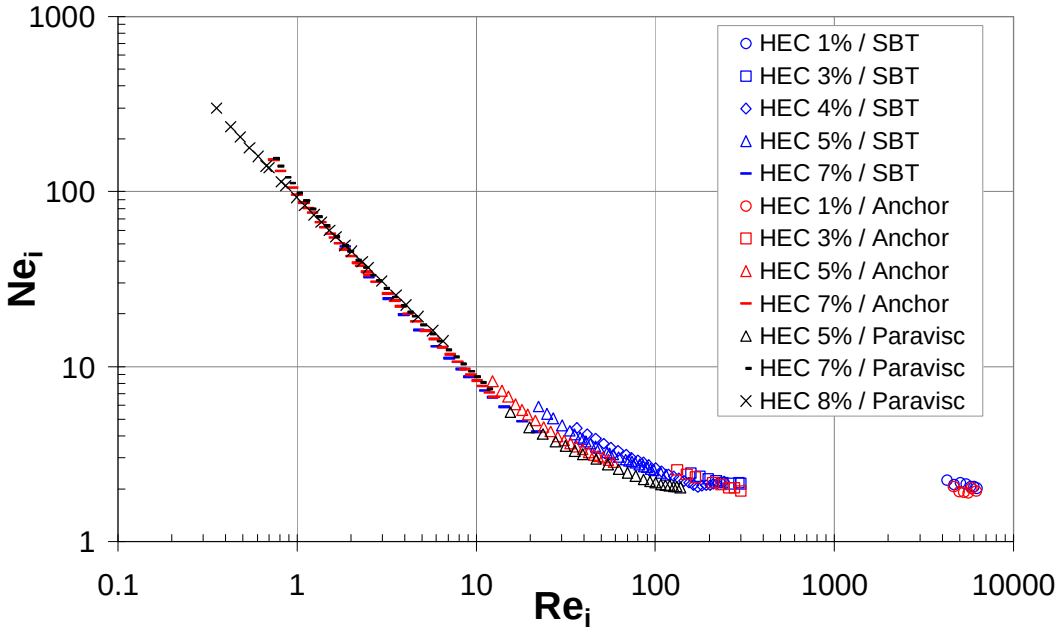

Figure 5-3: Effect of baffling on the power consumption of the pitched blade turbines

baffles. The main purpose of baffles is to break down the tangential momentum generated by the agitator by providing resistance to the rotational flow. One may consider a mix tank with a centered agitator operating in a low viscosity fluid. When there are no baffles present, the only resistance forces to the rotational flow are the wall drag forces and inertia. Relatively little power is consumed at a certain rotational impeller speed to overcome these forces (solid body rotation). Baffles introduce additional resistance to the flow and thus higher power consumption. The standard baffled tank provides the highest resistance, since it consists of four vertical baffles. The anchor agitator can be interpreted as two vertical baffles, thus providing less resistance to the rotational flow than in a standard baffled tank.

When comparing the anchor agitator with the PARAVISC®, the number of baffles and the baffle width are approximately the same, but the PARAVISC® blades are angled to the direction of the rotational flow component. Energy is required for re-directing rotational flow components into axial flow components on the baffle blades. It can be considered, that less energy is consumed for re-directing the rotational flow component with a blade angled to the direction of the rotational flow compared to a blade perpendicular to the rotational flow. In the case of laminar flow (Impeller Re < 10) where the viscous force dominates over the inertia, fluid rotational velocity near the wall is negligible. Thus the baffles have insignificant effect in altering the flow pattern and thus the power draw remains unchanged.

5.1.1.2 Anchor

Power consumption measurements and calculations for the anchor impeller were carried out in two different Newtonian fluids and in the laminar regime and the results are plotted in Figure 5-4. The data for both Newtonian fluids agree well and follow the linear relationship $NeRe=K_P$ in the laminar regime. The power constant $K_P = 295$ was obtained with the measured data and $K_P = 290$ with the CFD data. The deviation of less than 5% indicates a very good agreement between numerical simulation and experiments. The measured values are in good agreement with data from the literature (Table 2-1) as well.

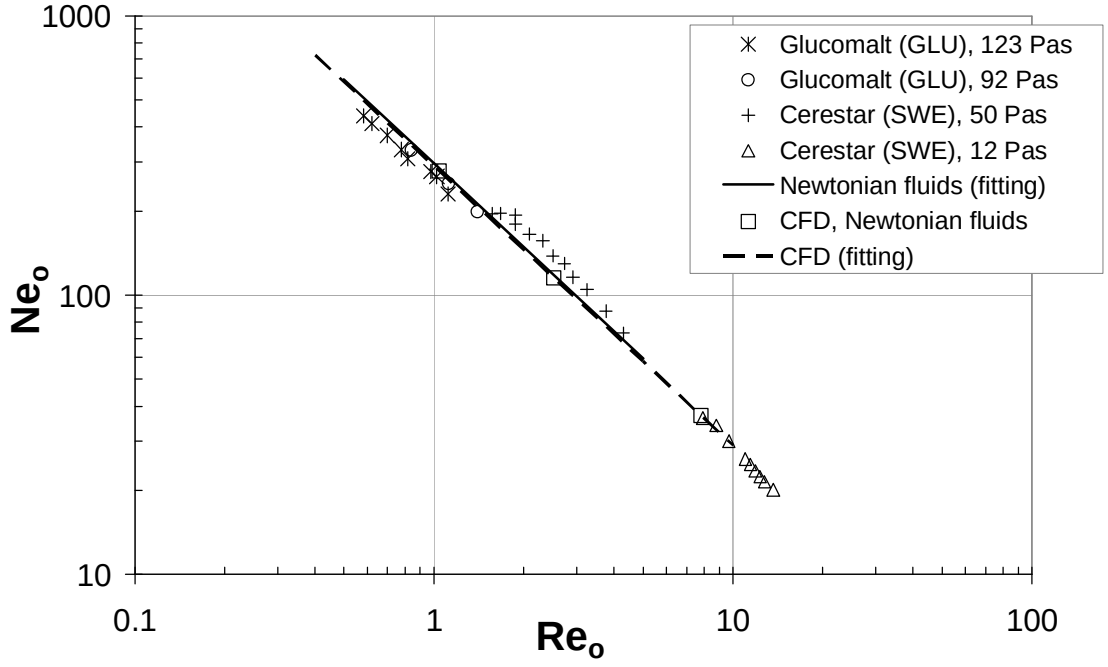

Figure 5-4: Measured and calculated power curve of the anchor impeller in Newtonian fluids

The power draw measurements in two different non-Newtonian fluids (HEC and CMC) in the laminar regime are presented in Figure 5-5. The shear constant K_S = 17.5 was determined experimentally for the anchor impeller. This is also in good agreement with previously published data (Table 2-2 – Chapter 2). The data indicate no measurable effect on the power consumption of the anchor impeller in the laminar regime due to the viscoelastic behavior of the HEC solutions. The power curves measured in the inelastic CMC and HEC solutions agree well with the power curve obtained in Newtonian fluids.

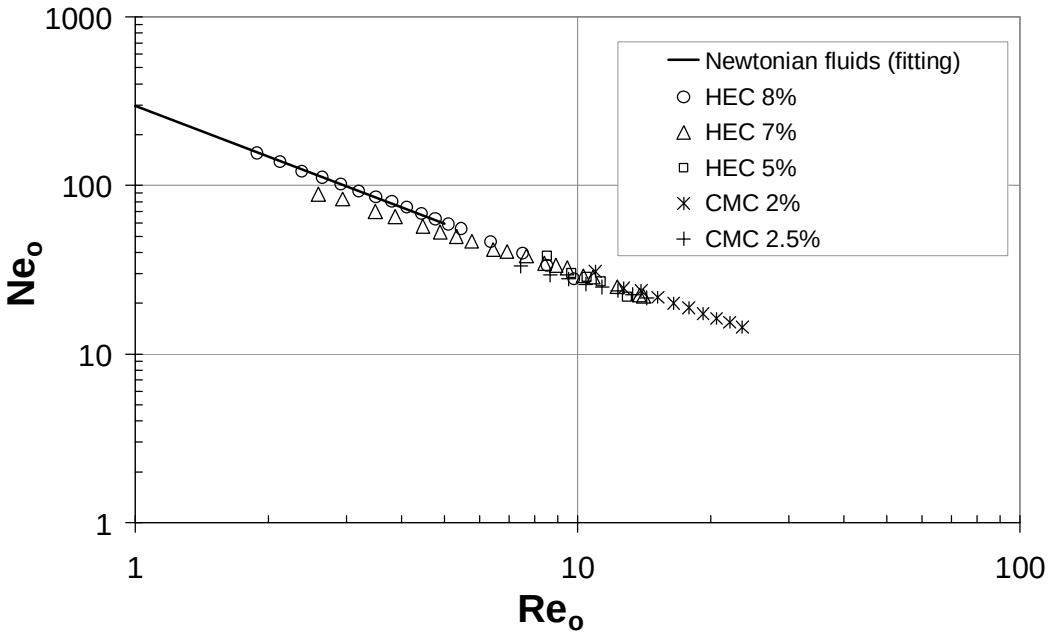

Figure 5-5: Measured power curve of the anchor impeller in non-Newtonian fluids

5.1.1.3 PARAVISC®

The power consumption of the Paravisc impeller in form of Newton number (Ne) versus Reynolds number (Re) is plotted in Figure 5-6. The power drawn by the Paravisc impeller was measured in three different Newtonian fluids. The power consumption of the Paravisc impeller was also calculated in the laminar regime using CFD. The data sets were fitted to obtain the power constants K_P. The power constant K_P = 385 was obtained with the measured data and K_P = 284 with the CFD data. A deviation of 26% was found between numerical simulation and experiments. The measured value of K_P is in good agreement with data from the literature (Table 2-1 in Chapter 2).

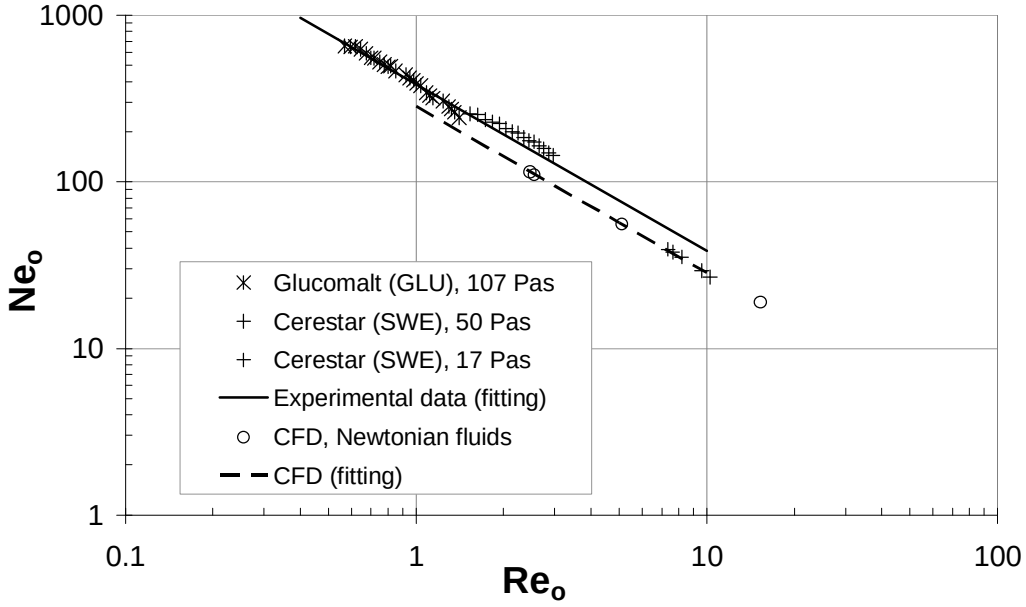

Figure 5-6: Measured and calculated power curve of the Paravisc impeller in Newtonian fluids

The shear constant K_S=28.8 was experimentally determined for the Paravisc impeller using the measured power consumption data in Newtonian and non-Newtonian fluids. The K_S value is also in good agreement with previously published data (Table 2-2 – Chapter 2). The power draw measurements in two different non-Newtonian fluids (HEC and CMC) in the laminar regime are presented in Figure 5-7. The measured data of power consumption of the Paravisc impeller using both the inelastic CMC and the viscoelastic HEC solutions agree well with the data obtained in Newtonian fluids. As already previously shown for PBT and anchor impeller, there is no measurable effect on the power consumption in the laminar regime due to the viscoelastic behavior of the HEC solutions for the Paravisc impeller either.

Table 5-1 summarizes the values for power constant K_P and Metzner-Otto constant K_S for the each of the investigated single impeller systems.

Table 5-1: Experimentally and numerically determined values of K_P and K_S for each single impeller system

	Dual PBT		Anchor		Paravisc	
	K_P	K_S	K_P	K_S	K_P	K_S
Measured	89	10.9	295	17.5	384	28.8
CFD	107	-	290	-	284	-
Deviation	20%	-	2%	-	26%	-

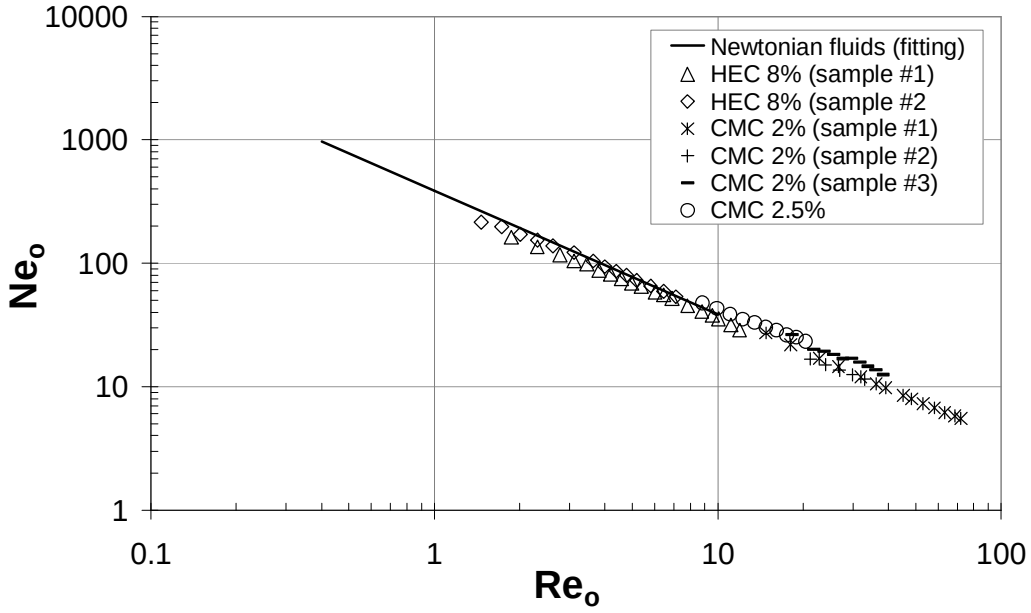

Figure 5-7: Measured power curve of the Paravisc impeller in non-Newtonian fluids

The measured K_P value for a dual set of pitched blade turbines agrees well with the values reported in the open literature for one single pitched blade turbine. For instance, Kuncewicz and Pietrykowski (2001) reported K_P=56 and Oldshue (1983) reported a K_P=42. The K_S measured for the PBT is in very good agreement with previously published data, i.e. Kelly and Gigas (2003) reported K_S=8.58 for a 45° pitched blade turbine.

For the close clearance impellers, the measured K_P values are also consistent with previously published data. Thibault and Tanguy (2002) reported a power constant of K_P=253 for an anchor impeller. Delaplace *et al.* (2000a) reported K_P=315 for the Paravisc impeller and later, Barar Pour *et al.* (2007) reported a value of 329. The deviations from published data of the same impeller are for instance due to differences in the geometry and measurement systems.

The calculated values of K_P are also presented in Table 5-1. The deviations from the experimental values are up to 26%. The measured power consumption in the different Newtonian fluids diverges from each other as well, as found for the pitched blade turbines and the Paravisc impeller. Therefore, some discrepancies found in the power consumption of the single impeller systems are due to experimental and numerical shortcomings, described as follows:

- dual set of pitched blade turbines (with D/T=0.51 and S/D=1) in a tank with a stopped anchor or Paravisc serving as baffles.

- proximity impeller anchor or Paravisc rotating alone with a motionless dual set of PBT in the center of the tank.
- The interpolation process in the numerical simulation leads to strong diffusive effects, in particular, in regions of steep velocity gradients.
- The quality of the hexahedral cell elements at the impeller surface plays a role in the torque calculation of the impeller, since the torque is calculated from the shear and normal forces at all nodes on the impeller blade surface. The angled blades of the Paravisc impeller pose an additional difficulty in the grid generation of good quality hexahedral elements. In the case of the anchor impeller, the straight blades offer a favourable condition to build well aligned cells with the blade surfaces and induced forces by the flow.
- The experimental uncertainty on the viscosity during the torque measurements due to its strong sensitivity to temperature deviations. In view of this, the friction heat generated by the high speed impellers raises the temperature around them, which may differ from the measured temperature in the bulk fluid. In case of the close-clearance impellers, the impeller friction heat plays no significant role, since the rotational speeds are relative low (0 - 43 rpm).
- The presence of small bubbles during the torque measurement influences the torque results. Some bubbles were unavoidably formed during the filling up the vessel and also during the rotation of the proximity impellers. The bubbles, in particular the very small ones remained trapped in the highly viscous bulk during the measurements. In the case of the proximity impellers, the effect of the trapped small bubbles in the bulk fluid is significantly small in comparison to the power resistance from the viscous forces due to the close vessel wall.
- The uncertainty on power draw measurement of the proximity impellers due to used instrumentation, as previously discussed in Chapter 3. The power losses in the motor and gearbox (bearings, seals and gears) were determined by a calibration curve, which is a function of the power losses versus impeller rotational speed. The calibration curve, in turn, was determined by extrapolating the power consumption of the impellers in different low viscosity Newtonian fluids, also water and air to a zero load (i.e. rotational speed zero). However, it is known that the power losses in the gearbox are dependent on the mixing load to some degree (King *et al.*, 1988).

Large proximity impellers like the anchor and Paravisc have a significantly larger K_S than the open impellers. The measured values of K_S for the proximity impellers are in good agreement with the previously reported values in the literature. Nagata *et al.* (1972) reported K_S=25 for an anchor impeller and, later, Foucault *et al.* (2005) reported K_S=22. For the Paravisc impeller, Delaplace *et al.* (2000a) reported K_S=33.7.

5.1.2 Co-axial mixing systems

In a co-axial mixer, the definition of a characteristic speed (N) and a characteristic length (D) for the system is challenging due to the presence of two different impellers with distinct diameters and rotational speeds. In addition, the rotating mode (co-rotating or counter-rotating) is expected to influence these characteristic parameters as well. All this is amplified by the use of non-Newtonian fluids, which require the characterization of an effective viscosity. Numerical simulations in a Computational Fluid Dynamics (CFD) software were employed to calculate the flow field in the co-axial mixing systems. The results for the calculated torque of the impellers are compared with the measured values.

5.1.2.1 Anchor combined with pitched blade turbines

The interactive effects in a co-axial mixer consisting of an anchor and a dual set of PBT for Newtonian and non-Newtonian fluids operating in co-rotating mode and counter-rotating are analyzed in this section. The dimensionless numbers Ne and Re were calculated using the characteristic length and speed of one of the impellers and varying the speed of the other impeller. Figure 5-8 shows the results based on the calculation of Ne and Re with inner impeller dimensions. A single characteristic power curve for PBT impellers is obtained regardless of the tip speed ratio (tr), rotating mode and fluid properties. The Metzner-Otto constant K_S=10.9, actually determined for a single impeller system, is not influenced by the presence of a second impeller in the vessel. Therefore, it can be used to determine the effective viscosity of the inner impellers in a co-axial mixer. Foucault *et al.*, (2004) reported similar results for their co-axial mixer configuration. The inner impeller power consumption is not affected by the anchor impeller. The fact that the power draw of the PBT does not alter with the speed of anchor might be explained by the relatively slow speeds of the anchor impeller (N_o= 0 to 43 rpm) and by the distance between both impellers. It is expected that the results will change if the impeller diameter ratios are sufficient small. This was observed by Heiser *et al.* (2007) in their co-axial mixing system composed of a helical ribbon and a central screw.

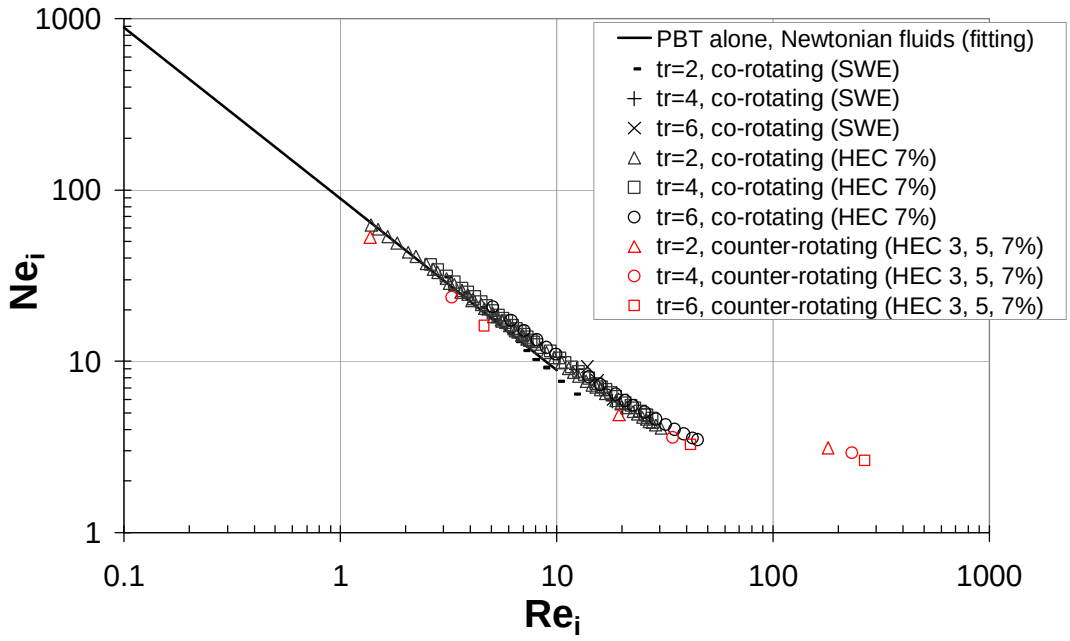

Figure 5-8: Measured power curves of PBT in a co-axial mixer with anchor as proximity impeller for different impeller tip speed ratios and rotating modes using Newtonian and non-Newtonian fluids

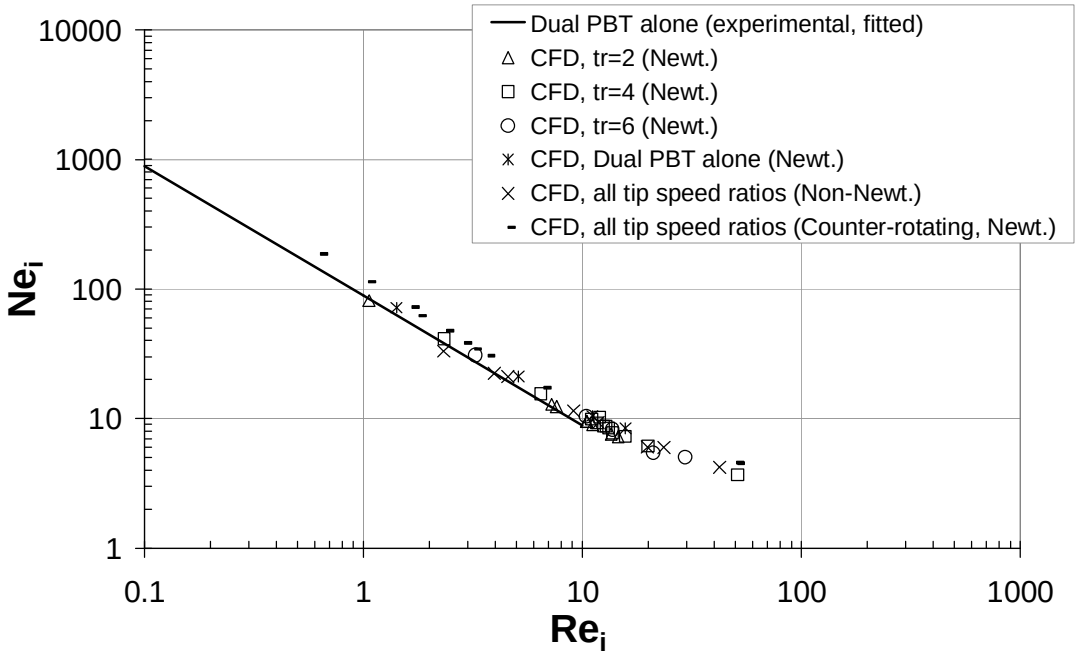

Figure 5-9: Calculated power curves of PBT in a co-axial mixer with anchor as proximity impeller for different impeller tip speed ratios and rotating modes using Newtonian and non-Newtonian fluids

Figure 5-9 shows the results obtained in the numerical simulations. CFD results show very good agreement with the experimental results, as the power draw of the dual pitched blade turbines is not affected by the anchor speed. CFD demonstrated the ability to predict

the torque of the inner turbines in Newtonian and non-Newtonian fluids with good accuracy, for both rotating modes and all investigated tip speed ratios (from 2 to 6).

Similar analysis is made to investigate the influence of the tip speed ratio on the power consumption of the anchor. Figure 5-10 shows the characteristic power curves of the anchor for different tip speed ratios and co-rotating mode in Newtonian. The dimensionless numbers are now related to the proximity impeller. In accordance with the theory, the experimental data follow curves with a slope of -1 in laminar regime. The data were fitted using the expression $NeRe=K_P$ and are denoted by the straight lines in Figure 5-10. The variation of the power constants K_P versus the tip speed ratio is summarized in Table 5-2. The data show that the power draw of the anchor decreases with increasing tip speed ratio in co-rotating mode. This can be explained when considering that in co-rotating mode, PBT impellers induce a tangential flow that drags the anchor blades, consequently decreasing its power consumption. As the tip speed ratio increases (i.e. increasing the rotational speed of the inner impeller), the additional shear field induced by the open impellers significantly influences the flow field around the anchor impeller and consequently its power consumption.

Figure 5-11 shows the characteristic power curves of the anchor for different tip speed ratios and co-rotating mode in non-Newtonian fluids. The data are in good agreement with the Newtonian data, which indicate that the Metzner-Otto constant of the single impeller system anchor, i.e. $K_S=17.5$ can be used to determine the effective viscosity of the co-axial mixer. Apparently, the shear rates at the vicinity of the anchor impeller don't change significantly when the inner impellers rotate.

The influence of the tip speed ratio on the power consumption of the anchor in a co-axial mixer in counter-rotating mode is illustrated in Figure 5-12. The power draw of the anchor impeller increases as the tip speed ratio increases. It can be noted that all the power draw curves decrease with the Reynolds number in the laminar regime with a slope -1, as expected. The values of the power constants for counter-rotating mode are also summarized in Table 5-2. In the counter-rotating mode, the direction of the tangential flow induced by the PBT is in a direction opposite to the induced tangential flow of the anchor. The effective drag on the anchor is enhanced thus increasing the power consumption of the anchor. As the tip speed ratio increases, so does the effective drag and consequently its power consumption.

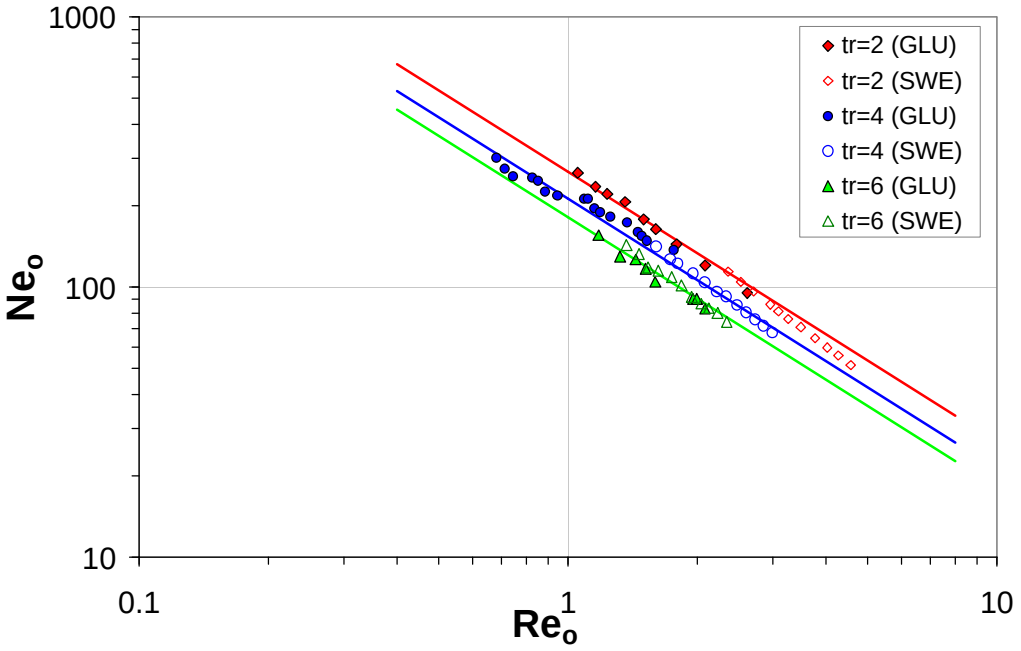

Figure 5-10: Measured power curves of anchor in a co-rotating co-axial mixer for different impeller tip speed ratios using Newtonian fluids

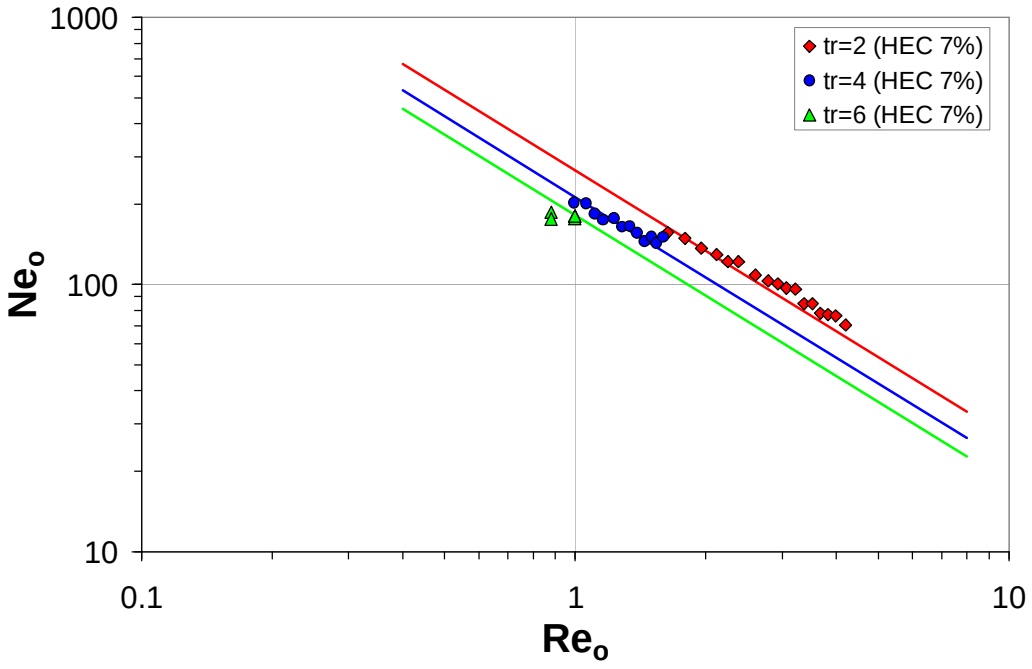

Figure 5-11: Measured power curves of anchor in a co-rotating co-axial mixer for different impeller tip speed ratios using non-Newtonian fluids

Figure 5-13 shows the calculated power curves of the anchor impeller in co-axial mixers in co- and counter-rotating mode. The results obtained in a CFD model show very good agreement with the experimental results. CFD demonstrated the ability to calculate the flow

field in a co-axial mixer consisting of an anchor and a dual set of pitched blade turbines with sufficient accuracy to design the power consumption of the inner and proximity impellers.

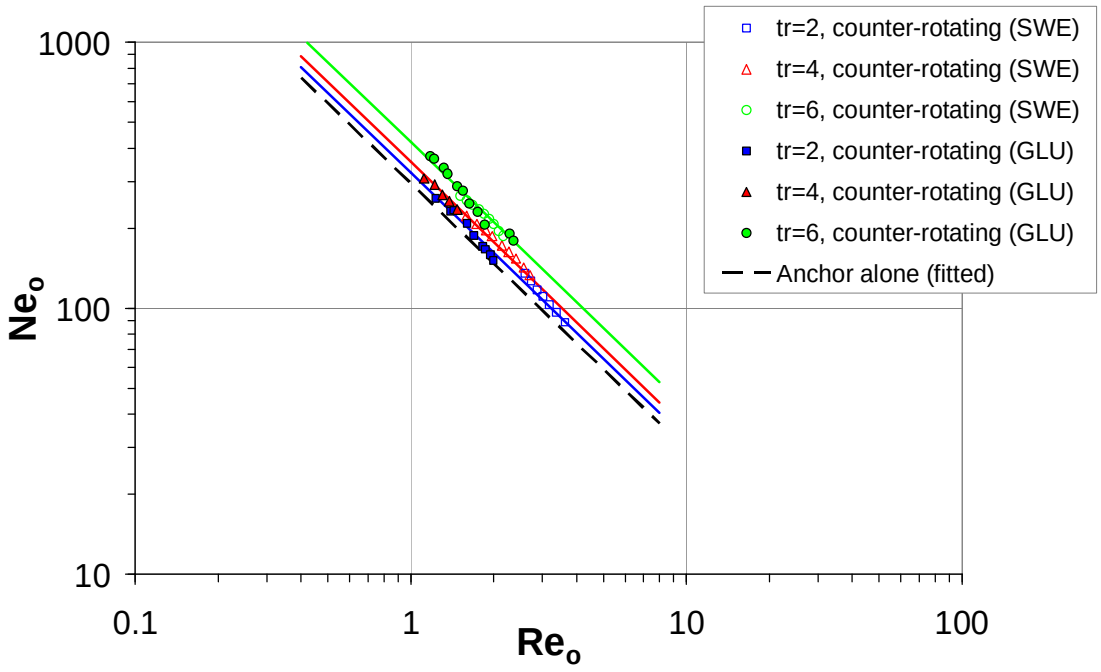

Figure 5-12: Measured power curves of anchor in a counter-rotating co-axial mixer for different impeller tip speed ratios in Newtonian fluids

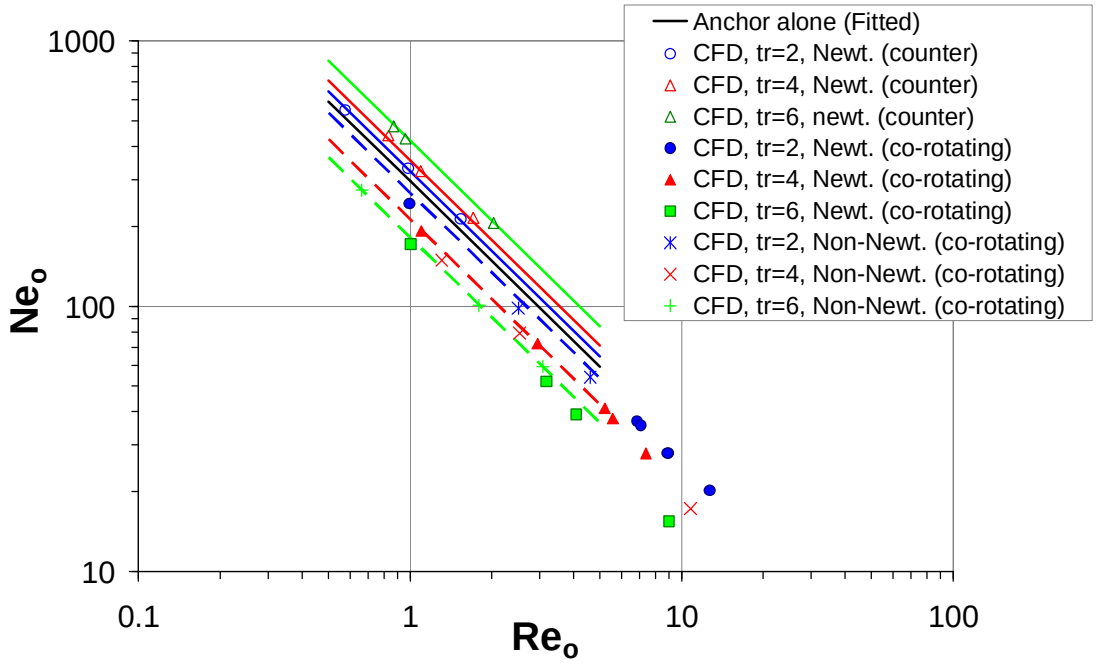

Figure 5-13: Calculated power curves of anchor in co- and counter rotating co-axial mixers for different impeller tip speed ratios in Newtonian and non-Newtonian fluids

Table 5-2: Values of K_P for power curves of anchor as function of the tip speed ratio

tip speed ratio	Co-rotating	Counter-rotating
2	268	323
4	213	355
6	182	421

5.1.2.2 Paravisc combined with pitched blade turbines

The interactive effects in a co-axial mixer consisting of a Paravisc impeller and a dual set of PBT for Newtonian and non-Newtonian fluids operating in co-rotating mode are analyzed in this section. As for the co-axial anchor with PBT, the dimensionless numbers Ne and Re are calculated using the characteristic length and speed of one of the impellers and varying the speed of the other impeller.

Figure 5-14 shows the power curves of the dual set of pitched blade turbines calculated using the characteristic length and speed of the inner impellers and varying the tip speed ratio. The power curves were measured in two different Newtonian fluids. These data points indicate that the power of the inner impellers in a co-axial mixer equipped with Paravisc as proximity impeller remained unchanged regardless of the tip speed ratio. The power curves of PBT show the same behavior as in the co-axial mixer equipped with the anchor, i.e. a single characteristic power curve for the inner impellers was obtained regardless of the Paravisc impeller speed and fluid properties. Using a proximity impeller other than anchor, i.e. the Paravisc impeller, which generates a different flow pattern, the power consumption of the pitched blade turbines is not affected by the Paravisc within the investigated configuration and operating conditions. The power curve of PBT alone measured in syrup Cerester (SWE) deviated from the power curves of PBT for different tip speed ratios, whereas the power curve of PBT alone measured in syrup Glucomalt (GLU) is however in very good agreement. This data scattering was observed in the power curves of the dual set of PBT alone (Figure 5-1) and are due to previously discussed experimental difficulties. The CFD results are also plotted in Figure 5-14. The calculated power consumption results of the PBT alone and in co-axial mixer agree well with each other and also with the averaged power curve of the PBT in Newtonian fluids (Kp=89). However, the CFD results for the co-axial mixer with Paravisc show a different trend than for the co-axial mixer with anchor, i.e. that the power consumption of the PBT seems to be slightly affected by the Paravisc speed in laminar regime. This can be attributed to a weakness in the model using the Paravisc or to the experimental shortcomings. In the sliding mesh method, the

interface between both moving zones consists of two independent meshed faces that slide during the calculation. The better the cells match when the faces slide in relation to each other, the better are the results from the necessary interpolation of the calculated variables in the interface. One possible reason is that the mesh quality in the moving zone and in its interface side was not as good as in the anchor model due to the complex form of the twisted blades of the Paravisc. Another possible reason is that the algorithm for the interpolation at the interface could not handle accurately the complex velocity components generated by a Paravisc and a PBT simultaneously. Paravisc generates a highly complex flow in all directions, in contrast to the anchor, which creates predominantly tangential flow. However, this requires further investigation to reveal the true reason.

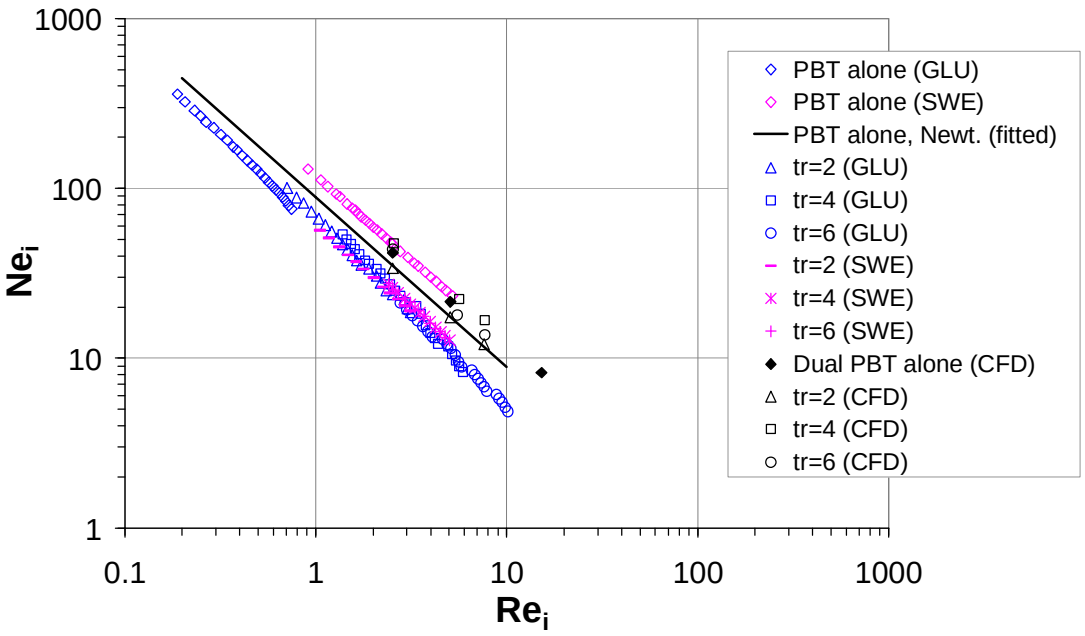

Figure 5-14: Measured and calculated power curves of the PBT in a co-axial mixer with Paravisc as proximity impeller for different impeller tip speed ratios using Newtonian fluids

The power curves measured in non-Newtonian fluids are plotted in Figure 5-15. The power curves measured in HEC and CMC2.5% are not equal, as expected. The power curves measured in HEC are lower and the power curves measured in CMC 2.5% are higher than the power curve measured in Newtonian fluids. However, the data set obtained in each non-Newtonian fluid is very consistent with each other, which indicates that the power consumption of the PBT in a co-axial mixer equipped with a Paravisc as proximity impeller doesn't change when the Paravisc impeller rotates. The measured power curves in

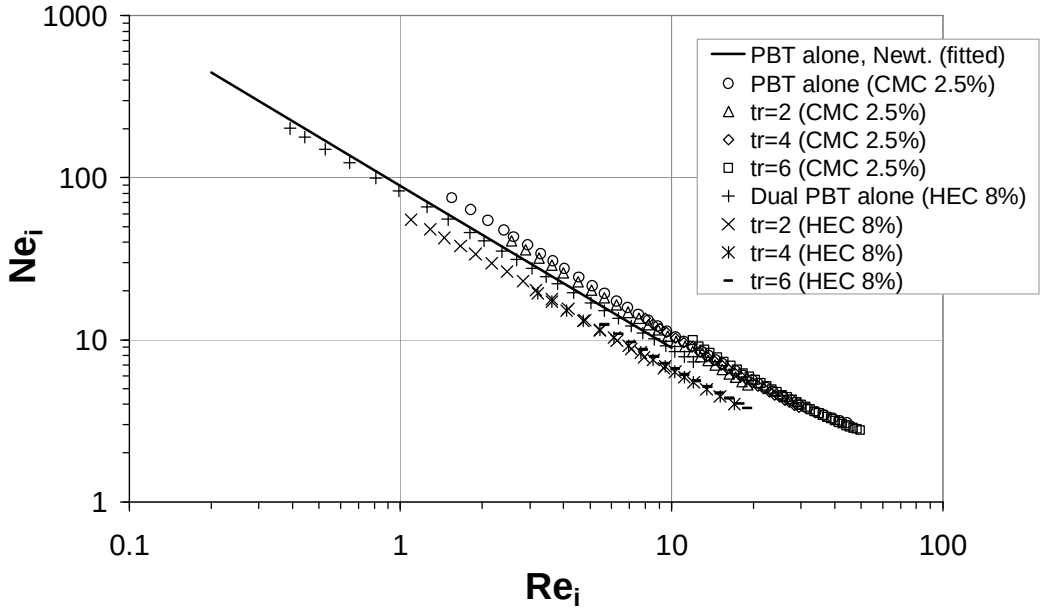

Figure 5-15: Measured power curves of the PBT in a co-axial mixer with Paravisc as proximity impeller for different impeller tip speed ratios using non-Newtonian fluids

CMC 2.5% are in turn in good agreement with the power curves of PBT alone measured in syrup Cerestar (SWE).

Figure 5-16 shows the characteristic power curves of the Paravisc for different tip speed ratios for Newtonian fluids. The dimensionless numbers are now related to the proximity impeller Paravisc. The power curves obtained in Newtonian fluids decrease with increased Reynolds numbers with slope -1. The power constants K_P are obtained by fitting the data points in laminar regime using the expression $NeRe=K_P$. Table 5-3 contains the variation of the power constants with the tip speed ratios for Paravisc as well. The experimental data indicate that the power drawn by the Paravisc impeller decreases with increased speed of the inner impellers when both impeller types are rotating in the same direction, as observed in the co-axial mixer equipped with an anchor. The pitched blade turbines induce a flow that drags the proximity blades of the Paravisc, and consequently decrease its power consumption. As the tip speed ratio increases (i.e. increasing the rotational speed of the inner impeller), the additional shear field induced by the central impellers significantly influences the flow field around the proximity impeller and consequently the power consumption. However, the rotation of the inner impellers affects the power consumption of each proximity impeller differently, as shown in Table 5-3. The data indicate that the design and consequently the generated flow patterns of the proximity impeller have a significant influence on the flow field interactions between the impellers and therefore on

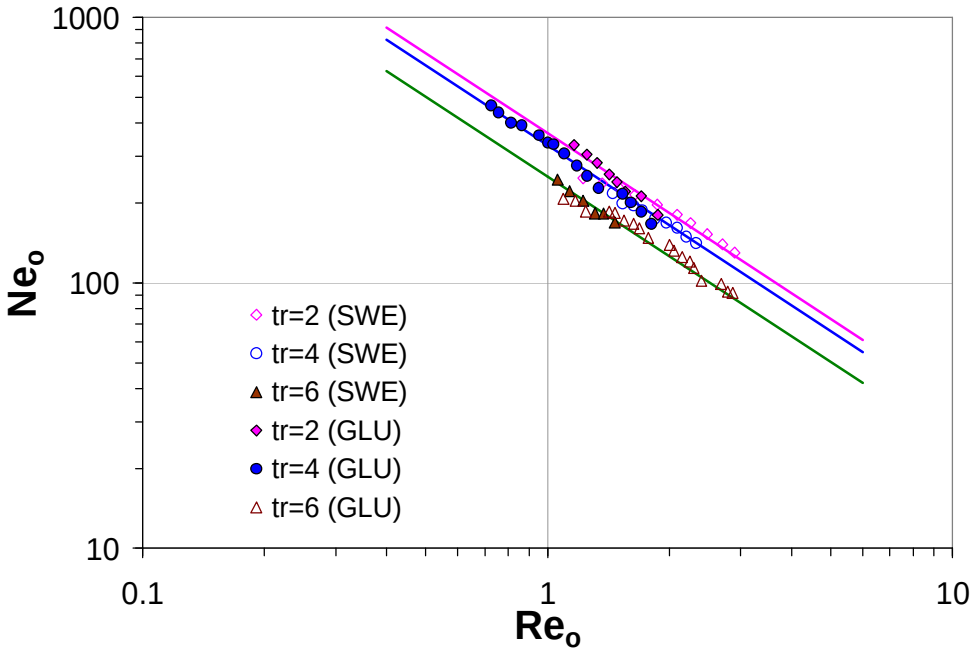

Figure 5-16: Measured power curves of Paravisc impeller in a co-axial mixer for different impeller tip speed ratios in Newtonian fluids

the overall co-axial mixing performance. The collaborative effect of proximity and inner impellers rotating in the same direction is enhanced in both investigated co-axial mixer configurations, as the power consumption data indicate.

Analogous analysis was carried out using two types of non-Newtonian fluids and the results are plotted in Figure 5-17. The non-Newtonian data also show that the power draw of the Paravisc is affected by the inner impeller speed. Increased the inner impeller speed decreases the power draw of the proximity impeller. The non-Newtonian data deviate only slightly from the Newtonian power curves, which indicate an overall good agreement. The Metzner-Otto constant K_S=28.8 of the Paravisc impeller could be used to determine the effective viscosity of the Paravisc in a co-axial mixer. Since the power curves were obtained in two different non-Newtonian fluids, it could not be determined that the K_S is a function of the flow index, at least not within the range of operating conditions in the investigation.

Figure 5-18 shows the calculated power curves of the Paravisc impeller in co-axial mixers in Newtonian fluids. The results obtained in the CFD model show similar trends as the experimental data. The power consumption of the Paravisc impeller is affected by the inner impeller speed. An increase in the inner impeller speed causes a reduction in the

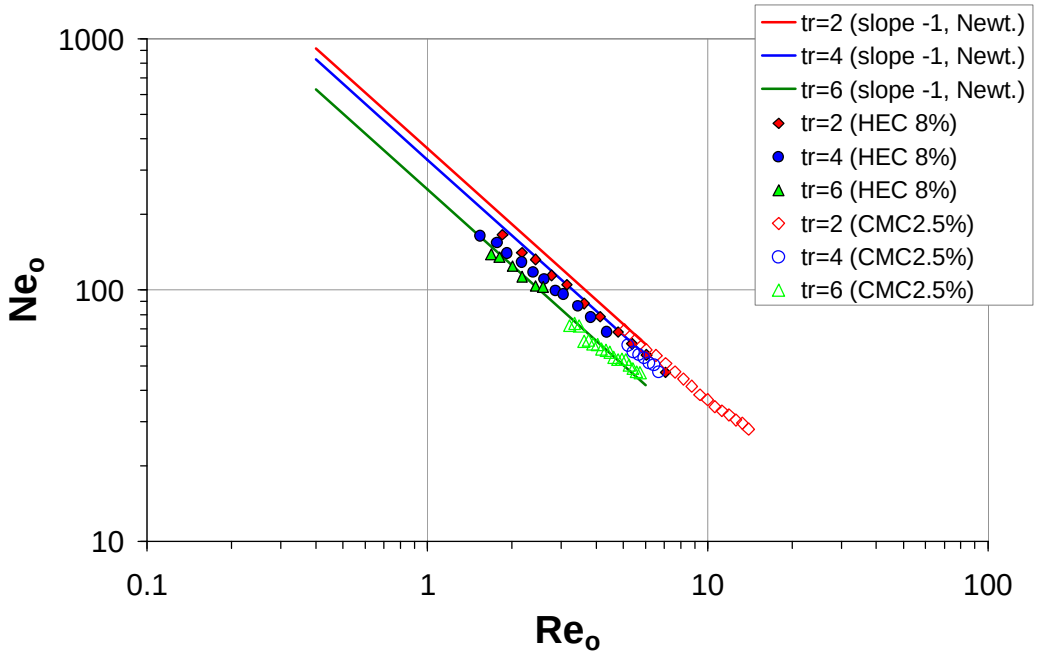

Figure 5-17: Measured power curves of Paravisc impeller in a co-axial mixer for different impeller tip speed ratios in Non-Newtonian fluids

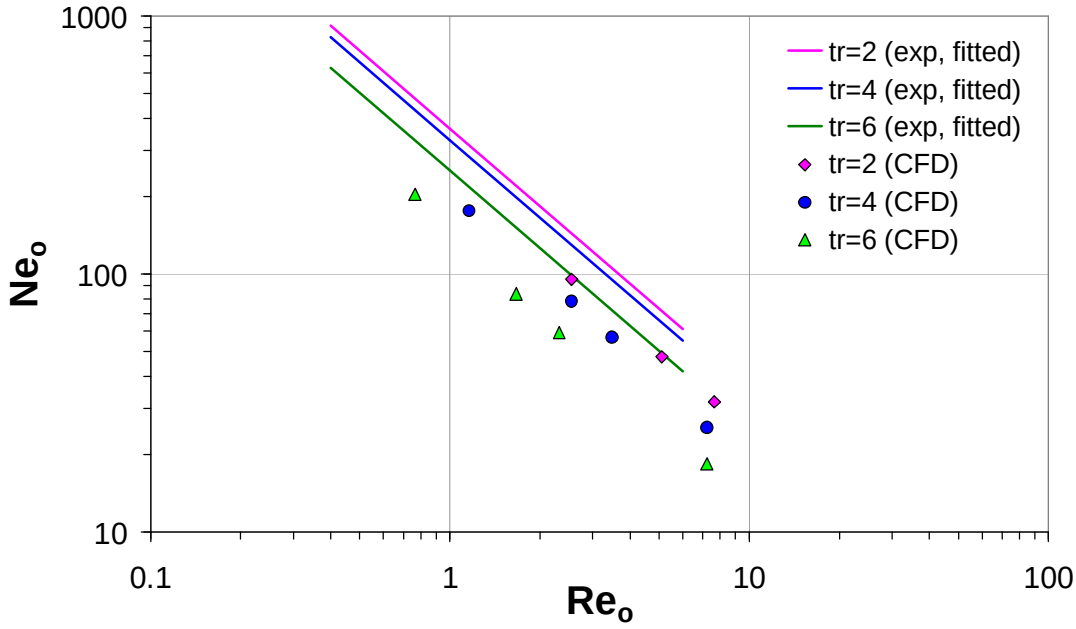

Figure 5-18: Calculated power curves of Paravisc impeller in a co-axial mixer for different impeller tip speed ratios in Newtonian fluids

power of the proximity impeller. However, the calculated reduction of the power consumption of the Paravisc impeller is under-predicted by 40%. The difference between experimental and CFD results is, as previously discussed, attributed to a weakness in the model for the Paravisc impeller.

Table 5-3: Variation of K_P of the proximity impellers in co-rotating mode with the inner impellers

Tip speed ratio (tr)	K_P anchor	K_P anchor decay	K_P Paravisc	K_P Paravisc decay
0	295	-	385	-
2	268	9%	366	5%
4	213	28%	330	14%
6	182	38%	252	35%

5.1.3 Correlated power curves for co-axial mixers

The power draw of the pitched blade turbines does not change with the tip speed ratio. For design purposes, it means that the standard power curve can be used to predict the power consumption of the PBT. However, the power drawn by the proximity impeller is a function of the tip speed ratio. In the present section, approaches are employed to describe the power consumption of the proximity impellers in the form of standard power curves. The correlated power curves require new definitions of the dimensionless numbers Reynolds and Newton numbers that describe the power consumption of the impellers. The Buckingham Π-theorem is applied to describe the force on the proximity impeller in co-axial mixers, which is a function of the fluid properties (ρ, η) , diameter of the proximity impeller (D_o), tip speed of the proximity impeller (v_o), but it is also a function of the diameter of the inner impellers (D_i) and the tip speed of the inner impeller (v_i):

$$F_o = f(\eta, \rho, v_o, v_i, D_o, D_i) \tag{5-1}$$

Different from the single impeller systems, the parameters of the inner impellers additionally influence the force on the proximity blades. Although the diameter of the inner impeller was kept constant in this investigation, it is not difficult to realize that it has an influence on the power consumption of the proximity impeller. The studies conducted by Köhler and Hemmerle (2003) confirmed the influence of the diameter ratio on the power consumption of the impellers. Following the Buckingham Π-theorem these variables can be reduced to four dimensionless characteristic numbers, which can be determined as following:

$$\frac{ML}{T^2}=\left(\frac{M}{L^3}\right)^a\left(\frac{M}{LT}\right)^b\left(\frac{L}{T}\right)^c\left(\frac{L}{T}\right)^d(L)^e(L)^f \tag{5-2}$$

For mass M: $1=a+b$

For length L: $1=-3a-b+c+d+e+f$

For time T: $-2=-b-c-d$

Three dimensional parameters can be selected, for instance ρ, v_o and D_o. The dimensionless groups are set up by combining the parameters selected previously and combining with the other parameters (such as F_o, η, v_i and D_i):

$$F_o = C(\rho)^{1-b}(\eta)^b(v_o)^{2-b-d}(v_i)^d(D_o)^{2-b-f}(D_i)^f \tag{5-3}$$

Equation Eq.(5-3) can be rearranged in terms of four dimensionless numbers as follows:

$$\frac{F_o}{\rho v_o^2 D_o{}^2} = C\left(\frac{\eta}{\rho v_o D_o}\right)\left(\frac{v_i}{v_o}\right)\left(\frac{D_i}{D_o}\right) \tag{5-4}$$

$$Ne_o = f\left(Re_o, \frac{v_i}{v_o}, \frac{D_i}{D_o}\right) \tag{5-5}$$

The power consumption of the proximity impeller in a co-axial mixer is a function of the Reynolds number of the proximity impeller, which includes the fluid properties and characteristic parameters of the proximity impeller, the tip speed ratio and the distance between the impellers.

For single impeller systems, it is common to expand the relationship $NeRe=K_P$ by including parameter ratios to account for variations in geometry for a particular impeller design, as given in Eq. (5-6):

$$Ne = K_P\, Re^{-1}(G_1)^a(G_2)^b\ldots \tag{5-6}$$

This form of relationship has been successfully validated and evaluated for a wide range of published data for anchors and ribbons, for instance, which are extensively used in the laminar regime (Harnby *et al.*, 1992).

The experimental data for Newtonian and non-Newtonian fluids are processed in such a way to develop power curves for the proximity impellers that account for the tip speed ratio, as the dimensionless analysis and the relationship in Eq. (5-6) indicate. The influence

of the diameter ratio is not taken into account for the moment because this dimensionless variable was kept constant in this work.

5.1.3.1 Power consumption of the anchor impeller in a co-axial mixer

As previously analyzed, the power curves of the anchor impeller in the laminar regime decreases with increased Reynolds number, are parallel and have a slope -1 The power curves in laminar regime can be described by the expression $NeRe=K_P$. The power constant K_P is a function of the tip speed ratio. The processing of the experimental data of the co-axial mixer configuration anchor and PBT in co-rotating mode and counter-rotating mode gives the following linear equations as the best fit to predict the power constants for both systems:

$$K_{P,\,coax}(tr) = -19.1\ tr + 295 \qquad \text{for anchor in co-rotation} \qquad (5\text{-}7)$$

$$K_{P,coax}(tr) = 18.8\ tr + 295 \qquad \text{for anchor in counter-rotation} \qquad (5\text{-}8)$$

When the tip speed ratio is zero, it means only the anchor is rotating in the vessel and K_P becomes the classical value for an anchor impeller (K_P=295). The deviation between measured and correlated data is given in Table 5-4. It is interesting that the slope constants found for both systems are very similar. Averaging both slope constants and keeping the original signs, the deviation doesn't increase substantially. It is also interesting that the inverse of the constant is 0.053, which is the distance from the edge of the inner impeller to the inner edge of the anchor impeller. This could suggest that for co-axial mixing systems, in which this distance is larger, the flow interactions and, thus, the influence of the tip speed ratio are weaker. The power consumption of the anchor in co-axial mixer approaches the power consumption of the anchor impeller alone.

Table 5-4: Measured and correlated K_P values for the co-axial mixing systems equipped with anchor impeller in co- and counter-rotating mode

tip speed ratio	Co-rotating			Counter-rotating		
	measured	correlated	deviation	measured	correlated	deviation
0	295	295	0%	295	295	0%
2	268	256.8	4.2%	323	332.6	3.0%
4	213	218.6	2.6%	355	370.2	4.3%
6	182	180.4	0.9%	421	407.8	3.1%

The single power master curves of each co-axial mixer configuration are obtained by introducing a speed ratio shift parameter K_{TR}, which is given in Eq.(5-9):

$$K_{TR} = \frac{K_{P,coax}(tr)}{K_P(tr = 0)} \tag{5-9}$$

The power consumption of the anchor impeller in a co-axial mixer for different tip speed ratios can be plotted as function of a modified Reynolds number, $Re_{o,\,mod}$, defined in Eq.(5-10):

$$Re_{o,mod} = \frac{Re_o}{K_{TR}} = \frac{\rho N_o^{2-n} D_o^2}{K_{TR} \cdot k \cdot K_{S,o}{}^{n-1}} \tag{5-10}$$

The single power master curves for the co-axial mixer configuration anchor combined with a dual set of pitched blade turbines in co-rotating mode and counter-rotating mode are plotted in Figure 5-19 and Figure 5-20, respectively.

The power master curves allow the estimation of the power draw of the anchor impeller in a co-axial mixer operating at various tip speed ratios ($0 \leq tr \leq 6$) in Newtonian and non-Newtonian fluids, in co-rotating and counter-rotating with power law index ranging from 0.4 to 1. A comparison between measured and calculated power consumption of the anchor impeller is plotted in Figure 5-21. The maximum relative error found for the co-axial mixers and fluids are summarized in Table 5-5.

Table 5-5: Error analysis details for the calculated power consumption of the anchor

	Max. Relative Error %	Relative Standard Deviation %
Co-rotating, Newtonian	16	3.5
Co-rotating, Non-Newtonian	17	5.3
Counter-rotating, Newtonian	10	2.8

It was demonstrated that the power drawn by the anchor decreases in a co-axial mixer in co-rotating mode and increases in a co-axial mixer in counter-rotating mode. Thus, the difference between the power consumed when the anchor is rotating alone and the power required when it is rotating in combination with open impellers depends on the drag effects caused by the open impellers on the anchor. This effect seems to be accounted for by the shift factor K_{TR}, which is a function of the tip speed ratio only. The Otto-Metzner constant K_S is not a function of the tip speed ratio, as the preceding power consumption analysis of the non-Newtonian data indicates. This was also a conclusion of the work presented by Rudolph *et al.* (2007) in which the procedure of Thibault and Tanguy (2002) was used to

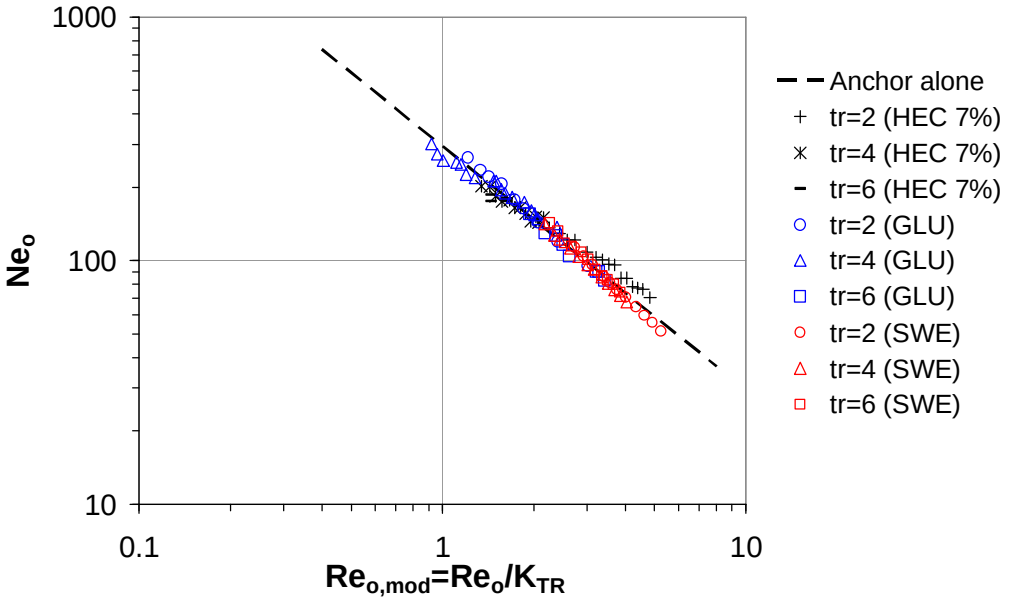

Figure 5-19: Single power master curve of the co-axial mixer consisting of anchor and a dual set of pitched-blade turbines in co-rotating mode

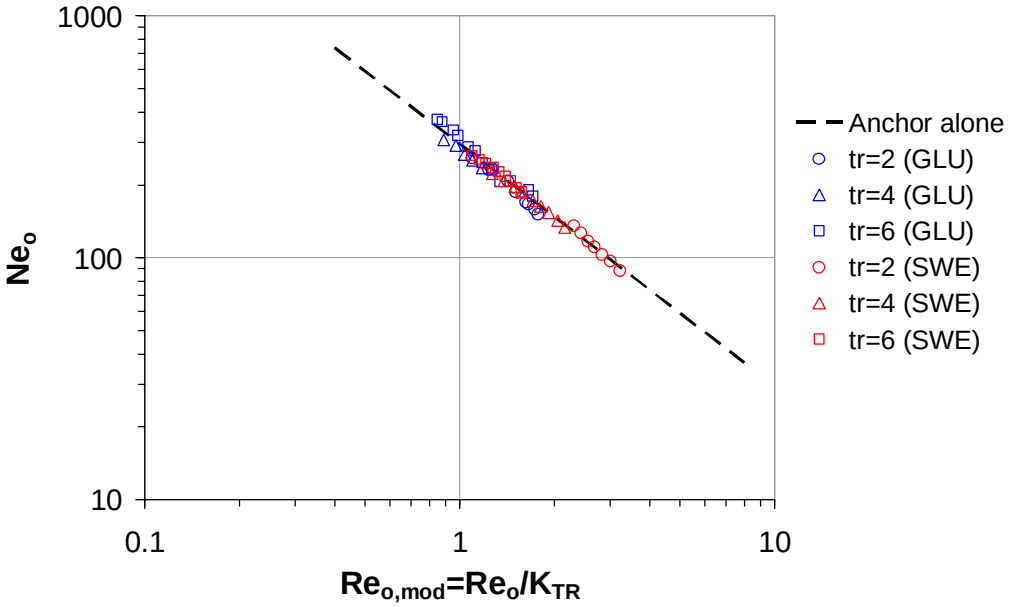

Figure 5-20: Single power master curve of the co-axial mixer consisting of anchor and a dual set of pitched-blade turbines in counter-rotating mode

obtain a single power master curve for the co-axial mixer anchor with a dual PBT in non-Newtonian fluids and co-rotating mode. The procedure to obtain the single power master curve in Rudolph *et al.* (2007) is laborious; but as shown here that the power constant K_P is a function of the tip speed ratio only. Thus introducing a tip speed ratio parameter is sufficient to account for the effect of the tip speed ratio.

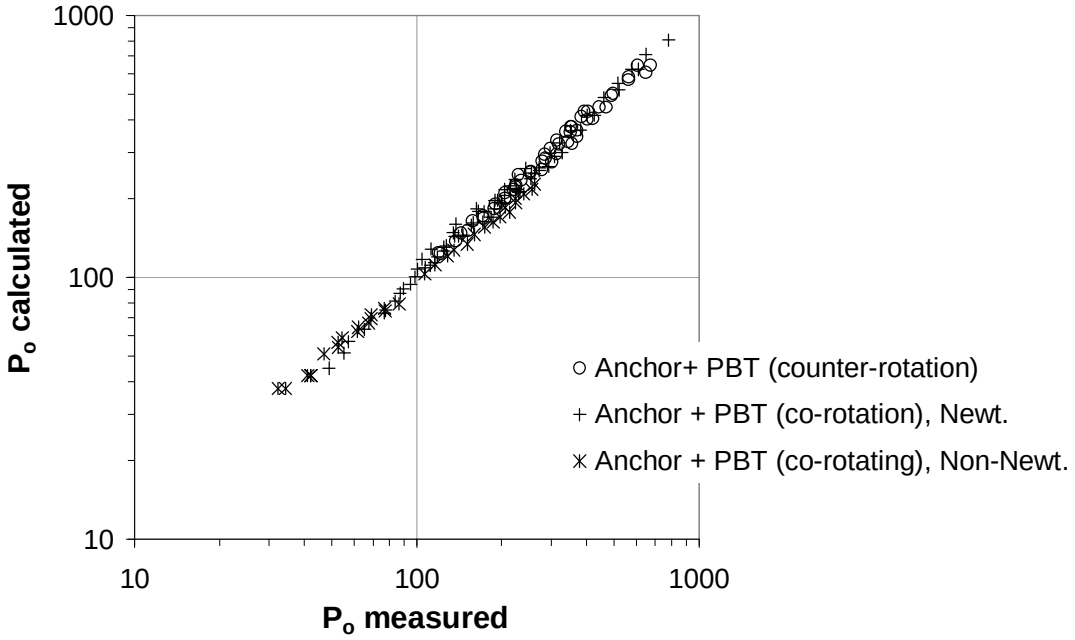

Figure 5-21: Comparison of measured and calculated power consumption of the anchor impeller in co-axial mixers

5.1.3.2 Power consumption of the Paravisc impeller in a co-axial mixer

Analogous analysis is conducted using the experimental data obtained in the co-axial mixer consisting of a Paravisc with a dual set of pitched blade turbines. The power curves of the Paravisc impeller in laminar regime decreases with increased Reynolds number. They are parallel and have a slope -1 in laminar regime. Thus, the power curves of the Paravisc can be described by the expression $NeRe=K_P$. The power constant K_P is a function of the tip speed ratio. The variation of the power constant of Paravisc with the tip speed ratio was fitted to the parabolic function given in Eq.(5-11):

$$K_{P,coax}(tr) = -3.61tr^2 - 0.316tr + 385 \qquad (5\text{-}11)$$

When the tip speed ratio is zero, the power constant corresponds to the case when only the Paravisc is moving. The deviation between measured and correlated data is given in Table 5-6.

In contrast to the configuration with anchor, the function of $K_{P,\,coax}$ (tr) is not linear and two independent constants are required to fit the data reasonably. The flow interactions between the inner impellers and the Paravisc are different from the interactions found in the co-axial mixer equipped with an anchor and inner impellers. The explanation might be

related to the complexity of the flow interactions encountered in each co-axial configuration. While the flow interactions in the configuration using the anchor occur essentially in the tangential direction, in the co-axial mixer using Paravisc, they occur in at least two directions, namely tangential and axial.

Table 5-6: Measured and correlated K_P values for the co-axial mixing systems equipped with Paravisc impeller

tip speed ratio	measured	correlated	deviation
0	385	385	0%
2	366	369.9	1.1%
4	330	326.1	1.2%
6	252	253.3	0.5%

The single power master curve for the co-axial mixer configuration Paravisc combined with a dual set of pitched blade turbines is obtained introducing the shift parameter defined in Eq.(5-9) in Eq.(5-10). The experimental data for Newtonian and non-Newtonian data is now plotted in form of a single power master curve, as shown in Figure 5-22.

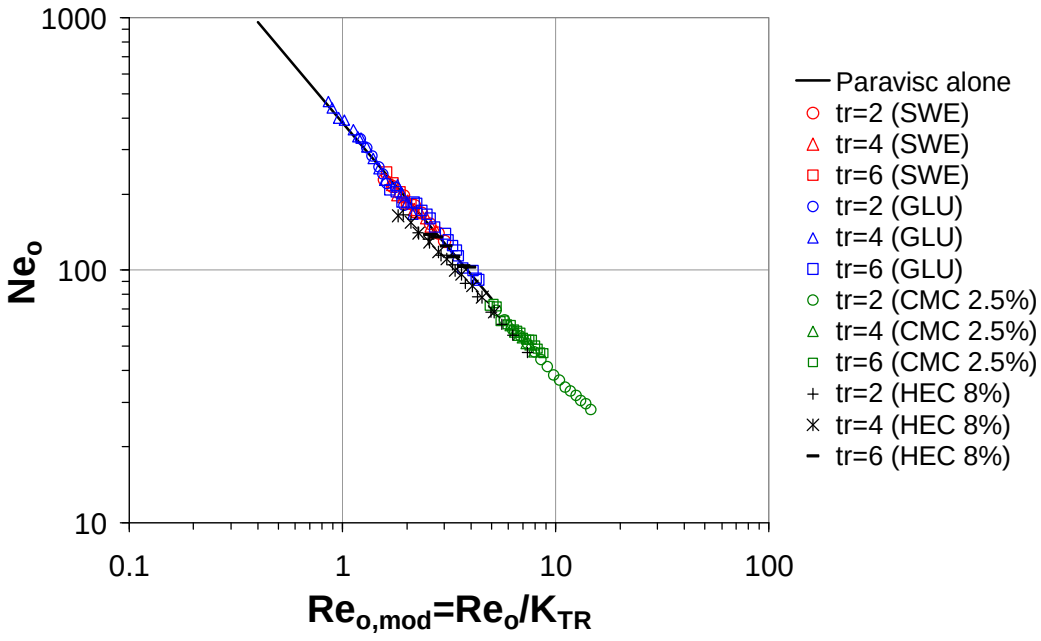

Figure 5-22: Single power master curve of the co-axial mixer consisting of Paravisc and a dual set of pitched-blade turbines

The $K_{P,coax}$ function in Eq.(5-11) allows the estimation of the power draw of the Paravisc impeller in a co-axial mixer operating at various tip speed ratios ($0 \leq tr \leq 6$) in Newtonian and non-Newtonian fluids, in standard co-rotating mode with power law index ranging

from 0.32 to 1. A comparison between measured and calculated power consumption of the Paravisc impeller is plotted in Figure 5-23. The maximum relative errors found for the power draw in different fluids are summarized in Table 5-7.

Table 5-7: Error analysis details for the calculated power consumption of the Paravisc

	Max. Relative Error %	Relative Standard Deviation %
Newtonian	9.7	2.4
Non-Newtonian	19	5.0

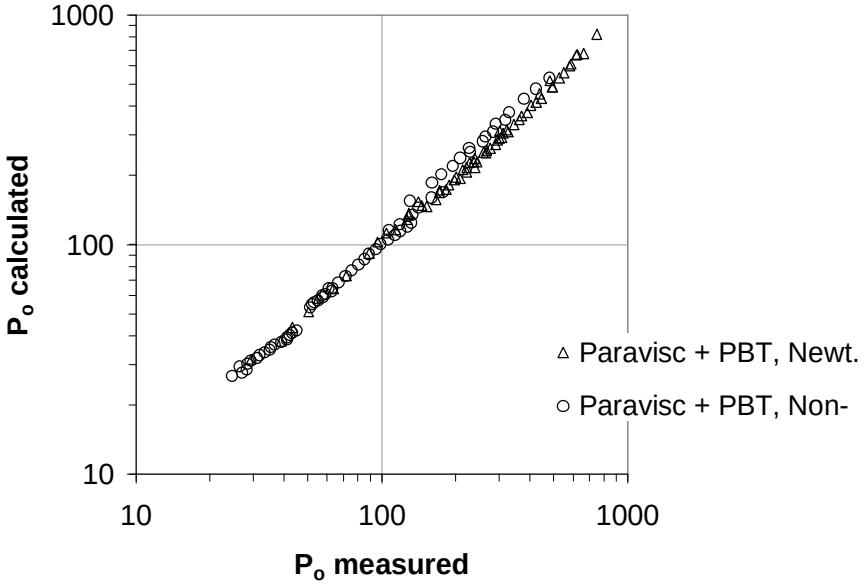

Figure 5-23: Comparison of measured and calculated power consumption of the anchor impeller in co-axial mixers

5.1.4 Power consumption correlations (review and validation)

In this section the validity of the newest correlations for Newton and Reynolds numbers proposed in the open literature are tested in the co-axial mixer configurations investigated in the present work. Farhat *et al*. (2008) proposed a characteristic speed for co-axial mixers as the sum of the tip speed of the inner impeller and the proximity impeller, as defined in Eq.(2-23). This should be valid for all rotating modes. The corresponding Newton and Reynolds number become:

$$Ne_{co\text{-}axial} = \frac{P_{total}}{\rho\left(N_i D_i + N_o D_o\right)^3 D_i^2} \tag{5-12}$$

$$Re_{co-axial} = \frac{\rho\left(N_i D_i + N_o D_o\right) D_i}{\eta} \tag{5-13}$$

Figure 5-24 shows the result of using the correlations defined by Farhat *et al.* (2008). The data don't collapse to the inner impeller power curve. The data obtained for the lowest tip speed ratio (tr=2) show the largest deviation. The "characteristic speed" as defined by Farhat is not universal. Apparently the definition works for co-axial mixing systems that operate at very high speed ratios. The "co-axial mixer speed" defined by Farhat requires that the tip speed of the inner impeller is increased by adding the tip speed of the anchor, so that the power of the inner impeller in co-axial mixers becomes the total power of the system, i.e. 100%. In systems operating at such high speed ratios, the tip speed of the anchor would not be significant and the power consumption of the inner impeller would be over 90% of the total power.

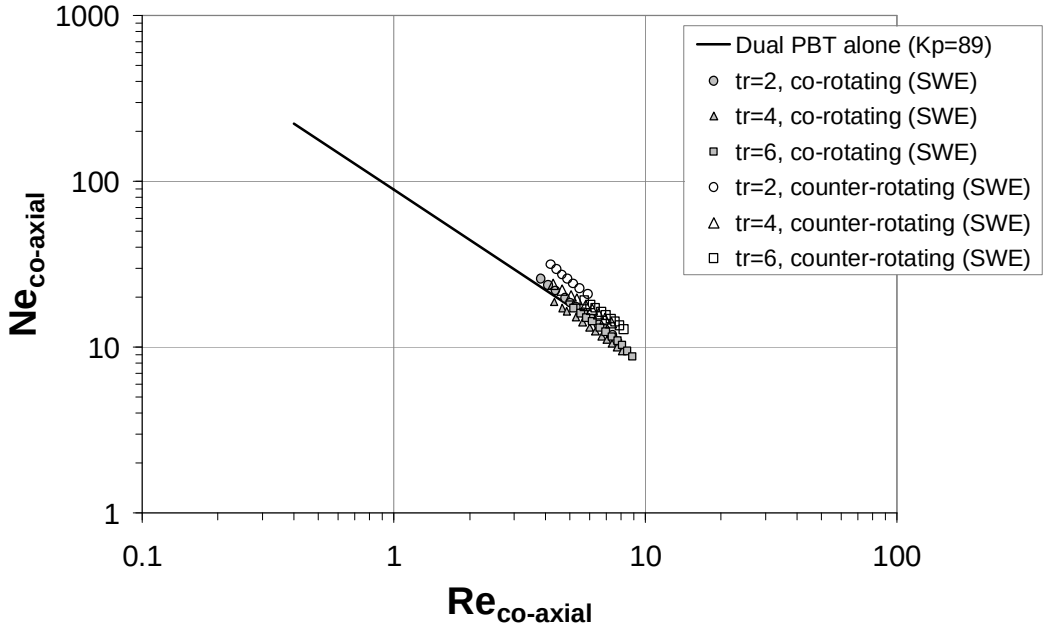

Figure 5-24: Correlated power curve of the co-axial mixer equipped with anchor and a dual PBT according to Farhat *et al.* (2008)

Figure 5-25 shows the averaged ratio between the power consumption of the inner impellers and the total power consumption of the co-axial system as function of the tip speed ratio for the investigated co-axial mixer consisting of anchor and PBT in both rotating modes. The power consumption ratios were measured in the Newtonian fluid with viscosity of 50 Pas.

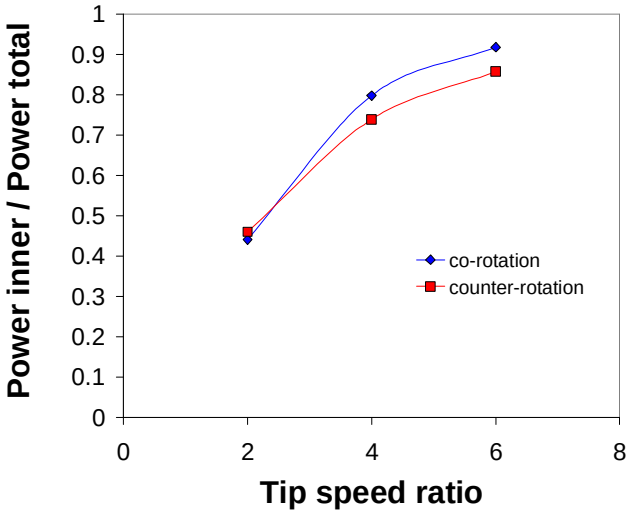

Figure 5-25: Power consumption ratio versus tip speed ratio (averaged data measured in Newtonian fluid with 50Pas)

Further investigations would be beneficial to identify the limitations of the proposed Farhat's correlation. It seems that the power drawn by the inner impeller, which is already very high and close to the total power of the system, is increased by a value which is the proximity impeller power draw, which is in turn much lower than the total power consumption of the system.

The correlations are not able to fit the data using the investigated co-axial mixer, because the anchor consumes a large portion of the power (approximately 60% for tip speed ratio 2 and 30% for tip speed ratio 4). The anchor has a significant tip speed as well. The sum of the tip speed ratios of PBT and anchor doesn't meet the tip speed of the inner impeller that corresponds to the total power of the system (100%). The correlation seems to fit well the data for high tip speed ratio 6 in co-rotating mode, where the inner impellers consume ~92% of the total power input.

The existence of a universal characteristic speed to describe the performance of co-axial mixers over a wide range of case scenarios (operating conditions, impeller design, geometric ratios, etc) is dubious. Simple combinations of the inner and outer impeller speeds are even more questionable in view of the complex flow interactions created in such hybrid impeller systems. The anchor impeller has a simple geometry and the flow interactions are predominantly occurring tangentially. However, the Paravisc impeller generates not only tangential flow, but also axial flow. The flow interactions between the impellers become even more complex to be described by a single dimensionless parameter.

5.2 Mixing time analysis

The measuring technique and the definition of mixing time are important in the mixing time analyses. It is not uncommon to find considerably differences in the results of different authors in the literature and this might be due to differences in the employed method to measure the mixing time and the definition of the mixing time (Hoogendoorn and Den Hartog, 1967). In this work, the method used to measure mixing time was the decolourization method, as described in Chapter 3. This method allows the visualization of the last stage of the blending process, which is the pivotal subject of interest for most of the practical applications. The definition of the mixing time by the applied method allowed theoretically a decolouration in places where the concentration differed by ±5% from the equilibrium stage. Therefore, the measured mixing times were the time to achieve 95% of homogeneity, i.e. θ_{95}, which is in this work denoted by θ only. However, in the practice, the method and the definition of the mixing time are subjective.

The decolourization method was suitable for very transparent liquids, which was the case for low concentrations of HEC, CMC solutions and glucose syrup. For solutions of HEC of 7%, for example, the measurements were difficult because of a number of factors, such as: (a) entrained air were dispersed into small bubbles that remained entrapped in the bulk due to the high viscosity of the liquid. The bubbles limited the visualization inside the tank. (b) Measurements of the pH were not reliable in such viscous liquid, as previously discussed in Chapter 3. Before each trial, it was necessary to set the pH to neutral. (c) The original colour of HEC 7% is not transparent, but dark orange, which is similar to the red colour of the acidified and not decolourized solution.

The time required for the entire vessel content to be decolourized in laminar flow can be exhaustively long due to persistent unmixed zones. There are parts of the liquid near the liquid surface, vessel walls and bottom that often were not decolourized. The definition of which size of those parts is taken into account and which is neglected requires subjective judgements. In this work, persistent stagnant zones were neglected, such as, (a) the small pockets of tracer on the liquid surface, (b) stable torus located below the upper impeller that appeared for some design configurations, (c) unmixed zone in the vessel bottom. The fine striations (filaments) near the proximity blades or wall were taken into account.

The presentation of the blend time data in dimensionless form is essential to generalize the results for scale-up and design of agitation systems. However, this is not trivial for co-

axial mixing systems, because the results are influenced by the presence of two impellers interacting in the system and parameters related to both impellers, such as viscosity and total power consumption. For industrial applications, it is important to characterize the agitation systems in terms of power consumption and mixing time simultaneously. The most efficient mixer is the one that can achieve the lowest mixing times at a minimum total power input. To the best knowledge of the author, there is no universal dimensionless correlation that describes the blending performance of different designs of co-axial mixers. For the analysis of the blend time as a function of operating parameters of the co-axial mixing systems, the conventional plot of Reynolds number (Re) versus dimensionless mixing time ($N \cdot \theta$) is not suitable. The use of characteristic numbers of one of the impellers in the co-axial system in the Reynolds number or in the dimensionless mixing time number ($N \cdot \theta$) does not allow a direct correlation to the total power input and thus the assessment of the overall blending efficiency. The use of relative rotational speeds is also insufficient and not applicable to different co-axial mixer configurations. Heiser *et al.* (2004) attempted to correlate their measured blend time data using relative rotational speeds, as proposed by Tanguy's work group (Foucault, 2004). The data fitting failed and the given reason was the significant difference between the co-axial mixer designs. Furthermore, relative speed is disadvantageous for design purposes, because an infinite number of speed combinations can give the same result. To analyze and decide which mixer or co-axial configuration is the most efficient, it is required to consider mixing time and total power input simultaneously.

5.2.1 Single impellers

Firstly, the effect of the baffle design on the mixing time of the dual set of pitched blade turbines in non-Newtonian fluids is investigated. The data in Figure 5-26 show the mixing time for a dual set of PBT in a baffled tank with four standard baffles, stationary anchor or stationary Paravisc. The Reynolds number is based on the apparent viscosity in the immediate vicinity of the inner impeller derived from the Metzner-Otto constant of the impeller. The data indicate that the type of baffling does not affect the mixing time characteristic, or that the anchor and Paravisc provide enough baffling at low Reynolds numbers. In general, the need for baffles decreases with increasing viscosity of the liquid, because the range of the shear field induced by the inner impeller reduces towards the wall. In the extreme case, the baffles are surrounded by motionless fluid although the inner impeller is operating.

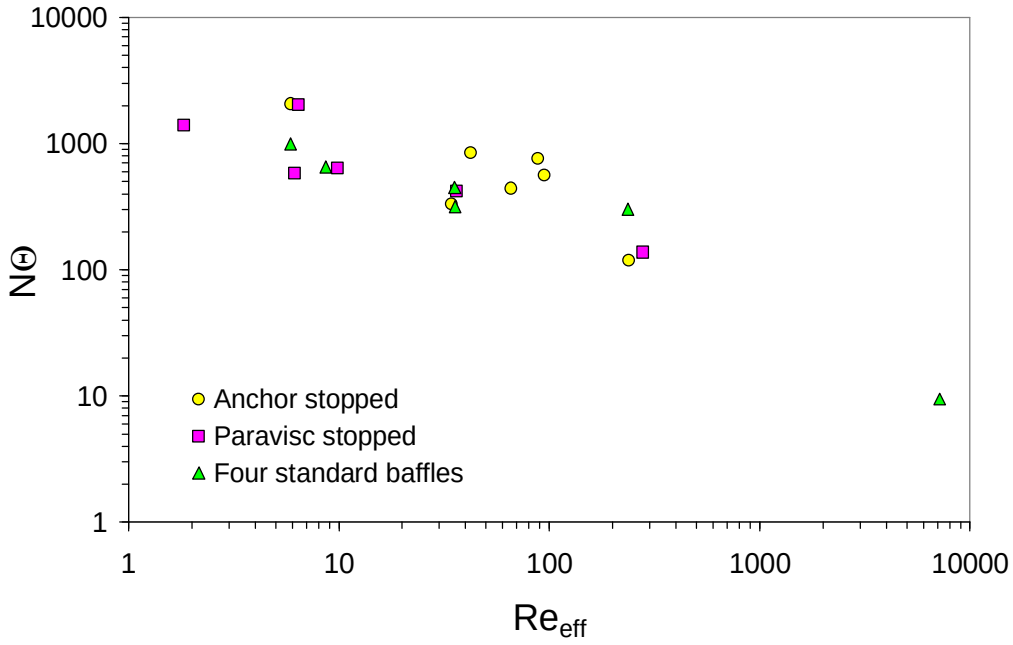

Figure 5-26: Mixing time curves of a dual set of PBT using different baffle types for non-Newtonian fluids

The mixing time characteristic curves of the investigated single impeller systems for Newtonian and non-Newtonian fluids are plotted in Figure 5-27. The data set of PBT includes all baffle types. The mixing time data points could be fitted using the following expressions:

$$N\Theta = a\, Re^{-b} \qquad \text{for open impellers} \qquad (5\text{-}14)$$

$$N\Theta = \frac{a}{1+\left(\frac{Re_{eff}}{b}\right)} \qquad \text{for proximity impellers} \qquad (5\text{-}15)$$

The regression parameters are in Table 5-8. The effective Reynolds number is calculated using the effective viscosity determined by applying the Metzner-Otto approach Eq.(2-11) and power law model Eq.(2-8), and given in Eq.(5-16):

$$Re_{eff} = \frac{\rho N D^2}{\eta_{eff}} \qquad (5\text{-}16)$$

The curves of the investigated proximity impellers show similar shape and trends. As the viscosity increases, the mixing time increases up to a certain value of Reynolds number, where an onset likely occurs, suggesting that the mixing time number Nθ remains constant. For very low Reynolds number, i.e. very high viscosities, a significant reduction in mixing time is not possible by only increasing the impeller rotational speed.

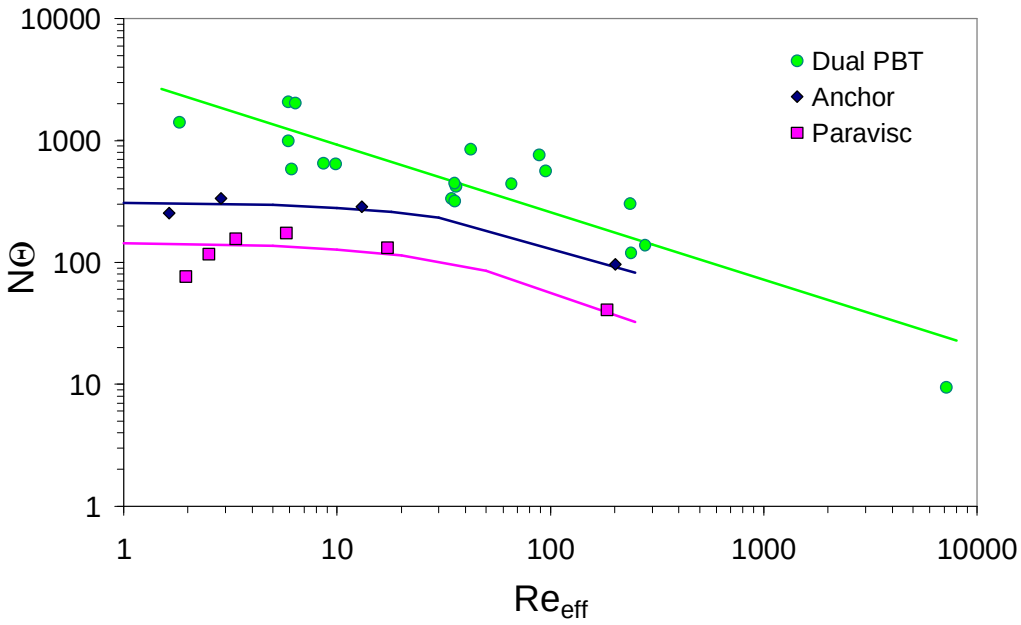

Figure 5-27: Mixing time curves of the single impellers for Newtonian and non-Newtonian fluids

The plateau in the curves can reveal the presence of persistent stagnant zones, which were not accounted in the measured mixing time. Thus, the mixing time doesn't increase infinitely. The onset Reynolds number could be determined for each impeller, if few more experimental data in the range of Reynolds number from 20 to 100 are obtained.

Table 5-8: Fitting parameters of Eq.(5-14) and Eq.(5-15)

	a	b	r-square
Dual PBT	3331	0.55	0.79
Anchor	312	90	0.88
Paravisc	146	71	0.45

The measured and fitted mixing time characteristic curves for the single impellers are compared to previously reported data in Figure 5-28, Figure 5-29 and Figure 5-30. The measurements of mixing time for a dual set of PBT in non-Newtonian fluids were reported by Garred (1996) in the BHR Group Limited Fluid Mixing Processes consortium report FMP060. The effective viscosity necessary to calculate the Reynolds number, was determined by assuming the same Metzner-Otto constant of our dual PBT system (K_S=10.9). The measured data and Garred's reported data are in reasonable agreement in view of the differences in the used measurement techniques, criterion of last unmixed zone and configuration. Although the impeller and tank diameter ratio used by BHR group was

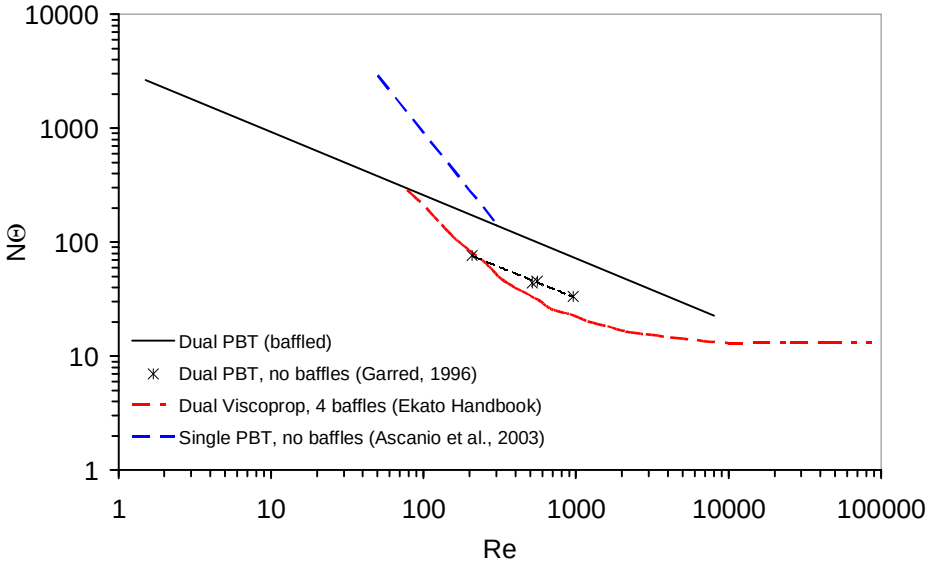

Figure 5-28: Measured mixing time curves for dual pitched blade turbines compared to previously reported data

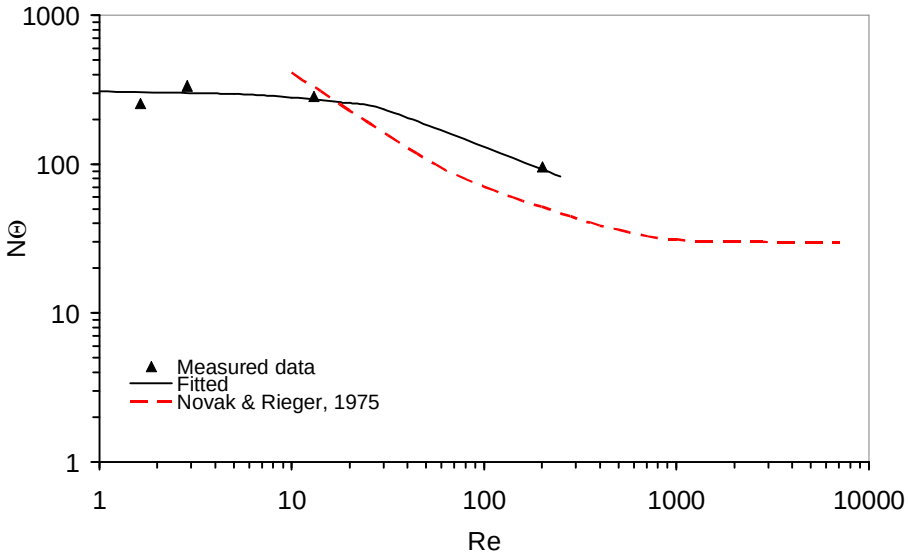

Figure 5-29: Measured mixing time curves for anchor impeller compared to previously reported data

the same used in this work , i.e. D/T=1/2, the relative position to bottom and liquid surface, the distance between the impellers (S), and other geometrical parameters that influence the blending rate, were different. It is expected that the impeller spacing (S) has a siginificant effect on the mixing time in laminar and transitional regime. This effect is related to the compartmentalization of the flow. Since the pumping capacity of the pitched blade turbines are strongly reduced as the viscosity increases, it is expected that the larger the spacing between the impellers, the worse is the flow exchange between both compartments. The

impeller spacing (S=T/3) used in the Garred's configuration were smaller than the one used in the present experiments S=T/2 and thus, would explain the reduced mixing time due to less flow segregation. The data for a dual VISCOPROP® (Ekato Rührtechnik GmbH) in transitional and turbulent regime are plotted for comparison. The curve of VISCOPROP® is also close to the ones of a dual set of PBT. The curve published from Ascanio *et al.* (2003) is for a single pitched blade turbine with 4 blades without baffles, which lies above the curves for dual impeller systems, as expected.

In Figure 5-29, the mixing time characteristic curve of the anchor impeller is compared to the one reported by Novák and Rieger (1975). The data points obtained in the range of $20 < Re < 300$ found very good agreement with the published data. The plateau shape given by the data for the anchor impeller in the very low Reynolds number is not common for this impeller. Reasons that explain this plateau could be attributed not only to the difference in the definition of the mixing time and experimental method but also to the fact that the stopped pitched blade turbines act as baffles. Previous studies of anchor impeller, for instance by Pedrosa and Nunhez (2000), reported that the fluid is poorly mixed at the center. The PBT as baffles in the central part of the vessel deflect the strong rotational (tangential) flow, creating internal circulation that enhanced the blending in the laminar regime. However, further data in this regime would be necessary to validate this hypothesis.

The mixing time characteristic curve of the Ekato Paravisc impeller is plotted in Figure 5-30 and compared to previously reported curves (Delaplace *et al.*, 2000a) and (Ekato Handbook, 2000). The measured curve suggests that the product $N\theta$ is constant in the laminar regime. Averaging the data points in the laminar regime, $N\theta=131$ is obtained for $Re<20$, which is in good agreement with those reported for Paravisc and for helical ribbon impellers (between 25 and 150). It is important to consider the fact that the applied experimental method to measure the blend time affects the mixing rate and the systems were different in terms of geometry and baffling. The mixing curve measured by Ekato is the lowest one and this is probably due to the effect of the baffles in the central part of the vessel. The system investigated by Ekato used standard baffles in the central part of the vessel. Barar Pour *et al.* (2007) investigated the blending performance of a Paravisc impeller recently and reported that Paravisc impeller failed to mix efficiently the central part of the tank when used alone. However, the performance increased significantly when an off-centered high speed impeller was acting as baffle.

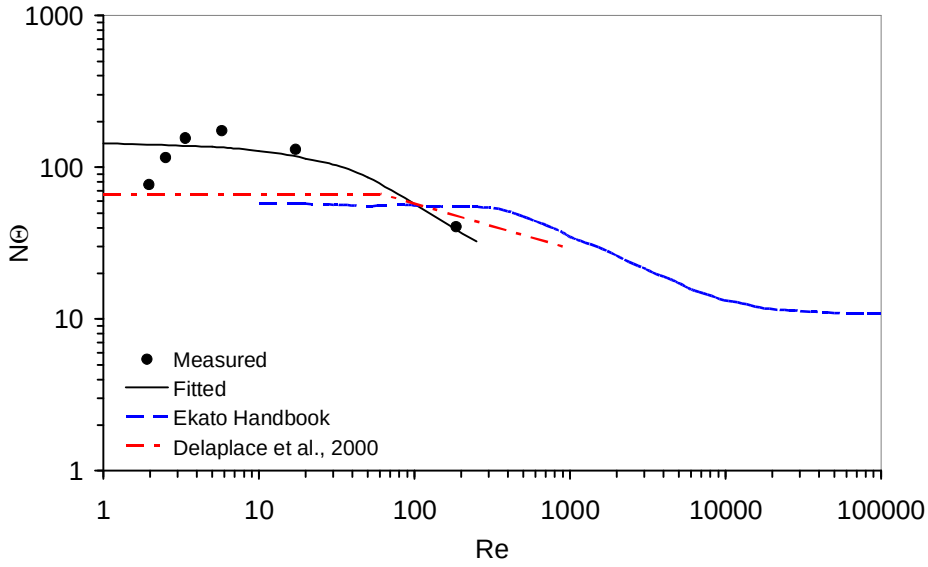

Figure 5-30: Measured mixing time curves for Paravisc compared to previously reported data

5.2.2 Co-axial mixers

In co-axial mixers, the blending performance is affected by the inner and proximity impeller mutual interactions. The effect of the key influencing parameters, such as viscosity, tip speed ratio, energy input and rotating mode, on the mixing time of the investigated co-axial mixers is analyzed. In the first stage of the analysis, the effect of one parameter is studied by keeping the rest constant. In the second stage, dimensionless numbers are introduced in the analysis.

5.2.2.1 Effect of the rheology

In this work, different non-Newtonian fluids were employed. Hence, mixing time experiments were carried out in a broad range of viscosity. A plot of mixing time as function of HEC weight concentration at constant total power input of 1 W/kg is given in Figure 5-31. Higher concentration of HEC means higher fluid viscosity. The plot contains data obtained in the investigated co-axial mixer configurations for three different tip speed ratios (tr = 2, 4 and 6). The data obtained in the single impeller systems are plotted as well for comparison. The data are not always sorted in terms of tip speed ratio, because this is separately analyzed in a later section. As expected, the mixing time increases significantly as the viscosity increases, regardless of the design of the agitation system. The data of Paravisc impeller for 1 W/kg indicate the same trend shown in the characteristic mixing time curve (Figure 5-30), i.e. further increase in the fluid viscosity does not increase the

mixing time. For high HEC concentrations, i.e. HEC 7%, the Paravisc impeller alone scored well as single impeller system. In comparison to co-axial mixing systems, it performed also well, achieving mixing times in the same order of magnitude or higher. Longer mixing times were achieved by the proximity impeller anchor. Experimental data were also obtained for higher total power input per unit mass (from 1 to 4 W/kg), however not for all designs and operation conditions. Thus, analogous plots for other energy inputs appear not complete, thus, not shown in that form. Only few data for co-axial anchor with PBT in counter-rotating mode could be obtained at this power input and an accurate comparison is difficult. The effect of rotating mode is discussed later.

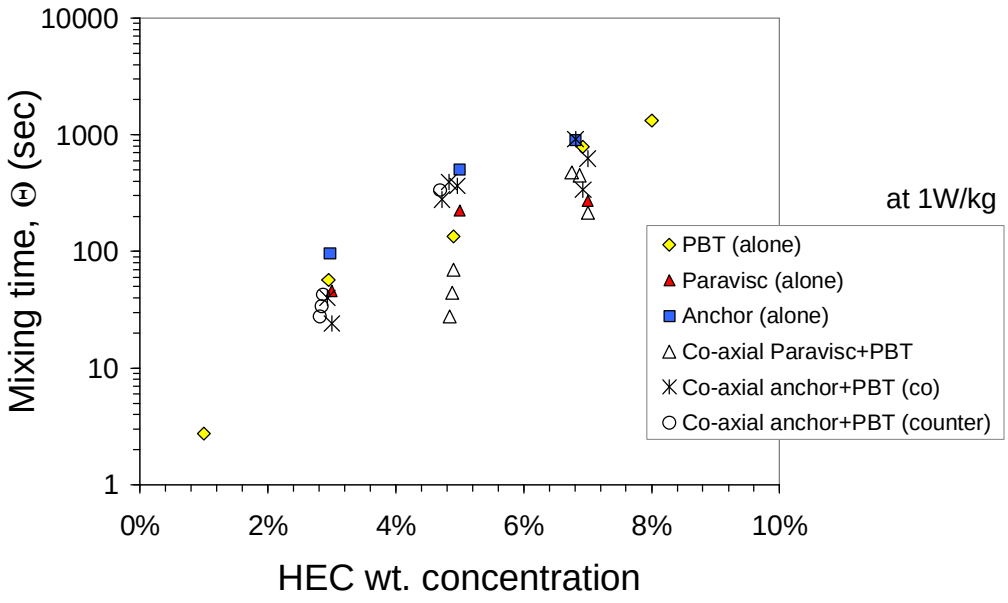

Figure 5-31: Mixing time as function of HEC weight concentration at constant total power input of 1 W/kg

5.2.2.2 Effect of the energy input

Figure 5-32 shows the measured blend times as function of the total power input per unit mass in aqueous solutions of CMC of 2% weight concentration for the co-axial mixers operating at three different tip speed ratios. The mixing times obtained in the stirred tank with PBT alone are plotted for comparison. As expected, the mixing time of all investigated agitation systems decreases with increased total power input. The data indicate that the configuration co-axial Paravisc with PBT showed the best performance regardless of the tip speed ratio and total power input. The anchor combined with PBT exhibits a lower performance in comparison to the single impeller system (PBT alone) at energy inputs 1

and 2 W/kg regardless of the tip speed ratio. However, the performance of this configuration increases at higher total power input (3W/kg), but only for high speed ratios. At tip speed ratio tr=6, the inner impellers rotates 11 times faster than the anchor and it seems the mixing task is mainly solved by the inner impellers. It is relevant to point out that the flow regime in CMC 2% is transitional (Reynolds number calculated using the inner impeller parameters). The good performance of the Paravisc with PBT can be explained by the enhanced axial pumping ability of both impellers, since Paravisc pumps upwards and the inner impellers pump downwards. The PBT alone in CMC 2% showed better performance than the co-axial configuration using the proximity impeller anchor for almost all operating conditions. Apparently, the anchor impeller does not contribute significantly to the bulk blending in this flow regime.

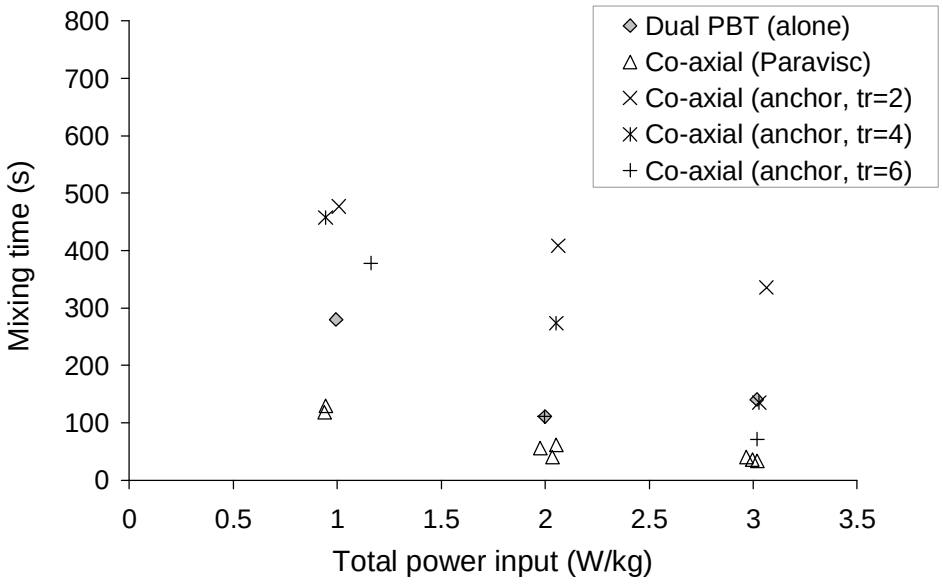

Figure 5-32: Mixing time as function of total power input in CMC 2%

The plot in Figure 5-33 shows the mixing time for the aqueous solution of HEC of 5% weight concentration as function of the total power input per mass unit. The data show a similar situation as described for CMC 2%. The Reynolds numbers of the inner impellers indicate that the regime is still transitional in experiments using this fluid. The co-axial mixer with Paravisc and dual PBT exhibits the best performance regardless of the tip speed ratio and total power input. The performance of the co-axial mixer anchor with PBT depends strongly on the set tip speed ratio in the transitional regime, which is denoted by the spread of the three data points at the same power input per unit mass. The mixing time data of the co-axial mixer with Paravisc obtained for the three tip speed ratios are more

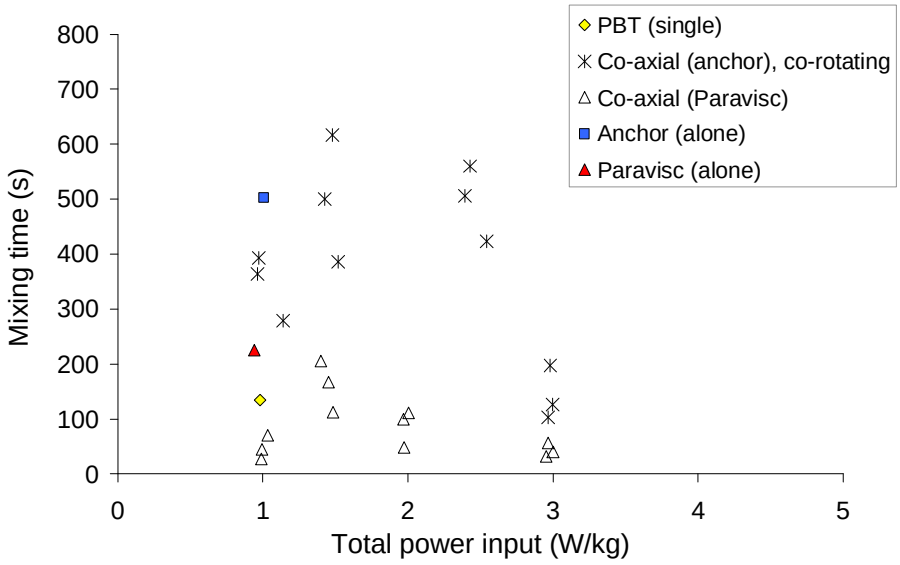

Figure 5-33: Mixing time as function of total power input in HEC 5%

close to each other, indicating a less pronounced dependence of the mixing time upon the tip speed ratio. At power input 3 W/kg, the mixing times of the co-axial using anchor approaches the values obtained in the co-axial mixer using Paravisc. The data obtained in HEC 5% is less consistent than the ones obtained in CMC 2%. The performance of the co-axial mixer with Paravisc at 1 W/kg and 1.5 W/kg seem not to be consistent to each other.

The situation changes when the flow regime is laminar. The measured blend times in HEC of 7% wt. concentration as function of the total power input per unit mass are plotted in Figure 5-34. The efficiency of the single impeller systems compared to the co-axial mixing systems is lower, with exception of the Paravisc at total power input 1W/kg. The mixing time obtained for the Paravisc alone decreases slightly with increasing power input. This is consistent with the mixing time characteristic curve of Paravisc that shows that increasing the impeller speed in the viscous regime, no further reduction of the mixing time can be achieved. The performance of the dual PBT is poor in this flow regime. The reason is that the axial pumping capacity of the PBT impellers decreases significantly in laminar flow, as previously discussed in Chapter 2. The co-axial mixer using Paravisc as proximity impeller gives in general the shortest mixing times at the investigated power inputs, but it depends on the tip speed ratio. The performance of the co-axial equipped with an anchor becomes equivalent to the performance of the co-axial mixer with Paravisc at the high power input per unit mass, i.e. 3 W/kg, in this flow regime as well.

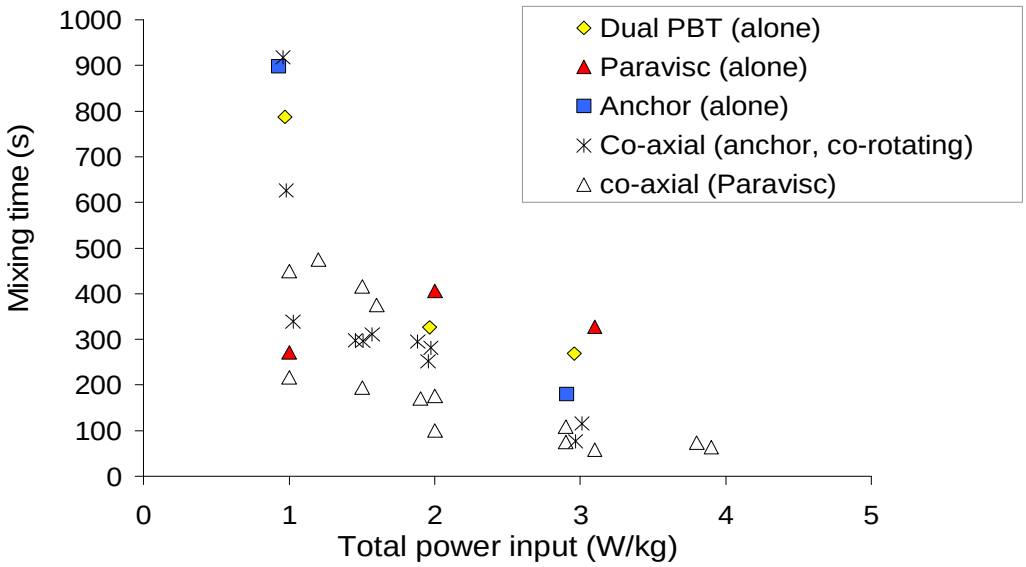

Figure 5-34: Mixing time as function of total power input in HEC 7%

5.2.2.3 Effect of the tip speed ratio

From the previous analysis, it could be concluded that the performance of the co-axial mixers depends on the tip speed ratio. In this section, the blending efficiency of the co-axial mixers is analyzed further in regards to the applied tip speed ratio. From the design perspective, it is important to operate the co-axial agitation systems at the most efficient tip speed ratio.

Figure 5-35 shows the effect of the inner impeller rotation on the mixing time of the co-axial mixers. The fluid properties are kept constant and also the rotational speed of the proximity impeller, which is 23 ± 4 rpm. The mixing time number, $N_o\theta$, on the abscissa is the product of the mixing time, θ, and the rotational speed of the proximity impeller, N_o. When the inner impeller tip speed is zero, the mixing time product is that for the proximity impeller alone. The data points show that the mixing time reduces with increasing inner impeller speed for both co-axial mixer configurations. The plot shows that the lowest mixing times are achieved at the highest tip speed ratios. However, this should not lead to the conclusion, that a high tip speed ratio is beneficial over a low tip speed ratio. The reason is that while increasing the rotational speed of the inner impellers, the total power input is significantly affected, resulting in a strong effect on the mixing time. It is obvious that the reduction in the mixing time by using a co-axial mixer configuration depends on the tip speed ratio. However, this effect is different with respect to the co-axial mixer configuration. For the co-axial mixer configuration using Paravisc, the mixing time is

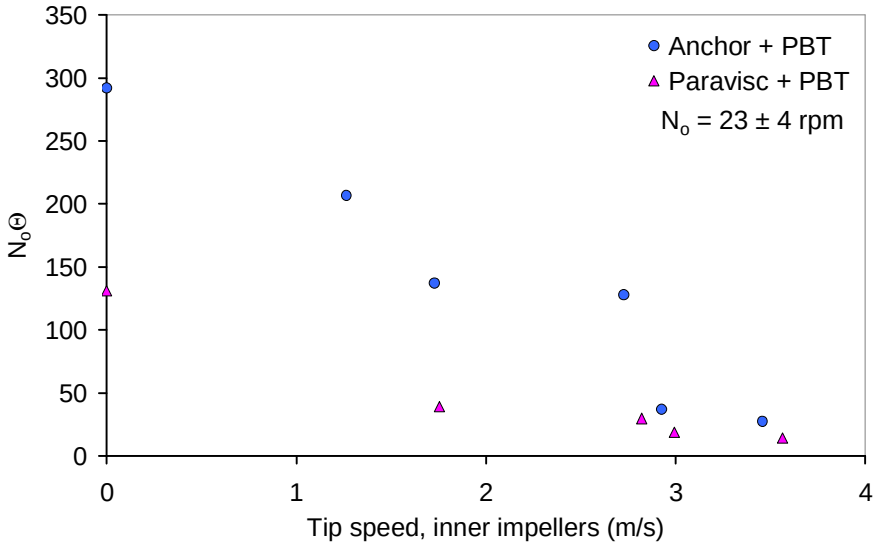

Figure 5-35: Effect of the tip speed of the inner impellers on the mixing time of co-axial mixers in CMC 2%

considerably low at a low inner impeller speeds (low tip speed ratio), and only decreases slightly as the tip speed ratio is increased. Apparently, further increase of the inner impeller speed didn't lead to significantly reduction in the mixing time for this co-axial mixer configuration in the transitional regime. For the co-axial mixer anchor and PBT, further increase of the inner impeller speed decreased the mixing time substantially.

A similar analysis was carried out for the laminar regime, using HEC 7% as the non-Newtonian fluid, as shown in Figure 5-36. Also in the laminar regime, the reduction rate in the mixing time by using a co-axial mixer configuration anchor with PBT depends strongly on the tip speed ratio. For the co-axial mixer Paravisc with PBT, the mixing time seems to be independent of the inner impeller speed in laminar regime. Once a "critical tip speed" is applied, further reduction in mixing time in this co-axial configuration could not be achieved by increasing the inner impeller speed. It indicates that the blending in the co-axial mixer is predominantly governed by the proximity impeller Paravisc in the laminar regime. In the case of the co-axial configuration anchor with PBT, the influence of the inner impeller speed on the mixing time is still significant.

A similar analysis was done to evaluate the effect of the tip speed of the proximity impellers on the mixing time of the co-axial mixers. The results are shown in Figure 5-37. The data are analyzed at constant fluid properties and constant rotational speed of the inner impellers. It can be read from the data that the influence of the anchor impeller on the

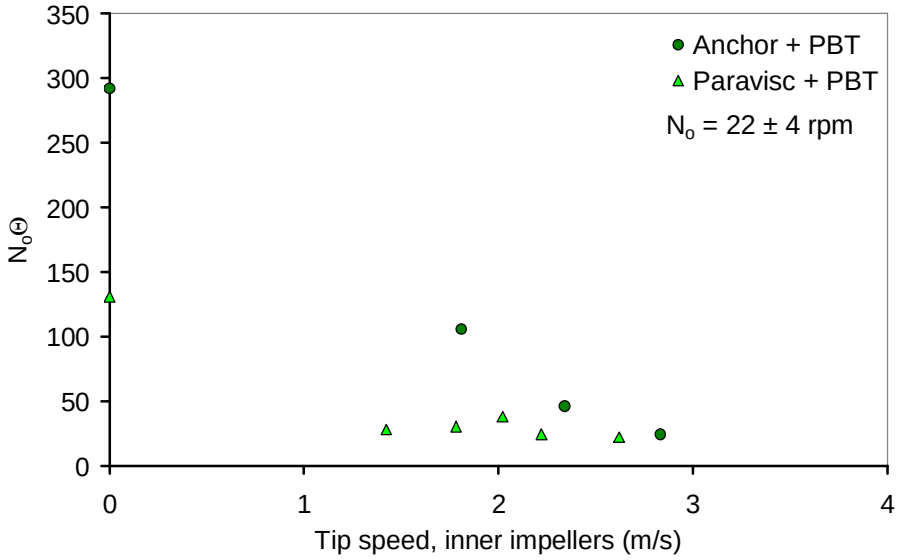

Figure 5-36: Effect of the tip speed of the inner impellers on the mixing time of co-axial mixers in HEC 7%

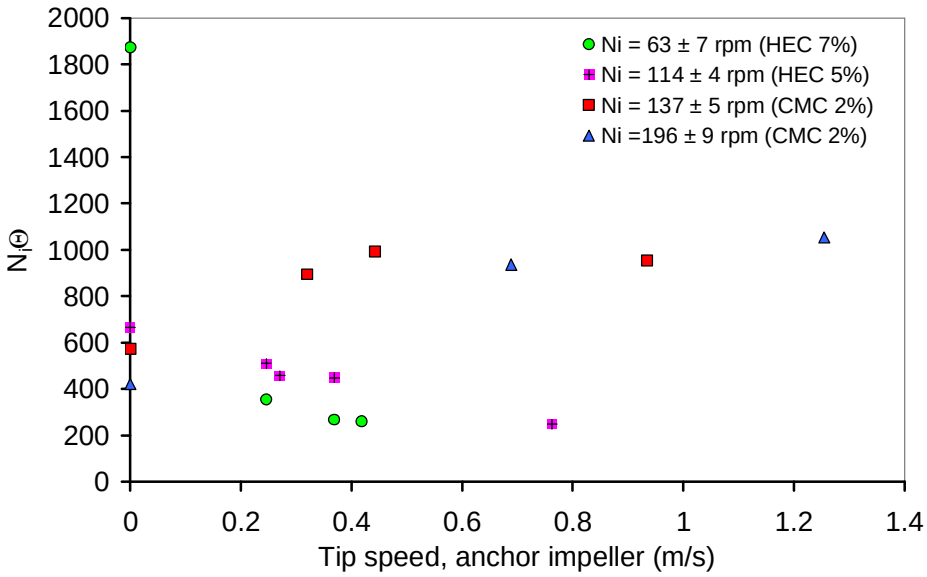

Figure 5-37: Effect of the tip speed of the anchor impeller on the mixing time of co-axial mixers in non-Newtonian fluids

mixing time decreases when the inner impeller rotational speeds increases and is in practical sense negligible when the inner impeller are rotating at sufficient high rotational speed. It is clear that anchor supports the blending when the inner impellers rotate at lower speeds. In case where the viscosity of the fluid is higher, like in HEC 7%, and the regime is

laminar (Re_i = 3 for N_i=63 rpm), the contribution of the anchor impeller to the mixing time is measurable. As expected, the blending efficiency of open impellers like pitched blade turbines decreases in laminar regime and the anchor impeller plays a significant role in the blending.

In summary, the analyses for the co-axial mixer configuration using anchor with PBT reveal the following trends: (i) the inner impeller speed has significant influence on the mixing time of the co-axial mixer in transitional and laminar regimes. (ii) In the transitional regime, the contribution of the anchor impeller in the blending depends on the inner impeller speed, i.e. when inner impellers are rotating at sufficient high speeds; the blending is predominantly governed by the high speed inner impellers. (iii) The role of the anchor impeller gains significance when the regime becomes laminar and/or when the inner impeller speed is low.

Figure 5-38 shows the effect of the proximity impeller Paravisc on the mixing time of the co-axial mixer. Both in transitional and laminar regime, the Paravisc impeller in a co-axial mixer configuration demonstrates a markedly important role in the blending task. Keeping the inner impeller speed constant, reduction in mixing times could be achieved in CMC 2% by rotating the Paravisc faster. This was observed for two constant inner impeller speeds that are relative high, N_i=146 and 210 rpm. In the laminar regime, denoted by the HEC 7% data, the inner impeller speed is kept constant at N_i = 75 rpm and shorter mixing times are also achieved when the Paravisc impeller speed increases. Apparently, the data for Paravisc indicate also a critical tip speed. The analyses of the co-axial mixer configuration Paravisc combined with PBT reveal the following trends: (i) there is a critical tip speed of the inner impellers, which determines roughly the maximum reduction in the mixing time in transitional and laminar regime. Further increase of the inner impeller speed didn't reduce the mixing time significantly. (ii) In the transitional regime, both Paravisc and PBT contribute to the blending, likely collaboratively. (iii) Blending is predominantly governed by the Paravisc in the laminar regime and/or when the inner impeller speed is low. Obviously, all the observations and trends here are valid only within the specified range of experimental conditions.

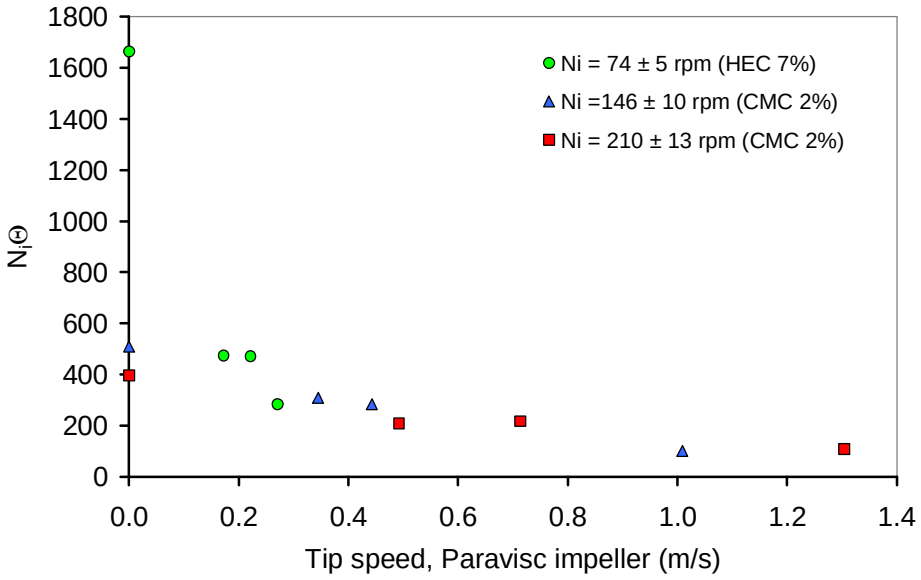

Figure 5-38: Effect of the tip speed of the Paravisc impeller on the mixing time of co-axial mixers in HEC 7% and CMC 2%

5.2.2.4 Effect of the rotating mode

It is possible to operate co-axial mixers in two modes: co-rotating and counter-rotating. The pitched blade turbines usually rotate in the direction, in which a downward axial pumping is promoted. In co-axial mixers, the proximity anchor impeller can be designed to rotate in the same direction as the pitched blade turbines, i.e. in the co-rotating mode or in the opposite direction, i.e. in the counter-rotating mode. If a proximity impeller with axial pumping capability, like the Paravisc impeller, is combined with the pitched blade turbines, the direction of rotation is most appropriately designed to enhance the overall pumping capability and flow circulation inside the vessel, i.e. the pitched blade turbines pump downwards and the Paravisc pumps upwards. It doesn't make sense to vary the rotating mode of the Paravisc, making both impellers to pump in the same direction.

The appropriate rotating mode is undoubtedly an important question in the design of co-axial mixers. In this work, this question is addressed in regard to blending efficiency in non-Newtonian fluids. If the mixer duty is different than the blending, the efficiency should be addressed differently. For instance, applications such as dispersion of fine solids into viscous bulk, emulsification or gas-liquid mixing require distinct performance characterization of the mixer.

The plots in Figure 5-39 show the mixing time as function of the tip speed ratio for the co-axial mixer configuration anchor with PBT in different rotating modes: co-rotating and

counter-rotating. The Reynolds numbers of the inner impellers indicate that the regime is transitional at the concentration of the non-Newtonian fluids used. The measured points that deviate strongly from the rest of the data are marked as open symbols. The data indicate similar trend regardless of the fluid, power input per unit mass and rotating mode. The mixing time reduces as the tip speed ratio increases, i.e. the performance of both co-axial mixers depends significantly on the tip speed ratio. The performance of both co-axial mixers in co-rotating and counter-rotating mode is comparable in the transitional regime.

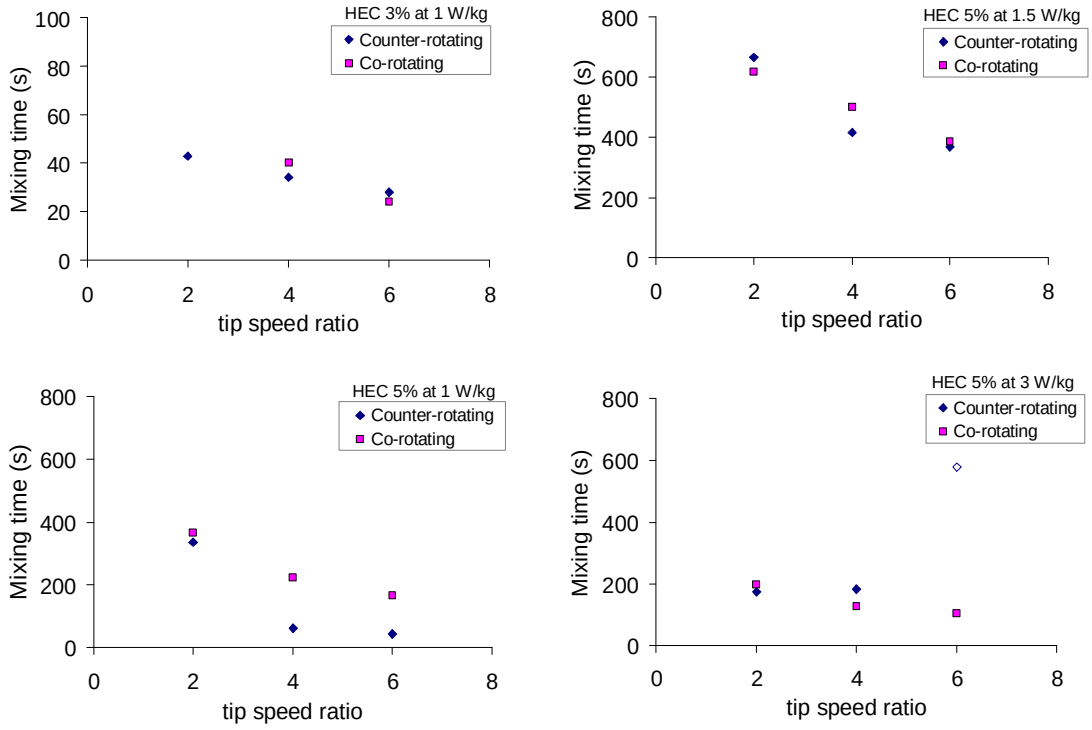

Figure 5-39: Mixing times as function of tip speed ratio for co-axial mixers rotating in different directions in non-Newtonian fluids (transitional regime)

In the laminar regime, the mixing time data for both configurations indicate no clear trend, as plotted in Figure 5-40. The co-rotating mode appears superior to the counter-rotating for most of the measured data points at constant fluid properties and power input per unit mass. The influence of the tip speed ratio is also not clear for the counter-rotating mode in this flow regime. The data points marked as open symbols in these plots are considered outliers and/or indicate that the mixing time measurement was interrupted at this mixing time due to persistent unmixed zones, or to any experimental difficulty.

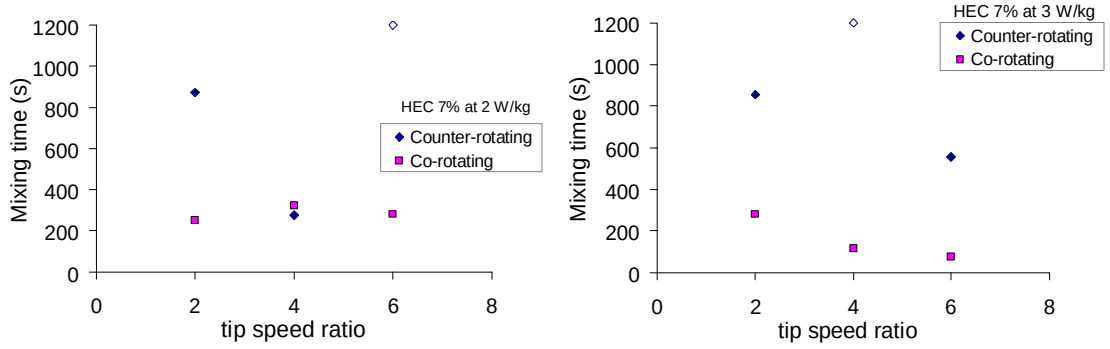

Figure 5-40: Mixing times as function of tip speed ratio for co-axial mixers rotating in different directions in the non-Newtonian fluid (laminar regime)

The role of inner impellers in the overall mixing time of the co-axial mixers is analyzed in Figure 5-41 for a constant speed of the anchor impeller (N_o =21 rpm) and fluid properties. The data show that increasing the inner impeller tip speed the mixing time reduces for both rotating modes. The mixing times obtained at the same inner impeller tip speed are quite similar, in view of the experimental deviations and slight difference in the anchor speed. This reveals that the inner impellers affect the performance of the co-axial mixers with the anchor in co- and counter-rotating mode in a comparable manner.

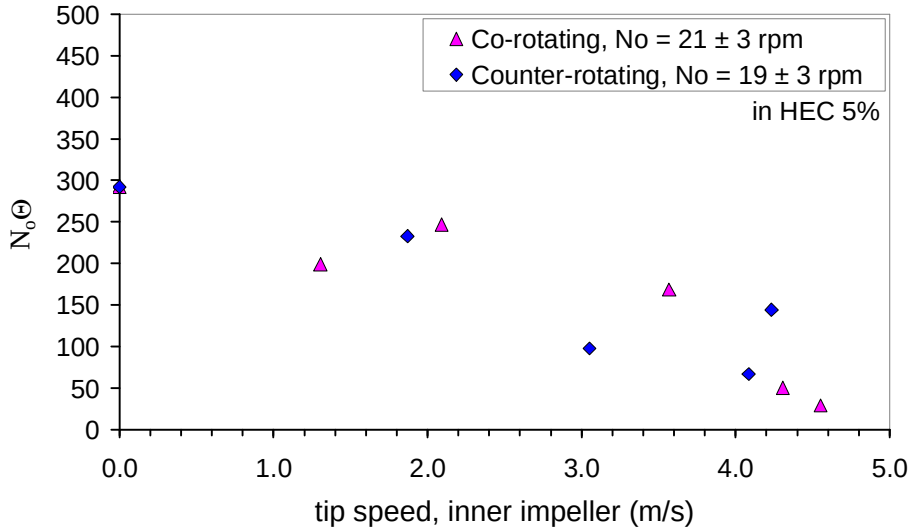

Figure 5-41: Effect of the tip speed of the inner impellers on the mixing time of co-axial mixers with anchor in different rotating modes in HEC 5%

Figure 5-42 plots the mixing time data as function of the anchor tip speed at constant fluid properties (HEC 5%) and roughly constant inner impeller rotational speed, N_i=124 rpm for counter-rotating mode and N_i=112 rpm for co-rotating mode. The data show that

the anchor tip speed has an effect on the mixing time of both mixer configurations at this flow regime and inner impeller speeds. However, the effect of the anchor rotational speed is different for both configurations. The contribution of the anchor impeller on the blending is more efficient when both impellers are co-rotating, because lower mixing times were obtained at the same anchor speed and at lower inner impeller speed, which means at lower power input. However, there are not sufficient data to verify this hypothesis for a broad range of inner impeller speeds and fluid viscosities.

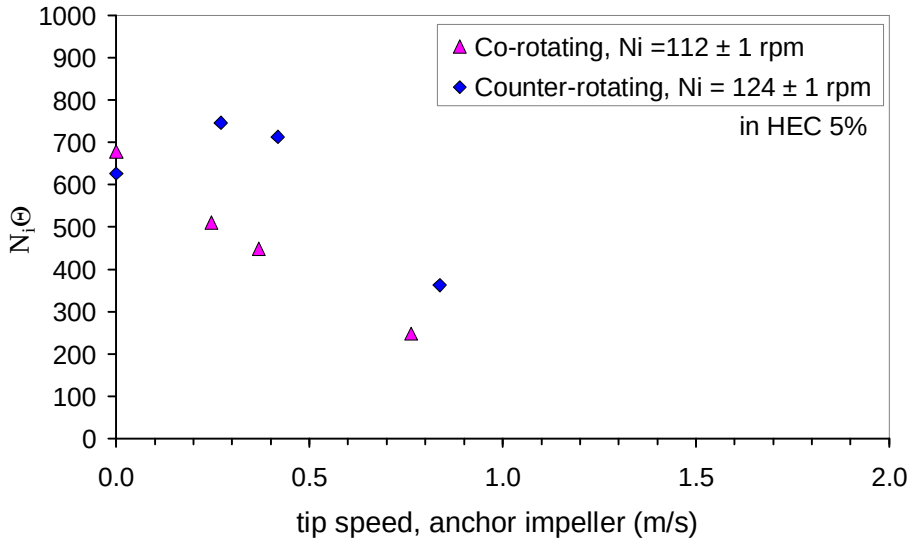

Figure 5-42: Effect of the tip speed of the anchor impeller on the mixing time of co-axial mixers in different rotating modes in HEC 5%

In summary, in the transitional regime, both rotating modes gave similar mixing times at the same tip speed ratio, energy input and fluid properties. The inner impeller speeds play an important role in the blending, since the higher the inner impeller speed is, the shorter is the mixing time regardless of the rotating mode. The anchor tip speed also plays a measurable role in the transitional regime, as the mixing time is reduced as the tip speed of the anchor increases. The effect of the anchor impeller is more efficient in co-rotating mode than in counter-rotating. In the laminar regime, the trends are not clear; however, the data suggest that the performance of the co-axial mixer in counter-rotating mode is worse than in co-rotating mode, as observed for most of the measured data points.

Foucault *et al.* (2004, 2005) made efforts to address the question of the most effective rotating mode in co-axial mixers. Co-axial mixer configurations consisting of an anchor and high speed dispersing turbines like Deflo, Sevin, Cowles, Rushton, were experimentally investigated in terms of power consumption and blending time. Newtonian and non-

Newtonian fluids were used and the flow regimes were transitional and turbulent. The conclusions drawn from their studies for transitional regime were that the co-rotating mode is more effective to blend viscous liquids than the counter-rotating mode and the inner impeller alone demonstrated better blending performance than the counter-rotating. In the turbulent regime, however, the blending is governed by the inner turbines only. The poor blending results of the counter-rotating co-axial mixers were explained by the poor pumping capability, especially close to the liquid surface.

In the present experiments, a more distinct vortex near the shaft could be observed when the impellers were in co-rotating mode. The vortex promotes the draw down of the low viscosity tracer, which was added to the surface to start a measurement. In the counter-rotating mode, tracer is trapped in the wakes behind the proximity impeller, from where it is mixed slowly with the bulk phase compared to the vortex, which quickly transports tracer to the high shear zone of the upper inner impeller.

5.3 Mixing time correlations (review and validation)

Foucault *et.al.* (2005) has proposed to use as a characteristic parameter for a co-axial mixing system the difference in rotational speed between inner impeller and proximity impeller for co-current mode of rotation and the sum of rotational speeds for counter-current mode. The authors applied this approach to co-axial mixing systems consisting of an anchor impeller and various dispersing turbines to obtain exponential dependencies between dimensionless mixing time and modified Reynolds number in the laminar regime for tip speed ratios between 10 and 20. In the transitional and turbulent regimes, this approach can not be applied because it makes use of the Metzner-Otto concept to determine the effective viscosity. In these regimes, Foucault *et al.* obtained constant dimensionless mixing times. The characteristic speed was defined as:

$$N_{R,co\text{-}rotation} = N_i - N_o \tag{5-17}$$

$$N_{R,counter\text{-}rotation} = N_i + N_o \tag{5-18}$$

The authors mentioned that these correlations were experimentally determined and were found to be the best choice among several other possible definitions. The correlation uses the Metzner-Otto constant of the inner impeller in the calculation of the effective viscosity by multiplying the Metzner-Otto constant of the inner impeller with the newly defined relative rotational speed N_R:

$$\dot{\gamma} = K_{S,i} \cdot N_R \tag{5-19}$$

Consequently the definition of the Reynolds number needs to be modified to account for the relative impeller speed. The general Reynolds number definition produces the modified Reynolds number for the co-axial system given in equation:

$$Re_{co\text{-}axial} = \frac{\rho \cdot N_R^{(2-n)} \cdot D_i^2}{k \cdot K_{s,i}^{n-1}} \tag{5-20}$$

Figure 5-43 and Figure 5-44 show the dimensionless mixing time over the modified Reynolds number for the investigated co-axial mixing systems in co-rotating mode. Data beyond a Reynolds number of 100 have not been used for fitting because the Metzner-Otto approach is strictly not applicable in the transitional regime.

For co-axial mixing systems with anchor impellers as proximity impeller (Figure 5-43) the data collapse reasonably well to one curve similar to those obtained by Foucault et al. (2005). In contrast to the anchor, the curves for the Paravisc impeller split up by the tip speed ratio (Figure 5-44). The lower the tip speed ratio, the lower the curve of dimensionless mixing time over modified Reynolds number. It is interesting that the mixing time number, $N_R\theta$, is constant at tip speed ratio tr=2, which is analogous to the mixing time characteristic curve of the Paravisc impeller alone. The mixing time number for the co-axial mixer at tr=2 is $N_R\theta$= 114, which is very similar to the mixing time number found for the Paravisc alone, $N_o\theta$= 131. At this tip speed ratio, the inner turbines rotate very slowly, suggesting that the blending is predominantly governed by the proximity impeller Paravisc. The plots show that the contribution of the Paravisc impeller to the overall mixing time differs from that of the anchor impeller, as discussed in the preceding section. The reason for this might be due to the ability of the Paravisc to promote axial mixing in contrast to the anchor impeller.

The approach presented by Foucault *et al.* (2005) does not apply for a proximity impeller with an axial pumping capacity. The required shift factor to collapse the mixing time data on a single curve might be linked to the overall axial pumping capacity of the co-axial mixer. Further investigations to confirm this observation are required.

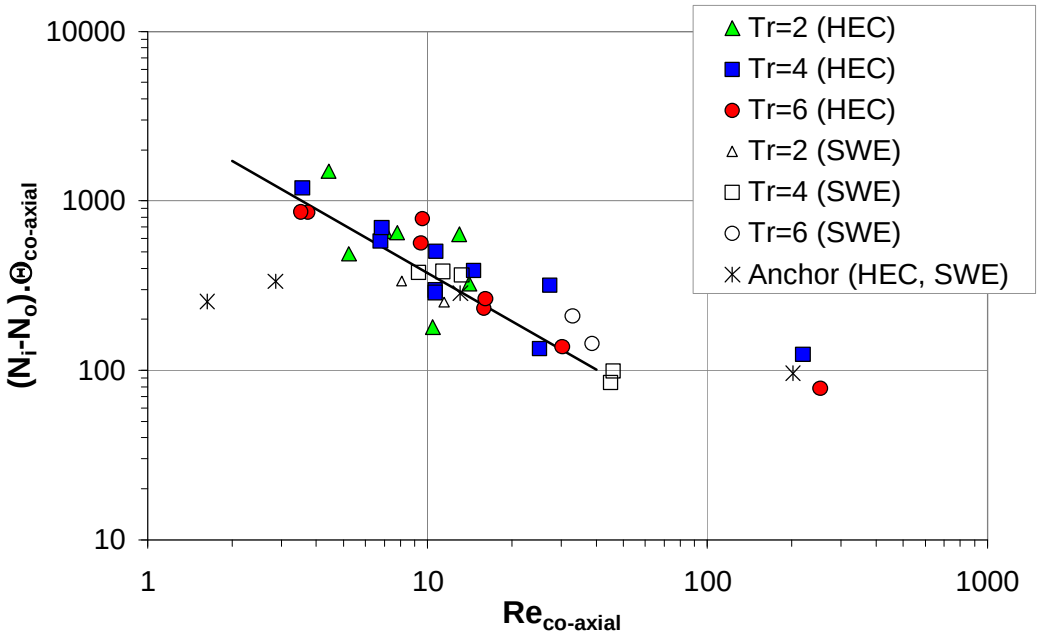

Figure 5-43: Dimensionless mixing time for the co-axial configuration anchor and PBT as a function of a modified Reynolds number according to Foucault *el al.* (2005)

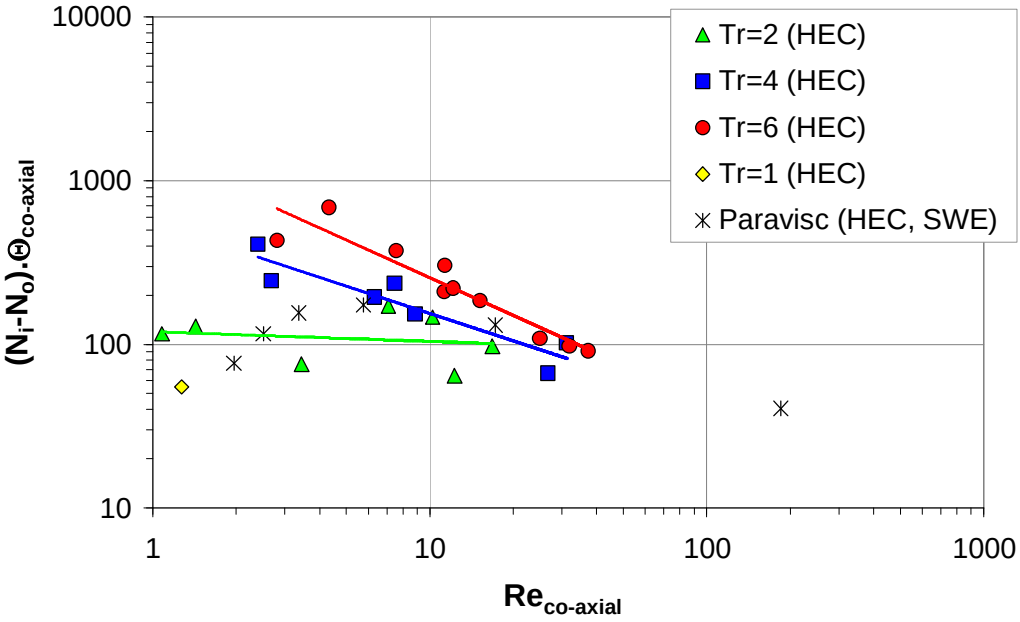

Figure 5-44: Dimensionless mixing time for the co-axial configuration Paravisc and PBT as a function of a modified Reynolds number according to Foucault *el al.* (2005)

Because this correlation does not consider the total energy input, it alone is not able to give information about the effectiveness of the system. Furthermore, using the relative rotational speed is disadvantageous for design purposes, because an infinite number of speed combinations give the same result. As for the analysis based on dimensionless

numbers of one of the impellers, efficiency analysis is complicated by the influence of total power draw. To decide which impellers, which tip speed ratio or which co-axial configuration is most efficient, both mixing time characteristics and power curves need to be considered simultaneously. Based on the limitations of the proposed correlation in the open literature, it is required to explore further design approaches to describe the efficiency of co-axial mixers.

5.4 Efficiency analysis of co-axial mixing systems

For the decision on which mixer or co-axial configuration is the most efficient, it is required that the mixing time and total power consumption by the mixing system are considered simultaneously. The characterization of the entire content of the vessel is required rather than the description of the flow at the vicinity of the impellers.

It seems therefore beneficial to use the vessel Reynolds number (Re_V) to describe the flow in the entire vessel volume:

$$Re_V = \frac{\rho T^2}{\Theta \eta} = \frac{1}{Fo} \tag{5-21}$$

where T is the vessel diameter, θ is the mixing time, i.e. the characteristic velocity is T/θ and the characteristic length is the tank diameter T. The inverse of the vessel Reynolds number is the Fourier number (Fo).

The problem of the characterization of the flow in the entire volume of the vessel is amplified when non-Newtonian fluids are used. The velocity decreases from the impeller tips to the wall and so do the shear rates. Hence, in the case of shear thinning fluids, the viscosity increases as the distance from the inner impellers increases. This raises the question which viscosity should be used in the Reynolds number to describe the flow generated by co-axial mixing systems. The Metzner-Otto concept stipulates that the average shear rate in the fluid near an impeller is proportional to the impeller rotational speed (N), and this is only valid in the laminar flow regime.

The disadvantage of this approach in the design of co-axial mixing systems is that the determined shear rate is based on the viscosity at the immediate vicinity of one impeller type (inner or outer). Furthermore, the mixing rate was critical at the wall region, actually the rate-limiting. It was frequently observed in the blend time experiments that the last unmixed zone in the vessel was the tracer striations in regions near the wall. The mixing

time to dissolve the unmixed torus located below the upper impeller that appeared for some design configurations and operating conditions was not the blending criterion in the present analysis, since the formed tori are usually very stable and blend time would be extremely high. The further analysis of the measured blend times regards the rate of mixing in the region near the proximity impellers as it is the rate that controls the blending of the entire vessel content. Thus, it seems adequate to determine the shear rate in this region when evaluating the mixing time of co-axial mixers. It would not be correct to determine the shear rate based on the velocity of the proximity impeller only, because, as previously discussed in the power consumption analysis, the tip velocity of the inner impellers affects the velocity field of the proximity impellers, experienced by the power consumption variation. Thus, the parameter to characterize the flow in the co-axial mixing tank was chosen to be the torque of the inner impellers, which influences the shear field in the tank and in case of non-Newtonian fluids, the viscosity.

The shear rate can be determined by means of a torque balance relating the shaft torque of the impellers (M) to the friction drag of the cylindrical tank body and bottom and drag of the baffles (in case one exists), Bird *et al.* (1960):

$$M = \eta \iint_S R\left(\partial v_\theta / \partial r\right)_S dS + \iint_A R p_{baffles} dA \tag{5-22}$$

The total area of the tank is denoted with S, A is the surface area of the baffles, v_θ is the tangential velocity, R is the radial distance from the impeller axis of rotation to the surface element dS or dA and $p_{baffles}$ is the pressure drop on the baffles. It was assumed that the vessel has a flat shape and the shear stress is constant in the entire vessel surface. The pressure losses due to baffles are assumed to be negligeble in the co-axial mixers and proximity impellers.

Integrating and re-arranging the equations, it gives:

$$M = \tau \cdot 1.5343 T^3 \tag{5-23}$$

$$\tau = \left(\frac{1}{1.5343}\frac{1}{T^3}\right) M \tag{5-24}$$

Now, the effective viscosity of the fluid can be calculated using the Ostwald-de Waele model:

$$\eta_{eff} = k^{1/n} \tau^{(n-1)/n} \tag{5-25}$$

The plot of $Ne^{1/3} \cdot Re$ versus Fo results in a mixing time characteristic. The dimensionless numbers are expressed as following:

$$Ne^{1/3}\, Re = \left(\frac{P_{total} D_i}{\rho} \right)^{1/3} \frac{\rho}{\eta_{eff}} \qquad (5\text{-}26)$$

The diameter of the inner impellers (D_i) was used in the dimensionless numbers. The torque of the inner impellers is employed to characterize the flow in the tank, so that using D_i makes the correlation consistent. In Figure 5-45 are the plots of the data of the mixing time characteristic of the investigated co-axial mixing systems.

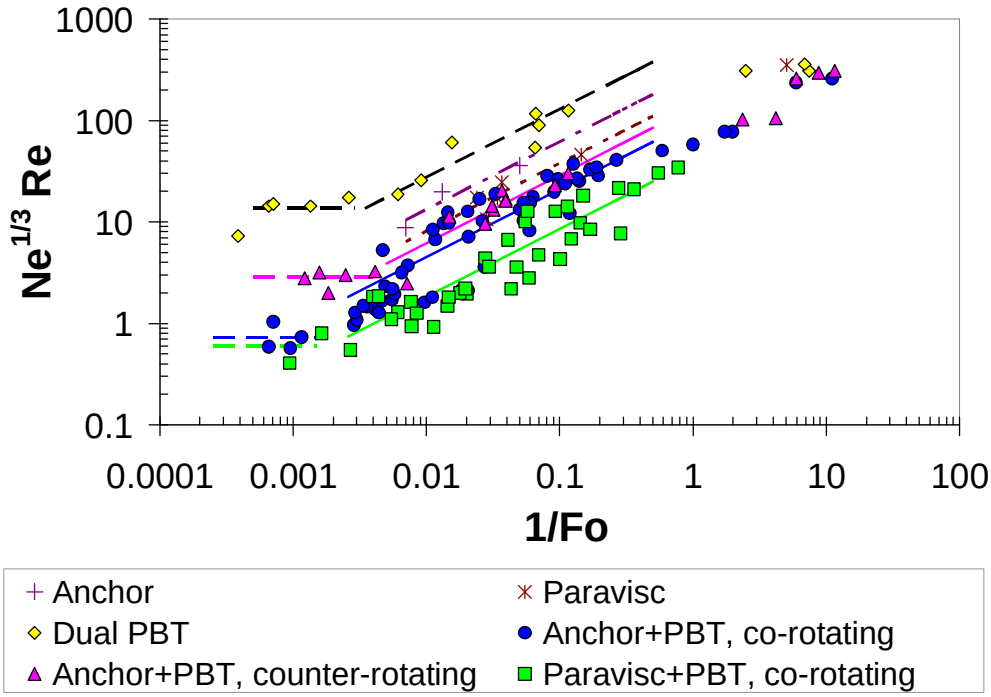

Figure 5-45: Mixing time characteristic curves for all investigated agitation systems in Newtonian and Non-Newtonian fluids

The data points for the investigated single impeller systems using their respective diameters are also plotted in Figure 5-45 for comparison. The approach to calculate the effective viscosity of the single impellers was different for the co-axial mixers, as previously described. In the case of non-Newtonian fluids, the effective viscosity was calculated as usual for single impeller systems, i.e. by means of the Metzner Otto concept. The individual Metzner-Otto constants of the impellers are given in Table 5-1.

As the viscosity increases, the data in Figure 5-45 indicate that there is a minimum Re_V in which the mixing time will not be reduced even if larger speeds (or larger P_{Total}) are

applied. For the systems investigated, the $Re_{V,min}$ was found to be 0.0027 for both co-axial configurations in co-rotating mode and for the dual set of the pitched blade turbines, and 0.007 for the co-axial configuration using anchor in counter-rotating mode. There is not sufficient data to identify the $Re_{V,min}$ for the proximity impellers (anchor and Paravisc) as single mixing systems.

Previous published work reported that the transitional regime starts at $1/Fo_{crit}=0.25$ (Zlokarnik, 1967) and $1/Fo_{crit}=1$ (Hoogendoorn and Den Hartog., 1967). The number of measurements is not sufficient to determine the $1/Fo_{crit}$ or $Re_{V,crit}$ with accuracy. However, the measured data in the present work suggest that the transitional regime starts at $1/Fo_{crit}=0.25$ for the co-axial mixer configurations.

The Newtonian and non-Newtonian data between $Re_{V,min}$ and $Re_{V,crit}$ were combined and fitted by using following expression:

$$Ne^{1/3} Re\, Fo^{2/3} = const. \pm \text{RSD} \qquad (5\text{-}27)$$

In Figure 5-46 are the plots of the fitted data using the proportionality constants, which can be found for each co-axial and single agitation systems with the respective relative standard deviation (RSD) in Table 5-9.

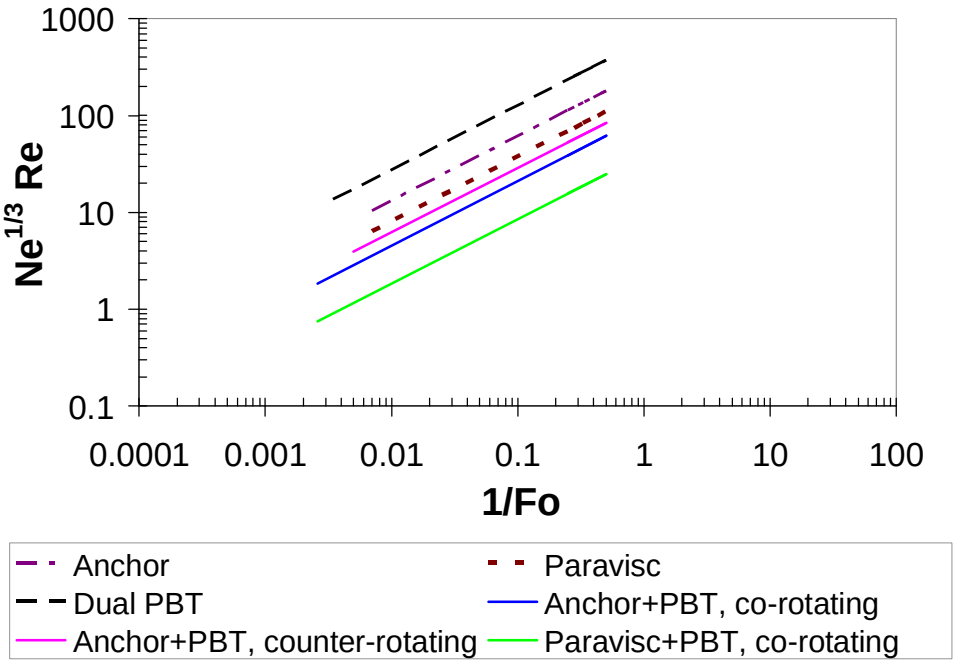

Figure 5-46: Mixing time characteristic curves for all investigated agitation systems in Newtonian and Non-Newtonian fluids

Table 5-9: Proportionality constants and relative standard deviation (RSD)

Configuration	constant	RSD
Dual set of PBT	597	35%
Anchor	287	18%
Paravisc	175	22%
Co-axial anchor + 2x PBT, counter-rotating	134	25%
Co-axial anchor + 2x PBT, co-rotating	98	49%
Co-axial Paravisc + 2x PBT	39	47%

The lower the proportionality constant, the more efficient is the agitation system. The co-axial mixer composed with Paravisc and pitched blade turbines is found to be the most efficient configuration among the investigated co-axial mixer designs. For single impeller systems, the dual set of pitched blade turbines shows the lowest efficiency and Paravisc the highest. The correlation indicates that the anchor combined with PBT in co-rotating mode is more effective than in counter-rotating mode, because this configuration achieves lower mixing times at constant total power input, viscosity and scale. The performance of all investigated co-axial mixer configurations is higher than the single impeller systems. It should be noted that this assessment is valid only for the laminar regime. The data in transitional regime suggest that the performance of the inner impellers as single system becomes equivalent to the performance of the co-axial mixer configuration anchor with PBT. Also the performance of the co-axial mixers anchor and PBT in co-rotating and counter-rotating mode becomes similar in the transitional regime.

The mixing efficiency of the co-axial mixers can be examined by re-arranging Equation (5-27) to:

$$\theta \propto \frac{\eta}{\rho}\left(\varepsilon_M \cdot D_i\right)^{-2/3} \tag{5-28}$$

Equation (5-28) shows that the mixing time reduces as the total power input of mass unit (ε_M in watt/kg) increases. The mixing time is also proportional to the fluid viscosity. In case of shear thinning fluids, the higher the torque of the impellers, the lower is the effective viscosity and the shorter the mixing time at constant geometry. The beneficial effect of larger inner impeller diameter in blending of non-Newtonian and Newtonian fluids in laminar regime is reflected in this expression as well. However, the effect of the outer diameter is not explicitly reflected in equation Eq.(5-28), only in the total power input, since it increases as the diameter of the proximity impeller increases.

The presented mixing time characteristic curves of the co-axial agitation systems aid the efficiency assessment of different configurations. The total power draw of the system can be predicted for a given mixing time. Since the power drawn by the inner impellers remains unchanged in the co-axial mixers, it can be determined using the available standard power curves. Thus, the power consumption of the proximity impeller to achieve a certain mixing time can be determined. The outer impeller diameter is addressed by the tank diameter. However, the information about the required rotational speed of the proximity impeller is not readily available. Consequently, power curves of the proximity impellers in co-axial systems are still required, as obtained in the preceding section of the power consumption analysis.

6 Conclusions, Recommendations and Outlook

Co-axial mixing tank systems seem to be very promising for chemical processes, in particular for applications, in which effective blending of the fluids throughout the range of viscosities and rheological properties that the processes traverse is required. Co-axial mixers exploit synergistically the preferred performance attributes of both open and proximity impellers. However, co-axial mixers are non-conventional, poorly investigated and complex agitation systems. The presence of two impellers that have different geometries and rotate with different speeds in the same vessel poses a challenge to determine the appropriate scaling parameters that govern the flow and mixing phenomena. Reliable design curves are required for practical application.

This doctoral thesis addressed the blending of highly viscous and non-Newtonian fluids in co-axial agitation systems, in particular in the laminar regime. An experimental and numerical study of a pilot-scale co-axial agitation system was carried out in order to explore and determine the design and mixing performance characteristics. The characterization of agitation performance was based on blend time and power consumption measurements for two co-axial design configurations using a dual set of pitched-blade turbine (PBT) as open impellers in combination with a proximity impeller at different operating conditions. Two proximity impellers were employed in this investigation, the standard anchor and a modified helical ribbon known as PARAVISC® (EKATO Rühr- und Mischtechnik GmbH). The effect of relevant operating parameters, such as viscosity, rotational speed ratio, rotating mode (co- and counter-rotation) and total energy input, on blend times and power consumption was investigated and analyzed. In support of the experiments, numerical simulations using the commercial CFD code FLUENT® were carried out to calculate the three-dimensional flow field of the co-axial mixing system.

The data and analysis showed that the power draw of the inner impellers was not affected by the speed of the proximity impellers. In contrast, the speed of the inner impellers affects the power draw of the proximity impellers. The power drawn by the anchor and Paravisc decreased with increased tip speed ratio in co-rotating mode. The power consumption of the anchor impeller in a co-axial mixer in counter-rotating mode was investigated. The data showed that the power draw of the anchor increased with increased

tip speed ratio. The non-Newtonian and Newtonian data are in good agreement for both co-axial mixer configurations, which indicate that the Metzner-Otto constant of the single impeller systems anchor and Paravisc® can be used to determine the effective viscosity of the proximity impeller in a co-axial mixing configuration. The results obtained in the CFD simulations demonstrated the ability to calculate the flow field with sufficient accuracy to determine the power consumption of the inner and the anchor impellers. The power consumption of the Paravisc® in the co-axial mixing configuration, however, was under-predicted by 40%.

The characterization of the power consumption and mixing time of co-axial mixing systems is not trivial because of the presence of two different impellers, with different geometries rotating at different rotational speeds in the same tank. Correlations to determine the power draw as well as to assess the efficiency of co-axial mixers are proposed in this thesis. Previously published correlations in the open literature for power consumption and mixing time of co-axial mixers were tested, but it has been found that they were not applicable to the investigated configurations.

In the present investigation, the experimental data for Newtonian and non-Newtonian fluids in laminar regime were correlated in dimensionless form to develop power curves for the proximity impellers. The power curves were processed into single power master curves by accounting for the tip speed ratio effect. This was done by introducing a speed ratio shift parameter, $K_{P,coax}$ (tr). In contrast to the configuration with anchor, the function of the shift parameter for the configuration with the Paravisc was nonlinear and two independent constants were required to fit the data. With the single master power curves, it is possible to determine the power drawn by the proximity impellers in the laminar regime for tip speed ratios varying from 0 to 6, for Newtonian and non-Newtonian fluids obeying a power law model.

The effect of the key influencing parameters, such as viscosity, tip speed ratio, energy input and rotating mode on the blend time of the investigated co-axial mixers was analyzed in two different forms: the direct comparison, where one parameter was studied by keeping the rest constant, and the analysis using dimensionless numbers. Both analyses showed similar trends and conclusions.

In this thesis, mixing time characteristic curves using well-known dimensionless numbers are proposed to aid the efficiency assessment of different configurations in laminar regime. In this concept, mixing time and total power consumption were considered

simultaneously. The experimental data and analyses demonstrated that the performance of the co-axial mixers was very distinct with respect to the proximity impeller design and flow regime. Within the range of investigated conditions, the results indicated that the co-axial mixer composed of Paravisc® and pitched blade turbines was found to be the most efficient configuration among the investigated co-axial mixer designs. The Paravisc® impeller in general played an important role in the blending, even when the rotational speed of the inner impellers was high. In this configuration, it was observed a critical tip speed ratio, in which further increase in the inner impeller rotational speed to reduce the blend time was not possible. The co-axial configuration using an anchor was not as efficient as expected in the transitional regime, since the single impeller system (dual PBT) achieved similar or shorter mixing time at the same total power input per mass. However, in the laminar regime, the contribution of the anchor impeller gained significance. The performance of all investigated co-axial mixer configurations was in general higher than the single impeller systems in the laminar regime. For single impeller systems, the dual set of pitched blade turbines showed the lowest efficiency and Paravisc® the highest. The data in transitional regime suggested that the performance of the inner impellers as single system becomes equivalent to the performance of the co-axial mixer configuration anchor with PBT. It was also shown that the anchor combined with PBT in co-rotating mode was more effective than in counter-rotating mode in the laminar regime, but the performance the both configurations seem to become similar in the transitional regime.

With the mixing time characteristic curves the total power draw of the system can be predicted for a given mixing time and agitation system design. Since the power drawn by the inner impellers remains unchanged in the co-axial mixers, it can be determined using the available standard power curves. Thus, the power consumption of the proximity impeller to achieve a certain mixing time can be determined.

The initial investment of two drivers for a co-axial mixing tank might be higher compared to the costs of a conventional standard baffled one. However, this must be individually balanced with the real benefits that a co-axial mixer can bring to the process, e.g. reduction of blending time, broad applicability regarding viscosity range, and possibly inhibition of fouling.

Although this thesis contributed to establish new fundamental knowledge about the fluid dynamics and performance of co-axial agitation systems in non-Newtonian viscous blending, further investigations are required for a common understanding about the fluid

mechanics, performance characteristics, design guidelines and scale-up criteria. Among the key conclusions are that there is a need in particular for: i) applying the available correlations in different scales and geometries; ii) defining the limitations of the available design correlations; iii) establishing the effect of the diameter ratio and incorporating in the design concept; iv) further measurements of mixing performance in transitional regime to verify observations and conclusions of this work; v) velocity measurement in co-axial mixing systems in combination with numerical flow simulations (for instance CFD) to elucidate the flow field characteristics of co-axial mixing systems in deeper details.

7 Appendix

Power law parameters as function of the HEC weight concentration

Viscosity as function of the shear rate and weight concentration of HEC in aqueous solution can be described by power law model, as following:

$$\eta(\dot{\gamma}, w) = k(w)\dot{\gamma}^{n(w)-1} \tag{7-1}$$

where the parameters of the power law model, *k* and *n* are function of the weight concentration of HEC (*w*) in aqueous solution divided by 100. For instance, *w*=0.07 for a HEC solution with 7% weight concentration (i.e. HEC 7%).

The functions of *k* and *n* are described by the following mathematical expressions:

$$k(w) = \sqrt{\frac{F + H.w^2 + J.w^4 + L.w^6}{1 + G.w^2 + I.w^4 + K.w^6}} \tag{7-2}$$

$$n(w) = A + B \cdot \left[1 - \left(1 + e^{\left(\frac{w + D \cdot ln\left(2^{\frac{1}{E}} - 1\right) - C}{D}\right)}\right)^{-E}\right] \tag{7-3}$$

The fitting parameters are defined as:

Parameters for *n=f(w)* Eq.(6-2)		Parameters for function *k=f(w)* Eq.(6-3)	
A =	0.90680731	F =	-0.53694093
B =	-0.50700677	G =	-491.155214
C =	0.03404728	H =	7668.05005
D =	0.00490948	I =	102217.222
E =	0.25209258	J =	-25334476.6
		K =	-6887950.97
		L =	$2.5496 \cdot 10^{10}$

8 References

ANSYS® ICEM CFD™, Software version 5.0 (2005). ANSYS Inc., Canonsburg, PA.

Ascanio G., Foucault S., Tanguy P. (2003): Performance of a new mixed down pumping impeller. Chem. Eng. Technology, 26, 8, 908 – 911.

Aubin J., Xuereb C. (2006): Design of multiple impeller stirred tanks for the mixing of highly viscous fluids using CFD. Chemical Engineering Science, 61, 2913 – 2920.

Baltussen J. (2005): The prediction of mixing patterns and mixing time of viscous shear thinning liquids. Benelux Fluent User's Group Meeting, October 5-6. Fluent Inc., Lebanon NH.

Barar Pour S., Fradette L., Tanguy P.A. (2007): Laminar and slurry blending characteristics of a dual shaft impeller system. Chemical Eng. Research and Design 85(A9), 1305 – 1313.

Bird R. B., Stewart W. E., Lightfoot E. N. (1960): Transport phenomena, Wiley International Edition, John Wiley & Sons, New York. Chapter 6, pg. 205.

Birtigh A., Lauschke G., Schierholz W.F., Beck D., Maul C., Gilbert N., Wagner H.-G., Werninger C. Y. (2000): CFD in der chemischen Verfahrenstechnik aus industrieller Sicht. Chemie Ingenieuer Technik (72), 3, pp. 175 – 193.

Bonnot S., Cabaret F., Fradette L., Tanguy P.A.(2007): Characterization of mixing patterns in a coaxial mixer. Trans IChemE, Part A, Chemical Engineering Research and Design, 2007, 85(A8), 1129 – 1135.

Brucato A, Ciofalo M., Gridafi F., Micale, G. (1998): Numerical prediction of flow fields in based stirred vessels: A comparison of alternative modelling approaches. Chemical Engineering Science, Vol. 53, No. 21, pp. 3653-3684.

Carreau P. J., Chhabra R. P., Cheng J. (1993): Effect of Rheological Properties on Power Consumption with Helical Ribbon Agitators. Fluid Mechanics and Transport Phenomena, AIChE Journal, vol 39, 9, 1421 – 1430.

Chavan V. V. (1983): Close-clearance helical impellers: a physical model for Newtonian liquids at low Reynolds numbers. AIChE Journal, Vol 9, N°2, 177 – 186.

Chowdhury R. and Tiwari K. K. (1979): Power consumption studies of helical ribbon-screw mixers. Ind. Eng. Chem. Process Des. Dev., Vol. 18, No. 2, 227 – 231.

Delaplace G., Leuliet J. C., Relandeau V. (2000a): Circulation and mixing times for helical ribbon impellers. Review and Experiments. Experiments in Fluid, 28, 170 – 182.

Delaplace G., Torrez C., André C., Belaubre N., Loisel P. (2000b): Numerical simulation of flow of Newtonian fluids in an agitated vessel equipped with a non standard helical ribbon impeller. Proc. of the 10th European Conference on mixing, Delft, Netherlands, 289 – 296.

Delaplace G., Guerin R., Leuliet J. C., Chhabra R. P. (2006): An analytical model for the prediction of power consumption for shear-thinning fluids with helical ribbon and helical screw ribbon impellers. Chemical Engineering Science 61, 3250 – 3259.

Ekato Handbuch der Rührtechnik (2000), EKATO Rühr- und Mischtechnik GmbH, Schopfheim.

Espinosa-Solares T., Brito de la Fuente E., Tecante A., Tanguy, P. A. (1997): Power consumption of dual turbine-helical ribbon impeller mixer in ungassed conditions. Chemical Eng. Journal, 67 (3): 215 – 219.

Fangary Y. S., Barigou M., Seville J. P. K., Parker D. J. (2000): Fluid trajectory in a stirred vessel of non-Newtonian liquid using positron emission particle tracking. Chemical Engineering Science 55 (2000), 5969 – 5979.

Farhat M., Rivera C., Fradette L., Heniche M., Tanguy P. A. (2007): Numerical and experimental study of a dual-shaft coaxial mixer with viscous fluids. Ind. Eng. Chem. Res., 46(14), 5021 – 5031.

Farhat M., Rivera C., Fradette L., Tanguy P.A. (2008): Revisiting the performance of a coaxial mixer. Ind. Eng. Chem. Res., 47, N°10, 5021 – 5031.

FLUENT® User's Guide (2006). Fluent Inc., Lebanon, NH.

Foucault S., Ascanio G., Tanguy P. A. (2004): Coaxial mixer hydrodynamics with Newtonian and non-Newtonian fluids. Chem. Eng. Tech., 27, 3, 324 – 329.

Foucault S., Ascanio G., Tanguy P. A. (2005): Power characteristics in coaxial mixing: Newtonian and non-Newtonian fluids. Ind. Eng. Chem. Res., 44: 5036 – 5043.

Foucault S., Ascanio G., Tanguy P. A. (2006): Mixing times in coaxial mixers with Newtonian and non-Newtonian fluids. Ind. Eng. Chem. Res., 45: 352 – 359.

GAMBIT® (2006). Software version 2.2. Fluent Inc., Lebanon, NH.

Garred E. (1996): Comparative mixing times in pseudoplastic fluids. BHR Group Limited Fluid Mixing Processes Consortium Report FMP 060 - Cranfield, Bedford.

Harnby N.; Edwards M. F.; Nienow A. W. (1992): Mixing in the process industries, 2nd ed.; Butterworth-Heinemann Ltd., Oxford.

Harvey A. D., Lee C. K., Rogers S. E. (1995): Steady-state modeling and experimental measurement of a baffled impeller stirred tank. Fluid Mechanics and Transport Phenomena. AIChE Journal, vol 41, 10, pp. 2177 – 2186.

Harvey A. D., West D. H., Tufillaro N. B. (2000): Evaluation of laminar mixing in stirred tanks using a discrete-time particle-mapping procedure. Chemical Engineering Science, 55, pp. 667 – 684.

Heiser M., Ritter J., Klepp G.-H. (2004): Experimentelle und numerische Untersuchungen von Koaxialrührwerken. Proceedings of the 7th Köthener Rührer-kolloquium, Fachhochschule Anhalt, Köthen, Germany.

Heiser M., Ritter J., Sperling R., Kraume M. (2007): Koaxialrührwerk zum Rühren hochviskoser und nicht-Newtonscher Medien. Chemie Ing. Technik, 79, 7, 1029-1034.

Hirschberg S., Mathys P., Rütti A. (2006): Validation of CFD simulations with LIF data for the Sulzer mixers SMX and SMR. Proceedings of the 12th European Conference on Mixing. June 27-30, Bologna. Pages 599 – 606.

Höcker H. (1979): Untersuchungen zum Leistungsbedarf und Stoffübergang in Rührreaktoren. Dissertation, Universität Dortmund.

Hoogendoorn C. J., Den Hartog A. P. (1967): Model studies on mixers in the viscous flow region. Chemical Engineering Science, vol. 22, 1689 – 1699.

Iranshahi A., Heniche M., Bertrand F., Tanguy P.A. (2006): Numerical investigation of the mixing efficiency of the Ekato Paravisc impeller. Chemical Engineering Science, 61, 2609 – 2617.

Jones D. S., Woolfson A. D., Brown A. F. (1997): Textural, viscoelastic and mucoadhesive properties of pharmaceutical gels composed of cellulose polymers. Int. Journal of Phamaceutics, 151, 223 – 233.

Kelessidis V. C., Maglione R., Tsamantaki C., Aspirtakis Y. (2006): Optimal determination of rheological parameters for Herschel-Bulkley drilling fluids and impact on pressure drop, velocity profiles and penetration rates during drilling. Journal of Petroleum Science and Engineering, 53, 203 – 224.

Kelly W., Gigas B. (2003): Using CFD to predict the behaviour of power law fluids near axial-flow impellers operating in the transitional flow regime. Chemical Engineering Science, 58, 2141-2152.

King R. L., Hiller R. A., Tatterson G. B. (1988): Power consumption in a mixer. AIChE Journal, Vol. 34, No. 3, 506 - 509.

Köhler S., Hemmerle W. (2003), Analysis of the power characteristic of a coaxial agitator with varied diameter and speed ratio of inner and outer mixing device. Proceedings of the 11th European Conference on Mixing, Bamberg, Germany, VDI-Gesellschaft Verfahrenstechnik und Chemieingenieurwesen (VDI GVC), Berlin, 14-17.

Kraume M., Zehner P. (2001): Experience with experimental standards for measurements of various parameters in stirred tanks – A comparative test. Chem. Eng. Res. Des. Trans IChemE, Vol 79 Part 8, 811-818.

Kraume M. (2003): Mischen und Rühren, Grundlagen und moderne Verfahren. Wiley-VCH Verlag, Weinheim, ISBN 3-527-30709-5.

Kuncewicz, Cz., Pietrzykowski, M. (2001): Hydrodynamic model of a mixing vessel with pitched-blade turbines. Chemical Engineering Science, 56, 4659-4672.

Kuriyama M., Inomata H., Arai K., Saito S. (1982): Numerical solution for the flow of highly viscous fluid in agitated vessel with anchor impeller. AIChE Journal, 28, 3, 385-391.

Lipp C. W., Melton L. A., Spradling R. W., Paulson K. A. (2002): DISMT – Determination of Mixing Time through Color Changes. Chemical Engineering Communications, 189, 322-338.

Liu S., Hrymak A. N., Wood P. E. (2006): Laminar mixing of shear thinning fluids in a SMX static mixer. Chemical Engineering Science, 61, 1753 – 1759.

Luo, J. Y., Issa, R. I. and Gosman, A. D. (1994): Prediction of impeller-induced flows in mixing vessels using multiple frames of reference, IChemE Symp. Ser. 136, 549 - 556.

Marschall M. E. and Bakker A. (2002): Computational Fluid Mixing. Fluent Inc., Lebanon.

Metzner A. B., Feehs R. H., Ramos H. L., Otto R. E., Tuthill J. D. (1961): Agitation of viscous Newtonian and non-Newtonian fluids. AIChE Journal, 7, 1, 3-39.

Metzner A. B., Otto, R. E. (1957): Agitation of non-Newtonian fluids. AIChE Journal, 3, 1, 3-10.

Metzner A. B., Taylor J. S. (1960): Flow patterns in agitated vessels. AIChE Journal, 6, 1, 109-217.

Murakami Y., Fujimoto K., Takafumi S., Yamada A., Asano K. (1972): Evaluation of performance of mixing apparatus for high viscosity fluids. J. Chem. Eng. Japan, vol. 5, 3, 297-303.

Murthy, J. Y., Mathur, S. R. and Choudhury, D. (1994): CFD simulation of flows in stirred tank reactors using a sliding mesh technique, IChemE Symp. Ser. 136, 341 - 348.

Murthy Shekhar, S. and Jayanti, S. (2003): Mixing of power-law fluids using Anchors: Metzner-Otto Concept revisited". AIChE Journal, vol. 49, No.1.

Nagata S., Nishikawa M., Katsube T., Takaish K. (1972): Mixing of highly viscous non-Newtonian liquids. Int. Chem. Engineering, Vol.12, No.1: 175-182.

Nagata S., Nishikawa M., Tada H., Gotoh S. (1971): Power consumption of mixing impellers in pseudoplastic liquids. Journal of Chemical Engineering of Japan, Vol 4, N°1, 72-76.

Nagata S. (1975): Mixing: Principles and Applications, Wiley.

Nienow A. W., Elson T. P. (1988): Aspects of mixing in rheologically complex fluids. Chem. Eng. Research and Design, 66, 5 – 15.

Novàk V. and Rieger F. (1975): Homogenization efficiency of helical ribbon and anchor agitators. The Chemical Engineering Journal, 9, 63 – 70.

Oldshue J. Y. (1983): Fluid mixing technology. McGraw-Hill Pub. Co., New York.

Paschedag A. R. (2004): CFD in der Verfahrenstechnik. Wiley-VCH Verlag GmbH & Co. KGaA, Weinheim.

Patankar, S. V. (1980): Numerical heat transfer and fluid flow. ISBN 0-89116-522-3.

Paul E. L., Atiemo-Obeng V., Kresta S. M. (2004): Handbook of industrial mixing. Wiley, New York.

Pedrosa S. M. C. P. and Nunhez J. R. (2000): The behavior of stirred vessels with anchor tape impellers. Computers and Chemical Engineering 24, 1745 – 1751.

Peters D. C. and Smith J. M.: (1969): Mixing in anchor agitated vessel. Can. J. Chem. Eng., 47, 268.

Rieger F. and Novàk V. (1973): Power consumption of agitators in highly viscous non-Newtonian liquids. Trans. of the Institution of Chemical Engineers, 51, 105–111.

Rieger F., Novàk V., Havelková D. (1985): Homogenization efficiency of helical ribbon agitators. The Chemical Engineering Journal, 33, 143–150.

Rivera C., Foucault S., Heniche M., Espinosa-Solares T., Tanguy P.A. (2006): Mixing analysis in a coaxial mixer. Chem. Eng. Science, 61, 2895–2907.

Rudolph L., Schaefer M., Atiemo-Obeng V., Kraume M. (2007): Experimental and numerical analysis of power consumption for mixing of high viscosity fluids with a co-axial mixer. Trans IChemE, Chemical Engineering Research and Design, Vol 85 (A5) 568–575.

Sawinsky J., G. Havas and A. Deák (1976): Power requirement of anchor and helical ribbon impellers for the case of agitating Newtonian and pseudo-plastic liquids. Chemical Engineering Science, vol. 31, 6, 507–509.

Shervin C. R., Raughley D. A., Romaszewski R.A. (1991): Flow visualization scale up studies for the mixing of viscoelastic fluids. Chemical Eng. Science, vol. 46, 11, 2867 – 2873.

Stein W. A. (1993): Rührleistung und Wärmeübergang auf der Innenseite eines Rührbehälters mit verschiedenen Wendel-Rührern. Forschung im Ingenieurwesen – Engineering Research Bd. 59, Nr.9, 165 – 172.

Szalai E. S., Arratia P., Johnson K., Muzzio F. J. (2004): Mixing analysis in a tank stirred with Ekato Intermig® impellers. Chemical Engineering Science, 59, 3793 – 3805.

Takahashi K., Arai K., Saito S. (1980): Power correlation for anchor and helical ribbon impellers in highly viscous liquids. Journal of Chemical Engineering of Japan, vol. 13, N° 2, 147-150.

Takahashi K., Yokota T., Konno H. (1984): Power consumption of helical ribbon agitators in highly viscous pseudoplastic liquids. Journal of Chemical Engineering Japan, vol. 17, 657–659.

Takahashi K., Horiguchi H., Mishima M., Yatomi R. (2006): Mixing characteristics in a vessel agitated by large paddle impeller MAXBLEND®. Proceedings of the 12th European Conference on Mixing, Bologna, Italy, AIDIC The Italian Association of Chem. Engineering.

Tanguy P. A, Thibault F. Brito-De La Fuente E., Espinosa-Solares T. and Tecante A. (1997): Mixing performance induced by coaxial flat blade-helical ribbon impellers rotating at different speeds. Chemical Engineering Science, Vol. 52, 11, 1733–1741.

Thibault F., Tanguy P. A. (2002): Power draw analysis of a coaxial mixer with Newtonian and non-Newtonian fluids in the laminar regime", Chem. Eng. Science, 57: 3861–3872.

Todtenhaupt E., Schneider T. (1990): Mischzeiten und Wärmeübergang in Koaxialrührwerken. Chem. Ing. Tech., 62, (3): 208–109.

Tschuor L., Widmer F. (1992): Charakterisierung eines Doppelwellen-Rührwerkes. Chem.-Ing.-Tech., 64, Nr.11, 1036–1038.

Ulbrecht J.J., Patterson G.K. (1985): Mixing of liquids by mechanical agitation. Gordon and Breach Science publishers, New York. ISSN:0734-1644.

Weetman R. J., Coyle C. K. (1989): The use of fluidfoil impellers in viscous mixing applications. AIChE Annual Meeting, San Francisco, CA.

Weetman R. J. (1991): Development of Transitional Flow Mixing Impeller. Proc. 7th European Conference on Mixing, Brugge, Belgium.

Weetman R. J. (1997): Automated sliding mesh CFD computations for fluidfoil impellers. Proc. 9th European Conference on Mixing, Paris, France.

Zalc J. M., Alvarez M. M., and Muzzio F. J., Arik B.E. (2001): Extensive Validation of Computed Laminar Flow in a Stirred Tank with Three Rushton Turbines. AIChE Journal, Fluid Mechanics and Transport Phenomena, vol. 47, N° 10, 2144 – 2154.

Zalc J. M., Szalai E. S., Alvarez M. M., and Muzzio F. J. (2002): Using CFD to understand chaotic mixing in laminar stirred tanks. AIChE Journal, Fluid mechanics and Transport Phenomena, vol 48, N°10, 2124 – 2134.

Zlokarnik M. (1967): Eignung zum Homogenisieren von Flüssigkeitsgemischen. Chemie-Ing.-Techn. 39, 9-10, 539–548.